Università degli Studi di Napoli Federico II

Scuola Politecnica e delle Scienze di Base

Dipartimento di Ingegneria Industriale

Dottorato - 35° Ciclo

Design and Optimization of Innovative Offshore Wind Turbine Floating Platforms and Mooring lines

Tutor
Prof. Domenico P. Coiro

Co-tutor
Ing. Giancarlo Troise

Candidato
Guido Lazzerini

Acknowledgments

I would like to thank Isabel, my family, my friends, my tutors and all my colleagues for their invaluable contribution and support, often necessary, in carrying out the work that has allowed the writing of this thesis. The PhD course has been a challenge for me to gain a deeper understanding of a new and hopefully useful technology. The transition to renewable energy is, in almost all areas of mankind's energy consumption, inevitable. However, this energy paradigm shift is filled with dangers, due to the large movement of money and the effect on people's living habits that it entails. Advances in renewable energy technologies, without which a complete transition would be impossible, are inexorably linked to socio-economic advances that are no less important. My effort in trying to make a small contribution to the progress of the transition is therefore multi-disciplinary in nature. It is precisely in this global interpretation of transition that the contribution of anyone who has made an effort to interpret the reality around us can be included. And through discussion, the interpretation of reality can appear clearer to us. It is this exchange of interpretations, which can take place in any area (technical or otherwise) of reality, that lays the most important contribution to my work from the people around me.

> "It is not enough to change the world. That is all we have ever done.
> That happens even without us.
> We also have to interpret this change.
> And precisely in order to change it.
> So that the world will not go on changing without us.
> And so that it is not changed in the end into a world without us."
>
> Günther Anders - The Obsolescence of Man, Volume II - 1956

Ringraziamenti

Ringrazio Isabel, la mia famiglia, i miei amici, i miei tutor e tutti i miei colleghi per il prezioso contributo e il supporto, spesso necessario, per portare avanti il lavoro che ha permesso la scrittura di questa tesi. Il percorso del dottorato ha rappresentato per me una sfida nel comprendere più a fondo una tecnologia nuova e, sperabilmente, utile. La transizione alle energie rinnovabili è, in quasi tutti gli ambiti del consumo energetico del genere umano, inevitabile. Questo cambiamento di paradigma energetico è però pieno di insidie, se non altro per il grosso movimento di denaro e l'effetto sulle abitudini di vita delle persone che esso comporta. Gli avanzamenti delle tecnologie per le energie rinnovabili, senza i quali una completa transizione sarebbe impossibile, sono legati inesorabilmente ad avanzamenti socio-economici che non sono di minore importanza. Il mio sforzo nel cercare di portare un piccolo contributo nel progresso della transizione è quindi di natura multi-disciplinare. E' precisamente in questa interpretazione globale della transizione che si può inserire il contributo di chiunque abbia fatto uno sforzo di interpretazione della realtà che ci circonda. E tramite la discussione, l'interpretazione della realtà ci può apparire più chiara. E' questo scambio di interpretazioni, che può avvenire circa qualsiasi ambito (tecnico o meno) della realtà, il più importante contributo al mio lavoro delle persone che mi circondano.

"Cambiare il mondo non basta. E' tutto ciò che abbiamo sempre fatto.
E questo cambiamento avviene in larga misura senza la nostra collaborazione.
Il nostro compito è anche d'interpretarlo.
E ciò, precisamente, per cambiare il cambiamento.
Affinché il mondo non continui a cambiare senza di noi.
E, alla fine, non si cambi in un mondo senza di noi."

Günther Anders - L'Uomo è Antiquato, Volume II - 1956

Abstract

The research activities carried out in this work were focused on the design and optimisation of floating offshore wind turbines. The floating offshore wind resource has a very large expected impact on the overall energy production scenario. According to an estimate by DNV, the global installed floating offshore wind capacity by 2050 is estimated to be 260 GW. Anyway, the exploitation of such valuable resource remains a technological challenge due to the harsh environment in which they operate and higher costs of installation and maintenance. To reach the ambitious de-carbonisation targets set by European regulations, and envisioned by DNV, the use of the wind resource at offshore sites in the Mediterranean (and also on the Italian coast) seems inevitable. Nevertheless, the installation in these sites presents peculiar conditions, which can be summarised as: lower average wind speed (implying lower energy production) compared to the North Sea, high seabed depths and the absence of an established supply-chain for offshore constructions. It is essential to develop routines and tools to ease the design and optimisation of such systems, in order to reduce the initial investment and thus the cost of produced energy, and to increase the competitiveness of the sector compared to other forms of renewable energy production. In this work, routines were developed for the preliminary design and optimisation of floating platforms and mooring systems, following the most common industry standards and guidelines (DNV-ST-0119, IEC 61400-3-2). A Python™ framework has been developed in which the processes of modifying the geometry and configuration of the platform and mooring lines and calculating the performance of the systems by means of time-domain simulation, carried out using open-source software, are implemented. The optimization of such systems is performed through non-gradient-based algorithms. The combination of such heuristic optimisation algorithms (e.g. genetic algorithms) and performance calculated through numerical simulations in the time domain offers a powerful tool for the design and optimisation of floating platforms and mooring lines, as it allows a large number of design variables to be explored and optimal solutions to be found in the presence of strongly non-linear objective functions. In a first case study, the optimisation environment was used to search for a floating platform and mooring line configuration to meet the requirements of an innovative control type for floating offshore wind farms. In this type of control, by increasing the yaw motion of the entire system, an increase in the wake mixing of the upwind turbines can be achieved to increase the flow velocity and thus the energy production of the turbines in the wake. In a second case study, design routines were used to develop a floating platform with an innovative shape and characteristics. The preliminary design phase was verified with numerical simulations with increasing fidelity and experiments in the towing tank of the University of Naples.

Sommario

L' attività di ricerca sviluppata in questo lavoro riguarda la progettazione e l'ottimizzazione di turbine eoliche offshore galleggianti. Il potenziale della risorsa energetica prodotta da turbine eoliche offshore galleggianti può avere un grande impatto sullo scenario globale della produzione energetica da fonti rinnovabili. Secondo una stima del DNV, la potenza totale dei sistemi eolici offshore galleggianti installati a livello mondiale entro il 2050 potrà ammontare a circa 260 GW. Tuttavia, lo sfruttamento di questa preziosa risorsa rimane una sfida tecnologica a causa dell'ambiente difficile in cui operano i sistemi e dei costi più elevati di installazione e manutenzione. Per raggiungere gli ambiziosi traguardi di decarbonizzazione fissati dai regolamenti europei, l'utilizzo della risorsa ventosa in siti offshore del Mediterraneo (e anche sulle coste italiane) appare inevitabile. Ciononostante, l'installazione in questi siti presenta condizioni peculiari, che possono essere riassunte in: minore velocità media del vento (che implica una minore produzione di energia) rispetto al Mare del Nord, elevate profondità del fondale e assenza di una supply-chain consolidata per le costruzioni offshore. È fondamentale sviluppare routine e strumenti per facilitare la progettazione e l'ottimizzazione di tali sistemi, in modo tale da ridurre il costo iniziale dell'investimento e quindi il costo dell'energia prodotta e aumentare la competitività del settore rispetto ad altre forme di produzione dell'energia. In questo lavoro, sono state sviluppate routine per il design preliminare e l'ottimizzazione delle piattaforme galleggianti e dei sistemi di ormeggio, seguendo le indicazioni dei più diffusi standard e linee guida del settore (DNV-ST-0119, IEC 61400-3-2). E' stato sviluppato in ambiente di programmazione Python™ un framework nel quale sono implementati i processi di modifica di geometria e configurazione della piattaforma e delle linee di ormeggio e il calcolo delle performance dei sistemi tramite simulazione nel dominio del tempo, effettuate tranute software open-source. L'ottimizzazione di tali sistemi viene eseguita mediante algoritmi non basati sul gradiente. La combinazione di algoritmi di ottimizzazione non basati su gradiente (ad esempio algoritmi genetici) e performance calcolate tramite simulazioni numeriche nel dominio del tempo offre un potente strumento per la progettazione e l'ottimizzazione di questi sistemi, in quanto consente di esplorare un gran numero di opzioni e di individuare le soluzioni ottimali, in presenza di funzioni obiettivo fortemente non-lineari. In un primo caso studio, l'ambiente di ottimizzazione è stato utilizzato per ricercare una configurazione di piattaforma galleggiante e di linee di ormeggio in modo tale da rispettare i requisiti di una tipologia di controllo innovativa per campi eolici galleggianti offshore. In questa tipologia di controllo, tramite l'incremento del moto di imbardata di tutto il sistema, si può ottenere un incremento del mescolamento della scia delle turbine sopravento per aumentare la velocità del flusso e quindi la produzione di energia delle turbine in scia. In un secondo caso studio, le routine di design sono state utilizzate per lo sviluppo di una piattaforma galleggiante con una forma e caratteristiche innovative. La fase di design preliminare è stata verificata con simulazioni numeriche con fedeltà crescente e con degli esperimenti nella vasca navale dell'Università di Napoli.

Contents

List of Figures

List of Tables

–1– Introduction

Floating Offshore Wind Turbines (FOWTs) are expected to be installed in large numbers in the next decades to contribute to the de-carbonization of the electricity supply all around the world. Electricity produced by FOWTs is predicted to cover 2% of the global supply by 2050, with a an average 19% annual growth from 2019 to mid-century [1]. According to an estimate by DNV, the global installed floating offshore wind capacity by 2050 will increase to 260 GW. The offshore wind resource in oceans with high depths, such as the Mediterranean sea (which was the focus of a EU study [2]), has a virtually unlimited potential of exploitation, but the production of energy from floating offshore wind turbines remains a technological challenge due to the harsh environment in which they operate and higher costs of installation and maintenance. Therefore, difficulties regarding the design, installation and maintenance operations and the intrinsic complexity of the FOWT systems lead to high Levelized Cost of Energy (LCOE) produced by this technology [3], compared for example to onshore wind systems and solar panels. It is vital for the development of the industry that the technology advancements would eventually lead to a drop in the LCOE. With the aim of reducing the LCOE, driven by government funding, both research and industry are putting their effort into optimizing the design of single FOWTs (with a particular focus on the substructures and mooring lines) and the global configuration of floating offshore wind farms. The large number of different designs for the substructures show testament to the youth of the technology. Moreover, floating offshore wind turbines are complex systems that can only be analyzed using multiphysics simulation tools. An important component of a FOWT is represented by the floating platform, which, together with the mooring lines, provides the hydrostatic stability and absorbs the peak loads coming from both sea-waves and the forces generated by wind on the turbine. The success of FOWTs as a renewable energy source and the achievement of the goals imposed by the governmental legislation on energy supply depend on the speed, quality and quantity of innovation in the field.

1.1 Motivation

As illustrated recently by M.K. Jensen [3], the innovation of the FOWTs technology depends on the following factors:

- research on design and optimization:
  - **integrated turbine design**;
  - **wind farm layout optimization**;
- industry development:
  - **wind farm maintainability**;
  - **power grid integration**;
  - **improved supply chain**;
  - **preparation of shipyards ready for the construction**;
- industry and research working closely together for innovation:
  - **upsizing of generator, rotor and tower height**;
  - **turbine reliability**;
  - **installation method**.

Based on the expected outcome of research and industry on the topics illustrated above, many studies have predicted a reduction of the LCOE of FOWTs by 2050, as shown in Fig. 1.1. Innovation is deemed to account for a reduction of 30% of costs of FOWTs by 2040 in the UK energy market (as shown in [4]). Nonetheless, to demonstrate the youth of the field at the moment of writing, just one demonstrator prototype has been installed in the whole Mediterranean sea by Saipem and CNR [5]. Interest in the development of FOWTs has been shown in Greece, for the energy supply of small islands, which may require only few MW of power generated by a limited number of FOWTs [6]. The design and optimization of FOWTs for the installation in the Mediterranean basin pose peculiar challenges, which, among the others, can be summarized in: lower average wind speed (which implies lower energy production) with respect to the North Sea, high depths and absence of a consolidated supply chain for offshore constructions. It is crucial to develop routines and tools to ease the design and optimization of such systems, while trying to simulate the performance with the highest fidelity allowed by computational resources. A simulation-based approach for the design and optimization of FOWTs involves the use of numerical models to simulate the behavior of the FOWT system with a chosen level of fidelity, and then use the analysed performance to carry-out optimization. The combination of optimization algorithms and numerical simulations offers a powerful tool for the design and optimization of FOWTs, as it

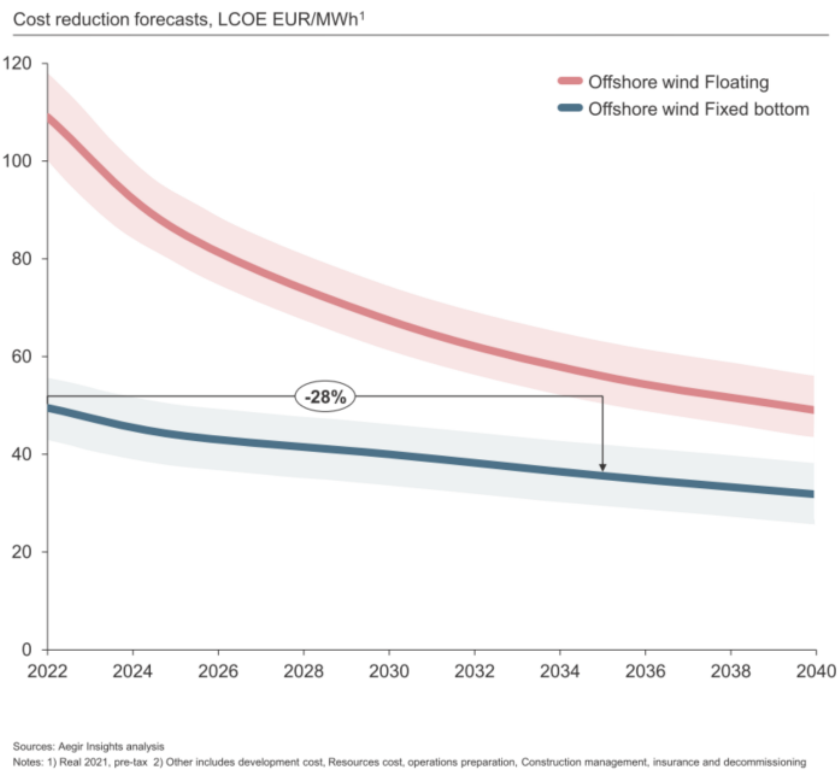

Figure 1.1: Forecast of costs reduction in terms of LCOE from 2022 to 2040 for offshore wind. From [3].

.

allows for the exploration of a large number of design options and the identification of the most optimal solutions. The motivation for this PhD thesis is to contribute to the field of FOWT design and optimization by developing design routines and a simulation-based optimization framework.

1.2 Aim

Overall, the proposed research aims to provide insights and possible solutions to the design and optimization challenges of FOWTs. The results of this study will contribute to the advancement of the field and support the development of more efficient and cost-effective FOWT systems.

1.3 Thesis structure

This chapter was dedicated to the introduction of the work. In the next chapter a general background for the modelling of floating offshore wind turbines is given. The third chapter illustrates the design methodologies for floating platform and mooring lines following standards, guidelines and innovative optimization found in literature. The development of simple routines and a more detailed framework for the design and optimization of floating offshore wind turbines is shown in chapter four. In the fifth chapter, the framework is showcased for the specific objective of motion amplification, driven by an innovative wind farm flow control. In the sixth chapter, a new floating platform concept is validated with numerical simulations and experiments.

–2–
Background

In this chapter, a general description of floating offshore wind turbines and the environment in which they operate is illustrated. This chapter is divided into four main sections. In the first part a description of the characteristics of offshore wind turbines is given. In the second part the floating offshore wind turbines are introduced and described. The integration of the systems into wind farms is shortly presented in section three, while, last but not least, the fourth section is dedicated to a brief indication of how the costs of floating offshore wind turbines are estimated.

2.1 Offshore wind turbines

The first offshore wind turbines were installed at the beginning of the third millennium in the North Sea [7] (e.g. Middel grunden, 2001; Horns Rev, 2002; Frederikshave, 2002;...) with some earlier plants (Vindeby Lolland, 1991; Tunø Knob, 1995 with 11 450 kW Bonius turbine and 10 500 kW Vestas, both with 3.5 m diameter piles), where shallow sea depths allowed for the installation of substructures fixed to the seabed. Installing an offshore wind turbine presents some valuable advantages (see [8]):

- virtually unlimited installation sites;
- low (or none) visual impact (*far from sight*);
- large energy production, due to high wind speeds with low turbulence, the latter being also beneficial for fatigue loads. The high average wind speeds found at offshore sites create the opportunity to generate a higher percentage of energy output compared to onshore wind turbines (higher capacity factor);
- low constraints on audible pollution allow larger turbine blades rotating at higher speeds;

- absence of land usage, excluding potentially expensive land rent.

It can be stated that an offshore installation site with the same area of an onshore one, allows for the installation of more and larger wind turbines. With the growing interest in offshore installations, it became clear that in sites with high depths (such as in the Mediterranean Sea or in the Atlantic Ocean), fixed bottom structures were neither feasible nor economically viable. Research started to focus on floating installations, with mooring lines connecting the floating substructure to the seabed, as shown in Fig. 2.1.

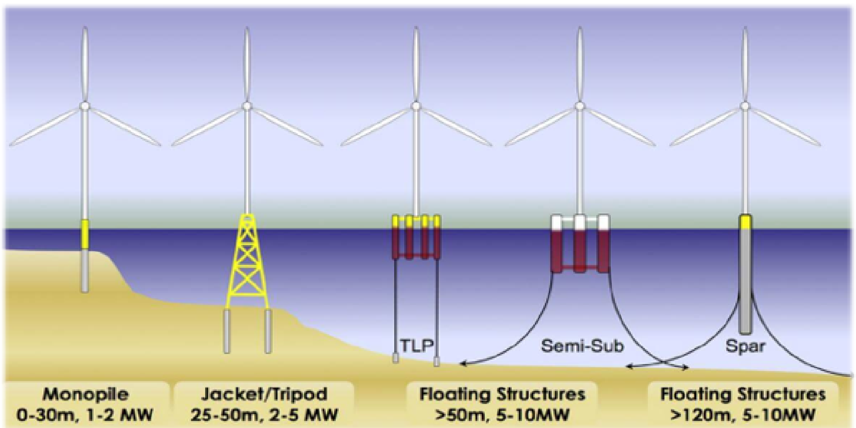

Figure 2.1: Different types of fixed bottom offshore wind turbines and floating offshore wind turbines with indications of usual installation depth. From [9].

.

As a general rule, fixed foundation offshore wind turbines are considered technically viable in areas with water depth less than 50-60 meters. Floating offshore wind turbines, instead, are considered technically viable in water depths from 50 to 1000 meters, where fixed bottom offshore technology is no longer convenient. Despite these great advantages with respect to onshore installations, there are still some technological challenges, common to all offshore installations, to be faced in the near future:

- offshore turbines operate in a very harsh environment (high humidity, salt aggression, bad weather limitations);
- the harsh environment leads also to difficulties for installation, maintenance and repair of wind turbines and power cables;
- requirement of specialized (expensive) vessels for construction and decommissioning.

At the moment these technological issues make offshore wind generally more expensive compared to onshore wind, as it can be seen in terms of LCOE (Levelized

Cost of Energy) in Fig. 2.2. Nonetheless, as shown in Fig. 2.2, in which the offshore wind cost is evaluated based on the fixed bottom wind turbines farms already in operation in the North Sea, a similar decreasing trend in the LCOE is expected for floating offshore wind turbines.

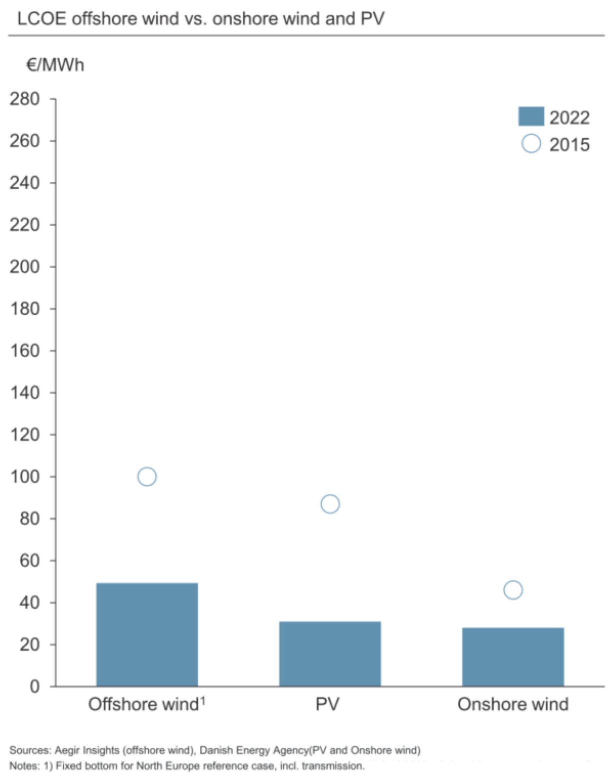

Figure 2.2: Comparison of LCOE from 2015 to 2022 for offshore wind, PV (photovoltaics) and onshore wind. From [3].

.

2.2 Floating offshore wind turbines

The interest in floating platforms for offshore wind turbines dates back to the beginning of the new millennium, with the first exploration of concept feasibility and practical challenges to be faced for the installation of floating systems (e.g. [10], [11]). The first concepts of floating platforms originated from shapes and design coming from the offshore oil & gas industry, which were already been studied thoroughly in the last century [12]. The need of simulating the coupled dynamics of FOWTs lead to the first work from J.Jonkman [13], who successfully developed a tool to simulate the floating offshore wind turbines, which ended-up in the well-known open-source software OpenFAST [14]. Since then, researchers and companies have put their effort into developing the most efficient and cheap integration of a wind turbine and the related substructure. Given the intrinsic complexity of these systems, the entire process of design and optimization is strongly iterative, as it has been shown in [15] and [16]. The first attempts of optimization of the floating platform for the specific aim of the installation of a wind turbine can be found in [17]. In the last decade researchers have focused on cost-effective design of floating platforms and mooring lines, exploring a very wide variety of solutions, such as semi-submersible concepts (see [18] for a detailed study on a semi-submersible concept). In this section the advantages of installing a floating offshore wind turbine are introduced and such a system is described in all its parts. As it was already stated in past researches (see e.g. [19]), there are major advantages of floating offshore wind systems with respect to fixed bottom systems, which could be summarized as follows:

- the possibility of accessing wind resource in deep waters whereas the bottom fixed wind turbines technology can only access a small fraction of the offshore wind resource worldwide due to depth limitations;
- being installed relatively close to the coastline, fixed bottom wind turbines still encounter a strong opposition from coastal urban area inhabitants (usually referred as NIMBY or "Not In My Back Yard" resistance). Floating offshore wind turbines could potentially be "invisible" from the mainland;
- lower manufacturing costs may be possible for floating systems, by using less material in construction and reducing the need of huge structures to be constructed at dock and then transported and erected at the installation site;
- floating offshore wind turbines could potentially be designed to be assembled in port and towed to the installation site using tugboats. This can result in cost savings and greatly increase flexibility in construction.

While the benefits of floating offshore wind are somehow straightforward, there are still significant obstacles that prevent a boost in the development of the industry, with the following being the most challenging,

- due to the intrinsic multi-disciplinary nature of the system (a floating offshore wind turbine requires aero-servo-hydro-elastic coupled analyses), simulation and modelling tools are still being developed and validated, and, the higher the complexity of the model, the longer the simulation time required for performance evaluation;
- the industry is in its "youth", with the absence of a standard "converged" design;
- experiments to validate designs and concepts are expensive, time consuming and require adequate tools and facilities (dedicated towing tank with wave generators). There are multiple well-known issues on the concurrent scaling

of hydrodynamics and aerodynamics while testing scaled models of offshore wind turbine;

- the dynamics of such systems when subjected to waves, wind and ocean currents becomes complex and greatly affects the operations of the wind turbine, which in turn leads to difficulties in guaranteeing the expected power output;

- manufacturing and installation operations are strongly related to the design of the floating platform. Until a converged technology is reached, the techniques adopted for manufacturing and installation will vary from design to design.

Some of the wind farm projects (and demonstrator) developed in the last years are listed in Table 2.1.

Table 2.1: Operating FOWT farms and demonstrators. $N°$ stands for number, D stands for diameter, H stands for height, f. p. stands for "floating platform", N/A stands for "not available" where information is missing. (*) Average wind speed at site retrieved from Global Wind Atlas [20].

Name	**Total power**	**Wind-speed**	**Turb.** $N°$	**Turb.** D	**Tower** H	**Approx. depth**	**Type of f. p.**	**Year**	**Ref.**
Floatgen Demo.	2 MW	8.5* m/s	1	80 m	80 m	30 m	Barge	2018	[24]
WindFloat Atlantic	25 MW	8.0* m/s	3	164 m	95 m	100 m	Semi-Sub.	2020	[22]
Kincardine Offshore	50 MW	9.5* m/s	5	164 m	N/A	70 m	Semi-Sub.	2021	[21]
Hywind Tampen	88 MW	10* m/s	11	N/A	N/A	260 m	Spar	2022	[23]

The issues illustrated briefly in this section will be addressed in the next sections.

2.2.1 Description of the system

The main parts of a floating offshore wind turbine are illustrated in Fig. 2.3. The wind turbine is composed by a tower, which is usually metallic and bears the weight and loads coming from the nacelle, a metallic capsule hosting the electrical generator assembly and the mechanical shaft, which transmits the torque from the rotor to the generator. The rotor is composed by blades with aerodynamic shape, usually built with composite materials, that transform the loads coming from the wind action into mechanical torque. The rotor and nacelle assembly is commonly referred as RNA. The offshore wind turbines are usually equivalent to onshore ones. In floating offshore installations the platform plays a fundamental role. It is usually built with metallic or reinforced concrete materials, and it provides the buoyancy force to keep the entire system afloat and stable under the external loads coming from waves and wind. The mooring lines connect the floating platform to the seabed through anchors, contributing to station-keeping and constraining the system position to the installation site. Finally, the power cables transmit the electricity produced inside the generator to an intermediate sub-station in the proximity of the offshore wind farm, or directly to land.

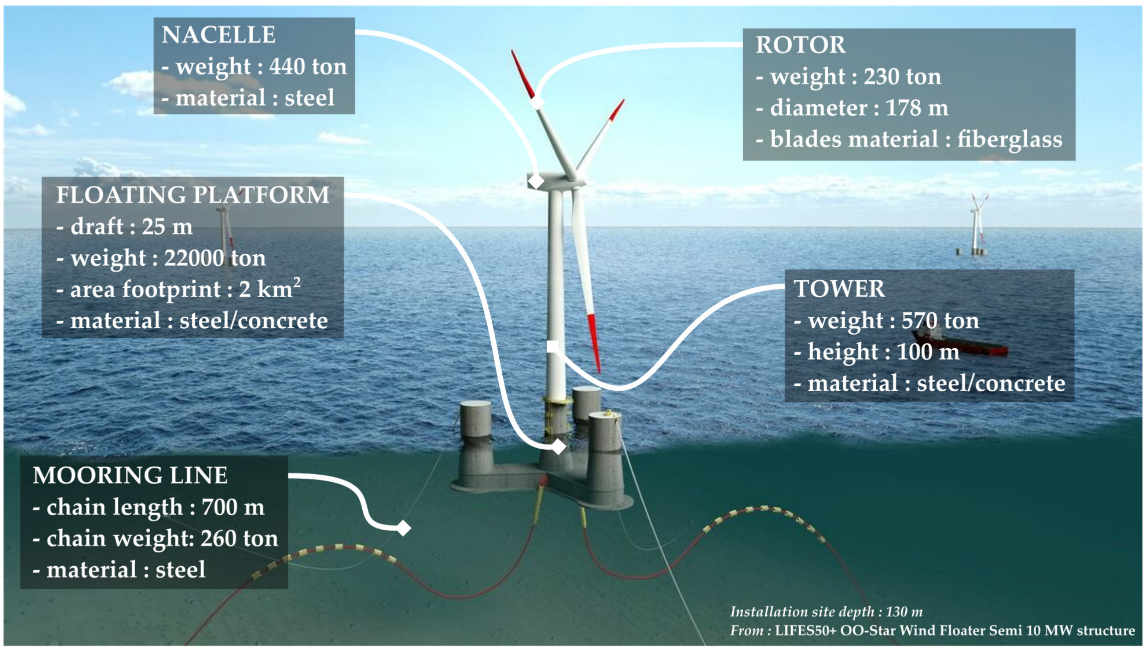

Figure 2.3: Illustration of a floating offshore wind turbine (based on the copyrighted concept OO Star Wind Floater, illustrated in [25]) with indications of the main components.

2.2.2 Floating platform concept comparison

Several concepts for the realization of floating turbine platforms have been presented in the vast literature on the subject (among the others, one of the first analysis was conducted in 2011 by J.Jonkman [26] while a more recent comprehensive study can be found in [27]). The main platform requirements, which define some preliminary design criteria, include:

- the need to withstand external tilting actions (in particular, the thrust acting on the wind turbine), ensuring a reduced inclination under normal operating conditions, in order to avoid significantly asymmetrical flow conditions on the rotor that may reduce production and generate high loads. In connection with this point, the need to provide sufficient static stability, provided by the hydrostatic righting moment generated by hydrostatic and mass actions. This requirement takes the form of two main aspects:

  - ensuring that, at the rated thrust on the turbine, the inclination is limited to a value considered acceptable for operations;
  - meet static stability requirements defined by regulations for safety issues;

- the need to resist the peculiar wave actions which occur at the installation site. In relation to stability, the differences between floating platform concepts are represented not only by a different geometry but also by the principle of generating the righting moments. The righting moment can be due to several contributions:

  - contribution due to the lateral displacement of the center of buoyancy, associated with the shape of the buoyant structure and in particular by waterplane area (intersection of the geometry of the structure with the sea surface);
  - contribution due to the vertical position of the center of gravity, associated with the vertical distance between the center of gravity (point of application of the weight) and the center of buoyancy (points of application of the buoyancy);
  - contribution due to the reactions of the mooring system.

The scheme of relevant characteristics involved in the assessment of platform stability is given in Fig. 2.4.

Each of these contributions can be of different magnitude and sign depending on the configuration considered. Depending on the relative magnitude of these two contributions, different construction solutions can be distinguished. The mooring system (discussed in more detail in the following section) can also participate significantly in defining the behavior of the structure. The most popular and studied types of platforms are illustrated in the list below.

- **Spar buoy**: the platform consists of a column, usually cylindrical, with a significant draft. Stability with respect to overturning actions is provided solely by the vertical position of the centre of gravity with respect to the centre of buoyancy (the centre of gravity is below the centre of buoyancy). The position of the centre of gravity and its stabilizing effect are usually achieved by placing an assigned amount of ballast (solid or liquid) at the bottom of the spar;

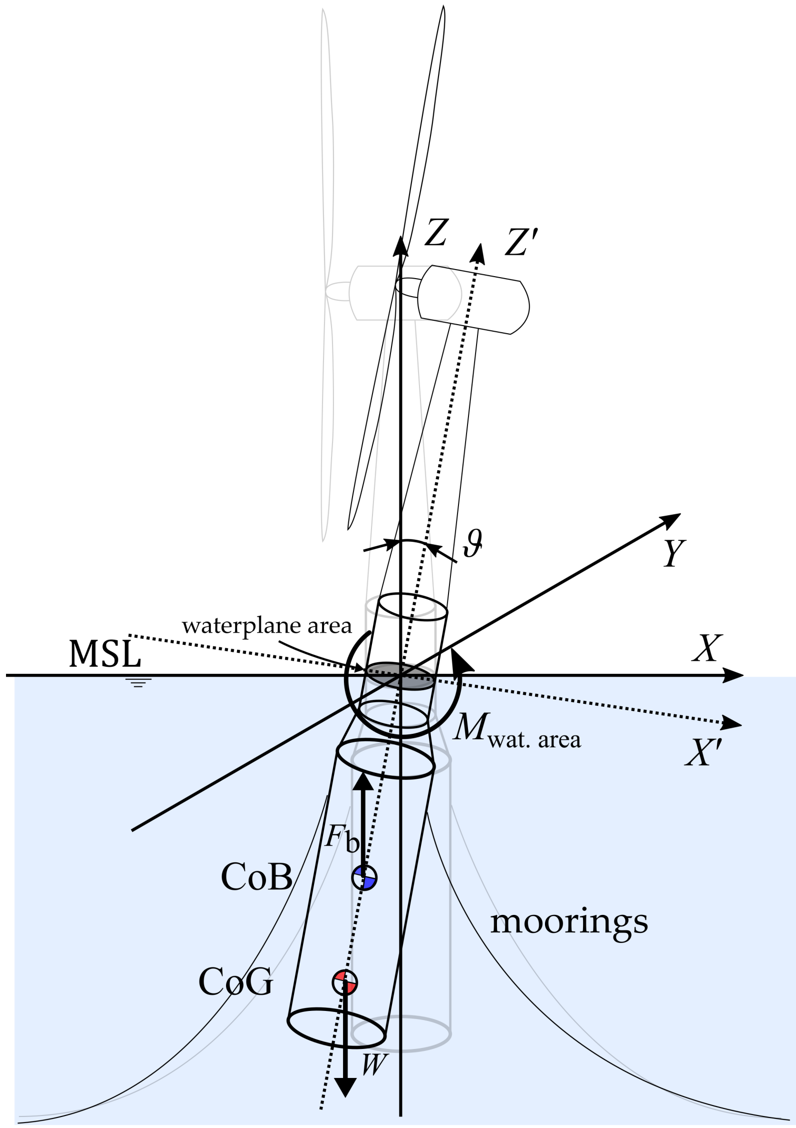

Figure 2.4: Scheme of a floating offshore wind turbine (spar-buoy type) with indications of the main characteristics relevant for hydrostatic stability. θ is the inclination angle (usually referred as heeling), CoB and CoG refer to the centre of buoyancy and centre of gravity respectively, SL stands for sea-level, $M_{wat.area}$ refers to the restoring moment due to the waterplane area.

- **Semisubmersible**: the platform is, in general, composed of column structures of relatively short length (reduced draft compared to the spar buoy case), connected together by transverse connecting elements (braces). At the base of the columns there are usually discoidal elements to dampen the vertical motion. This structure generally provides stabilizing action due to the combined contribution of the waterplane area and the position of its centre of gravity;
- **Tension Leg Platform or TLP**: this structure presents, similarly to the case of the semisubmersible, a relatively small draft, but in this case the fundamental contribution to stability is provided by the action of the mooring system, consisting in this case of a set of lines (chains or cables) generally strongly pretensioned;
- **Barge**: a barge platform can be considered as a semisubmersible with a very low draft, and a very large waterplane area. The hydrostatic stability is provided solely by the waterplane area, and the centre of gravity is very close to the mean sea level. The barge concept presents the advantages of the semisubmersible, can be installed in sites where the depth is even shallower, but suffers from the action of waves.

The different types of floating platform are illustrated in Fig. 2.5.

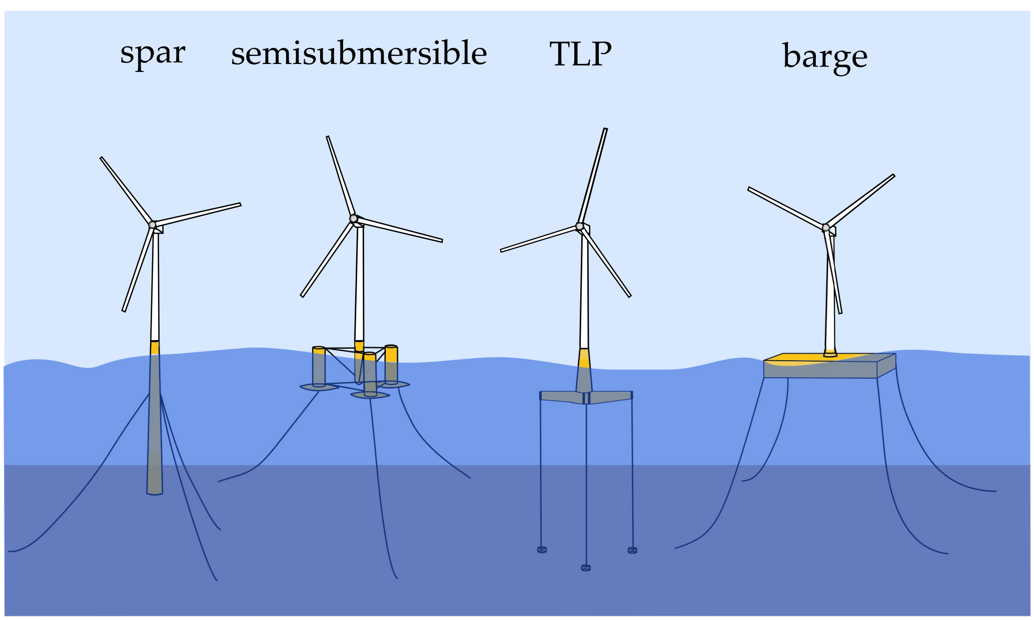

Figure 2.5: Main types of floating platforms.

In [27], the difference between the configurations considered in relation to the different contributions to the stabilizing action is also summarized by means of the graph in Fig. 2.6. The three configurations are shown at the vertices of a triangle. Each configuration is characterized by a main contribution to stability (ballast, buoyancy figure, moorings). It is noted that, in some cases, some of the contributions may even provide unstable contributions to the total reaction moment, which must still be righting.

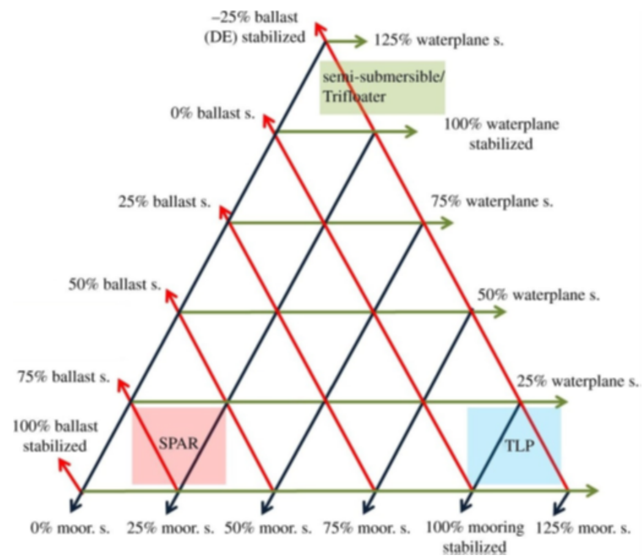

Figure 2.6: Summary of the different contributions to platform stability. The vertices of the triangle in the figure show the three types of platforms. Typical values of the percentages of each contribution to total stability are also shown. From [27].

The following tables (Tables 2.2, 2.3 and 2.4) list the main characteristics of the three stabilization modes, which influence the choice of floating platform type. The type of stabilization and the choice of the mooring lines affects the

Table 2.2: Spar buoy characteristics

Vantages	**Disadvantages**
Easy manufacturing	High draft
Intrinsically stable	Assembling only on site
Easy anchoring	Mooring lines occupy large area

dynamic behaviour of the system, when subjected to sea waves. In floating offshore wind farms, a dynamic electrical cable (also referred to as "power umbilical") connects the electricity generation system installed onboard to a substation from which the energy produced by several systems is gathered and transferred to the mainland. It was shown that the main design drivers of the dynamic electrical cables' configuration for FOWTs are the elongation, bending and twisting of the cable due to the dynamic motion of the system. The power cables used in floating offshore systems are usually equipped with structural metallic reinforcements in

Table 2.3: Semisubmersible characteristics

Vantages	**Disadvantages**
Low draft	Complex manufacturing
Assembling in dockyard	High costs for manufacturing
Easy transportation	Mooring lines occupy large area
Relatively easy maintenance	Complex interaction with waves

Table 2.4: TLP characteristics

Vantages	**Disadvantages**
Low costs	Complex mooring lines
High stability	Complex installation
Low mooring lines footprint	Complex decommissioning
Light floating platform	High risks if mooring lines fail

order to absorb dynamic loads. Moreover, the configuration should be able to bear the elongation due to the system displacement from its installation position, when an extreme weather event is present, and should be designed in order to avoid collision with the mooring lines in any condition. In particular, a solution that presents some advantages and was adopted in two demonstrator systems, which are described in [28], is the introduction of floating modules, attached to the power umbilical, in a section between the connection to the platform and the touching-down point, as shown in Fig. 2.7 (also referred to as "lazy wave cable".)

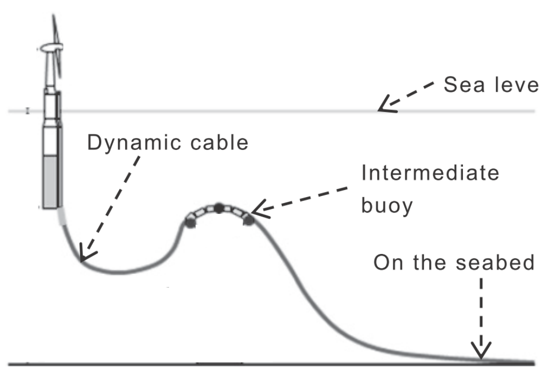

Figure 2.7: Configuration of the power cable with intermediate buoys. From [28].

As it was also shown for a floating offshore device which extracts energy from waves [29], this configuration allows the de-coupling of the motions of the touching-down point of the electrical cable and the floating wind turbine, and decrease the hang-off load at the connection point between the cable and the platform. The motion of the touch-down point should be prevented in order to avoid wearing of the waterproof layers of the power umbilical. The analysis of the power cable configuration and its effect on the dynamic response of the system is not considered in this work, as its stiffness is assumed to be negligible with respect to the one provided by the mooring lines.

2.2.3 Mooring lines

Mooring lines are defined as the connections of a floating body to the seabed that provide the restoring forces to:

- keep the floating body in reasonable proximity of a target location (site of installation);
- allow serviceability of the system.

In close connection with the study of the dynamic response of the floating platform, the simulation of mooring lines behavior plays a key role in the analysis and design of a floating offshore system. In the development of floating offshore installations, several possible solutions are available, presented by multiple sources in the literature. For example, a short list of different mooring types, transferred from the field of industrial applications related to the oil & gas sector to the field of FOWTs, is given in [30]:

- Spread moorings system: with several mooring lines radiating from the platform. The mooring lines can be either
  - catenary mooring, tensioned only by their own weight, associated with gravity anchors;
  - taut mooting (with partially pretensioned mooring lines);

  these two types of mooring lines require different types of anchors
- Tensioned anchor system, with tendons, generally used in the TLPs, in which the mooring lines, generally vertically connected to anchors fixed to the seabed, are subjected to high pretensioning and greatly reduce the possible horizontal displacements of the platform.

For completeness, the reference also indicates an additional type of mooring, referred to as single point mooring, with a connection to an external buoy, derived from the practice of offshore oil & gas installations. Mooring lines are generally made by means of chains or by means of natural or synthetic fiber cables.

2.2.4 Modelling

Floating offshore wind turbines (FOWTs) are complex systems that can only be fully simulated with highly integrated methods (see e.g. [31] and [13]). They operate in sea environment, facing sea-waves, storms, currents, corrosion and bio-fouling, and are subjected to the loads coming from the turbine interaction with wind. All the possible external interactions with the system are represented in Fig. 2.8, where the grey, blue and brown rectangles represents respectively the "wind interaction zone", the "sea interaction zone" and the "seabed interaction zone".

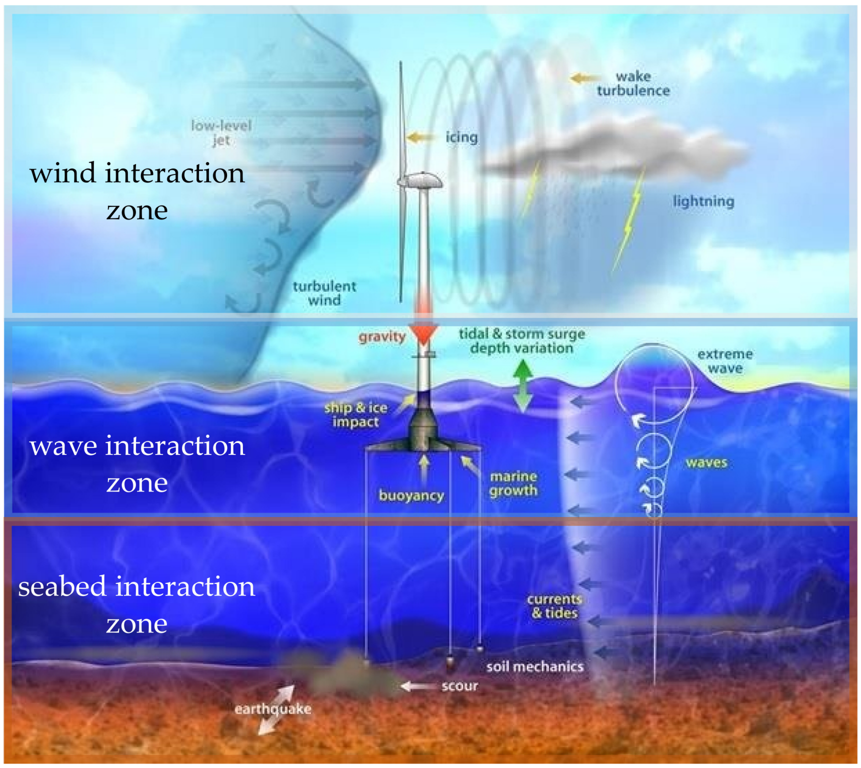

Figure 2.8: Illustration of external actions on a floating offshore wind turbine. From [14] with modifications.

At the same time, to provide a stable and efficient electrical power production, the turbine behaviour is usually governed by passive or active control systems. It is clear that complex motion and loads of the system can only be predicted by aero-hydro-servo-elastic simulation frameworks. In this section the methodologies for modelling floating offshore wind turbines and the environment in which they operate are illustrated.

Sea waves modelling

Waves can be considered as a combination of potential and kinetic energy in motion (energy which is being carried away from its origin). The main sources of the energy which is contained in sea waves (the *origin*) are four phenomena:

- Bodies moving on or near the surface causing low period, low energy waves.

- Wind perturbing sea surface, which generates the so-called gravity waves.
- Seismic disturbances (motion of the seabed) causing *tsunamis*.
- Lunar and solar gravitational fields causing the largest waves, the tides.

Hence, sea waves can be classified by wave period and relative energy content, as shown in Fig.2.9.

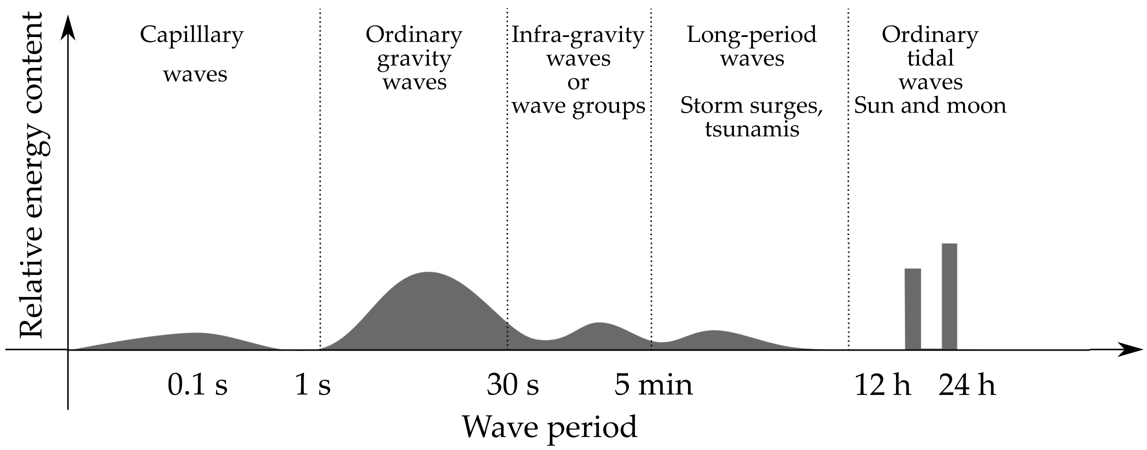

Figure 2.9: Energy content of sea waves w.r.t the total wave energy as a function of wave period.

Due to their period and energy content, gravity waves influences the dynamic of FOWTs, which must be designed to counteract wave forces. According to the Miles-Phillips theory (see [32]), sea waves generated by wind originate from a flat sea following two mechanisms; the first of which produces tiny ripples called capillary waves, and the second of which produces bigger waves called gravity waves. Tiny wavelets, which have a two-dimensional spectrum structure, first begin to grow from an entirely flat sea, due to the turbulence of air. This initial generation of capillary waves is due to perturbations in the surface wind, causing irregularities in the water surface. Once the sea contains capillary waves, there is an increase in surface roughness (crests-troughs), which allows the moving air to "grip" the surface of the water. The differences in the pressure distribution between crest (negative relative pressure) and troughs (positive relative pressure) causes the waves to grow at a rate which is exponential with time. High-frequency components of the spectrum dissipate while low-frequency components increase and form the final wave spectrum. The area where the sea undergoes the action of wind is referred to as "fetch". Despite being useful to understand the basic phenomena involved in the formation of gravity waves, some later experiments and observations have shown discrepancies with this theory. The exact mechanism of energy transfer from wind to waves has been disputed (see again [32]), but Miles's theory laid the foundation of wind–wave growth parametrization employed in wave spectrum generation.

A practical approach is to introduce empirical formulae for wave growth which have been derived from large data sets of experiments that make no attempt to separate the physical processes involved. They represent net wave growth from known properties of the wind field (wind speed and direction, fetch and duration) and are used to practically calculate the properties of sea waves. To simplify the study of sea waves we introduce the properties of regular-monochromatic (single frequency) waves, indicated in Table 2.5, and shown in Fig. 2.10.

Table 2.5: Regular wave properties

Property	**Symbol**	**Description**
Wave Period	T_{w}	Time in which a wave crest travels a wavelength (units of time)
Wave Frequency	f_{w}	Number of crests passing a fixed location per unit time
Wave Angular Frequency	ω_{w}	$2\pi f_{\text{w}}$ (units of angles per unit time)
Wave Length	λ_{w}	Distance between two crests (units of distance)
Phase Velocity or Celerity	c_{w}	Distance a wave crest travels per unit time (units of velocity)
Wave Height	H_{w}	Distance between the crest and the trough (units of distance)
Wave Amplitude	A_{w}	$H_{\text{w}}/2$ (units of length)
Wave Number	k_{w}	$2\pi/\lambda$ (units of 1/length)

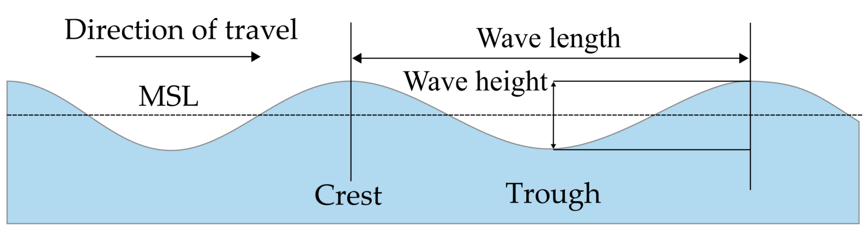

Figure 2.10: Illustration of the properties of a regular wave.

Regular sea waves can be analysed under the assumptions of constant depth $d_{\text{seab.}}$ and wave height to wave length ratio (also referred to as wave steepness) equal or less than 1/50. When these assumptions are valid, linear theory can predict the kinematic properties of waves with high accuracy. For a wave travelling in the X direction, as shown in Fig. 2.10, a mathematical expression for the free-surface displacement η_{w} is

$$\eta_{\text{w}} = \frac{H_{\text{w}}}{2} \cos\left(\frac{2\pi x}{\lambda_{\text{w}}} - \frac{2\pi t}{T_{\text{w}}}\right) \tag{2.1}$$

where the period T_{w} is given by:

$$T_{\mathrm{w}} = 2\pi \left[\frac{2\pi g}{\lambda_{\mathrm{w}}} \tanh\left(\frac{2\pi d_{\text{seab.}}}{\lambda_{\mathrm{w}}} \right) \right]^{-1/2} \tag{2.2}$$

For a regular wave with period T_{w} and wave length λ_{w}, the celerity is $c_{\mathrm{w}} = \lambda_{\mathrm{w}}/T_{\mathrm{w}}$. This can be written also as $c_{\mathrm{w}} = \omega_{\mathrm{w}}/k_{\mathrm{w}}$, where ω_{w} is the wave angular frequency and k_{w} is the wave number (the number of crests per unit distance).

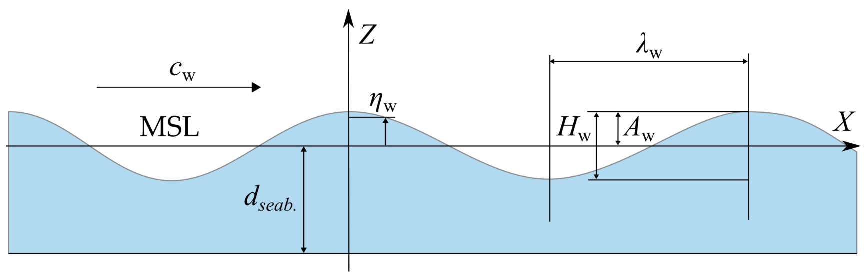

Figure 2.11: Illustration of a regular wave travelling in one dimension in space (e.g. fixing $t = 0$).

A notable result of linear theory is that the water particle velocity components can be expressed as:

$$u_{\mathrm{w}}(x,t) = \frac{\pi H_{\mathrm{w}}}{T_{\mathrm{w}}} \frac{\cosh\left[k_{\mathrm{w}}(z+h)\right]}{\sinh(kh)} \cos(k_{\mathrm{w}}x - \omega t) \tag{2.3}$$

$$w_{\mathrm{w}}(x,t) = \frac{\pi H_{\mathrm{w}}}{T_{\mathrm{w}}} \frac{\sinh\left[k_{\mathrm{w}}(z+h)\right]}{\sinh(k_{\mathrm{w}}h)} \sin(k_{\mathrm{w}}x - \omega t) \tag{2.4}$$

The effect of decreasing water depth is to modify the circular path of water particles which is a characteristic of deep water conditions. In intermediate and shallow waters the water particles travel in elliptic paths. From the period T_{w} an expression for the wave length can be obtained:

$$\lambda_{\mathrm{w}} = \frac{g T_{\mathrm{w}}^2}{2\pi} \tanh\left(\frac{2\pi d_{\text{seab.}}}{\lambda_{\mathrm{w}}} \right) \tag{2.5}$$

This implicit relationship between wave length, wave period and depth can be used to numerically (or graphically) calculate the wave length, for an assigned depth. Eq. 2.3 and eq. 2.3 demonstrate that quantities describing kinematics of linear waves scale proportionally to wave height H_{w} but depth plays an important role. The expression for celerity becomes:

$$c_{\mathrm{w}} = \frac{g T_{\mathrm{w}}}{2\pi} \tanh\left(k_{\mathrm{w}} d_{\text{seab.}}\right) \tag{2.6}$$

Despite being used to introduce and calculate the properties of an ideal monochromatic sea wave, regular waves do not happen in nature. Observing a fixed point in a real sea state in time, and recording the height of the sea level w.r.t. the MSL, we can introduce the concept of "irregular wave". Irregular waves have variable frequency and height and statistical methods are used to analyse them.

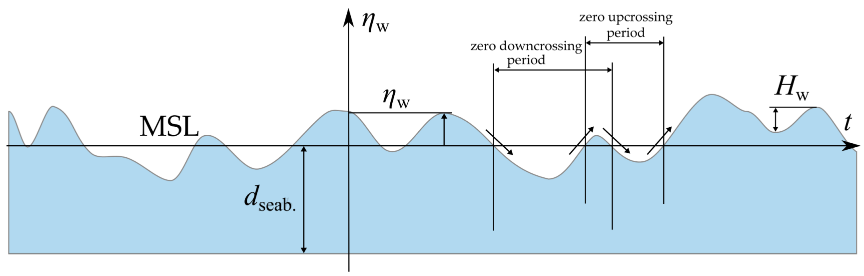

Figure 2.12: Illustration of an irregular wave recorded at a point (e.g. $x = 0$) in time, hence the abscissa axis represents time.

To determine the properties of irregular waves, the following concepts are introduced:

- Number of waves chosen for the analysis (N_w)
- Zero up-crossings i.e. points of intersection of water surface profile with the mean sea level (MSL), when the wave surface is traced from trough to crest. Zero up-crossing period is defined as the time elapsed between two up-crossings passing by a specific point.
- Zero down-crossings i.e. points of intersection of water surface profile with the mean sea level (MSL), when the wave surface is traced from crest to trough. Zero down-crossing period is defined as the time elapsed between two down-crossings passing by a specific point.
- Average wave height ($H_{w,avg} = \frac{1}{N_w} \sum_{j=1}^{N_w} H_{w_j}$)
- Root mean square wave height $\left(H_{w,rms} = \sqrt{\frac{1}{N_w} \sum_{j=1}^{N_w} H_{w_j}^2}\right)$
- Significant wave height ($H_{w,S}$ or $H_{w,1/3}$), which is the average value of the 33% highest waves heights.
- One-tenth wave height ($H_{w,1/10}$), which is the average value of the 10% highest waves heights.
- Maximum wave height ($H_{w,max}$), which is the maximum value of the wave heights.

Irregular waves are random in height, period and direction, nonetheless these properties can be related to the wind speed and direction which generated them. A random sea can be considered to be composed of N_{w} regular waves of various heights H_{w_i}, wavelengths λ_{w_i} and periods T_{w_i}. For a mono-directional wave the expression representing the summation of N_{w} regular waves at a given x coordinate is:

$$\eta_w(t) = \sum_{i=1}^{N_{\mathrm{w}}} \frac{H_{\mathrm{w}_i}}{2} \cos\left(\frac{2\pi t}{T_{\mathrm{w}_i}} - \phi_{\mathrm{w}_i}\right) \tag{2.7}$$

where ϕ_{w_i} represents the relative phase shift between the waves. For the i^{th} regular wave, the expression of the energy per unit of width $\overline{E}_i$ obtained from linear theory is:

$$\overline{E}_i = \frac{\rho_{\mathrm{wat.}} g H_{\mathrm{w}_i}^2 \lambda_{\mathrm{w}_i}}{8} \tag{2.8}$$

To evaluate the energy of all the component waves passing a point, it is useful to represent the wave height term of the equation as:

$$\frac{H_{\mathrm{w}_i}^2}{8} = S_{T_{\mathrm{w}}}(T_{\mathrm{w}_i})\, \delta T_{\mathrm{w}_i} \tag{2.9}$$

Where $S_{T_{\mathrm{w}}}(T_{\mathrm{w}})$ is referred to as the wave spectral density or, more commonly, the wave spectrum and δT_{w_i} is the elemental wave period. The units of $S_{T_{\mathrm{w}}}(T_{\mathrm{w}_i})$ are [m^2/s]. The wave spectral density associates an energy content (proportional to the square of wave height) to each harmonic component encountered in a wave field. Attention must be given to the parameter of the spectral density. Wave spectral density can be also expressed in terms of frequency rather than period. The relationship between the wave spectrum density as a function of the period and the wave spectrum density as a function of frequency is:

$$S_{T_{\mathrm{w}}}(T_{\mathrm{w}_i})\, \delta T_{\mathrm{w}_i} = -S_{\omega_{\mathrm{w}}}(\omega_{\mathrm{w}_i})\, \delta\omega_{\mathrm{w}_i} \tag{2.10}$$

and in this formulation $S_{\omega_{\mathrm{w}}}(\omega_{\mathrm{w}})$ units of measurement are [m^2/Hz]. Wave spectra define the energy content of a sea state, and in turn, can be used to generate random sea states time-histories. Pierson and Moskovitz (in 1964) found an expression valid for fully developed sea based on open ocean measurements (under the assumption that the wind has been blowing for a sufficient time that equilibrium between wind and waves is reached). The general expression of the spectra is:

$$S_{\mathrm{w,P\text{-}M}}(\omega_{\mathrm{w}}) = \frac{\alpha g^2}{\omega_{\mathrm{w}}^5} \exp^{-\beta\left(\frac{\omega_{\mathrm{w},0}}{\omega_{\mathrm{w}}}\right)^4} \tag{2.11}$$

the constants determined from open ocean measurements are:

$$\alpha = 8.1 \times 10^{-3}$$
$$\beta = 0.74$$

while the wave spectral density (and as a consequence the significant wave height) are related to the wind velocity measured 19.5 m above the sea level $V_{19.5}$ in the chosen site through the constant $\omega_{\mathrm{w},0}$:

$$\omega_{\mathrm{w},0} = \frac{g}{V_{19.5}} \tag{2.12}$$

Hasselmann (in 1973), after analyzing data collected during the Joint North Sea Wave Observation Project JONSWAP, found that the wave spectrum is never fully developed. It continues to develop through non-linear, wave-wave interactions even for very long times and distances. The so-called JONSWAP spectrum is thus a Pierson-Moskowitz spectrum multiplied by an extra peak enhancement factor γ^r:

$$S_{\mathrm{w,JON}}(\omega_{\mathrm{w}}) = \frac{\alpha g^2}{\omega_{\mathrm{w}}^5} e^{-1.25\left(\frac{\omega_{\mathrm{w},0}}{\omega_{\mathrm{w}}}\right)^4} \gamma^r \tag{2.13}$$

$$\text{with} \quad r = e^{\left[-\frac{\left(\omega_{\mathrm{w}}-\omega_{\mathrm{w,P}}\right)^2}{2\sigma^2\omega_{\mathrm{w,P}}^2}\right]} \tag{2.14}$$

In the JONSWAP spectrum the parameters are defined as follows:

$$\alpha = 0.076\left(\frac{V_{10}}{F_w g}\right)^0.22$$
$$\gamma = 3.3$$
$$\omega_{\mathrm{w,P}} = 22\left(\frac{g^2}{F_w V_{10}}\right)^{1/3}$$
$$\sigma = \begin{cases} 0.07, & \omega_{\mathrm{w}} \leq \omega_{\mathrm{w,P}} \\ 0.09, & \omega_{\mathrm{w}} > \omega_{\mathrm{w,P}} \end{cases}$$

Reference system and basic definitions

The floating structure is considered to be a single rigid body, to simplify the study of the dynamic response. Following a convention adopted in marine engineering, the six degrees of freedom (DOFs) of the system, shown in Fig. 2.13, are referred to as:

- **Surge** for the X direction translation.
- **Sway** for the Y direction translation.

- **Heave** for the Z direction translation.
- **Roll** for the X direction rotation.
- **Pitch** for the Y direction rotation.
- **Yaw** for the Z direction rotation.

The inertial reference system usually employed to describe the dynamics of a offshore wind turbine has the origin at the point which is the interface between the symmetry axis of the tower (Z axis) and the mean sea level. The X axis points in the upward direction, usually parallel to the hub axis when the rotor is not yawed. The Z axis points in the opposite direction w.r.t gravity.

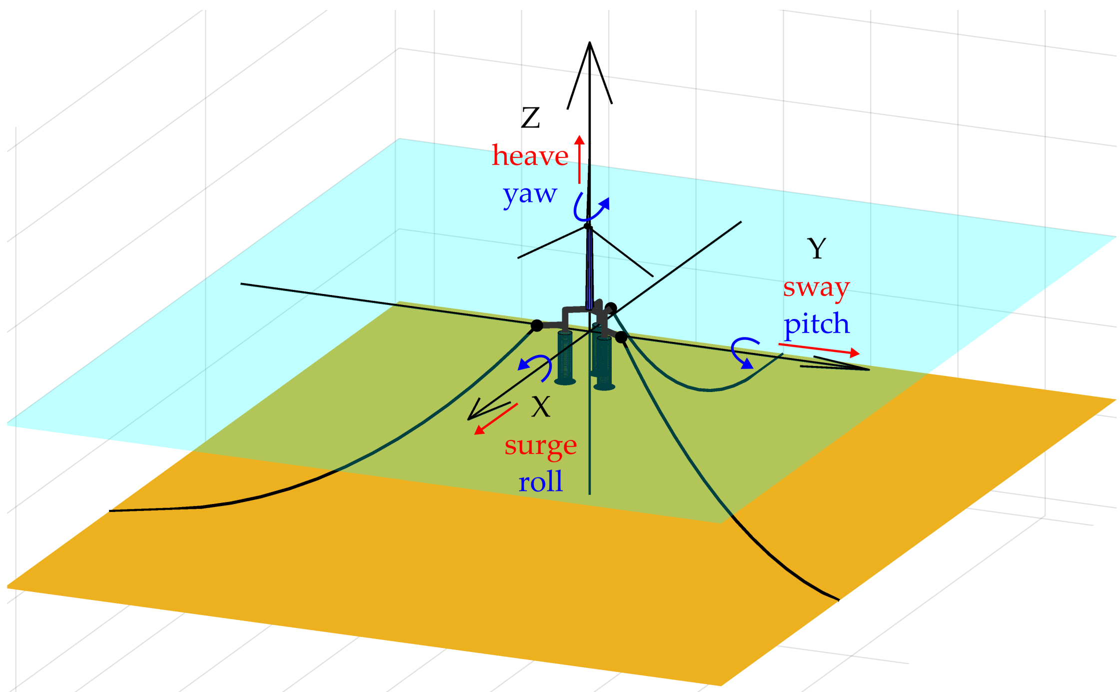

Figure 2.13: Illustration of reference system used for evaluation of motion on a floating offshore wind turbine

When the system is not considered completely rigid, other DOFs of a floating offshore wind turbine may include:

- Modal coordinates of the elastic deformation of the tower in all directions.
- The relative rotation between the nacelle and the tower (it usually happens around the Z, and it is called **nacelle yaw**).
- The rotation of the rotor with respect to the nacelle.

- The rotation of each blade around its constructive axis (referred to as **blade individual pitch**).
- Modal coordinates of the elastic deformation of each blade.

Wind loads

Wind loading distribution acting on the blades are shown in Fig. 2.14. The aerodynamic action of wind acting on the blades plays the fundamental role of generating the mechanical torque (usually indicated with the letter Q) that spins the shaft and allows the production of electricity.

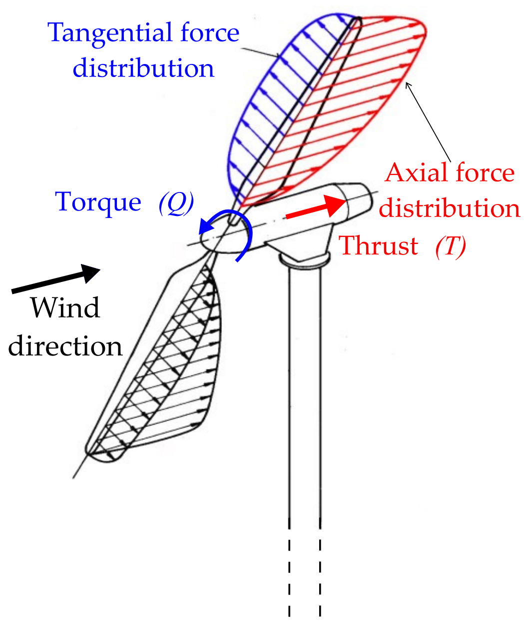

Figure 2.14: Illustration of loads due to wind on a rotor, the integral of the tangential force distribution on blades times the distance from rotation axis is equal to the torque (Q), while the integral of the axial force distribution on blades is equal to the thrust (T).

The physical mechanism behind the creation of the aerodynamic force can be summarized as follows:

1. Air flow impacts on the blade and «spreads» trying to follow the airfoil shape.
2. Due to the airfoil shape itself, the air flowing on the upper side tends to accelerate with respect to the air flowing on the lower side.
3. For the Bernoulli principle, the acceleration on the upper side leads to a decrease of the pressure, and the deceleration on the pressure side leads to an increase of the pressure.

4. The pressure distribution generates the aerodynamic forces.

The forces acting on each blade element (airfoil) contribute to the overall tangential force and axial force on the rotor. The thrust and torque can be evaluated through the analysis of all the aerodynamic actions at each blade element, for a given operating condition. At each section the airfoil encounters different velocities and angles of attack, defined as in Fig. 2.15.

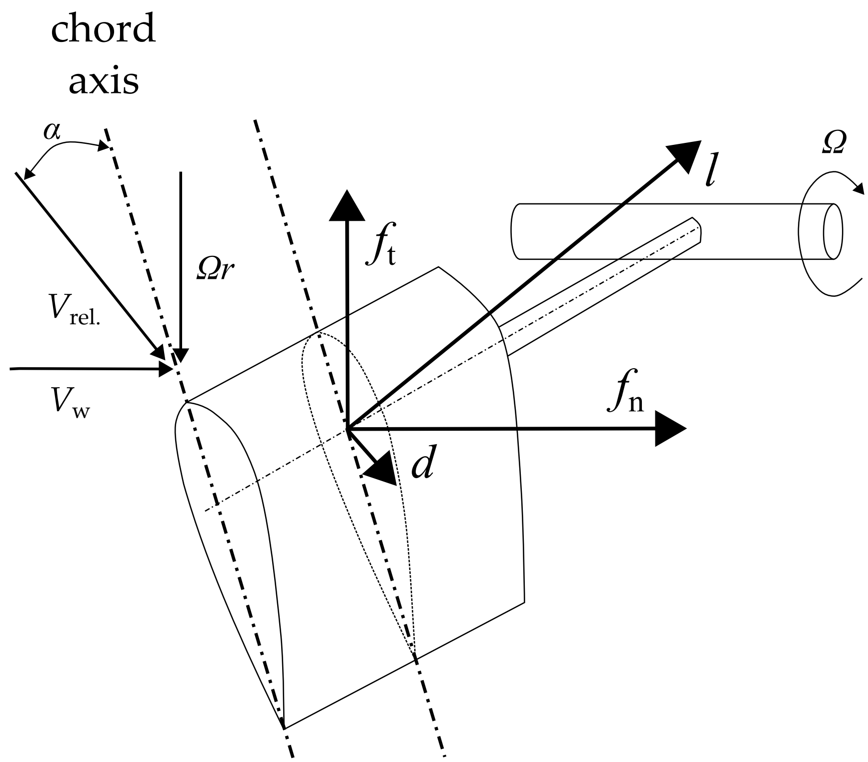

Figure 2.15: Illustration of the forces generated at a section of the blade. Tangential force is represented by f_t, the axial (also normal to the blade surface) force is represented by f_{n}, lift is represented by l, drag is represented by d. The blade section at a radial coordinate r encounters the peripheral velocity due to rotation (Ωr) combined with the wind velocity V_{w}, which result in the relative velocity $V_{\text{rel.}}$. The angle between the relative velocity and chord axis is referred to as angle of attack α.

The relative velocity $V_{\text{rel.}}$ varies along the length of the blade, both in absolute value and direction. This is, mainly, because the peripheral velocity Ωr is highest at the tip of the blade and decreases towards the hub of the turbine (it vanishes at the rotation axis). This variation in relative velocity and angle of attack creates a difference in the amount of lift and drag generated by different sections of the blade. To address this issue, wind turbine blades are twisted along their length. The angle of attack must be kept as constant as possible to maintain an optimal aerodynamic efficiency across the entire length of the blade, especially when wind turbines are operating at the nominal condition. Each section of wind turbine blades is typically characterized by a twist angle (θ) as shown in Fig. 2.16, which allows the optimization of the sectional lift-to-drag ratio, in nominal operating conditions. The design characteristics of blades, and the algorithms to design the blades in order to optimize the operations of wind turbines are thoroughly described in [33].

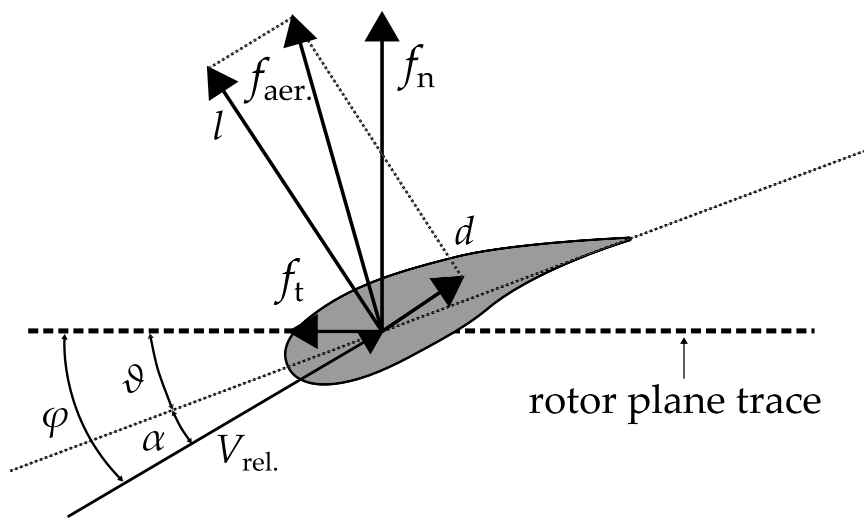

Figure 2.16: Illustration of a blade section with indication of the sectional twist θ. The total aerodynamic force is referred to as f_{aer}. The angle between the relative velocity and rotor plane is referred to as inflow angle ϕ.

Since the axial (or normal) and tangential forces are calculated section per section (hence they are *forces per length*), the thrust dT and the torque dQ on a control volume of thickness dr are obtained as the product of the normal and tangential forces acting on a blade section for the number of blades, and the distance r from the rotation axis for the torque, as shown in Fig. 2.17.

Theories and methodologies to predict the aerodynamic performances of turbines have been developed throughout the years. The aerodynamics of turbines is very similar (specular) to that of propellers. Theories developed to predict propeller performances are useful for turbines as well. One of the simplest and oldest theories to predict rotor performance is the "momentum theory" or "actuator disk theory " developed in the mid-nineteenth century by Rankine and Froude. The momentum theory makes use of linear momentum balance and angular momentum balance and the concept of stream tube containing the actuator disk (which models the turbine), to evaluate global quantities such as thrust and torque. A drawback of this theory is represented by the absence of viscous drag generated by the blades. A modification of the original momentum theory with blade element analysis (called Blade Element Momentum Theory or BEMT) is nowadays largely

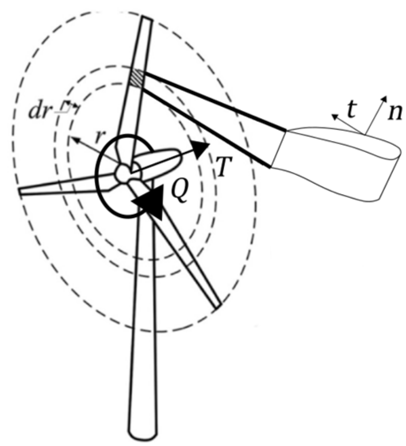

Figure 2.17: Illustration of annular sections in which the rotor is divided when the calculation of the thrust and torque is performed through BEMT calculations.

adopted for turbine analysis and design and extensively explained in [33]. BEMT methods are largely employed for evaluating the power and thrust of turbines in most of the operating conditions (especially near the design point). BEMT methods have the clear advantage of being fast and relatively accurate in predicting global forces and torque, but they can not intrinsically model most of the tridimensional evolution of the flow (such as the root and tip vortex or wake evolution), which in turn may play an important role in the performance of offshore wind turbines. Several attempts to extend BEMT methods with corrections for root and tip vortices (see e.g. [34] or [35]) have shown that the accuracy can be improved, and BEMT may be used to accurately predict performance. BEMT arguably represents a good compromise in computational speed and accuracy for preliminary design, and it was succesfully used since the beginning of wind energy industry. More recently, the speed-up of processors has lead many designers to employ codes which solve high-order approximations of Navier-Stokes equations (such as Reynolds Averaged Navier-Stokes (RANS) or Large-Eddy Simulations(LES)). The successful use of CFD simulations to analyse the performance of wind turbines was shown in many works e.g in [36], [37] or in [38], where a fully-coupled CFD simulation was carried out for a FOWT with both aerodynamic and hydrodynamic flow-fields. Due to the capability of solving the entire flow-field, CFD is also used for analysing complex 3D phenomena. A medium fidelity tool to simulate wind turbines, and in particular offshore wind turbines is represented by Lifting Line Free Wake methods (as shown in [39]). Following an approach which has already been tested in aeronautical industry for fast but accurate calculations of forces on wings (see [40], or for a full and recent implementation in modern programming language [41]) the blades are modelled as "lifting lines" and the potential flow theory that is mathematically based on Laplace's equation describes the flow field. Velocities induced by the "free wake" elements are evaluated at each control point defined by a pre-determined mesh on elements bounded to the lifting surface and, consequently, the forces are obtained through the application of the Kutta-Joukowski equation at the same elements. A complete calculation of the inductions in all directions is intrinsically integrated in this methodology. In fact, the huge advantage of applying this methodology lays in the possibility of the calculation of the wake evolution in time and space (see [42]). This methodology is usually more accurate but also more time consuming than BEMT, and many simulation tools leave to the user the possibility of employing one or the other to simulate rotor aerodynamics as in the software referenced here ([43] and [14]). In order to evaluate the power production performance of the system, the non-dimensional power coefficient is defined as

$$C_P = \frac{P}{\frac{1}{2}\rho_{\text{air}} V_{\text{tot}}^3 S} \tag{2.15}$$

where P is the output mechanical power of a turbine, V_{tot} is the absolute value of the wind speed, S is the reference surface (the turbine disk area) and ρ_{air} is the air density. The power coefficient is usually reported as a function of the Tip Speed Ratio (TSR), another non-dimensional quantity representing the speed at the blade tip normalized with respect to the wind speed,

$$\text{TSR} = \frac{\Omega R}{V_{\text{tot}}} \tag{2.16}$$

where R is the turbine radius and Ω the rotational speed. Each turbine generates a force perpendicular to the rotor plane, namely the thrust, that can be non-dimensionalised as

$$C_T = \frac{T}{\frac{1}{2}\rho_{\text{air}} V_{\text{tot}}^2 S} \tag{2.17}$$

where T is the thrust acting on the rotor. The turbine performance are evaluated from the relations of mechanical power and thrust coefficients with the TSR. As it can be seen from Eq. 2.15 the mechanical power generated by the turbine is a function of the cube of wind speed. Once the $C_P(\text{TSR})$ relationship is known and the generator control strategy is chosen in order to obtain the rotational speed of the shaft Ω corresponding to each operating condition of the turbine, the $P - V$ curve of the system can be estimated, allowing to calculate the overall production performance. A proper control strategy of the electrical generator is crucial for power extraction maximization and losses reduction. In this work BEMT implementations are used for the calculation of rotor aerodynamics in the code [14], or, when only the global effect of wind loads is needed, the thrust is modelled as a constant force, with values found in literature for reference wind turbines.

Hydrostatics and hydrodynamics

First, it is assumed that the body (floating platform) is immersed in a fluid with density ρ and within a gravity field with acceleration g. Each body submerged in a fluid (i.e. displacing a volume of fluid equal to its submerged volume), is subjected to a force referred to as "buoyancy". This force acts on the surfaces of the submerged part of the body and can be calculated as follows:

$$\boldsymbol{F}_{\mathrm{b}} = \iint_A p(z)\boldsymbol{n} dA = \rho g \forall_{\mathrm{d}} \tag{2.18}$$

where $p(z)$ is the pressure (normal stress) as a function of depth, $\boldsymbol{n}$ is the normal to the surface and A and $\forall_{\mathrm{d}}$ are the submerged surface area and displaced volume of the body, respectively. The force acts at the centre of buoyancy, which is the centre of gravity of the displaced volume. The motion and orientation of the body and the local surface elevation causes the displaced volume to change with time, this correspondingly changes the magnitude and direction of $\boldsymbol{F}_{\mathrm{b}}$. Depending on the spatial distribution of $\forall_{\mathrm{d}}$, this can also induce a buoyancy moment on the body. To take into account hydrostatic force variation, a linearization is possible (see e.g. [44]), if the following hypotheses are valid:

- surface elevation approximately constant;
- approximately same shape of the waterplane area when the submerged volume changes.

Expressing the motion of the body away from equilibrium as a simple translation and rotation:

$$\boldsymbol{dr} = [\delta x, \delta y, \delta z, \delta\theta_x, \delta\theta_y, \delta\theta_z] \tag{2.19}$$

the buoyancy force/moment can be expressed as:

$$\boldsymbol{F}_{\mathrm{b}} = \boldsymbol{F}_{\mathrm{b,eq.}} - [C] \cdot \boldsymbol{dr} \tag{2.20}$$

Where $\boldsymbol{F_{b,eq.}}$ is the buoyancy force/moment at equilibrium, and $[C]$ is usually referred as to the hydrostatic stiffness matrix, and is composed of a set of integrals over the waterplane area, shown as grey area in Fig. 2.4. Once the static forces acting on a submerged body are calculated, the wave-induced loads and motions on marine structures (hydrodynamics) can be determined. Similarly as it was illustrated in the last section for aerodynamics, several numerical solutions of the hydrodynamic problem of body-fluid interaction exist. The flow-field (governed by Navier-Stokes equations) may be resolved through CFD analyses, e.g. using Volume-of-Fluid-Reynolds-Averaged-Navier-Stokes (VOF-RANS) equations, as in [45], in which this methodology was applied to calculate the dynamic of a wave-energy converter. This approach is able to model the highly non-linear dynamics of body interaction with waves, using incompressible two-phase Reynolds averaged

Navier–Stokes. This solution intrinsically includes non-linear waves, viscous flow characteristics and large amplitude motions. This being said, CFD methodologies, which are also applied in the field of FOWT simulation, such as in [46] [38] [47], are time-consuming, and furthermore they require a great effort to prepare the body (surface of a 3D model) and the flow-field meshes. To greatly simplify the estimation of forces and motions, we can assume that loads generated by potential flow phenomena and by viscous effects can be superimposed. This subdivision, commonly adopted in marine engineering [44], allows the calculation of non-viscous and viscous loads independently, through approximated theories. Potential flows develop under the assumptions of:

- incompressible;
- inviscid fluid;
- irrotational motion.

A further useful simplification can be done by considering the origin of each phenomenon contributing to the body-fluid interaction. As shown in Fig. 2.18, we can explain potential flow effects through the following considerations,

- loads generating when the body is fixed and is subjected to incident waves:
  - Froude-Krylov forces, due to the unsteady pressure field that generates from the variation of the velocities of fluid in the proximity of the body;
  - Diffraction forces, due to the reaction of the fluid that is disturbed by the body;
- Loads generating when the body is moving and the fluid is calm:
  - added mass, due to the volume of the fluid in the proximity of the body that is accelerated by the body motion, which creates an additional inertia;
  - radiation damping, due to the dissipation of energy generated by the creation of a wave field by the body motion.

To estimate each contribution to the loads, for a body interacting with a fluid that is (at least approximately) describe by potential flow, we need to introduce Laplace's equation for the potential of the velocity field as follows:

$$\nabla^2 \phi = 0 \tag{2.21}$$

where the gradient of this potential $\nabla\phi$, i.e. the velocity field $\boldsymbol{v}$ is defined as,

$$\boldsymbol{v} = \nabla\phi = \frac{\partial \phi}{\partial x}\boldsymbol{e_x} + \frac{\partial \phi}{\partial y}\boldsymbol{e_y} + \frac{\partial \phi}{\partial z}\boldsymbol{e_z} \tag{2.22}$$

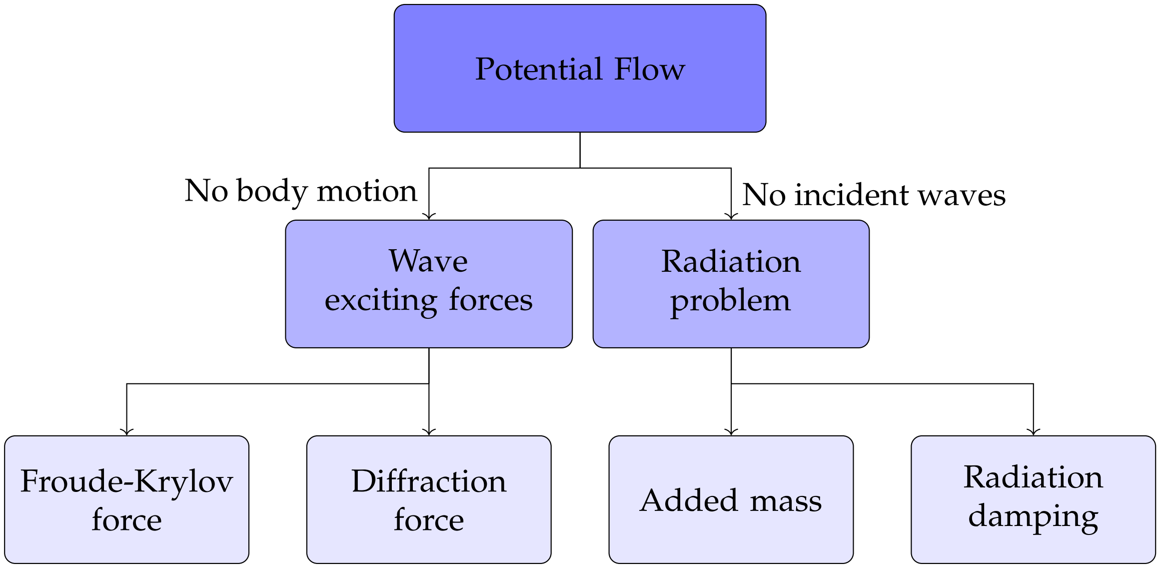

Figure 2.18: Simplified scheme for potential flow effects.

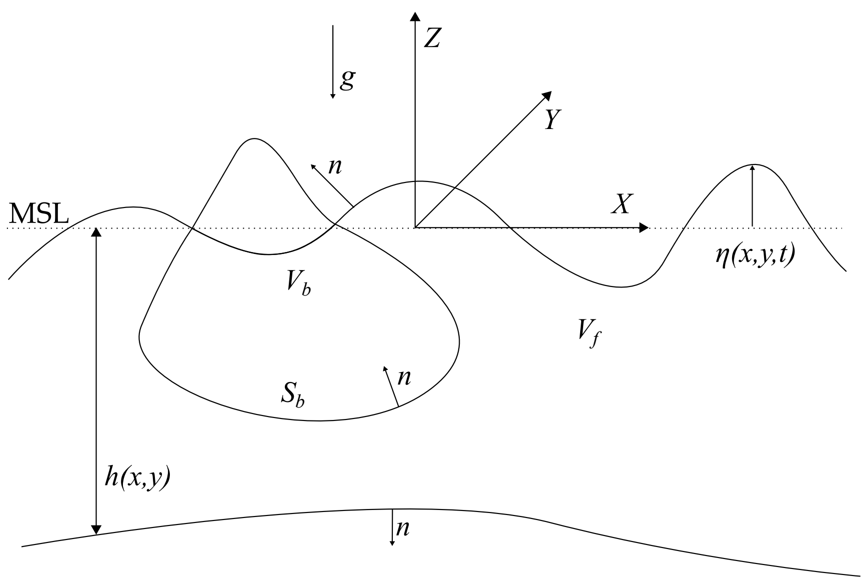

Figure 2.19: Illustration of the volume of fluid in which the potential flow theory is applied.

To solve the body-fluid interaction problem in the flow-field defined by the fluid around the body, shown in Fig. 2.19, the choice of appropriate boundary conditions is needed.

In the linear potential flow theory (see [48]), these boundary conditions are linearized under the assumption of wave amplitude much smaller than the wave length. The bottom and body boundary conditions are the no-flux conditions given by

$$\frac{\partial \phi}{\partial n} = 0 \quad \text{with } z = -h \tag{2.23}$$

and

$$\frac{\partial \phi}{\partial n} = v_n \quad \text{on } S_b \tag{2.24}$$

On the free surface, two conditions, one based on the kinematics of free surface motion and the other on the continuity of pressure across the free surface,

$$\frac{\partial \eta}{\partial t} + \frac{\partial \phi}{\partial z} = 0 \quad \text{with } z = 0 \tag{2.25}$$

which is the kinematic condition and

$$\frac{\partial \phi}{\partial t} + g\eta = 0 \quad \text{with } z = 0 \tag{2.26}$$

which is the pressure continuity across the free surface (obtained through Bernoulli's equation). Two additional assumptions are made:

- the floater undergoes negligibly small motions away from the equilibrium position;
- solutions are assumed to be harmonic;
- wave energy associated with disturbance due to the body is radiated in all direction (Sommerfeld condition).

This linear boundary value problem can be solved using a so-called panel method (or Boundary Element Method) allowing the calculation of pressures on the body surface for a given condition of the free surface (mono-chromatic wave), such as in the frequency-domain analysis performed by the software NEMOH, based on the work from [49]. The motion of a generic floating body in dimension j can be modelled with the equation due to Cummins [50]:

$$(M_{ij} + A^{\infty}{}_{ij})\ddot{x}_j(t) + \int_{-\infty}^{t} K_{ij}(t-\tau)\dot{x}_j(\tau)d\tau + C_{ij}x_j(t) = F_j{}^{w}(t) - F_j{}^{m}(x, \dot{x}, t) \tag{2.27}$$

in the above expression the indices i and j represent the degree of freedom of motion and the direction of the acting force, respectively. In this equation M represents the inertia matrix of the body, A is the added mass matrix, K is the kernel matrix, which can be calculated from the radiation damping matrix B, C is the hydrostatic stiffness matrix, F^w are the forces due to waves, F^m are external forces due to moorings (which will be treated in the remainder of the work). The added mass and radiation damping matrices are calculated in a frequency domain analysis from the disturbance (radiation) potential, indicated with ϕ_r, which is generated from the reaction of the fluid (following Newton's third law) when the body moves in calm fluid (radiation problem). Applying the no-flow condition, the gradient of the disturbance potential on the surface of the body S_b must be equivalent to the local body motion $\boldsymbol{V_b}$:

$$\frac{\partial \phi_r}{\partial n} = \nabla \phi \cdot \boldsymbol{n} = \boldsymbol{V_b} \quad \text{on } S_b \tag{2.28}$$

The solution of the potential ϕ_r on the geometry can be integrated to calculate the total forcing (which is a complex number due to the harmonic nature of the solution) in the i^{th} direction, due to a mono-chromatic motion in the j^{th} direction, with frequency ω:

$$A_{ij} - \frac{i}{\omega} B_{ij} = \rho \iint_{S_b} n_i \phi_{r,j} dS \tag{2.29}$$

The infinite added mass can be calculated as

$$A^{\infty}{}_{ij} = \lim_{\omega \to -\infty} A_{ij}(\omega) \tag{2.30}$$

The time convolution kernel matrix is referred to as the radiation impulse response function, or IRF, can be calculated as follows:

$$K_{ij}(t) = \frac{2}{\pi} \int_0^{\infty} \omega A_{ij}(\omega) \sin \omega t d\omega = \frac{2}{\pi} \int_0^{\infty} B_{ij}(\omega) \cos \omega t d\omega \tag{2.31}$$

In Cummins' equation, the integral of the radiation IRF represents the fluid memory effects that incorporate the energy dissipation due to the radiated waves generated by the motion of the body. It is also called the retardation or memory matrix. For wave excitation forces $F_j^{\,w}(t)$ a disturbance potential and a force X_j which acts on the body are generated. The Haskind relations (see [44]) allows these forces to be expressed in terms of the radiation potential:

$$X_j = -i\omega\rho \iint_{S_b} (n_i \phi_0 - \phi_{r,j} \frac{\partial \phi_0}{\partial n}) dS \tag{2.32}$$

where ϕ_0 is the potential of the incident wave. As done for the kernel matrix, the corresponding IRF is calculated as follows:

$$H_{ij}(t) = \frac{1}{2\pi} \int_{-\infty}^{\infty} X_j(\omega) e^{i\omega t} d\omega \tag{2.33}$$

A time convolution of the IRF gives the time-domain excitation forces:

$$F_j^e(t) = \int_{-\infty}^{\infty} H_{ij}(\tau)\eta(x_0, y_0, t-\tau)d\tau \tag{2.34}$$

where $\eta(x_0, y_0, t-\tau)$ is the wave elevation at the reference position (x_0, y_0) at instant t.

Morison's equation

Viscous loads are generated by viscous phenomena, such as vortex shedding, drag and lift. In the evaluation of hydrodynamic actions on moving bodies subjected to wave, the magnitude of viscous loads may be predominant w.r.t. loads coming from potential flow phenomena (e.g. wave excitation forces). This is particularly true for slender cylinders, as shown in Fig. 2.20.

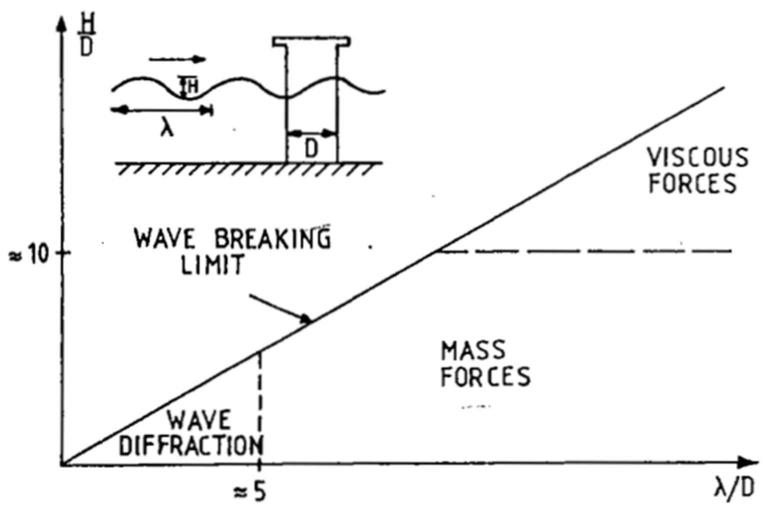

Figure 2.20: Illustration of the relative importance of viscous forces w.r.t. potential flow effects for a fixed cylinder (diameter D) subjected to a wave with height (H) and length (λ). From [51].

Full Morison equation approach is able to model hydrodynamic loads on slender cylindrical bodies (D/λ < 0.2). This is especially useful for calculating distributed hydrodynamic loads.

Assuming a slender cylinder with projected areas and immersed volume, as shown in Fig. 2.21, the axial and normal loads can be written in two parts, drag and inertial forces. These two forces can be decomposed on the normal and axial directions as follows:

$$F_{\mathrm{m}}^{\mathrm{ax}} = \frac{1}{2}\rho V^{\mathrm{ax}}|V^{\mathrm{ax}}|C_D^{\mathrm{ax}}A_{\mathrm{p}}^{\mathrm{ax}} + \rho V^{\mathrm{ax}}C_M^{\mathrm{ax}}\forall_{\mathrm{d}} \tag{2.35}$$

$$F_{\mathrm{m}}^{\mathrm{n}} = \frac{1}{2}\rho V^{\mathrm{n}}|V^{\mathrm{n}}|C_D^{\mathrm{n}}A_{\mathrm{p}}^{\mathrm{n}} + \rho \dot{V}^{\mathrm{n}}C_M^{\mathrm{n}}\forall_{\mathrm{d}} \tag{2.36}$$

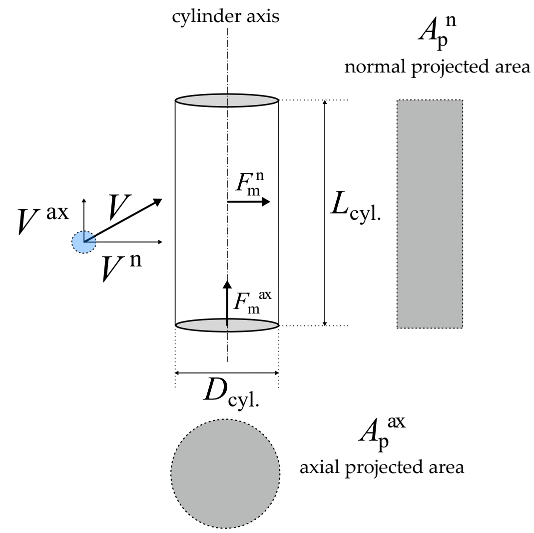

Figure 2.21: Illustration of axial and normal forces that can be calculated through Morison's equation.

where V is the instantaneous velocity of water particles in the proximity of the cylinder, which is decomposed in the axial V^{ax} and normal V^{n} components, C_D is the drag coefficient (axial and normal) and C_M is the added mass coefficient (axial and normal). $F_{\mathrm{m}}^{\mathrm{ax}}$ and $F_{\mathrm{m}}^{\mathrm{n}}$ have the same direction of the axial and normal velocities. C_D and C_M depend strongly on the flow characteristics. The drag and inertia coefficients are in general dependent on viscous and inertial forces relevance in the flow-field conditions. The Reynolds number, the Keulegan-Carpenter number and the relative roughness are used as non-dimensional numbers to characterize the flow-field conditions. The coefficients also depend on the shape and orientation of the body. For a cylinder of diameter $D_{\mathrm{cyl.}}$, the Reynolds number is defined as,

$$Re_{D_{\mathrm{cyl.}}} = \frac{V_{\mathrm{ref.}} D_{\mathrm{cyl.}}}{\nu_{\mathrm{fluid}}} \tag{2.37}$$

and the Keulegan-Carpenter number as

$$KC_{D_{\mathrm{cyl.}}} = \frac{V_{\mathrm{ref.}} T_{\mathrm{ref.}}}{D_{\mathrm{cyl.}}} \tag{2.38}$$

where $V_{\mathrm{ref.}}$ is a reference velocity, ν_{fluid} is the kinematic viscosity of the fluid, and $T_{\mathrm{ref.}}$ is a reference period of the waves. Re and KC will assume different values for different operating conditions, being based on both environmental, geometrical and kinematic conditions. In general, an averaged value for the coefficients can be used for a set of operating conditions which do not differ too much from each other (see e.g. drag identification in [52]). A major issue in the identification of these coefficients still arise from the fact that relative velocities can not be predetermined based only on the kinematic conditions of the flowfield, but are affected by the dynamic behaviour of the body as well. A procedure to evaluate the drag coefficient that should be used to evaluate Morison's equation forces is as follows:

1. Evaluate the conditions imposed by the flow-field (e.g. expected periods, height of the waves or sea current speed);
2. Set the geometrical features of the body; the Morison's equation also requires that the orientation of the body will not change drastically in the conditions which are going to be modelled.
3. Evaluate the non-dimensional numbers ($Re_{D_{\text{cyl.}}}$ and $KC_{D_{\text{cyl.}}}$) for each condition chosen in point 1.
4. From previous experiments and/or numerical simulations, relate the coefficients to the non-dimensional numbers (an example of the relationship between drag coefficient and Reynolds number for flows around cylinders is shown in Fig. 2.22).
5. The drag coefficient can be calculated from the relationships found in literature. If the conditions that are going to be modelled are very different (e.g. different wave spectra and significantly different dynamics of the body), it is suggested to evaluate the drag coefficient for the different conditions, and average the found values.

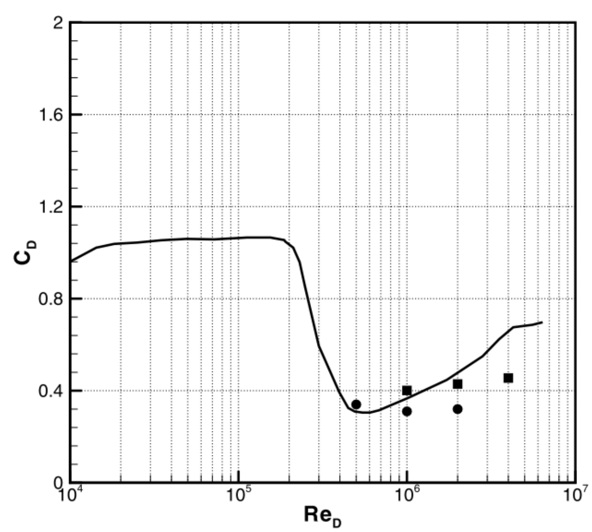

Figure 2.22: Drag coefficient as a function of the Reynolds number for flows around cylinders.(●) represents CFD Large-Eddy-Simulations analyses, and (■) CFD RANS simulations. This graph is used to determine C_D^{ax} as a function of Reynolds number. From [53].

Mooring lines modelling

Certain parameters must be assigned to model the mooring system, in particular the following characteristics, which are common to all mooring systems, must be defined:

- environmental conditions (depth h, water density $\rho_{wat.}$, gravity acceleration g);
- material properties (mass of mooring line per unit length w, mooring line stiffness E, breaking load MBL)
- configuration parameters of the mooring system, comprising:
  - number of mooring lines;
  - orientation of lines;
  - positions of the fairleads (connections to the floating body) and anchors (connections to the seabed).

Following the approach shown in [51], a static analysis of the forces exerted by a single mooring line on a floating body is possible starting from the actions on a section of the mooring line, shown in Fig. 2.23b. First, we assume that a spread mooring system is adopted, in which a part of the mooring line is always laying on the seabed (shown in Fig. 2.23a as the distance between anchor and touchdown point $x_{\text{A,t.p.}}$). The tension in the line, which applies the restoring forces on the floating body, indicated as T_{C}, is mainly generated by the weight of the line itself, and partially to the elasticity of the cables (which is characterized by the elastic module E_{C} and the cross-sectional area A_{C}). The "stiffness" of the mooring cables changes with its geometric (the actual position of the line) and elastic state (the elongation of the cable), hence for the static analysis of the cable we assume a fixed geometry and external loading (fixed load at the fairlead).

To simplify the static analysis, we also assume:

- horizontal seabed;
- cable in a vertical plane (neglecting bending stiffness);
- neglect dynamic effects in the line.

We can write the mooring line section tangential (Eq. 2.39) and normal (Eq. 2.40) equilibrium as,

$$dT_{\text{C}} - \rho g A_{\text{C}} dz = \left[w_{\text{C,wat.}} \sin\phi - f_{\text{C}} \left(1 + \frac{T_{\text{C}}}{A_{\text{C}} E_{\text{C}}} \right) \right] ds \tag{2.39}$$

$$T_{\text{C}} d\phi - \rho g A_{\text{C}} z d\phi = \left[w_{\text{C,wat.}} \cos\phi - d_{\text{C}} \left(1 + \frac{T_{\text{C}}}{A_{\text{C}} E_{\text{C}}} \right) \right] ds \tag{2.40}$$

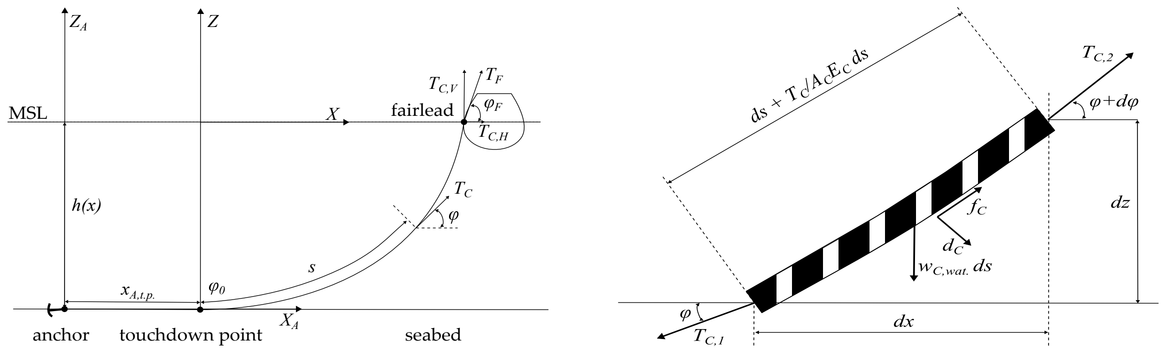

(a) Mooring line (b) Mooring section

Figure 2.23: Illustration of a single mooring line (left), and a section of the mooring cable (right), used for static calculations of the forces exerted by the mooring line on a floating body. Two coordinate systems are defined, one with the center in the anchor ($\{X_\text{A}, Z_\text{A}\}$) and the other in the projection of the touchdown point on the MSL ($\{X, Z\}$). The two coordinate systems have the axes aligned with the vertical and horizontal directions. The horizontal direction and the cable tangent create the angle ϕ. The curvilinear coordinate along the cable is indicated with the letter s. The weight in water of the cable, the normal force and the tangential forces due to hydrodynamics on the cable are indicated with $w_\text{C,wat.}$, d_C and f_C respectively.

where the term $\rho g A_\text{C}$ represents the hydrostatic force per unit length on the section, and it has been added to correct the weight in water of the cable. The solution to these non-linear equations may be approximated if the dynamic loads due to hydrodynamic action of water f_C and d_C are neglected, and the cable is considered inelastic ($E_\text{C} \to \infty$). By introducing the effective tension,

$$T_\text{C}' = T_\text{C} - \rho g A_\text{C} z \tag{2.41}$$

we obtain,

$$dT_\text{C}' = w_\text{C,wat.} \sin\phi ds \tag{2.42}$$

$$T_\text{C}' d\phi = w_\text{C,wat.} \cos\phi ds \tag{2.43}$$

which can be re-arranged and integrated (see [51]) to obtain the cable configuration, when subjected to an horizontal tension at the fairlead $T_\text{C,H}$, in terms of the curvilinear and vertical coordinates:

$$s = a_\text{C} \sinh\left(\frac{x}{a}\right) \tag{2.44}$$

$$z + h = a_\text{C}\left[\cosh\left(\frac{x}{a}\right) - 1\right] \tag{2.45}$$

where $a = T_\text{C,H}/w_\text{C,wat.}$, and the tension along the cable can be calculated from

$$T_\text{C} = T_\text{C,H} + w_\text{C,wat.} h + \left(w_\text{C,wat.} + \rho g A_\text{C}\right) z \tag{2.46}$$

the suspended length of the cable $l_{\text{C,s.}}$ is calculated from the curvilinear coordinate s (Eq. 2.44) as follows:

$$l_{\text{C,s.}} = a_{\text{C}} \sinh\left(\frac{x}{a}\right) \tag{2.47}$$

A common methodology to calculate the properties of a single-mooring line to sustain a prescribed maximum fairlead tension $T_{\text{C,H,max}}$ is obtained if we assume that the mooring line will be entirely suspended (from anchor to fairlead) and it will not exert any vertical force on the anchor (drag-anchor), as shown in Fig. 2.24b.

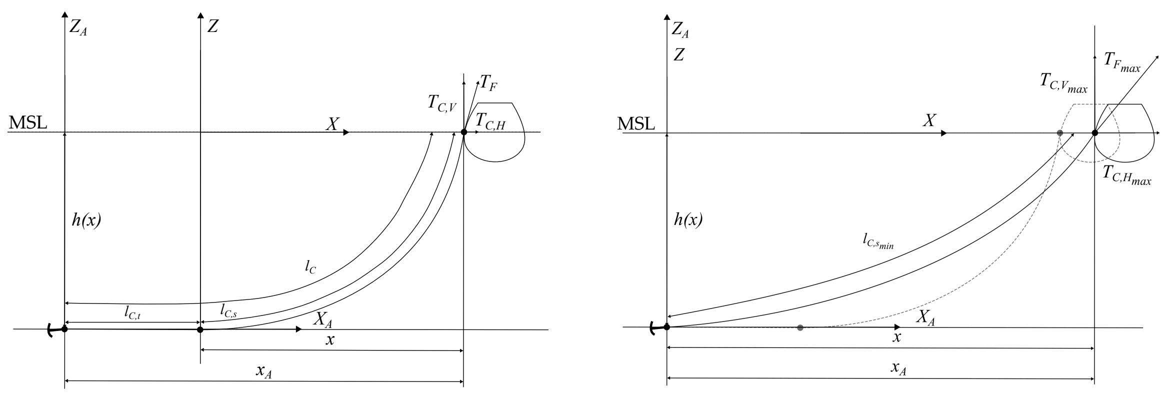

(a) Tension at the fairlead: $T_{\text{C,H}}$.

(b) Tension at the fairlead: $T_{\text{C,H,max}}$.

Figure 2.24: Illustration of the displacement of the floating body w.r.t. the anchor. The suspended line length varies with the tension.

By assuming that the mooring line is tangent to the seabed at $z = 0$ when $T_{\text{C,H,max}}$ is applied, the following relationships are obtained. First, the maximum tension is obtained from the horizontal tension and the weight of the line in water,

$$T_{F_{\max}} = T_{\text{C,H,max}} + w_{\text{C,wat.}} h \tag{2.48}$$

Then, a minimum suspended line length $l_{\text{C,s,min}}$ is found to avoid vertical loads on the anchor:

$$l_{\text{C,s,min}} = h\sqrt{\frac{2T_{F_{\max}}}{w_{\text{C,wat.}} h} - 1} \tag{2.49}$$

If the line length l_{C} is given, the position of the floating body (fairlead) w.r.t. the touchdown point is calculated from the suspended length $l_{\text{C,s.}}$ as follows:

$$x_{\text{A}} = l_{\text{C}} - l_{\text{C,s.}} + x \tag{2.50}$$

which can be furtherly simplified to get a function of the characterstics of the mooring, horizontal tension (a_{C}) and depth h:

$$x_{\mathrm{A}} = l_{\mathrm{C}} - h\sqrt{1 + 2\frac{a}{h}} + a\cosh^{-1}\left(1 + \frac{h}{a}\right) \tag{2.51}$$

The last two relationships are also used to evaluate the necessary $x_{\mathrm{A},0}$ (fairlead distance from anchor when $T_{\mathrm{C,H}} = 0$) to limit the offset of the floating body from the equilibrium position, also referred to as "admissible offset" $\Delta x_{\mathrm{adm.}}$, when the maximum horizontal tension is applied ($T_{\mathrm{C,H}} = T_{\mathrm{C,H,max}}$). From relationships between distance, as shown in Fig. 2.25, we obtain that the anchor scope $x_{\mathrm{A},0}$ is

$$x_{\mathrm{A},0} = x_{\mathrm{A,max}} - \Delta x_{\mathrm{adm.}} \tag{2.52}$$

which, for a known displacement at the maximum horizontal tension $x_{\mathrm{A,max}}$ as in 2.50, returns the value of $x_{\mathrm{A},0}$ as a function of the admissible offset.

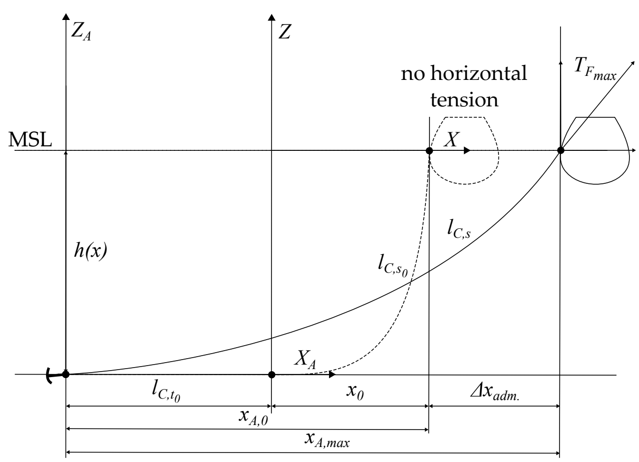

Figure 2.25: Illustration of the displacement of the floating body with no tension (dashed lines) and with maximum tension (continuous line).

To improve the accuracy of the estimation of a single mooring line configuration when the displacements (and the elongation of the cable) become large, elasticity must be taken into account. The equations of the tangential and normal equilibrium (Eq.s 2.39 and 2.39) are still valid. Following the approach of [51], the relationships for the tensional state and horizontal displacement from touchdown point of the floating body are obtained for an elastic cable. The horizontal tension $T_{\mathrm{C,H,el.}}$ is calculated as:

$$T_{\mathrm{C,H,el.}} = \frac{T^2_{\mathrm{C,V,el.}} - \left(w_{\mathrm{C,wat.}} h - \frac{1}{2}\frac{(w_{\mathrm{C,wat.}}\ l_{\mathrm{C,s.}})^2}{E_{\mathrm{C}} A_{\mathrm{C}}}\right)}{2\left(w_{\mathrm{C,wat.}} h - \frac{1}{2}\frac{(w_{\mathrm{C,wat.}}\ l_{\mathrm{C,s.}})^2}{E_{\mathrm{C}} A_{\mathrm{C}}}\right)} \tag{2.53}$$

while the displacement of the floating body from touchdown point is expressed by the coordinate:

$$x = \frac{T_{\text{C,H,el.}}}{w_{\text{C,wat.}}} \log\left(\frac{T_{\text{C,el.}}}{T_{\text{C,H,el.}}} + T_{\text{C,V,el.}}\right) + \frac{T_{\text{C,H,el.}}}{E_{\text{C}} A_{\text{C}}} l_{\text{C,s.}} \tag{2.54}$$

the total tension can be calculated from:

$$T_{\text{C,el.}} = \sqrt{T^2_{\text{C,H,el.}} + T^2_{\text{C,V,el.}}} \tag{2.55}$$

In the remainder of this work, the elastic catenary mooring lines equations will be used for the preliminary design of a mooring system. A mooring system composed by more than one cable is usually referred to as "spread mooring system". To analyse the reaction of a spread mooring system, a solution for elastic, multi-line mooring systems is needed. In a simplified analysis, the force applied by the floating body is directed along a single line, and the displacement of the floating body is along this line as well, as shown in Fig. 2.26. Despite this condition is not common in the dynamic response of a floating body subjected to waves and wind, it is useful to verify the tensional state of the most elongated line in a multi-line mooring system (in which other lines contribute to forces) when the body is subjected to a given load (e.g. the thrust of a wind turbine), similarly to what was shown in [54].

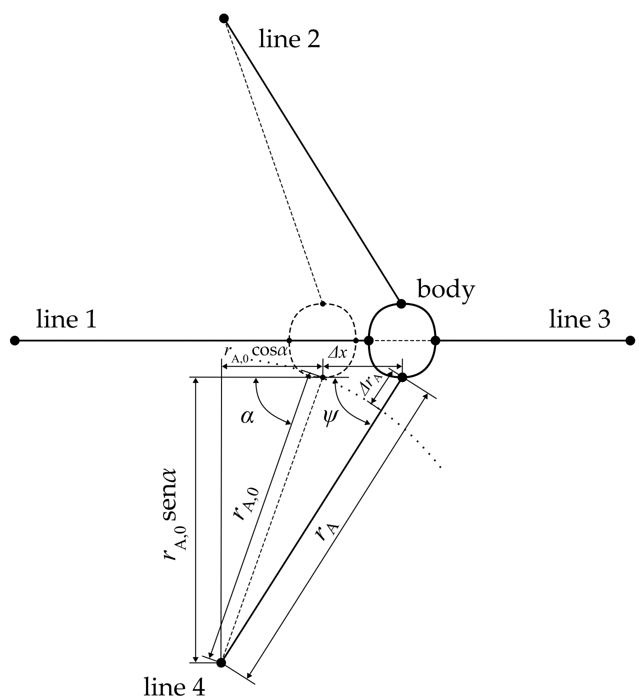

Figure 2.26: Illustration of the displacement of a floating body anchored through a multi-line mooring system.

From Fig. 2.26, we can use geometrical relationships to calculate the elongation of line 4 (Δr_{A}), due to a displacement of line 1 Δx. The elongation of line 4 is the difference between the final and the initial fairlead-anchor distances respectively,

$$\Delta r_{\text{A}} = r_{\text{A}} - r_{\text{A,0}} \tag{2.56}$$

Assuming that the initial position of the line given by the fairlead-anchor distance and the angle between the two lines (in our case line 4 - line 1) $r_{\text{A,0}}$ and α are known, we start by writing the relationship between r_{A} and $r_{\text{A,0}}$ as follows:

$$r_{\text{A}} = \sqrt{r_{\text{A,0}}^2 \text{sin}\,\alpha^2 + r_{\text{A,0}}\cos\alpha + \Delta x^2} \tag{2.57}$$

which, can be simplified to get

$$r_{\text{A}} = r_{\text{A,0}}\sqrt{1 + 2r_{\text{A,0}}\cos\alpha\frac{\Delta x}{r_{\text{A,0}}} + \frac{\Delta x}{r_{\text{A,0}}}^2} \tag{2.58}$$

hence by combining Eq. 2.56 and Eq. 2.58, we obtain the elongation of line 4

$$\Delta r_{\text{A}} = r_{\text{A,0}}\left(\sqrt{1 + 2\cos\alpha\frac{\Delta x}{r_{\text{A,0}}} + \frac{\Delta x}{r_{\text{A,0}}}^2} - 1\right) \tag{2.59}$$

In the following chapters, Eq.2.59 will be used to calculate the configuration of a spread mooring system, to obtain the total forces exerted on the fairleads, which are the resultants of the tensions of each line along their corresponding direction. For example, if we refer to Fig. 2.26, the total horizontal force exerted by the mooring system becomes

$$F_{\text{H,moor.sys.}} = \sum_{i=1}^{N_{\text{lines}}} T_{\text{C,H},i}\cos\psi_i \tag{2.60}$$

where ψ_i is the angle between the horizontal line and a generic i^{th} line in the current configuration. As it was shown by [55] and more recently in [56], an iterative solution of an elastic spread mooring system, composed by line elements connected by nodes at which the forces are evaluated, is possible via the implementation of a routine that determines:

- with an inner loop, the geometry of each element;
- with an external loop, the tensional state at each node, using force-balance equations.

This iterative implementation can be also used for evaluating the response of the mooring system in time, updating the static configuration and tensional state due to external loading (coming from the fairleads, hydrodynamics and the reaction of anchors, when present) at each time step. An iterative design procedure for spread catenary mooring lines will be implemented in the next chapter.

2.3 Wind farm integration

Floating offshore wind turbines are expected to be built in arrays composed by many turbines, just as it has been done with fixed foundations offshore wind farms (nearly 50% of the current fixed foundations wind farms are composed by more than 40 systems [57]). The construction of wind farms allows:

- to increase the total power, thus the energy production;
- to exploit economies of scale for:
  - the construction of the sub-components;
  - the assembling of the systems;
  - the rent of the offshore vessels for the installation of the wind farm;
  - the rent of the offshore vessels maintenance of the systems;
  - the decommissioning of the wind farm.

This two-folded advantage makes building large wind farms appealing for investors in the field. A wind farm comprises the electrical systems needed to export the generated energy to land. In the case of an offshore wind farm, the electrical infrastructure is made up of the array cables, offshore export cables, onshore export cables, onshore substations, and offshore substations, as shown in Fig. 2.27,

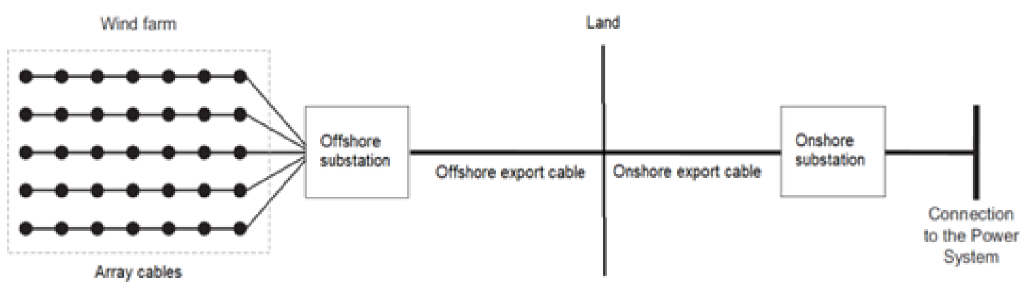

Figure 2.27: Scheme for electrical infrastructure of offshore wind farms. From [58].

Several issues arise when building arrays of wind turbines, which are common to onshore wind farms as well, such as,

- the need to optimize the electrical power infrastructure, to minimize the power losses and the overall costs of the electrical cables (as it was demonstrated for an onshore wind farm in [59]);
- the loss of wind speed and increment of turbulence in the wakes of upwind rows of wind turbines (these are also called *wake effects*) which cause power losses and increased fatigue loads in the *shadowed* downwind systems. Most

of the practical models to account for wake losses in wind farms are based on the work from Jensen [60], which developed a model to calculate the speed decrement at a certain distance in the wake due to an upwind turbine with a specified thrust coefficient.

The solution to these issues become non-trivial because short distances between turbines are needed to avoid high costs of electrical infrastructure (and low occupation of area at the installation site), while long distances would be ideal to avoid wake interaction. Optimization of the layout of offshore wind farms is hence needed, as shown in [61], through the concurrent modelling of both . New prospects can arise for wind farm flow control [62], i.e. the control of the behaviour and evolution of flows in the wind farm, through sensors and actuators that influence the configuration of the systems, to increase the global energy production. These approaches comprise:

- wake steering, that is the actuation of yaw or other control system of upwind turbines to "displace" the wake from downwind ones (see [63]);
- induction control, which requires the adaptation of upwind turbines aerodynamic loading (for example through blade pitching) for the benefit of downstream systems [64];
- wake mixing, which works by deliberately increasing turbulence in the wake to trigger the re-energizing of the wake (also referred to as wake recovery).

In the remainder of the work, a particular attention will be given to the "wake mixing" control, following the approach that was proposed in [65]. In particular, in floating offshore wind farms, wake mixing performance may be improved, leading to greater energy yields, or control of the turbine may be decreased without affecting wake mixing performance, thereby reducing turbine loading, if the motion of the system can be designed to help in wake mixing.

2.4 Economical assessment

As mentioned in the introduction, the total energy produced from a wind farm and the overall costs over the entire lifetime of the farm are the real drivers for the decisions of investors in the floating offshore sector to proceed with the development of a project. A joint evaluation of these two characteristics of a wind farm is necessary to compare it to other sources of energy. Levelized Cost of Energy or LCoE measures lifetime costs divided by energy production. LCoE allows the comparison of different technologies (e.g., wind, solar, natural gas) of unequal life spans, project size, different capital cost, risk, return, and capacities. It is defined in [66] as the actualized energy price required for a project to exactly meet its operating costs in a year and the share of capital costs and decommissioning costs in that year, i.e. the minimum price at which energy must be sold for an energy project to break even.

$$\text{LCoE} = \frac{[(\text{CAPEX} + \text{DECEX}) \cdot \text{CRF} + \text{OPEX}]}{\text{AEP}} \tag{2.61}$$

where the following quantities must be introduced:

- CAPEX [€]: CAPital EXpenditures
- DECEX [€]: DECommissioning EXpenditures
- OPEX [€/year]: OPerational EXpenditures
- CRF [1/year]: Capital Recovery Factor
- AEP [MWh/year]: Annual Energy Production

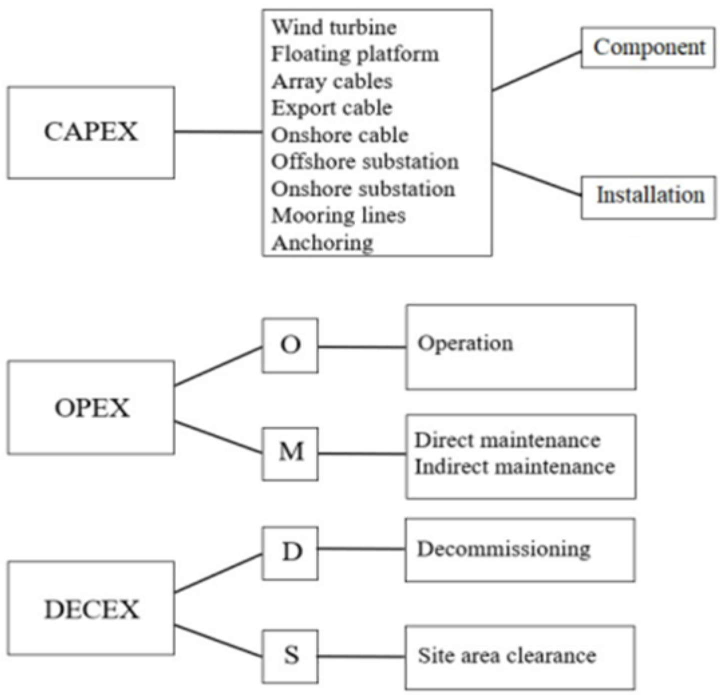

Figure 2.28: Scheme of costs of offshore wind farms. From [67].

A further categorization of costs is shown in Fig. 2.28. To evaluate the economical feasibility of a wind turbines farm, it is crucial to develop methodologies for the estimation of the LCoE in the preliminary design phases. When evaluating any change to the design of a wind turbine, it is critical that the designer evaluate the impact of the design change on the system cost and performance.

The designer must consider several elements of this process: CAPEX, operations and maintenance (O&M), levelized replacement cost (LRC), and annual energy production (AEP). As wind turbines grow more sophisticated and increase in size, the impact of design on these elements is not always clear. For example, increasing AEP may increase CAPEX. If one step does not balance out the other, proposed improvements may actually have a negative overall impact. It may be useful to find easy relationships to scale costs with a limited set of input parameters. For each subsystem, sum of costs associated with material (mass) and labor necessary to build it are evaluated by simple models, which only need a limited set of input parameters. In most cases, cost and mass models are a direct function of rotor diameter, machine rating, tower height, or some combination of these factors. The results of each model must be in the same currency and updated with the current inflation rates for consistency. Where cost data is available from different years, it must be converted before the cost and scaling factors are developed. Cost data should be based on a mature design, with mature component production. For the evaluation of costs associated with installation and AEP, a preliminary characterization of the site of installation is needed (siting phase). One of the methods to evaluate the AEP for a specific wind turbine, installed in a specific site, is to numerically integrate the power curve and the frequency of each given wind speed. An availability factor may be introduced to take account for times of energy production interruptions.

–3–
Design methodology for floating platforms as subcomponent of FOWTs

The design of a new floating platform (and new mooring lines) to support an offshore wind turbine usually involves many "non-linear" steps back and forth in the process (see e.g. [68] and [69]). For example, after establishing the main dimensions and weights of the floating platform parts, based on hydrostatic stability, one can find unsatisfactory dynamics of the system in free-oscillation response and harsh sea conditions, and be obliged to return to the first steps of the design. Following an approach common to many engineering standards such as [70] or [71], the design is carried-out applying limit loading states, i.e. the conditions beyond which the structures will no longer satisfy the design requirements. These limits define the constraints to be applied when analysing a particular design feature. To categorize the type of limit state applied in FOWT design, the standard introduces:

- ultimate limit states (ULS), which correspond to the maximum loading that can be resisted by the system;
- fatigue limit states (FLS), which correspond to the repeated loading (load cycle) that can be resisted by the system over its lifetime;
- accidental limit states (ALS), which correspond to abnormal conditions of loading and damages to the structures;
- service limit states (SLS), which correspond to the loading state that can be faced by the system while ensuring normal service (e.g. conditions during production of energy).

A brief visualization of the process of designing a floating platform (and where the requirements are assessed) for a given FOWT installation (e.g. in a specific site for a wind farm) is given in the scheme of Fig. 3.1 in which it is important to highlight that each step forward means an increase in complexity of the model and an increment in computational time for simulations. To ease this process, the conceptualization should start with assumptions which at least provide the boundaries of exploration of selected variables to reduce the design space. In fact, as shown in Fig. 3.1, the choice of floating platform type based on hydrostatic stability properties can be considered a part of the conceptualization itself. Furthermore the characteristics of different types of floating platforms can be well or bad-suited for specific sites of installation and wind turbines dimensions.

3.1 Summary of the design procedure

The approach for the design procedure can be summarised in the following points.

1. Selection of how the platform is hydrostatically stabilized.
2. Definition the hydrostatic properties (the most relevant geometric and inertial properties are already defined in this step).
3. Preliminary analysis of hydrodynamic properties by potential methods or a combination of potential methods and Morison's force. At this point a rough estimation of natural periods of oscillation is possible.
4. Selection of representative sea-states and wind forces on the turbine.
5. Selection of mooring system properties.
6. Preliminary analysis of dynamic forces generated on the platform by wave motion (frequency/time domain analyses).
7. Preliminary analysis of structural loads, and rough estimation of materials and manufacturing feasibility.
8. Coupled aero-hydro-servo-elastic simulations.
9. Experiments for tuning/validation of numerical simulations.

As regards the computational time, it is important to highlight that, by accepting a relative level of uncertainty, it is possible to carry out all the calculations needed by steps 1. to 5. through spreadsheets.

3.2 Driving requirements

The requirements listed in the last section are described below.

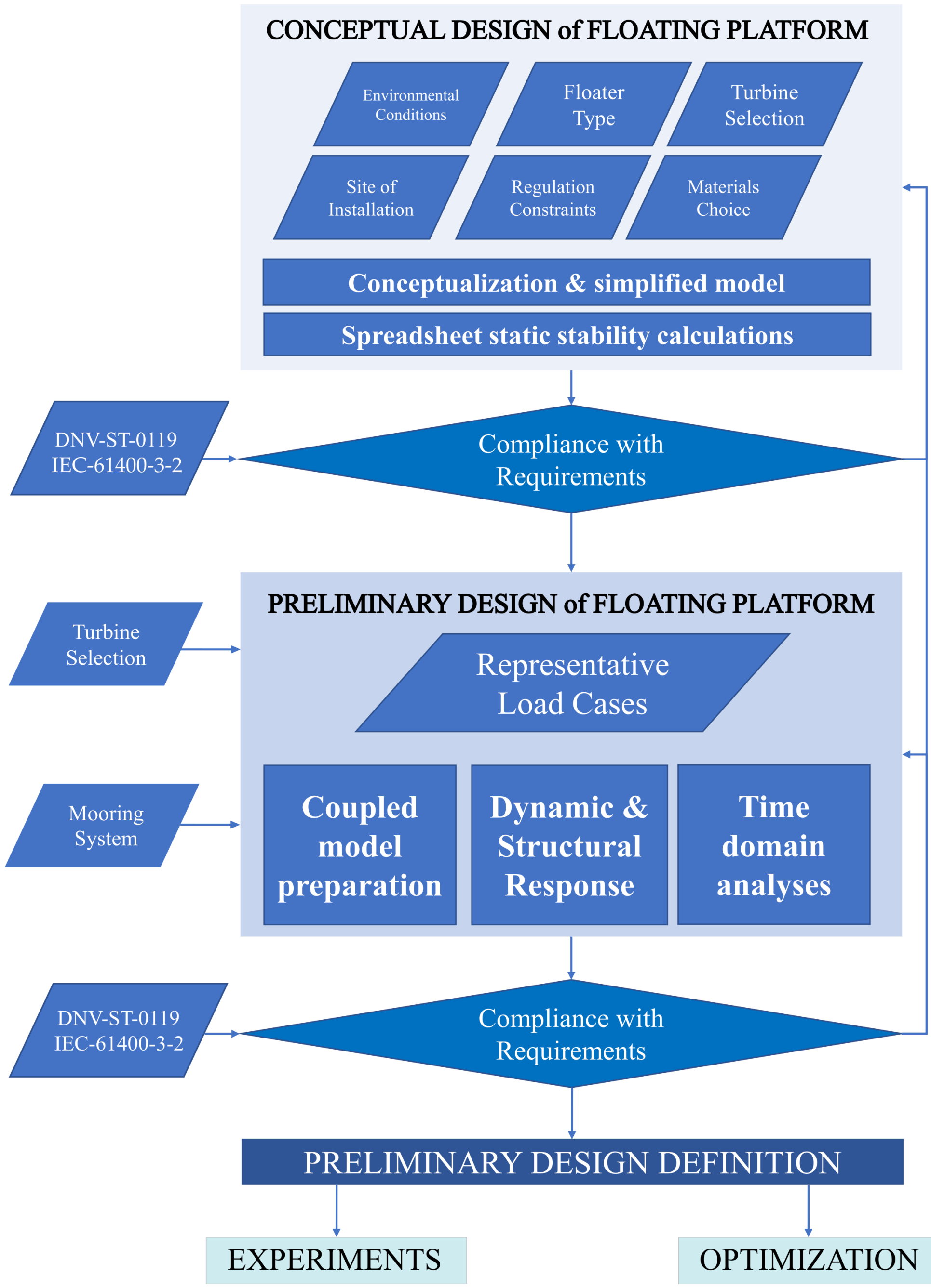

Figure 3.1: Possible sequential scheme for floating platform conceptual and preliminary design. The iterative nature of the process is shown with the feedback arrows departing from the "Compliance with Requirements" diamond boxes.

3.2.1 Buoyancy equilibrium

The buoyancy is essentially the force calculated following Archimede's principle. This requirement implies that the floating platform submerged volume (usually referred to as displacement) must be large enough so that the buoyancy force F_b calculated as,

$$F_\mathrm{b} = \rho_\mathrm{wat.} g \forall_\mathrm{d} \tag{3.1}$$

must support the total weight of the system (W_FOWT) at the desired draft level. In Eq. 3.1, $\rho_\mathrm{wat.}$ represents the water density, g the gravity acceleration at sea level, and $\forall_d$ the total displaced volume, that is the sum of all volumes below the sea level). The buoyancy equilibrium condition is expressed as:

$$F_\mathrm{b} \overset{!}{=} W_\mathrm{FOWT} \tag{3.2}$$

If a specific draft is assumed, the displaced volume is fixed, hence the only variable which is capable of being modified is the weight of the system, that can be changed by adding (or removing) ballast. The ballast weight, volume and density are design variables which should be carefully checked and adjusted (usually several times) during the design process. This constraint may be seen as a serviceable limit state (or SLS), given the fact that the loss of static equilibrium would hinder normal operations of the system.

3.2.2 Static stability

The structure must be hydrostatically stabilized through floating platform shape or mooring lines pretensioning. A parametric analysis can been performed to check the static heeling angle caused by the presence of the thrust (shown in 2.14) generated by the rotor. A simplified expression for the equilibrium condition has been obtained from the balance between righting and heeling moment. First, we assume that the thrust is directed in the X direction, which means that the inclination will be around the Y axis, as shown e.g. in Fig. 2.4. This hypothesis allows the calculation of the static stability around one axis per time. The righting moment expression was linearized around the resting condition of the floating platform, based on the water-plane section inertia and the meta-centric height, obtaining the stiffness around the pitch axis (indicated with the symbol K_{55}), according to the following formula:

$$C_{55} = z_\mathrm{CoG}\, W_\mathrm{FOWT} - z_\mathrm{CoB}\, W_\mathrm{FOWT} - C_{55,\mathrm{wat.area}} - C_{55,\mathrm{moor.sys.}} \tag{3.3}$$

where the term $C_{55,\mathrm{moor.sys.}}$ depends on the mooring line stiffness (and it is prevalent for TLPs), $C_{55,\mathrm{wat.area}}$ represents the contribution of the water-plane area (see also [72]), which can be calculated from the sectional inertia I_y as follows:

$$C_{55,\mathrm{wat.area}} = \rho_\mathrm{wat.} g I_y \tag{3.4}$$

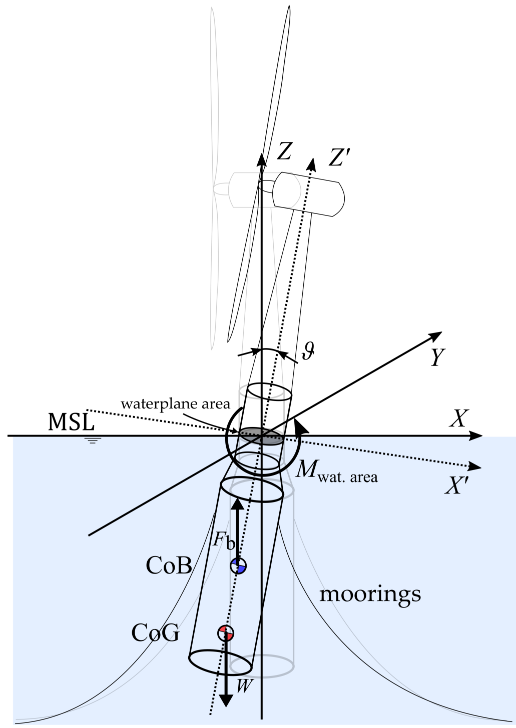

Figure 3.2: Scheme of a floating offshore wind turbine (spar-buoy type) with indications of the main characteristics relevant for hydrostatic stability.

The overturning moment is calculated considering the thrust of the turbine applied at the hub height z_{hub} and the arm defined by the vertical distance to the centre of buoyancy z_{CoB}. The static heeling angle θ_{static} can be calculated as,

$$\theta_{y,\text{static}} = \frac{T \cdot |z_{\text{hub}} - z_{\text{CoB}}|}{C_{55}} \tag{3.5}$$

To avoid excessive misalignment between the turbine axis and the wind-speed direction an upper boundary to the heeling angle is assumed to be a driving requirement for preliminary design. According to [73] and [74], a threshold of about $5\,\text{deg}$ must be imposed when the wind turbine is subjected to the rated thrust force. In [16], a static heeling angle of $3.5\,\text{deg}$ is obtained with the rated thrust force. This constraint may be seen as a SLS, providing that the structures may bear higher heeling angles, but with a significant loss of the serviceability of the system (the energy production would be altered). Besides this preliminary assessment, standards like [70] require a stability criterion based on the work done by the righting moment against heeling actions. This requirement states that the area below the righting moment curve up to the down-flooding angle overcomes the area below overturning moment by a given factor (i.e. righting moment area $> 1.3 \times$ heeling moment area). This criterion is shown in Fig. 3.3, where, applying the criterion, the blue area must be at least 1.3 times the red area. These two stability

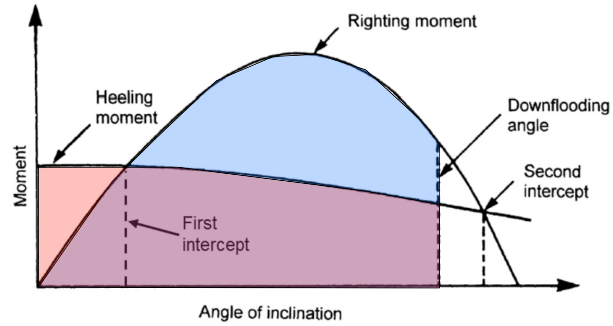

Figure 3.3: Illustration of heeling and righting moments for the determination of the stability criterion. The blue color indicates the area under the righting moment curve, while the red color indicates the area under the heeling moment. From [70] with modifications.

requirements, together with the hydrostatic equilibrium, are used to assess the dimensions and weights of an initial configuration of each new configuration.

3.2.3 Natural periods

After defining an initial configuration which satisfies the minimum stability requirements, an hydrodynamic solver is needed to evaluate the added mass and radiation damping matrices. These quantities are necessary to estimate the natural periods of oscillations, which should be outside of the range of possible sea-wave periods encountered by the system according to [12], to avoid resonances. Being highly dependent on the weights and inertia of the system and the hydrostatic stiffness matrix, another iteration on the dimensions may be necessary to try to avoid low natural periods. A general expression for the (undamped) natural period of the i^{th} DOF is:

$$T_{\text{nat.},i} = 2\pi\sqrt{\frac{m_{ii} + a_{ii}}{C_{ii}}} \tag{3.6}$$

Where the natural period is indicated by $T_{\text{nat.}}$, and m_{ii} and a_{ii} are the diagonal i^{th} elements of the mass and added mass matrices, respectively. For example, a simplified expression for the natural period in heave is

$$T_{\text{nat.},33} = 2\pi\sqrt{\frac{m_{\text{FOWT}} + a_{33}}{C_{33}}} \tag{3.7}$$

where the term $W_{33,add}$ represents the added mass in heave and C_{33} the hydrostatic stiffness in heave, which can be calculated from the water-plane area as,

$$C_{33} = \rho_{\text{wat.}} g A_{\text{wat.area}} \tag{3.8}$$

It is clear that changing the dimensions of the floating platform to tune the heave natural period means changing all the terms of Eq. 3.7. For example, trying to increase the mass of the floating platform to increase W_{FOWT} inevitably means increasing the draft, ballast and likely the water-plane area, counteracting the increment on the numerator of Eq. 3.7. This is also a solution that should be avoided to keep the price of manufacturing the structure (and the material consumed) as low as possible. A possible solution is to increase the added mass by adding an heave-plate, with a negligible impact on the overall weight of the structure. The simplified expressions for undamped natural periods shown in this section allow fast hand (or spreadsheet) calculations of the possible resonance ranges of the system, but are approximated through neglecting damping (which plays a fundamental role in heave, and modify the resonance peak), the coupling between DOFs, and linearizing the hydrostatic matrix coefficient (as it was done implicitly in Eq. 3.8). Moreover, the effect of mooring lines stiffness and mass is not accounted for in Eq. 3.7, yielding an uncertainty of the natural period $T_{\text{nat.},33}$. Fully-coupled simulations represent a valid solution to determine in a more accurate way the damped, coupled period of oscillations.

3.2.4 Design of mooring lines

According to [75], and similarly to floating platforms, mooring lines design procedure is related to the behaviour of the system in service and ultimate load states. It can be stated that the design of floating platforms and mooring lines must be carried-out simultaneously, because both influence the behaviour in service and survivability of a FOWT. Some of the design constraints which are more influenced by the characteristics of the mooring lines are:

- maximum surge offset;
- natural periods (especially surge/sway and yaw periods);
- footprint on the seabed (the distance between the yaw axis and the furthest anchor).

3.2.5 Site wave climate

The wave climate of a specific installation site is defined by the time history of successive sea states over a given reference period (on the order of years). A single sea state, in turn, consists of a sequence of waves, usually of varying amplitude and period, detected over a given observation interval (typical time intervals considered in standards for defining a sea state are between 1 and 3 hours). The statistical distribution of waves in a sea state is defined by a frequency spectrum, which represents the energy content associated with each frequency component present in the time history of the sea surface elevation. A characterization of the wave climate of a site can be performed through the joint distributions of two characteristic parameters of the spectrum:

- the significant height $H_{\mathrm{w,s}}$, defined in Sec. 2.2.4;
- the peak period (or frequency) of the spectrum.

Based on historical data of waves, which can be extracted from online databases such as [76], extreme sea states are estimated. This database has the advantage of a great extent of available data (available as time series over several years) and the great completeness, having simultaneous wind and wave climate data. The analysis can be conducted using the environmental contour approach, which allows determining the envelope of sea states with assigned return period. The combination of the wave climate and the wind climate of a site of installation go under the name of "metocean conditions".

3.2.6 Structural integrity

The integrity of the structures composing a FOWT must be checked in the selected operating conditions at the installation site, and for the entire lifetime of service of the system, ensuring safe operations of wind turbine. The constraints on structural integrity are usually adopted from engineering standards, such as the aforementioned DNV-ST-0119 [70]. It should be noted that following this standard means that *"the floating wind turbine structures and their station keeping system nominal annual probability of failure is* 10^{-4}. Given the immaturity of the field, some innovative system concepts are suggested to be designed with an additional robustness w.r.t. the standard. The same standard states that the design principle and design method for limit state design of floating wind turbine structures is the *design by partial safety factor method*. This methodology requires that a constraint expressed through a safety factor is applied for load effects in the structure for each applied load process. In the case of a FOWT, due to the aforementioned nonlinearities and the coupling between the loads and dynamics of the system, it is required that *"the design of the floating wind turbine structure are performed by direct simulation of the combined load effect of simultaneously applied load processes in the time domain"*. The safety of a specific structure may be expressed through a general design load effect S_D and a design resistance R_D in the form:

$$S_D <= R_D \tag{3.9}$$

where a generic design load effect $S_{D,i}$ is obtained from a characteristic load effect $S_{k,i}$ (obtained in a structural analysis, given a design load case) with the imposition of a load factor $\gamma_{S,i}$ (which represents a level of safety over the characteristic load), as follows:

$$S_{D,i} = \gamma_{S,i} S_{k,i} \tag{3.10}$$

The design load effect S_D represents the most unfavourable combined load effect resulting from a specific load case (the simultaneous occurrence of loads on the structure). The design resistance R_D represents the resistance of the material of the structure, and is affected by the structure geometry, configuration and possibly by the loading state itself. It is obtained from the design material strength σ_D by a capacity analysis, and it is also reduced by a material factor $\gamma_{R,i}$ as follows:

$$R_{D,i} = \gamma_{R,i} f(\sigma_D) \tag{3.11}$$

Following the approach of [70], in the remainder of the work, load combinations relevant for ULS design are those loads effect with a return period of at least 50 years. For load combinations relevant for FLS design, the characteristic load effect history is defined as the expected load effect history. Using coupled analyses, a structural analysis model must be developed to check the stresses derived from the actions of:

- loads arising from waves and currents (sea state condition);
- loads arising from wind;
- tidal effects;
- earthquakes, marine growth and ice loads;
- abnormal loads arising from occurrence of faults and transient conditions.

The load combinations to be applied to check structural integrity are usually defined in tables shown in the standards. In this work, we remark the focus on environmental loads which apply to ULS and SLS. Environmental loads for ULS are those load (or load effect) with a return period of 50 years, while for SLS environmental loads are usually determined by the mean climate conditions which can be found at the installation site. The analysis of the installation site climate, in terms of statistical distributions, allows the determination of the environmental loads. The definition of a design load case (DLCs) is the topic of the next section.

3.3 DLC based analysis

A DLC is defined by the following characteristics:

- design situation, to identify the DLC;
- DLC identification number;
- wind condition, characterized by wind speed and turbulence level;
- sea state condition, usually characterized by wave height, period and spectrum;
- wind and wave directions;

- currents, characterized by current speed and turbulence level;
- water level;
- other conditions such as transient conditions and faults;
- load factor defined by the same standard.

DLC for the analysis of offshore wind turbines are defined in [77] and those which are specific for floating platform and mooring analysis are defined in [70]. Among the others, the importance of fatigue assessment, following standardized DLCs, of the tower and platform members of a system composed by a wind turbine and a three-column semi-submersible, was shown in [78]. During the INNWIND project, the DTU 10MW RWT [79] mounted on the "Triple Spar" platform was checked against loads defined in the DLC1.6 with a wind speed of 13 m/s and a sea state defined by $H_{\text{w,s}}$ =10.9 m and $T_{\text{w,P}}$ =14.8 s, as shown in [80].

3.4 Optimization

Optimization procedures can be used to improve the overall performance (in terms of production, structural resistance and costs) of an offshore wind system, and consequently of floating offshore wind farms, through the controlled and combined modification of selected design variables via numerical algorithms. Optimization processes are used in a phase which usually comes after preliminary design, to refine an already validated concept.

3.4.1 Mathematical formulation

An optimization problem is formally represented by the following relationships:

$$\begin{array}{lc}
\text{change} & \boldsymbol{X}_{\text{var.}} = [x_{\text{var.},1}, \ldots, x_{\text{var.},i}, \ldots, x_{\text{var.},N}] \\
\text{to find} & \min\limits_{\boldsymbol{x}_{\text{var.}} \in \boldsymbol{X}_{\text{var.}}} \left(\boldsymbol{F}_{\text{obj.}}(\boldsymbol{X}_{\text{var.}})\right) = \min\limits_{\boldsymbol{x_{var.}} \in \boldsymbol{X}_{\text{var.}}} \left[f_{\text{obj.},1}, \ldots, f_{\text{obj.},r}, \ldots, f_{\text{obj.},M}\right] \\
\text{subject to} & \boldsymbol{H}_{\text{constr.}}(\boldsymbol{X}_{\text{var.}}) = [h_{\text{constr.},1}, \ldots, h_{\text{constr.},s}, \ldots, h_{\text{constr.},P}] \leq 0
\end{array}$$

Where the N-dimensional vector $\boldsymbol{X}_{\text{var.}}$ represent design variables, which undergo modification during the optimization process; $\boldsymbol{F_{obj.}}$ represents an M-dimensional vector of objective functions, which model a specific performance that should be optimized in the process and are formulated to be minimized; $\boldsymbol{H_{constr.}}$ represents a P-dimensional vector inequality constraints, which allow the designer to impose some conditions on the design. The objective functions and constraints vectors are multidimensional (possibly non-linear) functions of the system performance and the "$\min$" operator is generalized for multi-objective optimizations (i.e. the minimization leads to Pareto optimal solutions, as formally expressed in [81], and showcased in [82]).

3.4.2 Design space

First, following the design requirements, the objectives, the constraints, the design space should be defined. As demonstrated previously in this chapter, the intrinsic iterative process of design of FOWTs configurations leads to a huge choice of design variables, for example the floating platform dimensions, masses distribution and the mooring lines characteristics. It is usually assumed that the site of installation (and consequently the metocean conditions) and the turbine configuration are fixed, hence the design variables are typically:

- floating platform shape;
- floating platform geometry parameters;
- floating platform mass distribution;
- ballast characteristics;
- mooring lines type;
- mooring lines number;
- mooring lines cable type;
- mooring lines length and fairleads and anchors positions.

It is important to define the correct boundaries for the design variables, to prevent unfeasible solutions which would be discarded anyway. The general design variable belongs inside a predetermined range as follows:

$$x_{\text{var.},i} \in [x_{\text{var.},i,\text{lower}}; x_{\text{var.},i,\text{upper}}] \tag{3.12}$$

To define the lower $x_{\text{var.},i,\text{lower}}$ and upper $x_{\text{var.},i,\text{upper}}$ boundaries the designer imposes geometrical, structural and configuration consistencies.

3.4.3 Objective functions and constraints

The design requirements mentioned in this chapter form the basis on which objectives and constraints of optimization processes are chosen. A general expression for an objective function, evaluated with the design space at a certain step of the optimization, is:

$$f_{obj.,r}(\boldsymbol{X}_{\text{var.}}) = \left| \frac{\text{performance}_r(\boldsymbol{X}_{\text{var.}}) - \text{goal}_r}{\text{goal}_r} \right| \tag{3.13}$$

The word "performance" may represent a generic characteristic of the response of the system, such as the static heeling angle or the surge acceleration of the nacelle, or an estimation of the costs of the system. The normalization can be used for a weighted-averaged single-objective function which represents more than one goal, allowing to use a single-objective optimization algorithm, so that,

$$F_{\text{obj.}}(\boldsymbol{X}_{\text{var.}}) = \sum_{r=1}^{M} w_r \left| \frac{\text{performance}_r(\boldsymbol{X}_{\text{var.}}) - \text{goal}_r}{\text{goal}_r} \right| \tag{3.14}$$

where the weight w_r allows to choose the relative importance of each objective. A generic constraint, which is a function of the design variable at a certain step of the optimization as well, is imposed as,

$$h_{\text{constr.},s}(\boldsymbol{X}_{\text{var.}}) = \text{performance}_s(\boldsymbol{X}_{\text{var.}}) - \text{constraint}_s \leq 0 \tag{3.15}$$

The objectives and constraints of FOWT optimization have a twofold aim, taking into account at least two parameters, in which one is related to the LCoE and the other one is related to structural integrity. To avoid difficulties in the interpretation of results, a low number of objective functions (ideally one) is preferable although the high number of design requirements leads necessarily to constrained optimizations. It is then common to find multi-constrained, single- or multi-objective optimizations. Each verification of constraint relationships and evaluation of the objective function(s) needs the estimation of a certain FOWT performance. While the representation of costs is usually carried-out with simple expressions which relate the total cost with the bulk material and manufacturing expenses for the structures, the evaluation of a certain response of a FOWT during operations is not trivial. It is up to the designer to choose the fidelity level of the evaluation. The highest level of fidelity is represented by time-domain coupled simulations (*simulation-based approach*), which tend to be time-consuming but allow the representation of the non-linearities of the phenomena involved in FOWT dynamics (present in hydrostatics, hydrodynamics, aerodynamics, mooring lines behaviour, structural deformations and control). The choice of the complexity of simulations (i.e. the accuracy of the "modelling environment" see [82]) FOWTs performed in the optimization process depends on:

- the ability of the simulation tool to reproduce the performance needed for the estimation of constraints and objective function (or a particular phenomenon which affects the performance);
- the expected accuracy of the evaluated performances;
- the expected time consumption of the entire optimization process;
- the availability of sufficient computing capabilities.

Increasing the complexity level of the simulations leads to more qualitative, accurate but longer optimization processes, with the same computing capabilities. In

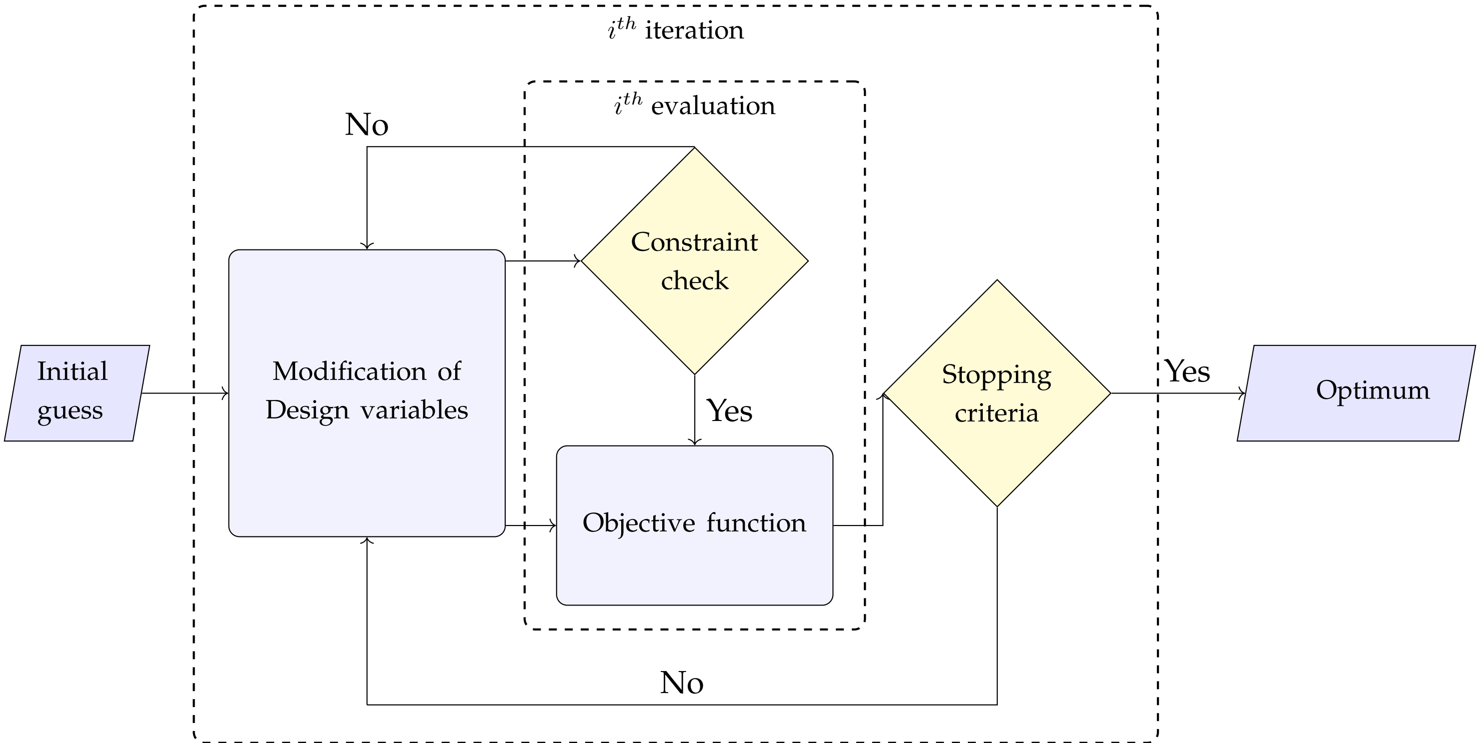

Figure 3.4: Simplified scheme for an optimization algorithm.

the field of floating offshore wind turbines, different approaches have been developed to evaluate the response of the system. The evaluation of the performance in a frequency-domain analysis, as shown in [83] [84] [85] [86] through linearization of hydrodynamic, aerodynamic and mooring loads allows to avoid time-marching simulations, but at the cost of neglecting non-linearities. Time-domain simulations which aim to resolve the complexity in the interaction between aerodynamics (e.g. wake effects in a wind farm), hydrodynamics, control logic and structural deformations may be required to enhance accuracy (as done in [87] [88] [89] [90]).

3.4.4 Algorithm

Finally, an algorithm is implemented to minimize the objective function(s) through the iterative modification of the design space variables. An algorithm performs the operations needed to find the optimal solution, and shown schematically in Fig. 3.4.

Different algorithms are needed for single- or multi-objective objective functions, constrained or unconstrained problems. The optimization algorithms which have been proved to be more efficient in finding optimal solutions in the field of FOWTs are the heuristic evolutionary algorithms (see [91] for an exhaustive description). These algorithms try to mimic the natural evolution by selection which applies the principle of the "survival of the fittest" in a certain population of

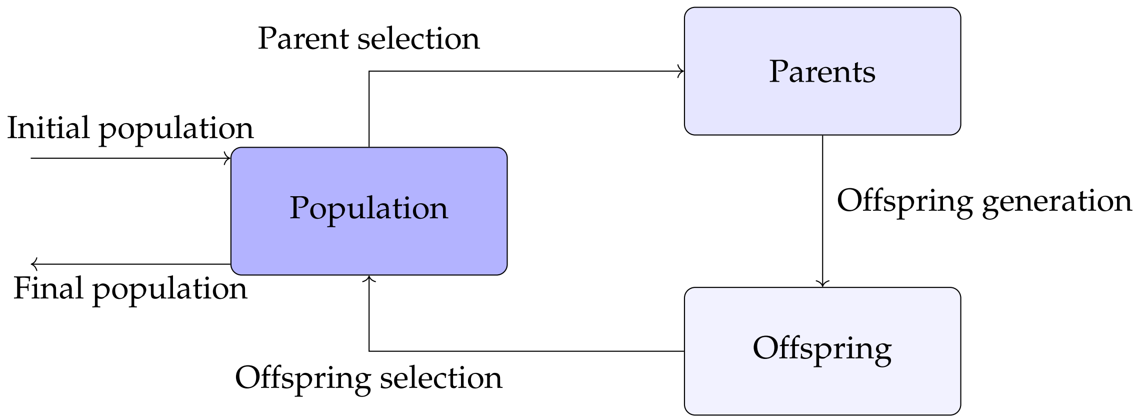

Figure 3.5: Simplified scheme for evolutionary algorithm.

individuals (in nature this is represented by a species of animals, plants and so on). Differently from gradient-based approaches which are based on the gradient estimation of the objective function to find global optimum, evolutionary algorithms do not require the continuity of the objective function, because no assumption is made on the mathematical nature of the optimum. Hence, they are particularly well-suited for the evaluation of non-linear discontinuous objective functions. A general scheme for evolutionary algorithms is shown in Fig. 3.5.

In this type of algorithm, the "population" represents a group of vectors of the design variables (also called "individuals"). Each individual, which is potentially a candidate solution to the optimization problem, is then characterized by a "fitness function" which represents its performance in terms of the objective function. The progress towards the optimal solution is guaranteed by a mechanism that allows to discard individuals based on their fitness functions, from one iteration to the next (in evolutionary algorithms an iterations is referred to as "generation"). The generation of new individuals, for each iteration step, is arguably the most important feature of the evolutionary algorithms, allowing for a wide range of candidate solutions. The process to generate new individuals, which are referred to as "offspring", involves the recombination and mutation of the design variables that characterize the "parent" individuals, which have already been selected from the population because they performed better in terms of fitness function ("parent" selection mechanism). Furthermore, the mutation routines introduce a stochastic in this process. Offspring undergo the last selection mechanism, which is also called "survivor selection", because the offspring of an iteration become the survived population of the next. The specifics of the parent selection, recombination, mutation and selection mechanisms vary depending on the algorithm. A stopping criteria is also needed, usually the maximum number of iterations, or a condition on the characteristics of the population. In the remainder of the work, the differential evolution algorithm implemented in the Scipy Python™ module [92] based on the theoretical work presented in [93] is used. In particular, the "best1bin" strategy is used to create candidate solutions. In this strategy, the offspring is generated by 3 parents, in which one of them is the best performing individual of the last generation. A mutated individual at the i_{th} generation, represented by a vector of the design space, $\boldsymbol{x_i}'$ is created as follows:

$$\boldsymbol{x_i}' = \boldsymbol{x_{i-1}}_{,\text{best}} + k_{\text{mutation}} \left(\boldsymbol{x_{i-1}}_{,\text{rand.}_1} - \boldsymbol{x_{i-1}}_{,\text{rand.}_2} \right) \tag{3.16}$$

Where $\boldsymbol{x_{i-1}}_{,\text{best}}$ is the best individual of the last generation, $\boldsymbol{x_{i-1}}_{,\text{rand.}_1}$ and $\boldsymbol{x_{i-1}}_{,\text{rand.}_2}$ are two random individuals of the last generation and k_{mutation} is a scalar mutation coefficient defined by the user. The process continues by creating a trial vector $\boldsymbol{x_i}_{,\text{trial}}$. Using a binomial distribution (the "bin" in "best1bin"), a random integer in the interval [0, 1] is created for each design variable. The design variable is selected from $\boldsymbol{x_i}'$ if the value from the binomial is smaller than the recombination constant (which is defined previously by the user); else, the original candidate $\boldsymbol{x_{i-1}}_{,\text{best}}$ design variable is used. The strategy also imposes that at least one design variable is always loaded from the mutated individual. Then, the trial candidate's fitness is evaluated through the objective function. If the trial candidate $\boldsymbol{x_i}_{,\text{trial}}$ performs better than its corresponding individual of last generation $\boldsymbol{x_{i-1}}$ it will replace it. If it is also superior to the top candidate overall, it also takes its place. This strategy allows for different levels of exploration of the design space and convergence speed, through the setting of the recombination and mutation constants.

3.5 Experimental testing

Experiments in a controlled and scaled environment have been used to investigate the dynamic response of FOWT systems, when the construction of prototypes is not economically feasible (e.g. in the preliminary phases of design). Experiments are aimed to: estimate the dynamic characteristics of a full-scale system; validate the results of numerical simulations; tune the variables in the model which present a high level of uncertainty in numerical analyses (e.g. in drag identification). Ideally, experiments should be able to recreate the complex interactions of the aero-servo-hydro-elastic response of FOWT, and the environmental loads that produces it, in a scaled facility. In practice, the following facilities are needed:

- a wave basin to generate the wave field;
- a rack of fans to generate the wind field.

The combination of a rack of fans in a wave basin would allow the generation of the combined action of waves and wind. The scaled model of a FOWT comprises:

- a scaled model of the floating platform;
- a scaled mooring system;

- a scaled model of the wind turbine.

The main scaling relationships considered in the definition of a scaled model for a FOWT are given below.

3.5.1 Froude scaling

Froude's number is defined by the following relationship:

$$Fr = \frac{V_{\text{ref}}}{\sqrt{gL_{\text{ref}}}} \tag{3.17}$$

where V_{ref} represents a characteristic velocity of the phenomenon under consideration, L_{ref} a characteristic length, and g the acceleration of gravity. This quantity represents the ratio between the orders of magnitude of the inertial forces and the gravity forces. The Froude number becomes particularly important in the study of phenomena in which gravity forces have significant effects, as in the case of gravitational surface sea waves. If the Froude number is kept constant between the full scale system (the FOWT in its real environment), and the scaled model in the experimental test, "similarity according to Froude" is attained. Similarity according to Froude is often considered of primary interest in the experimental study of systems subject to sea wave actions, because the relative importance these actions and the inertial forces (e.g. the forces which generate from the acceleration of the system masses) remain constant between the full and the model scale. The behavior of a system subjected primarily to inertia and mass actions can be studied by means of a scaled model, considering the scaling relationships given below. Structures that are geometrically similar have the same shape but have different dimensions. In scaled experiments, the full scale system and the model must have the same shape, hence the geometrical similarity is enforced. The greek letter λ is used to define the ratio of geometric dimensions, hence, if we also apply the Froude similarity, the main physical quantities of interest scale according to the following relationships:

- Linear dimensions (geometry, wave heights): λ
- Velocity: $1/\lambda^{1/2}$
- Period: $\lambda^{1/2}$
- Forces: λ^3
- Mass: λ^3
- Power: $\lambda^{3.5}$

The preceding relationships can be used to estimate the characteristics of the scaled model from the characteristics of the full-scale model, or, conversely, to convert the results of experimental tests on the scaled model to the full-scale system. A comprehensive analysis of the Froude similarity and a full table for all the scaling laws is found in [12].

3.5.2 Reynolds scaling

As already seen in this work, the Reynolds number is defined as follows:

$$Re_{\text{ref.}} = V_{\text{ref.}} L_{\text{ref.}} / \nu_{\text{fluid}} \tag{3.18}$$

The Reynolds scaling implies that the ratio between the viscous and the inertial forces in a fluid is kept constant between the model and the full scales. This ratio is of primary importance in the experiments involving the calculation of wind loads on turbines, because if affects the aerodynamic performance of blades (see [94]). Reynolds number is also important for the viscous damping affecting marine structures. In FOWTs experiments, two Reynolds number for two different phenomena can be defined. The first concerns the wind interaction with the wind turbine (Re_{air}), while the second concerns the water interaction with the floating platform and mooring lines ($Re_{wat.}$). Several practical issues arise when trying to match the full scale Reynolds numbers in FOWTs experiments:

1. If the chosen dimensions of the model are small, such as in the case of small facilities, the Reynolds number concerning aerodynamic phenomena scaling would impose high velocities of the wind speed (the velocity should scale according to $1/\lambda$). These velocities are usually impractical for wind generation facilities. An academic attempt to match Reynolds scaling has been shown in wind tunnel experiments of mini wind turbines [95].

2. The performance of a wind turbine is also affected by the TSR, which is the ratio between flow and peripheral velocities. To keep the TSR constant between full scale and experiments, the peripheral velocity (and in turn the rotational velocity of the rotor) should be increased with the flow velocity. For very high velocities, the TSR scaling would imply very high rotational speeds. The feasibility of high rotational speeds and the related increased centrifugal forces remain challenging, hence the Reynolds number scaling is usually disregarded in wind turbines experiments (this is valid for experiments onshore turbines as well).

3. The Reynolds number in water ($Re_{wat.}$) scales as $\lambda^{3/2}$ when the Froude scaling is applied. Hence the two non-dimensional numbers can not be scaled simultaneously. This issue leads to the mismatching of viscous damping forces between full and model scales, in the hydrodynamic response. Attention should be paid to interpret viscous damping in FOWTs experiments.

The different methodologies to model the thrust force, which plays a fundamental role in the FOWTs dynamics, are listed below.

- A disk which generates drag when subjected to wind. The drag disk is able to model static thrust, but it is not well-suited to model changes in the turbine behaviour [96]. This solution may appear easy to implement from a model design point of view, but it requires the wind generation system, which is not always available in experimental facilities.

- A geometrically scaled turbine has been used in the experiments shown in [97], but the scaled aerodynamic actions are reproduced through adjustments of the wind speed (generated by a rack of fans) and the rotational speed of the rotor. Hence the masses and the length ratios are correctly achieved, while the scaled wind loads are obtained through a different control strategy of the turbine.

- A redesigned wind turbine for low Reynolds numbers ("performance-matched"), such as in [98], [99] and [100], to keep the same $C_T -$ TSR curves. Geometry is not well-scaled and the same distribution of masses is hard to achieve.

- In order to avoid the necessity to model (and/or redesign) the wind turbine and the usage of a wind generation system, several attempts to recreate wind turbine loads through the usage of a fan have been carried-out in experimental campaigns (see [101] and [102]). The fan is usually controlled by means of a

- Another solution to model the wind loads is represented by a setup of wires attached to the top of the tower, and controlled by winches. This solution has been applied in [103], where the turbine is also geometrically scaled. This hybrid approach presents the advantages of fully representing loads and geometry at the model scale, but requires complex instrumentation of the system and a specific control algorithm.

–4–
Development of FOWT design routines and optimization framework

This chapter is dedicated to the development of routines to aid the design and optimization of FOWTs, and in particular, the floating platform and mooring lines which support the wind turbine. In the remainder of the chapter we assume that:

- a rough estimation of the masses of the wind turbine which is going to be installed is known.
- some of the characteristics of the site of installation are known (e.g. depth, tides and metocean conditions). This hypothesis is restrictive in the sense that even in the preliminary design phases of a FOWT some information on the site of installation are needed.

4.1 Buoyancy equilibrium - weight and inertia calculations

As shown in Eq. 3.2, the buoyancy must be equal to the weight of the entire system, for a given draft. Assuming to fix the draft, the calculation of weight, inertia and volumes in the first phases of preliminary design is performed by means of simple geometrical considerations. The structures of floating platform are constituted mainly by hollow cylinders, due to the following reasons:

- simplicity of manufacturing;
- satisfactory structural properties.

Thus a cylinder with constant thickness $t_{\text{cyl.}}$, as shown in Fig. 4.1, will be analyzed in this section.

The relationships that are used to calculate the properties of a hollow cylinder with its symmetry axis corresponding to the Z axis are listed in the following Table

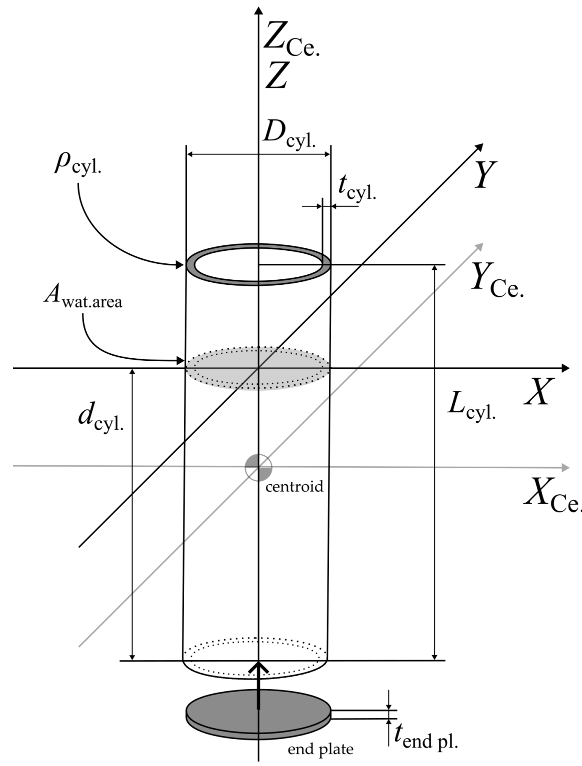

Figure 4.1: Illustration of a hollow cylinder.

4.1. Two coordinate systems are defined, both have the Z axis along the rotation axis of the cylinder but one has its center at the intersection between the symmetry axis and the sea-level $\{X, Y, Z\}$, while the other has its center in the geometrical centroid of the cylinder $\{X_{\text{Ce.}}, Y_{\text{Ce.}}, Z_{\text{Ce.}}\}$.

When the cylinders are inclined w.r.t. the MSL, it is useful to introduce the formula to calculate the inertia moments around a reference system centered in its centroid. Two coordinate systems are defined, one has its center at one of the two end of the cylinder $\{X', Y', Z'\}$, while the other has its center in the geometrical centroid of the cylinder $\{X_{\text{Ce.}}, Y_{\text{Ce.}}, Z_{\text{Ce.}}\}$. The symmetry axis of the cylinder is inclined w.r.t. both the $Z_{\text{Ce.}}$ and the Z' axes.

To transform a moment of inertia $I_{\text{ax.}}$ to the moment of inertia referring to an axis passing through the center of mass and parallel to the former $I_{\text{ax.}_{\text{CoG}}}$, the well-known Huygens-Steiner theorem is applied, which can be expressed in the following form:

$$I_{\text{ax.}_{\text{CoG}}} = I_{\text{ax.}} - mr^2 \tag{4.1}$$

where r is the distance between the two axes. This formula can be used to calculate the moment of inertia of a solid composed of more than one cylinder, as in the case of floating platforms.

Table 4.1: Cylinder properties.

Property	**Symbol**	**Formula**
Volume		
Cylinder volume	$\forall_{\text{cyl.}}$	$\pi \frac{D_{\text{cyl.}}^2}{4} L_{\text{cyl.}}$
Cylinder displaced volume	$\forall_{\text{d, cyl.}}$	$\pi \frac{D_{\text{cyl.}}^2}{4} d_{\text{cyl.}}$
Filled volume	$\forall_{\text{fill., cyl.}}$	$\pi \left[\frac{D_{\text{cyl.}}^2}{4} - \left(\frac{D_{\text{cyl.}}}{2} - t_{\text{cyl.}} \right)^2 \right] L_{\text{cyl.}}$
Mass		
Lateral volume mass	$m_{\text{lat., cyl.}}$	$\rho_{cyl.} \ \forall_{\text{fill., cyl.}}$
End plate mass	$m_{\text{end pl.}}$	$\rho_{\text{cyl.}} \pi \frac{D_{\text{cyl.}}^2}{4} \ t_{\text{end pl.}}$
Total mass	$m_{\text{cyl.}}$	$m_{\text{lat., cyl.}} + \sum_{k=1}^{N_{\text{end pl.}}} m_{\text{end pl.}_k}$
Inertia		
Moment ar. symmetry axis	$I_{z_{\text{Ce.}}} = I_z$	$\frac{1}{2} \ m_{\text{lat., cyl.}} \left[\frac{D_{\text{cyl.}}^2}{4} - \left(\frac{D_{\text{cyl.}}}{2} - t_{\text{cyl.}} \right)^2 \right]$
Moment ar. transversal centroid axis	$I_{x_{\text{Ce.}}} = I_{y_{\text{Ce.}}}$	$\frac{1}{12} \ m_{\text{lat., cyl.}} \left\{ 3 \left[\frac{D_{\text{cyl.}}^2}{4} - \left(\frac{D_{\text{cyl.}}}{2} - t_{\text{cyl.}} \right)^2 \right] + L_{\text{cyl.}}^2 \right\}$

Table 4.2: Inclined cylinder properties.

Property	**Symbol**	**Formula**
Inertia		
Moment ar. Z'	$I_{z'}$	$\approx \frac{1}{3} \ m_{\text{lat., cyl.}} \ L_{\text{cyl.}}^2 \sin^2 \gamma_{\text{cyl.}}$
Moment ar. centroid axis $Z_{\text{Ce.}}$	$I_{z_{\text{Ce.}}}$	$I_{z'} - m_{\text{lat., cyl.}} \ \left(\frac{1}{2} L_{\text{cyl.}} \ \sin \gamma_{\text{cyl.}} \right)^2$

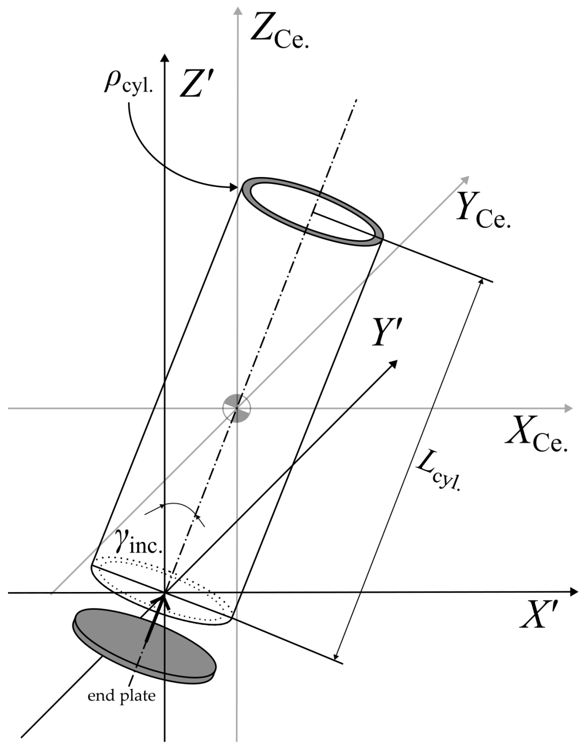

Figure 4.2: Illustration of a hollow inclined cylinder.

4.2 Stability analysis

A stability analysis is needed to validate the behaviour of the system when subjected to overturning moments. First, when analysing floating platforms which are not TLPs, a conservative assumption is made by excluding the mooring lines stiffness from the analysis. By neglecting the mooring lines restoring moment the stability analysis will underpredict the value of the total restoring coefficient of the system. To perform an hydrostatic stability analysis of a floating platform two approaches can be considered,

- a simple analysis with the application of the equations 3.3, 3.3 and 3.5. The quantities needed to perform this analysis can be calculated from geometrical and mass distribution considerations. This approach assumes that the waterplane area and the equilibrium position are constant (the draft does not change), which can be considered a valid approximation only for small heeling angles;

- a more sophisticated analysis which relies on the re-calculation of the static equilibrium and waterplane area when the overturning moment is applied. The calculation of the equilibrium is inherently iterative because the heeling angle must be recalculated when the displaced volume changes and viceversa.

This approach can be used to estimate the hydrostatic properties of a floating body for large heeling angles.

As regards the approximated analysis, the waterplane area and the sectional moment of inertia of the hollow vertical and inclined cylinders can be calculated from the formula presented in Table:

Table 4.3: Sectional properties of hollow cylinders.

Property	Symbol	Formula vert. cyl.	Formula inc. cyl.
Area			
Waterplane area	$A_{\text{wat.area}}$	$\pi \frac{D^2_{\text{cyl.}}}{4}$	$\pi \frac{D^2_{\text{cyl.}}}{4 \cos \gamma_{\text{inc.}}}$
Inertia			
Waterplane inertia	$I_{\text{wat.area}}$	depends on axis (see [104])	depends on axis (see [104])

4.3 Iterative design procedure for catenary mooring systems

The design procedure for catenary moorings shown in this work is aimed to the calculation of the geometrical, structural and configuration properties of a catenary mooring system composed by link chains, which is able to withstand the tension generated by an assigned force $F_{\text{H,max}}$ directed along the surge axis of the floating platform, and transmitted to the moorings through the fairleads, with the most stressed line completely suspended. Gravity anchors are assumed, which are a common choice when anchors are designed so they are not subjected to vertical tensions in any load condition. A schematic representation of a mooring system composed by 4 lines which is connected to a body (represented by a ring with four fairleads) subjected to a design force $F_{\text{H,max}}$ is given in Fig. 4.3.

The procedure verifies that the admissible tension of the most stressed mooring line (e.g. line 1 in Fig. 4.3) is above the maximum tension generated by the external force T_{max}, and calculates a safety margin SM, defined as,

$$\text{SM} = \frac{0.95\ \text{MBL}}{T_{\text{max}}} - 1 \tag{4.2}$$

where the MBL has been reduced by a material factor according to the rules of DNV-ST-0119 [70]. At the end of the procedure, a simplified expression can be introduced to roughly estimate the expected price of the mooring lines. The cost

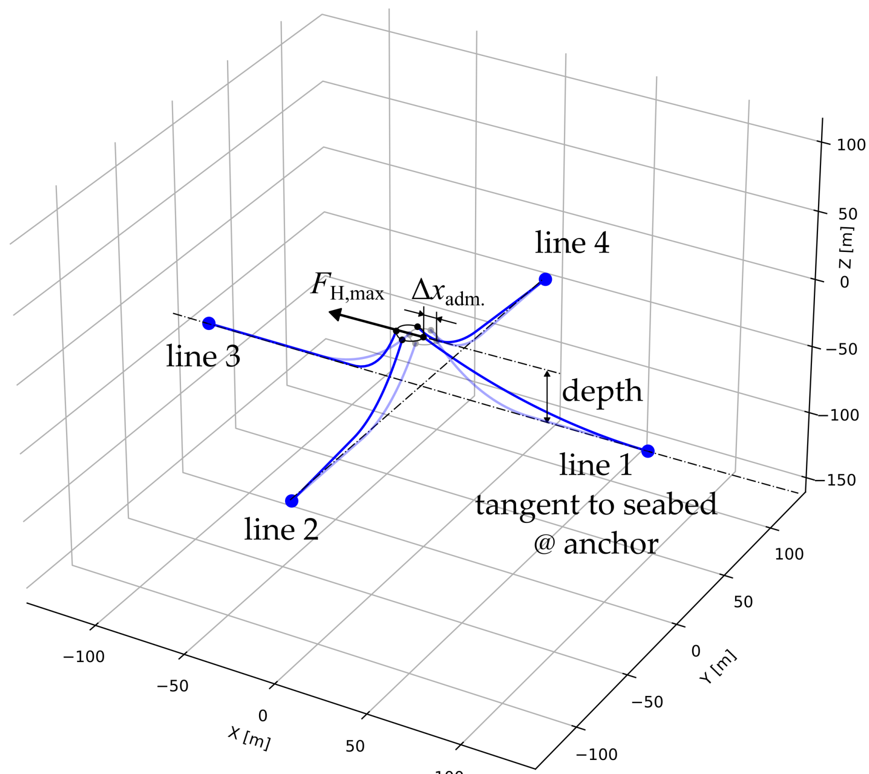

Figure 4.3: Illustration of a spread mooring system (blue lines) composed by 4 lines which is connected to a body (represented by a ring with four fairleads) subjected to a design force $F_{\mathrm{H,max}}$. The configuration without external force is plotted with semi-transparent lines.

of mooring lines is proportional to the material employed to build the chains (i.e. the total mass) and to the quality of the material (a coefficient c_{lines} that can be expressed in [€/kg]). The total cost C_{lines} can be calculated based on the following simplified relationship, which can also be found in [75].

$$C_{\text{lines}} = c_{\text{lines}} w_{\text{C,air}} \sum_{i=1}^{N_{\text{lines}}} l_{\text{C},i} \tag{4.3}$$

where c_{lines} is the cost per unit weight of the chain, $w_{\text{C,air}}$ its weight per unit length and $l_{\text{C},i}$ the length of the i^{th} chain in the mooring system.

4.3.1 Assumptions

The following characteristics are needed as input to the design procedure.

- Environmental conditions (depth h, water density $\rho_{\text{wat.}}$, gravity acceleration g).
- Load conditions (design force $F_{\text{H,max}}$ along the surge direction, safety factor SF, allowable surge platform displacement $\Delta x_{\text{adm.}}$).
- Mooring system configuration parameters.
  - Mooring lines type. The type of line defines the relationships between the geometry of the mooring line and the weight, stiffness and breaking load.
  - Number of mooring lines N_{lines}.
  - Orientation of the lines.
  - Location of fairleads: height and horizontal distance from the turbine axis (or other reference point on the platform).

If a link chain is used for the mooring lines, the geometrical characteristics and material properties (mass of the mooring line per unit length w_{C}, mooring line stiffness E_{C}, breaking load MBL) can be expressed as a function of the diameter of the line, as indicated in [105]. The diameter of the chain is indicated with $D_{\text{ch.}}$, and it is shown in Fig. 4.4. The following characteristics are based on the grade of the link chain, which is a measure of the quality of the chain, and represents the maximum stress that the chain can bear per millimeter squared. Stud chain links are also available and have increased values of resistance (see Fig. 4.4).

For a Grade R3 link chain, the Minimum Breaking Load (in [N]) is calculated as follows,

$$\text{MBL}(D_{\text{ch.}}) = 0.0223\ D_{\text{ch.}}^2\ (44 - 0.08 D_{\text{ch.}}) \tag{4.4}$$

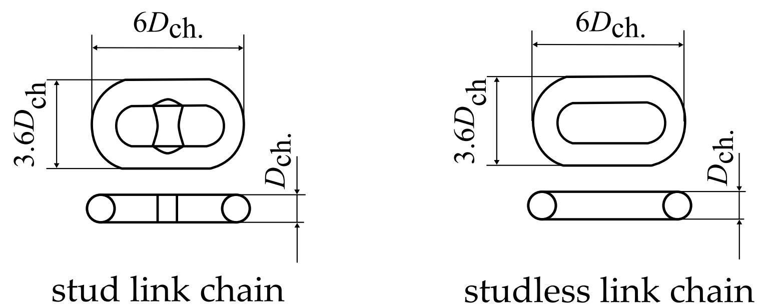

Figure 4.4: Illustration of two types of chain link (stud and studless).

The weight in air (in [kg/m]) of the cable is

$$w_{\text{C,air}}(D_{\text{ch.}}) = 0.0219\ D_{\text{ch.}}^2 \tag{4.5}$$

hence, the weight in water (in [N/m]) of the cable is

$$w_{\text{C,wat.}}(D_{\text{ch.}}) = g w_{\text{C,air}} - \rho_{\text{wat.}}\ g \frac{\pi D_{\text{ch.}}^2}{4} \tag{4.6}$$

The young modulus (in [N/mm^2]) is

$$E_{\text{C}}(D_{\text{ch.}}) = [1000(120.28 - 0.53 D_{\text{ch.}})] \tag{4.7}$$

then the stiffness (in N),

$$E_{\text{C}} A_{\text{C}} = [1000(120.28 - 0.53 D_{\text{ch.}})] \cdot \frac{\pi D_{\text{ch.}}^2}{4} \tag{4.8}$$

The procedure goal is to define the following characteristics of a spread mooring system:

- Link chain diameter $D_{\text{ch.}}$.
- Length of cables l_{C} (same value for all mooring lines).
- Anchor scope $R_{\text{A},0}$ (same value for all mooring lines).

4.3.2 Algorithm

A summary of the design procedure, which comprises several iterative steps, is given below.

1. Starting with an initial guess for the diameter of the chains $D_{\text{ch.}}$, a first routine calculates the characteristics of a single-line mooring system, which with an assigned force $F_{\text{H,max}}$ (parallel to the mooring line, as line 1 in Fig. 4.3) on the floating body, has the length of the cable equal to the minimum suspended

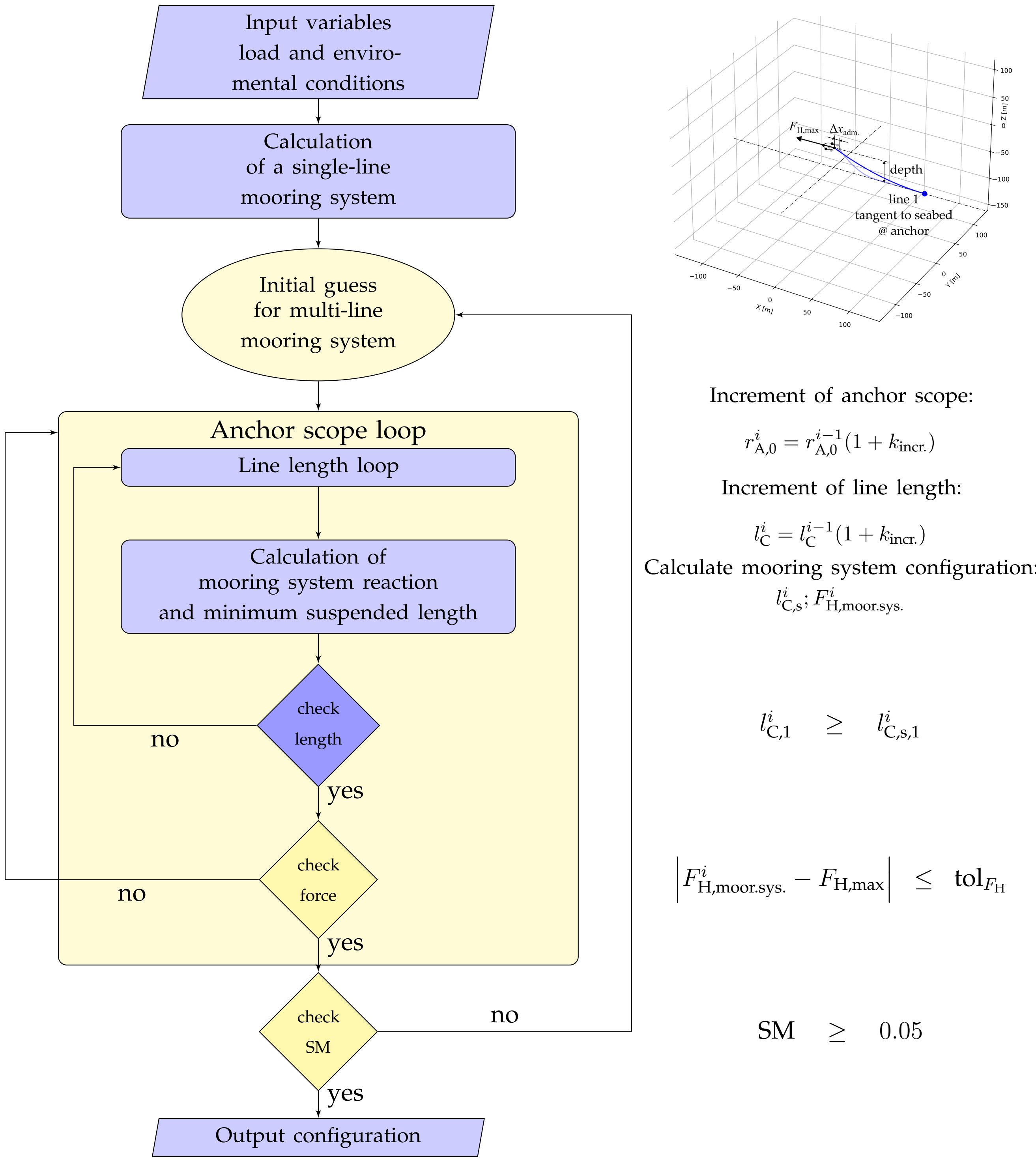

Figure 4.5: Scheme for mooring lines design algorithm.

length to have a tangent line at the anchor (i.e. $l_{\mathrm{C}} = l_{\mathrm{C,s}}$). This first calculation is performed by writing the horizontal tension of the line as a function of the suspended length $T_{\mathrm{C,H,el.}}\,(l_{\mathrm{C,s.}})$ by using the following relationship between vertical tension in the cable and suspended length:

$$T_{\mathrm{C,V,el.}} = l_{\mathrm{C,s.}} w_{\mathrm{C,wat.}} \tag{4.9}$$

and Eq. 2.53, Eq. 2.53 and Eq. 2.55. The suspended length $l_{\mathrm{C,s.}}$ that satisfies the imposed conditions is found by solving the equation

$$F_{\mathrm{H,max}} - T_{\mathrm{C,H,el.}}(l_{\mathrm{C,s.}}) = 0 \tag{4.10}$$

in the interval $l_{\mathrm{C,s.}} \in [h; l_{\mathrm{C,s.,adm.}}]$, where $l_{\mathrm{C,s.,adm.}}$ can be chosen based on the maximum admissible footprint. From the suspended length, the tensions in the cable and a prescribed $\Delta x_{adm.}$, the anchor scope $r_{\mathrm{A,0}}$ can be calculated.

2. A multi-line mooring system is introduced at this point. An initial guess for the chain diameter, length of the cable and anchor scope of the remaining lines (lines 2-3-4 in Fig. 4.3) is taken from point 1.

3. The floating body displacement at the design point is prescribed and fixed to the value $\Delta x_{\mathrm{adm.}}$. The configuration of the most elongated line is fixed by the condition imposed at point 1. Through Eq. 2.59, the displacement of all the mooring lines is calculated, and by using the current position of the lines, the tensions are determined.

4. The calculation of the total horizontal force $F_{\mathrm{H,moor.sys.}}$ exerted by the mooring lines in this condition, as defined in Eq. 2.60, shows that this value is not equal to $F_{\mathrm{H,max}}$ because of the combined action of the other mooring lines (the mooring lines reaction is not balancing the external force). In particular, if there is a line in the opposite direction w.r.t. the most elongated line, the total reaction $F_{\mathrm{H,moor.sys.}}$, calculated with the initial guess multi-line system, is smaller than $F_{\mathrm{H,max}}$.

5. An external search loop increases the anchor scope r_{A} by a factor $(1 + k_{\mathrm{incr.}})$, to increase the tension in the lines (and consequently the total reaction), while a nested one changes the line length $l_{\mathrm{C,s.}}$ to guarantee that the final configuration respects the following conditions:

   - the displacement of the floating body at the design point is $\Delta x_{adm.}$.
   - the most stressed line is totally suspended and tangent to the seabed at anchor (following the illustration of Fig. 4.3, we write the condition for the first line, $l_{\mathrm{C,1}} \geq l_{\mathrm{C,s,1}}$);

- the total horizontal force exerted by the mooring system is equal to the external assigned force $F_{\mathrm{H,max}}$, or

$$F_{\mathrm{H,moor.sys.}} = F_{\mathrm{H,max}} \tag{4.11}$$

  This condition is verified within a tolerance referred to as $\mathrm{tol}_{F_{\mathrm{H}}}$.

A solution for the final configuration is found when all these conditions are satisfied simultaneously. The two nested loops are shown in Fig. 4.5. The increment factor $k_{\mathrm{incr.}}$ and the tolerance error on the total reaction of the system $\mathrm{tol}_{F_{\mathrm{H}}}$ influence the speed and the chances of convergence of the process. In particular, if the increment factor is small, the chances of convergence are higher, but the computational time increases. The value of $k_{\mathrm{incr.}}$ does not influences the quality of the solution found. If the safety margin SM on the most stressed line is less than 0.05 (recall from Eq. 4.2 that the safety margin value is 0 when the tension in the line is exactly equal to 0.95 MBL), the diameter of the chains is increased in an external loop, and a new initial guess is provided to the two inner loops.

The result of this procedure is a multi-line mooring system which, complying with the simplified requirements listed above, has the shortest anchor scope and shortest cable length.

4.4 Optimization framework for platform geometry and mooring lines

This section describes the development of an optimization framework for the platform and mooring lines configuration of a FOWT, taking into account the requirements of a novel wake recovery control strategy developed in the FLOATECH project (the considered control strategy applied to FOWTs is described in [106]). The optimization procedure aims at accelerating the wake recovery characteristics by promoting wake mixing through an increased platform motion. Furthermore, thanks to the generality of the pre-processor of the FOWT model, a slight modification of the routines of the framework would allow the optimization of different configuration, for different objectives (e.g. the minimization of platform motion). Subsequently, a description of the proposed overall design-optimization process is given and the development of a pre-processor to manage modifications of the floating platform geometry and mooring lines is illustrated. This part of the document describes a possible approach to the problem of designing or optimizing a platform-mooring-turbine system with specified constraints and goals, which can be employed for the implementation of the chosen wake mixing control strategy. Acting on the configuration of the mooring lines can be useful in achieving the desired frequency and dynamic characteristics of FOWTs. Thus, together with the geometrical characteristics of the platform, which are of primary interest, the mooring parameters must be taken into account in the design process. In the optimization process, an initial reference configuration should be assumed. Starting from an established design that satisfies structural and operational requirements, the parameter space is explored in search of a modified configuration. The implementation of the procedure will account for a set of optimization targets and constraints. In particular, to avoid unfeasible excessively expensive solutions, a preliminary cost variation analysis should be integrated in the process. In the presented approach a simplified cost model is assumed to estimate the cost variation based on the difference between the modified system and the reference one.

4.4.1 Optimization process scheme

The design process schematically summarized in Fig. 4.6 relies on a simulation-based approach which are common in literature for design and optimization of floating platforms for offshore wind turbines. A time-domain approach employing

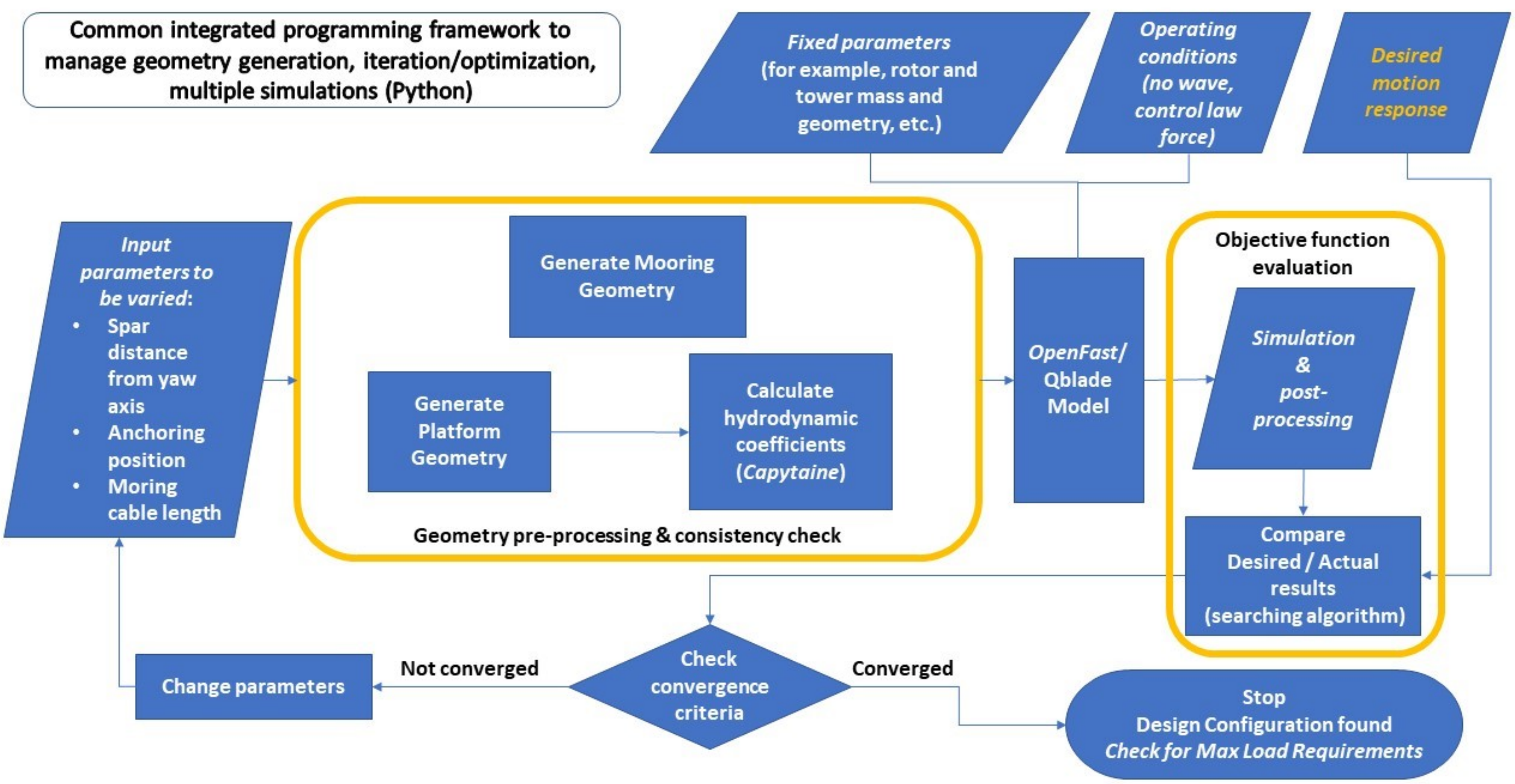

Figure 4.6: General scheme for platform-mooring design process.

OpenFAST [14], an open-source aero-servo-hydro-elastic simulation framework, was selected based on the possibility to implement control schemes and wake analysis in a next phase of the optimization. The main (and only) drawback of time-domain approach is the required computational time. In fact, the optimization framework works independently from the time-domain analysis software which evaluates the performance, and more sophisticated codes, such as QBlade [107] can be used. This work is focused on the definition of a FOWT platform optimization procedure and its implementation in a software framework, using the results of multidisciplinary simulations. The specific simulation tool can be changed at a later time, with suitable code adjustments, eventually taking benefit of the improved modelling techniques available in QBlade. A schematic description of the process assumed in the optimization framework is reported in the following sequence.

1. The computations of the dynamic parameters of interest (oscillations and, eventually, loads) are performed using OpenFAST time-domain simulations. The inputs to the simulation block can be classified as follows:

    - fixed configuration parameters (e.g., rotor and tower mass and geometry, aerodynamics, etc.);
    - operating characteristics and control (wind, control laws);
    - variable input parameters, in the current implementation:
        - spar radius, draft;
        - heave plate position;
        - mooring cable length;
        - fairlead positions;
        - anchor radius from yaw axis.

    These inputs can be varied during the design procedure in order to reach the desired goal.

2. In order to define a consistent configuration (platform geometry and mooring lines integration with the wind turbine), a pre-processor needs to be implemented. This part of the process generates a set of input files for the computation, describing a configuration based on the assigned input parameters. The pre-processor performs several operations:

    (a) generates the input files for the mooring system;

    (b) generates the surface mesh files needed for hydrodynamic calculation (using the open-source code Gmsh [108]); in this step an equilibrium analysis is performed, in order to set the platform in the equilibrium position around which hydrodynamic analyses are performed;

    (c) run the hydrodynamic analysis in order to get the hydrodynamic coefficients in the frequency domain, needed to describe the behaviour of the platform interaction with water;

(d) if needed, adds the Morison's coefficients for viscous damping directly in the OpenFAST input files;

(e) perform a consistency check to verify that physical constraints are not violated and to avoid unfeasible geometries.

3. The design constraints are checked before performing OpenFAST simulations.

4. Once the geometries and the hydrodynamic data are determined, simulations are performed by OpenFAST. Simulation results are post-processed and analysed to get the desired information (in the current implementation, a parameter of the spectral response).

5. The procedure can be integrated in an optimization loop. An optimization procedure would be preferable in case of many design variables (say, more than two) that can vary in a relatively large range of values. The choice of the range of variation of the design variables is fundamental and is driven by two conflicting necessities: on one hand, a larger parameter space can more easily contain a solution fully satisfying all the design requirements, on the other hand, besides the larger computational time, larger ranges of variation of the parameters may lead to a solution very different from the original design, implying structural difficulties and a possible large cost increase. Depending on the optimization algorithm specifications, the convergence criteria is checked on the cost function to decide whether the loop continues or ends.

4.4.2 Summary of tools employed in the optimization framework

The simulation and analysis tools employed in the current work are indicated in the following list:

- Geometrical preprocessing tool: the geometry preprocessor Gmsh [108] is an open-source code aimed at the generation and manipulation of geometries through a command line interface; it also allows the discretization of generated geometries.

- Mesh manipulation tool: the Python™ library named Meshmagick [109] is a tool aimed at managing meshed geometries, particularly oriented to the study of floating bodies; it also allows hydrostatic calculations on the analysed geometries.

- Numerical processing tool: Capytaine [110] is a Python™ implementation of a BEM numerical code based on the software Nemoh [111], developed by the French research centre LHEEA, aimed at solving the wave-body interaction problem in the frequency domain.

- FOWT time domain simulation tool: the multi-physics simulation code OpenFAST [14], developed by NREL, is capable to perform a fully coupled aero-servo-elastic simulation of the response of a floating wind turbine, accounting for geometrical, structural and aerodynamic properties of the FOWT configuration under given conditions.

4.4.3 Configuration pre-processor

The pre-processor operations are illustrated in the scheme of Fig. 4.7, divided into blocks which are more extensively described in the list below.

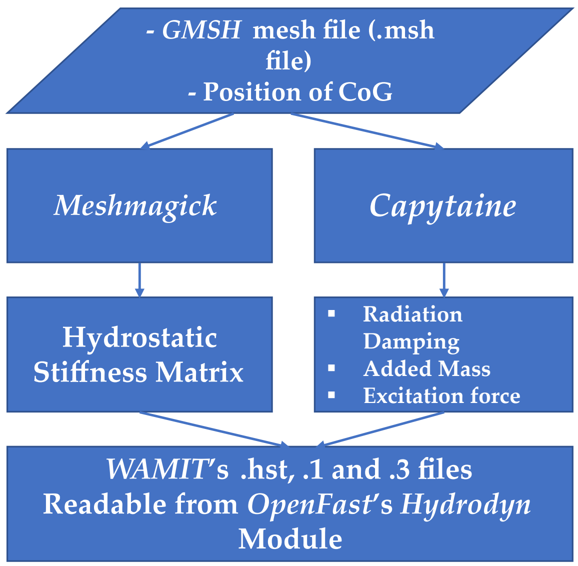

Figure 4.7: General scheme for configuration pre-processor.

The following codes are involved in the pre-processing stage:

- Meshmagick [109] and Capytaine [110] Python™ modules are used in the current framework for calculating hydrostatic stiffness matrix and hydrodynamic coefficients;
- Capytaine is a hydrodynamic calculation software based on Nemoh [111]. (The package implements a BEM solution of the diffraction and radiation problems using the linear potential flow wave theory.);
- a post-processor that convertes the output of Capytaine internally into WAMIT format to make it readable by the OpenFAST's Hydrodyn module.

The design variables are reported in Table 4.4.

Table 4.4: Possible design variables

Design Variable	**Units**
Platform	
Spar Height	m
Spar Diameter	m
Heave Plate Diameter	m
Heave Plate Thickness	m
Mooring Lines	
Fairlead Radius	m
Fairlead Height	m
Mooring Cable Length	m
Anchor Radius	m

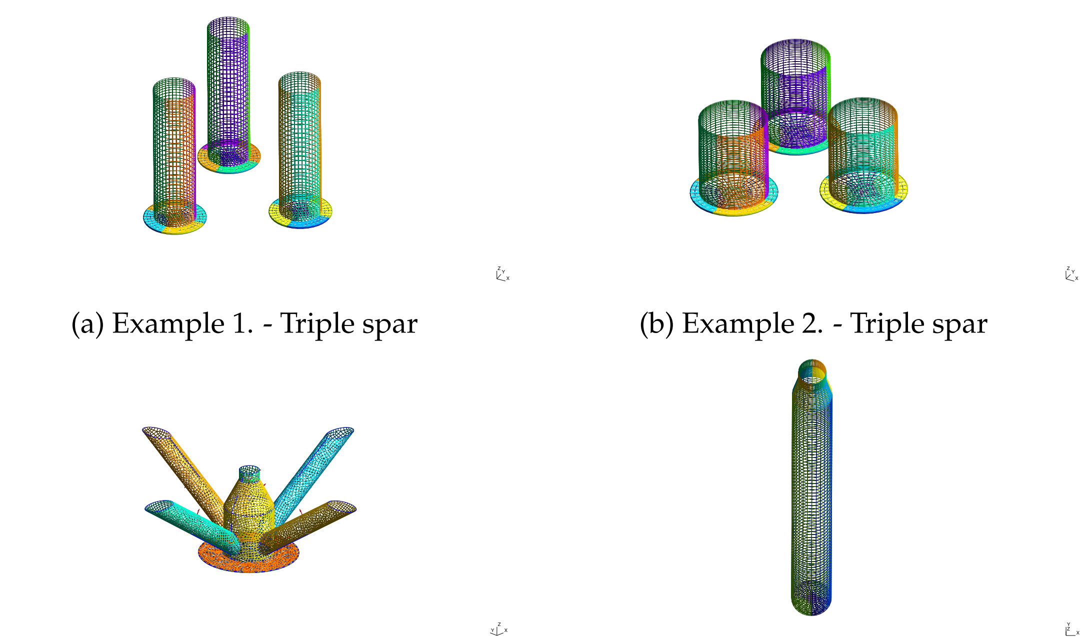

(a) Example 1. - Triple spar

(b) Example 2. - Triple spar

(c) Example 3. - Four inclined spars.

(d) Example 4. - Single spar.

Figure 4.8: Examples of mesh of submerged part of floating platform generated by the pre-processor through Gmsh [108].

–5–
Platform optimization for wake loss mitigation in wind farms

5.1 Introduction

This chapter show-cases the utilization of the optimization framework for the requirements prescribed by an innovative control strategy to mitigate wake losses in wind farms. The aim is to increase specific platform motions to enhance turbulent wake mixing, hence the re-energization of the wakes. First, a set of results obtained in a preliminary study of the platform configuration are reported. Then, the optimization has been performed following two different approaches, based on two different possible definitions of the control strategy requirements. Initially, the design goal has been defined by targeting a given platform natural frequency. In a second approach, the design goal has been set to the maximization of the oscillation response amplitude under a given external loading, simulating the control action. Finally, the design approach which is deemed more suitable for the implementation in an optimization procedure is presented together with some application examples. The final outcome of the this chapter is the demonstration of the capabilities of a parametric framework to be used in further optimization activities, possibly coupled with innovative control strategies and using more advanced simulation tools.

5.2 Preliminary studies

A preliminary study of a candidate platform configuration has been carried out. The choice of the platform configuration is discussed and an estimation of the possible exploitable range of natural frequencies for platform motion is given.

5.2.1 Description of the assumed platform configuration

In order to define the design parameter space, a specific platform configuration has been chosen, among different available choices. In particular, a triple spar geometry has been used for this study. The considered geometry is illustrated schematically in Fig. 5.1. The platform geometry is composed by three cylindrical spar elements connected using braces (the braces are not represented in figure). At the base of each spar a heave plate (a plate element used to dampen the heave oscillations) is present.

Figure 5.1: Front view of the DTU 10MW turbine, installed on a triple-spar type platform. Reproduced from [112].

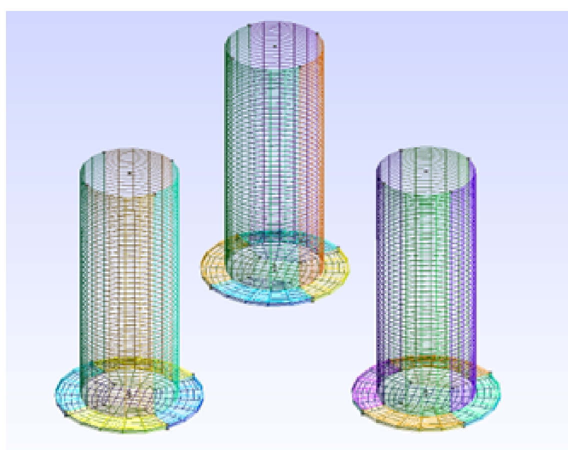

Figure 5.2: Schematic representation of the submerged part of the floating platform generated through Gmsh [108].

In Fig. 5.2 a schematic geometry is presented together with a mesh discretization of the submerged surface, to be used in numerical analysis. The turbine tower is mounted on top of the connection point of the platform braces. In the current study, the DTU 10MW wind turbine has been considered. The model of the turbine is essentially based on the work reported in [112]. From this reference, the main geometrical characteristics have been retrieved. A model of the considered floating wind turbine is also present in the public domain and has been used as the baseline configuration for the further development of the study.

5.2.2 Choice of the platform configuration

The reasons of the choice of such configuration can be summarized in the following points, as emerged from discussions within the work-group on the comparison with other configurations:

- the use of three buoyant bodies reduces the need for large drafts, which may limit the applicability of the studied configuration to sites with large seabed depth, in comparison with a single spar configuration;
- other available configurations, such as tension leg platforms (TLP), may have higher natural frequencies, incompatible with preliminary estimations of the expected required frequency for the application of the desired wake control technique;
- the geometry of the Triple Spar model, although relatively simple, seems to be more flexible, offering a wider range of available parameters to be changed in the design process in comparison with simpler geometries (such as the spar buoy).

On the other hand, some possible *short comings* of this choice, which were noted during the configuration design stage, should be pointed out:

- the presence of large bodies at significant distance from the yaw axis is associated with larger damping on the yaw degree of freedom, which are detrimental for the implementation of control schemes requiring a large yaw motion, as in one of the possible wake control patterns to be considered (named Helix).

Despite this possible drawback, the triple spar configuration has been considered suitable for the purpose of this study.

5.2.3 Baseline configuration

Source of the baseline data

The preliminary analyses were intended to estimate the range of variation of the natural frequency of the assembled turbine-platform system. The above indicated baseline configuration has been assumed as the reference and the effect of modifying some parameters of interest has been explored. Some data of the baseline configuration, based on the DTU 10 MW floating wind turbine, are reported in the following subsections.

Main configuration data

The assumed water depth is equal to 180 m. The aerodynamic characteristics are available for the reference DTU 10MW turbine in the same above cited reference ([112]). However, for the preliminary exploration of the natural frequency ranges, the dynamic response in parked rotor conditions without wind was analysed. The main characteristics of the wind turbine and platform are listed in Table 5.1, while the characteristics of the mooring lines are listed in Tables 5.2 and 5.3.

Table 5.1: Baseline platform and turbine data.

Turbine/tower/platform main characteristics	**Value**	**Unit**
Diameter	178.23	m
Hub height	119	m
Tower height	90.63	m
Total mass (nacelle&rotor + tower + platform)		
Total mass	29341.5	t
Yaw inertia		
Nacelle inertia	7326	kg m^2
Platform inertia	2.0235E10	kg m^2

Table 5.2: Baseline mooring lines characteristics.

Mooring Lines Characteristics	**Value**	**Unit**
Number of cables	3	-
Unstretched length	610	m
Cable diameter	0.31	m
Mass density	594	kg/m
Stiffness	1.38E9	N
Depth of anchors	180	m

Table 5.3: Morison's equation coefficients used for mooring lines.

Drag (D) and added mass (M) coefficients			
C_M^{ax}	C_M^{n}	C_D^{ax}	C_D^{n}
0.8	0.25	2.0	0.4

5.2.4 Analysis of baseline configuration natural frequencies

General considerations on model definition

A simplified representation of the system is reported in Fig. 5.3. The characteristics of the mooring system significantly affects the motion response of the platform at the frequency of interest, and consequently, the process of optimization is done simultaneously for the floating platform and mooring lines. The mooring system considered in this work comprises a set of catenary mooring lines. During this preliminary stage of the study, the catenary mooring line type has been accounted for by looking at the typical frequency ranges of various mooring systems. An indication of the typical frequency range can be found for example in [113]. The frequency range of mooring-platform types like TLPs (Tension Leg Platforms) or spar buoys is generally further from the expected frequency range deemed useful for the wake control strategies to be adopted, which is assumed to be in a neighborhood of 0.01 Hz.

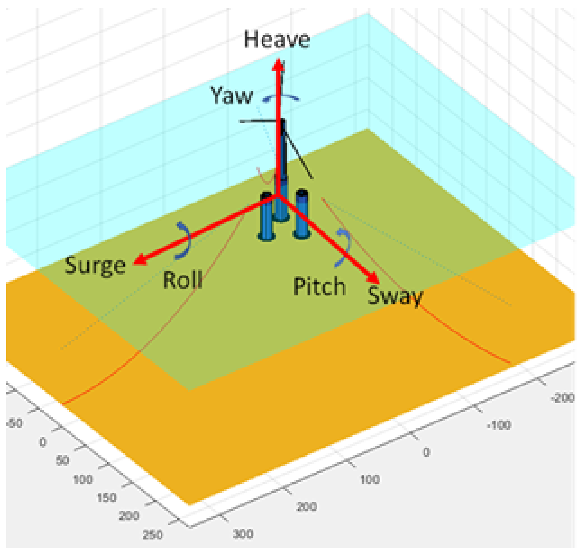

Figure 5.3: Schematic of the turbine-platform-mooring system. Axonometric view and degrees of freedom of the rigid body motion.

Simulation setup and response analysis

With the objective of estimating the natural frequencies of the turbine-platform, an OpenFAST model was employed and the following assumptions were made:

- still air;
- still water;

- deactivated control system;
- fixed rotor.

The analysis procedure can be described as follows:

- damped oscillations after a given displacement on each different DOFs are observed in a time-domain simulation in OpenFAST;
- a simulation time >1800 s is assumed (in some cases larger time lengths have been considered in order to get a finer resolution in the frequency domain analysis);
- a frequency domain analysis of the free decay response is performed, determining the PSD (Power Spectral Density) frequency peak for each degree of freedom.

Preliminary results

The natural frequencies have been determined for the baseline configuration, searching the peak values in the power spectral density (PSD) diagram. The most interesting results are reported in the following subsections. These results match the ones obtained for the baseline configuration in the Life50+ project [114] and are reported as a reference for comparison with the generated modified geometries.

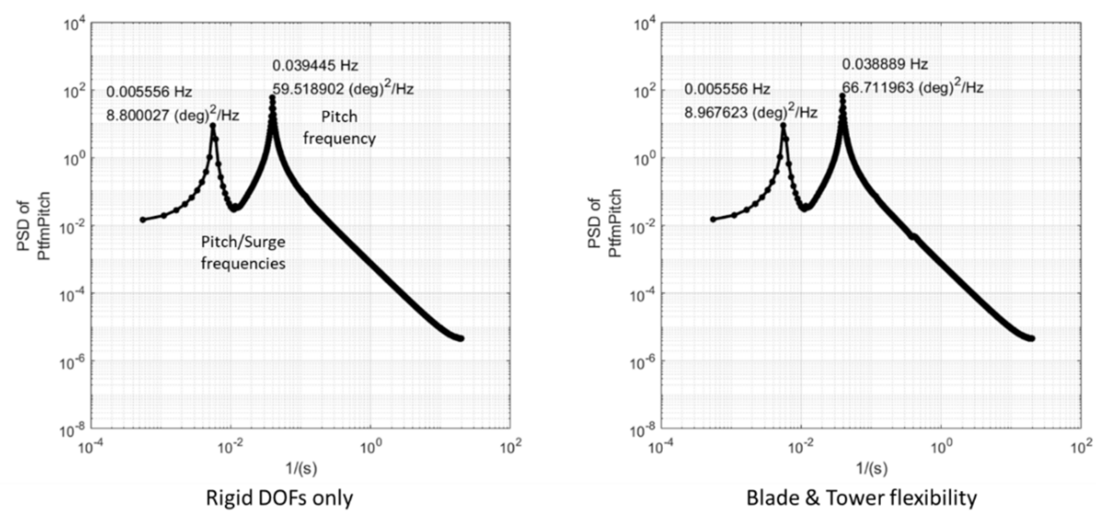

Figure 5.4: Free decay response in frequency domain, plots of Power Spectral Density (deg^2/Hz) vs. frequency (Hz) for pitch/surge response. Reference Configuration.

In Fig. 5.4 the PSD analysis of the free decay in the pitch/surge mode is reported,

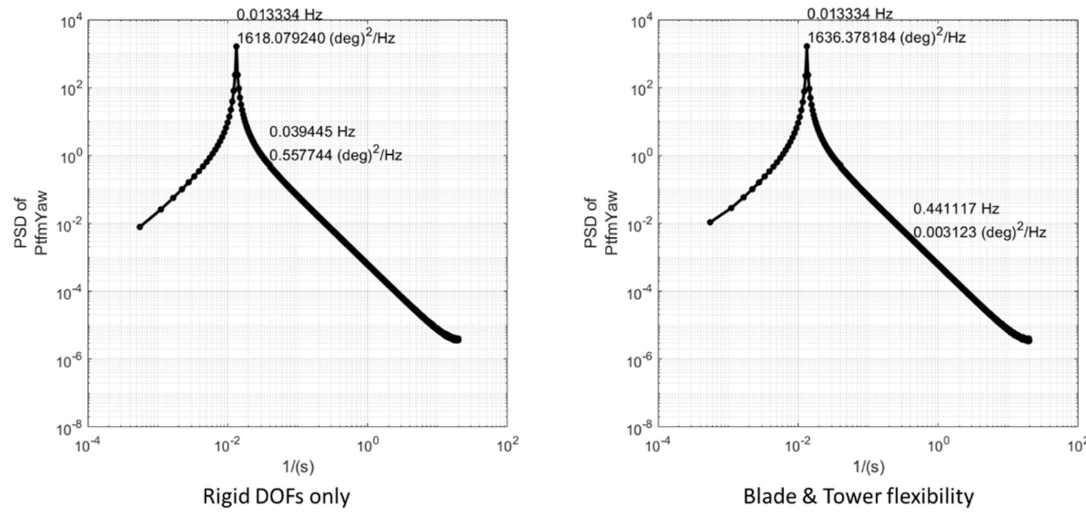

Figure 5.5: Free decay response in frequency domain, plots of Power Spectral Density (deg^2/Hz) vs. frequency (Hz) for yaw response. Reference Configuration.

while in Fig. 5.5 the same results for the yaw mode are indicated. In Fig. 5.4 and Fig. 5.5, two results are plotted: on the left the PSD of the response obtained assuming rigid motion is reported, while on the right the flexibility of tower and blades is accounted for; anyway, no significant effect can be noted due to flexibility. It can be noted that the pitch mode is coupled with the surge mode. Two distinct peaks can be detected in the figure, which may be associated to the pitch and surge modes: in order to help interpreting the meaning of the two peaks, in Fig. 5.6 a comparison of the PSD of the free decay with and without the effect of mooring is reported. It can be seen that the coupling can be associated to the effect of the mooring and that the second peak is closer to the pitch peak frequency of the response with no mooring. As a validation of the use of the baseline data, and to define a set of reference values, the following table reports the estimated natural frequencies next to the corresponding results reported in the references [15] and [112], which report slightly different values.

Table 5.4: Comparison between natural frequencies values found in literature and current model calculations.

Mode	Reference [112]	Reference [15]	Current (Rigid)	Current (Flexible)
Surge	0.005 Hz	0.006 Hz	0.0056 Hz	0.0056 Hz
Sway	NA	0.006 Hz	0.0056 Hz	0.0056 Hz
Heave	0.06 Hz	0.060 Hz	0.0594 Hz	0.0594 Hz
Roll	NA	0.038 Hz	0.0394 Hz	0.0389 Hz
Pitch	0.04 Hz	0.038 Hz	0.0394 Hz	0.0389 Hz
Yaw	NA	0.013 Hz	0.0133 Hz	0.0133 Hz

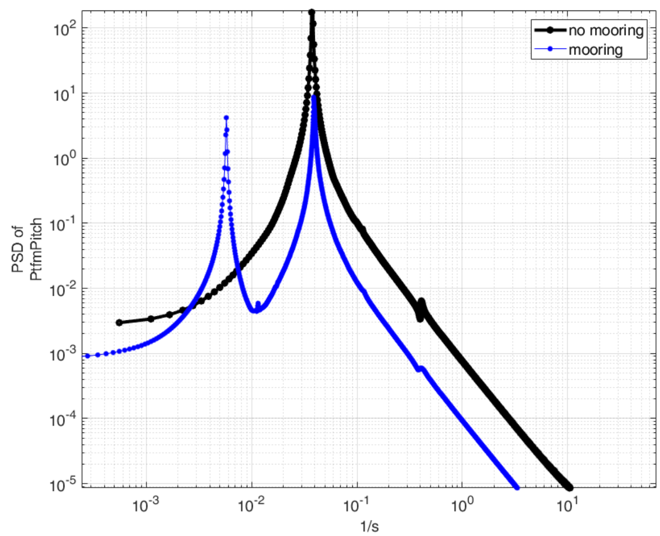

Figure 5.6: Comparison of the Power Spectral Densities (deg^2/Hz) of the free decay pitch response with (blue curve) and without (black curve) mooring lines.

5.2.5 Effects of mooring parameters on the natural frequencies

In order to study the frequency ranges of the system (platform-mooring-turbine) and their dependence on the mooring configuration, a series of analyses has been performed changing some geometrical parameters of the mooring lines. The geometrical parameters investigated in this study are reported in the following list:

- unstretched cable length;
- fairlead position;
- fairlead – anchor relative distance.

The results of the parametric study are reported in the following paragraph considering separately each configuration parameters. The main objective of this study is to highlight the parameters with major influence on the required platform motion response, in order to define the parameter space for the implementation of the optimization framework. The adopted wake mixing control strategy can benefit from the tuning of the platform yaw response, in the case of the Helix approach, or on the tuning of the pitch response, in the case Pulse approach. The preliminary analysis will therefore be applied to the study of the yaw and pitch natural frequencies. In this initial phase of the study, both yaw and pitch response have been taken into account. During the successive development of the work, the focus of the study has been restricted to the yaw response only, considering only the Helix control strategy, which has been deemed more promising due to some possible drawbacks of the Pulse approach.

Effect of mooring cable length

The effect of changing the cable length is estimated for fixed initial positions of the fairleads on the platform and fixed anchor positions. The fairlead positions are defined assuming a given distance from the yaw axis and a given height above sea level. Similarly, the anchor position is defined by a given distance from the yaw axis.
Fairleads and anchors are equally spaced on circles centred around the yaw axis. For fixed position of the fairleads and anchors, the length of the cable is changed,

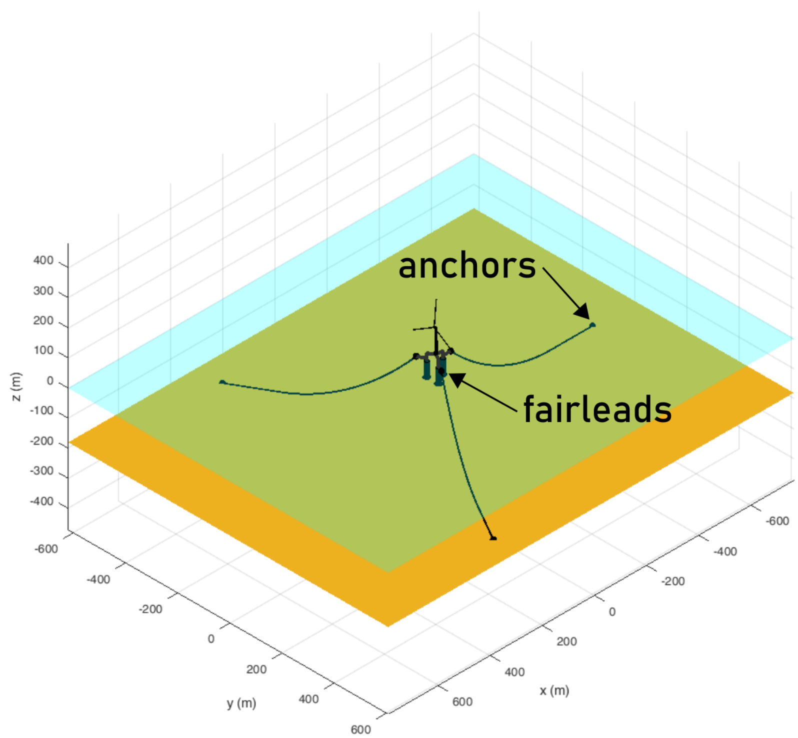

Figure 5.7: Schematic of the turbine-platform-mooring system. Fairlead and anchor positions.

with longer cable corresponding to mooring lines with more slack.

Effect of mooring cable length on yaw frequency

The PSD peak period has been analysed for the free decay after an initial yaw displacement, considering different cable lengths, as reported in Fig. 5.8. In the figure, an approximate value of the desired natural period for yaw motion ($\approx$100 s) is indicated, showing that changing the cable length seems to be an effective way to modify the natural frequency in the yaw degree of freedom towards the target value.

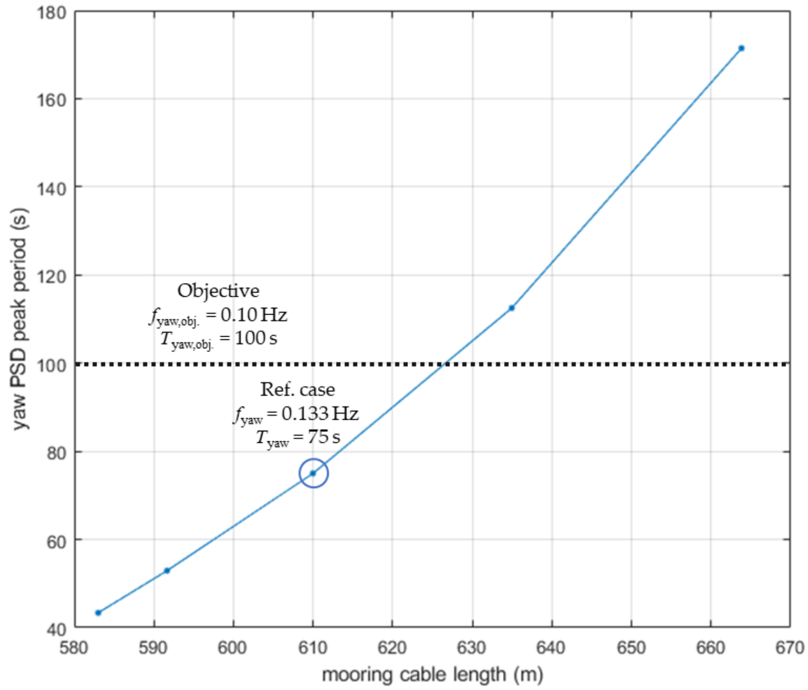

Figure 5.8: Effect of mooring cable length on the yaw period.

Effect of mooring cable length on pitch/surge frequency

In the case of the free decay after an initial pitch displacement, a coupled response in pitch and surge can be observed (as illustrated in the PSD reported in Fig. 5.4). The results for the peak frequencies are reported in Fig. 5.9 for both the coupled peak values. The larger period can be associated to a predominantly surge mode, while the lower one can be associated to a predominantly pitch mode. It can be noted that the pitch mode is less affected by changes in mooring length, while the surge mode seems to be more significantly affected. A possible explanation of such difference may be related to the fact that no other restoring effect is present on the surge mode except the effect of mooring lines, thus yielding a larger importance of the mooring on such degree of freedom, while the pitch mode is significantly affected also by the platform hydrostatic restoring actions, thereby reducing the relative importance of mooring changes. In this case the mooring length should be slightly reduced compared to the baseline configuration to approach the approximate desired frequency of 0.01 Hz (period of about 100 s).

Effect of fairlead position

The distance of the fairlead from the yaw axis (here indicated as fairlead radius) has also been considered. It has to be noted that changing the fairlead position, should, in principle, require a redesign of the platform structure according to the modified

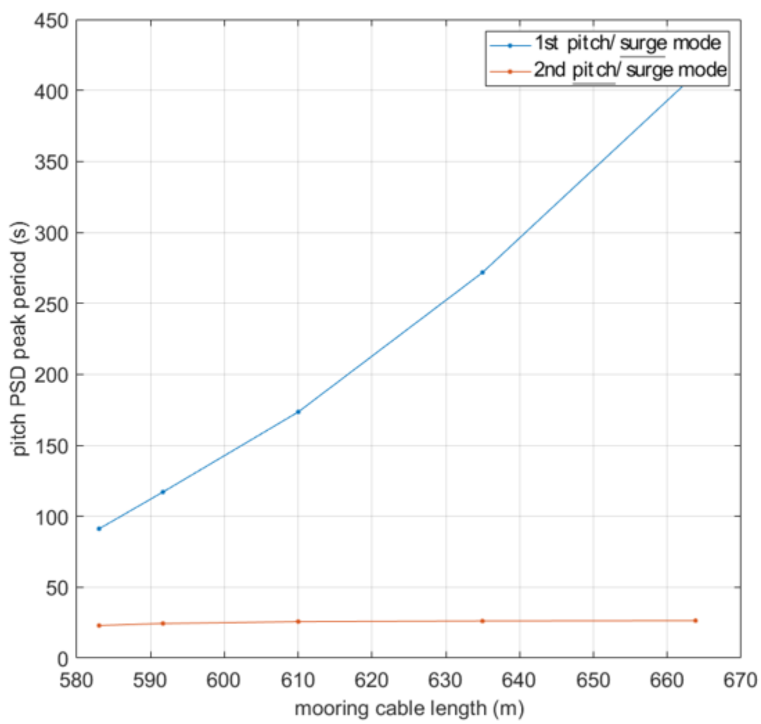

Figure 5.9: Effect of mooring cable length on the pitch and surge periods.

locations of the mooring attachment points. This structural modification has been neglected at this stage of the analysis. The effects of fairlead radius variation on the yaw and pitch/surge modes are reported in the following figures.

Effect of fairlead position on yaw frequency

The effect of fairlead radius on the yaw natural frequency is reported in Fig. 5.10, for two different mooring configurations. In order to separately assess the effects of fairlead position and mooring line length, the mooring cables length are changed with the position of the fairleads, so as to keep a constant ratio between cable length and fairlead-anchor distance. Two cases are considered, one with a mooring cable about 6% longer than the anchor-fairlead point-to-point absolute distance, one with a mooring cable about 10% longer than the anchor-fairlead distance. It can be noted, as previously observed, a significant effect of the mooring cable length.

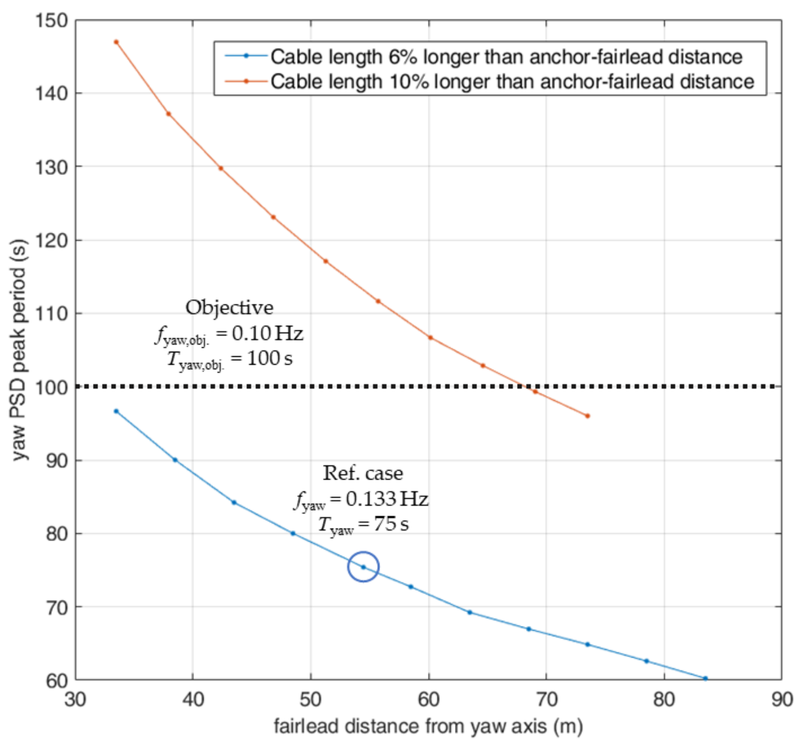

Figure 5.10: Effect of fairlead radius on the yaw period.

Effect of fairlead position on pitch/surge frequencies

The effect of fairlead position has also been assessed, considering a variation of the fairlead radius with a constant ratio of the mooring line length to the distance between fairlead and anchor equal to 1.10 (cable mooring 10% longer than the fairlead-anchor distance). In this case a negligible effect can be observed on the pitch/surge frequencies, which remains approximately constant for varying fairlead position, as indicated in Fig. 5.11. Thus, this parameter has not been investigated in details.

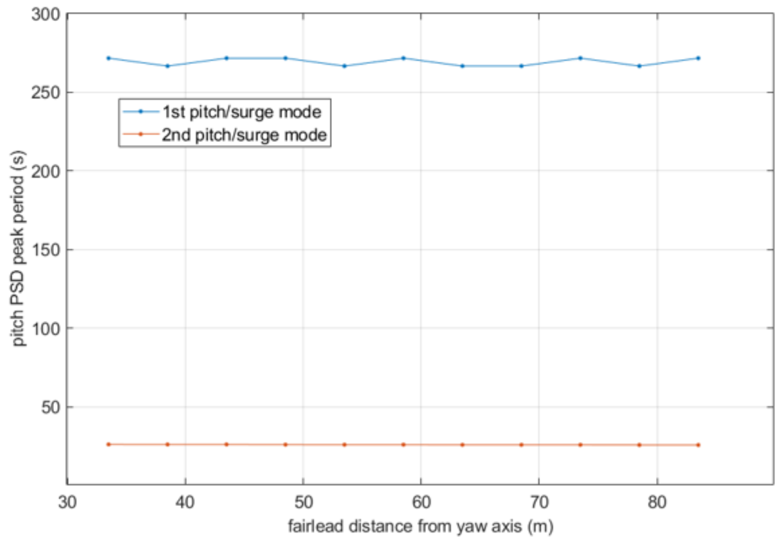

Figure 5.11: Effect of fairlead radius on the pitch and surge periods.

Effect of fairlead height above sea level on pitch/surge mode

In the context of the parametric study of the mooring system, the variation of fairlead height has additionally been observed with respect to the effect on pitch/-surge mode frequencies, as reported in Fig. 5.12. In this figure, a geometrical limit to the lower fairlead position is indicated (dashed vertical line), as imposed by the draft of the spar: it can be seen that non-negligible changes to natural frequency could, in principle, be obtained only for very large variation of the vertical position, exceeding the spar vertical dimension. In this case, similarly to the fairlead radius case, the predominantly pitch mode seems substantially insensitive also to this mooring system parameter, while some noticeable effects can be seen on the surge coupled mode.

Observations on the mooring lines preliminary study

Some observations derived from the analysis of the performed simulations can be summarized:

- it is difficult to identify a way to tune pitch and surge motion modes (which are more interesting for the Pulse control strategy) by changing mooring lines

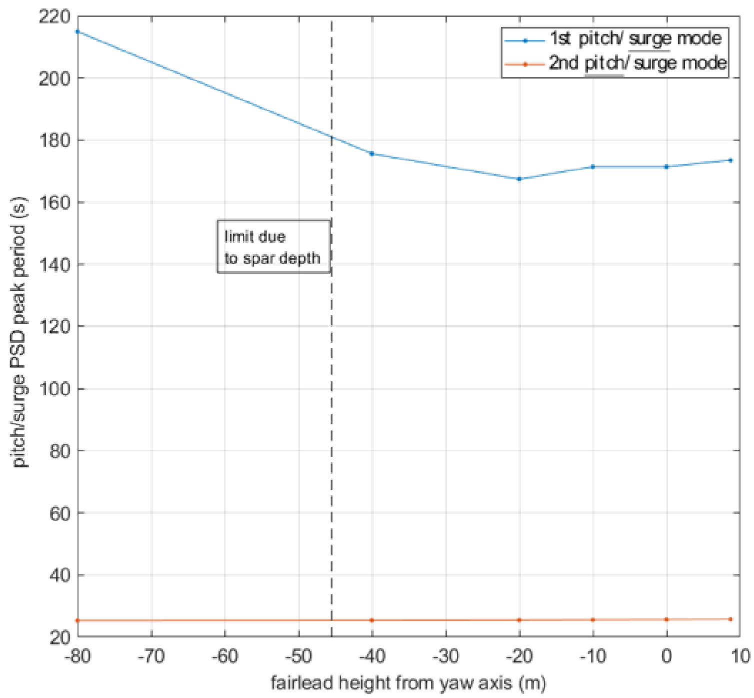

Figure 5.12: Effect of fairlead height on the pitch and surge periods.

characteristics, due to the prevailing effect of buoyant restoring forces determined by the geometry of the platform; yaw mode seems to be potentially more easily tuned to match Helix strategy requirements;

- the explored parameters (mooring cable length and fairlead position) have shown different levels of effectiveness with respect to the objective of tuning the platform response; cable length seems to be the most effective parameter, particularly for the control of yaw motion response;

- results indicate that fairlead distance from the yaw axis could be interesting for adapting the substructure natural frequencies to the requirements of the "Helix" approach, with a small impact on surge/pitch mode. The structural feasibility and the impact on costs of the configuration variation is missing at this preliminary stage of the analysis and will be introduced later during the definition of the optimization framework.

5.2.6 Validation of the framework: Hydrostatics and hydrodynamics from Meshmagick – Capytaine

The aim of this part of the work was to validate the successful generation of input and output files within the modules of the framework described in Sec.4.4. The hydrodynamic data potential-flow solutions are generated by the two software Meshmagick and Capytaine. The former is used to study the equilibrium condition and the latter to generate the hydrodynamic coefficients from the radiation-diffraction problems. To validate the results for the hydrodynamic data provided to OpenFAST, the following comparisons were carried out.

Free Response of the OC3 Hywind Spar with NREL 5MW Turbine

First, the free response of the platform-wind turbine assembly to platform displacements and rotations was simulated in calm wind and still water conditions. Considering the quantity and quality of the data available in literature for the OC3 Hywind Spar platform designed for the NREL 5MW wind turbine [115], the first comparison was made between the original simulation of the free response (with hydrodynamic files generated through WAMIT) and our simulations with hydrostatic and hydrodynamic files generated through Meshmagick-Capytaine. The free response due to a unit displacement (for both translational and rotational degrees of freedom) was analysed in terms of power spectral density of the excited degree of freedom time history. The first three plots (reported in Fig. 5.13) concern the translatory degrees of freedom (surge-sway-heave) while Fig. 5.14 concern rotational degrees of freedom (roll-pitch-yaw). No major differences are observed between the simulation results with hydrodynamic data generated by the two compared codes, so it can be deduced that Capytaine and Meshmagick hydrodynamic and hydrostatic calculations predict the same behaviour as the reference calculation for the free response of the system.

Free-response of the Triple Spar Platform with DTU 10MW Turbine

The aforementioned OpenFAST publicly available model of the Triple Spar Platform with the DTU 10 MW Turbine mounted on top, makes use of a hydrodynamic and hydrostatic database estimated utilizing the software AQWA [116]. A second validation comparison was made using the hydrodynamic files and the hydrostatic stiffness matrix calculated by Meshmagick and Capytaine against the available DTU10MW-Triple Spar data. The free response due to a unit displacement (for both linear and angular degrees of freedom) was analysed in terms of power spectral density of the excited degree of freedom (Fig. 5.15 and Fig. 5.16). Time-series of the simulations with unitary initial displacements are shown in Fig. 5.17, Fig. 5.18, Fig. 5.19, Fig. 5.20, Fig. 5.21 and Fig. 5.22. No major differences are observed so it can be deduced that Capytaine and Meshmagick hydrodynamic and hydrostatic calculations lead to the same behaviour predictions as the reference model with respect to the free response of the system.

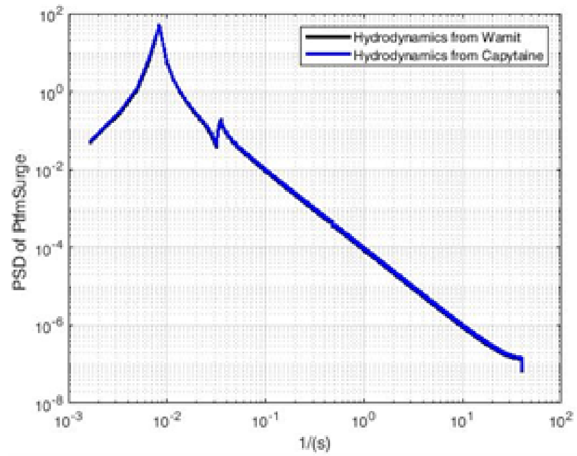

(a) Surge

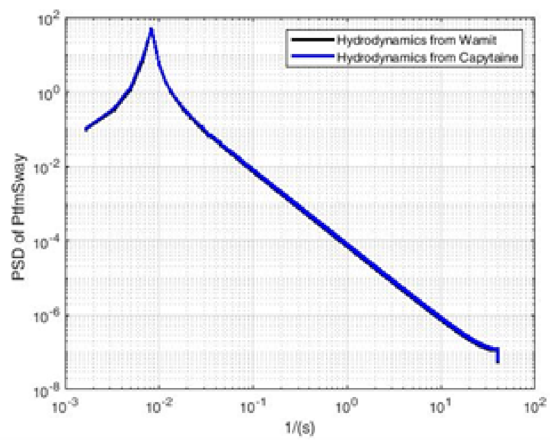

(b) Sway

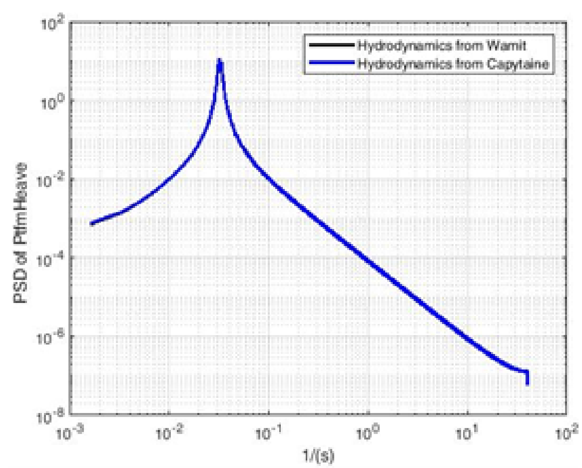

(c) Heave

Figure 5.13: Power Spectral Density (m^2/Hz) vs. frequency (Hz) of the free responses of OC3-Hywind Spar – NREL 5MW Turbine assembly due to unitary translational initial displacements. The power spectral density functions were obtained through the fast Fourier transform of the response signals with a total time of the simulations of 1800 s.

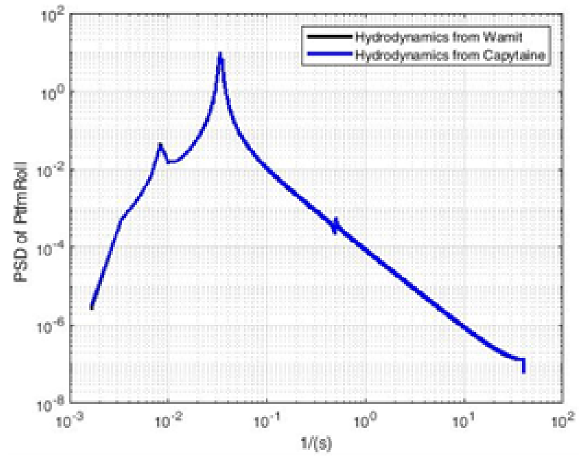

(a) Roll

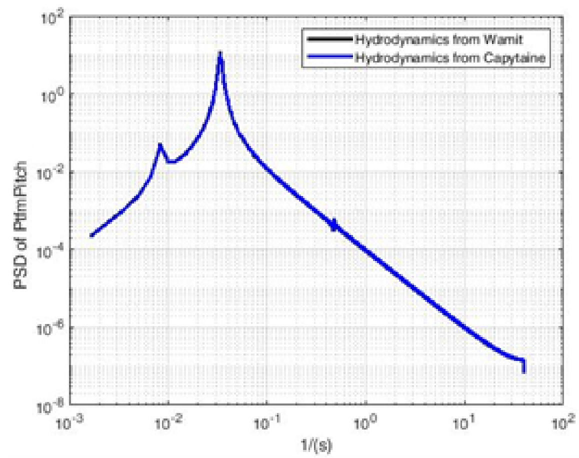

(b) Pitch

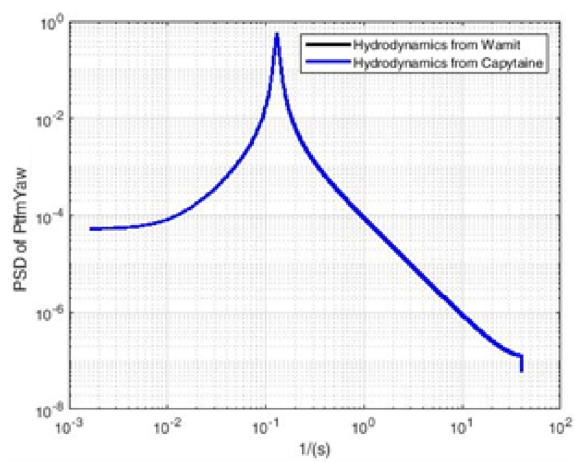

(c) Yaw

Figure 5.14: Power Spectral Density (deg^2/Hz) vs. frequency (Hz) of the free responses of OC3-Hywind Spar – NREL 5MW Turbine assembly due to unitary angular initial displacements. The power spectral density functions were obtained through the fast Fourier transform of the response signals with a total time of the simulations of 1800 s.

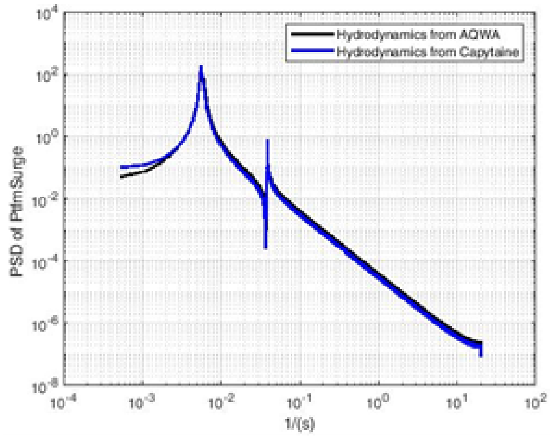

(a) Surge

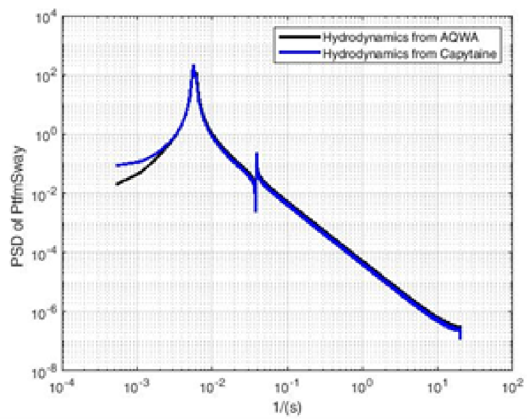

(b) Sway

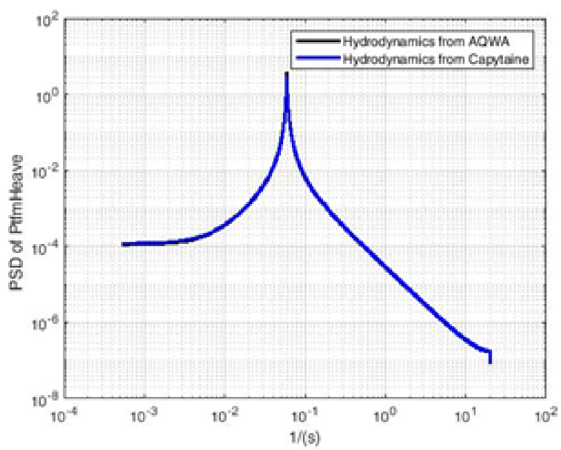

(c) Heave

Figure 5.15: Power Spectral Density (m^2/Hz) vs. frequency (Hz) of the free responses of Triple Spar Platform with DTU 10MW Turbine assembly due to unitary translational initial displacements. The power spectral density functions were obtained through the fast Fourier transform of the response signals with a total time of the simulations of 1800 s.

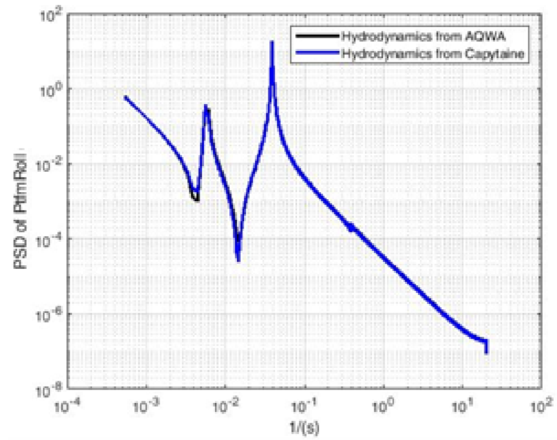

(a) Roll

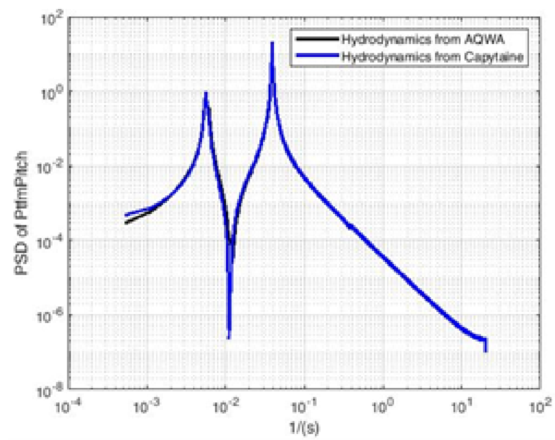

(b) Pitch

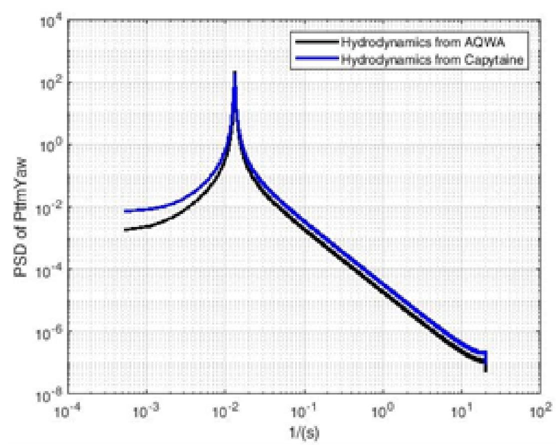

(c) Yaw

Figure 5.16: Power Spectral Density (deg^2/Hz) vs. frequency (Hz) of the free responses of Triple Spar Platform with DTU 10MW Turbine assembly due to unitary angular initial displacements. The power spectral density functions were obtained through the fast Fourier transform of the response signals with a total time of the simulations of 1800 s.

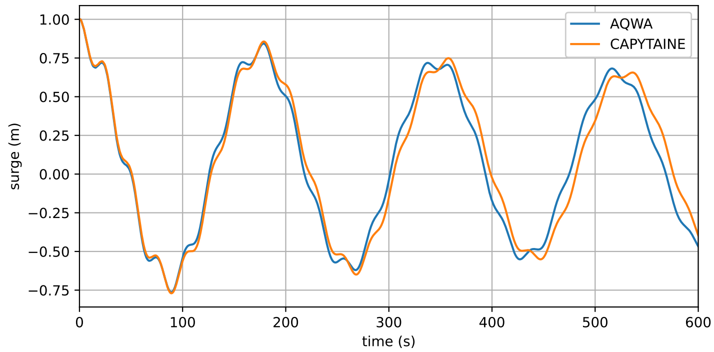

Figure 5.17: Surge free decay due to a unitary surge initial displacement.

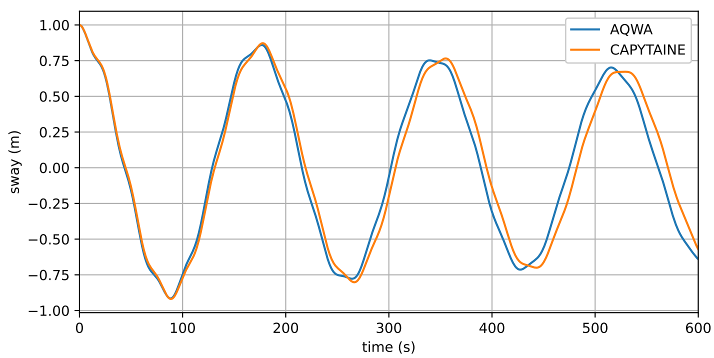

Figure 5.18: Sway free decay due to a unitary sway initial displacement.

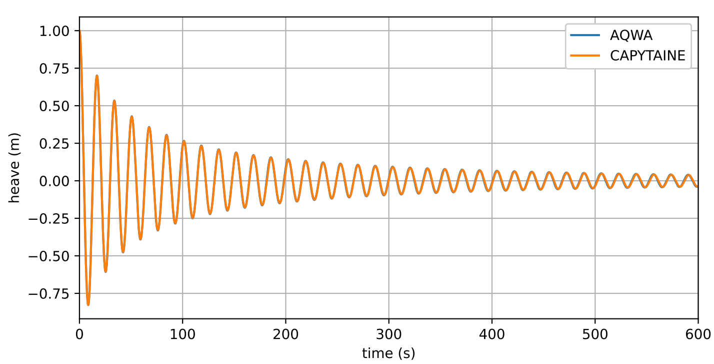

Figure 5.19: Heave free decay due to a unitary heave initial displacement.

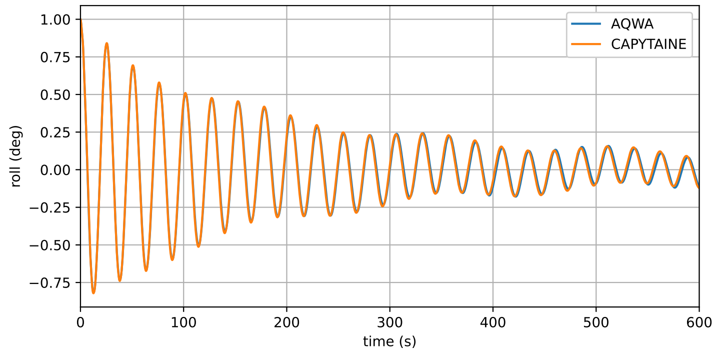

Figure 5.20: Roll free decay due to a unitary roll initial angle.

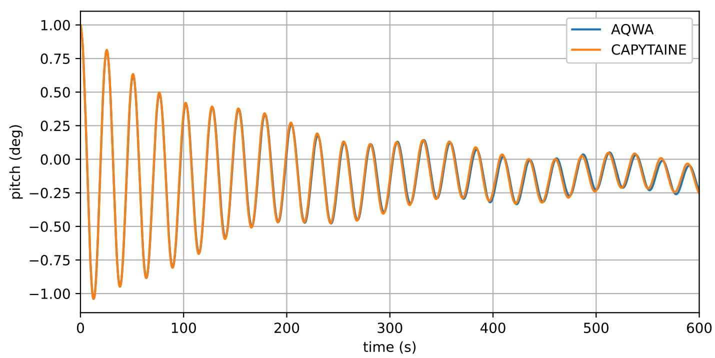

Figure 5.21: Pitch free decay due to a unitary pitch initial angle.

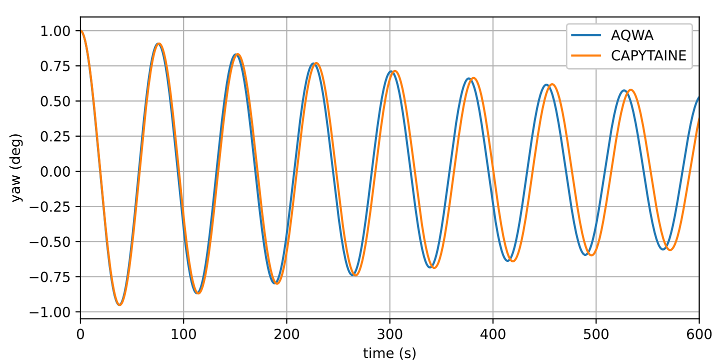

Figure 5.22: Yaw free decay due to a unitary yaw initial angle.

5.3 Preliminary optimization procedure setup

Previous studies indicated that an oscillation of the platform excited by the “Helix” strategy, acting on blade pitch control, could augment wake mixing leading to an increased power production of the trailing wind turbines in a floating offshore wind farm, as shown in [65]. The oscillation of the platform will be excited with a prescribed frequency, given by the control logic. In this first preliminary analysis, a simplified goal has been set: match a specified natural frequency of floater/-mooring system, in order to determine a response amplification at the desired excitation frequency. Thereby the required blade pitch oscillation amplitude shall be reduced while the wake mixing stays at a comparable level. This would lead to a reduced work load on the control mechanism. This simplified objective is schematically visualized in Fig. 5.23: First, aerodynamic and control related studies are performed in order to characterize the wake recovery behavior. Second, a desired natural period is defined (in this study the required period has been set to 100 s). Third, a configuration complying with the stated requirement is searched for using optimization techniques.

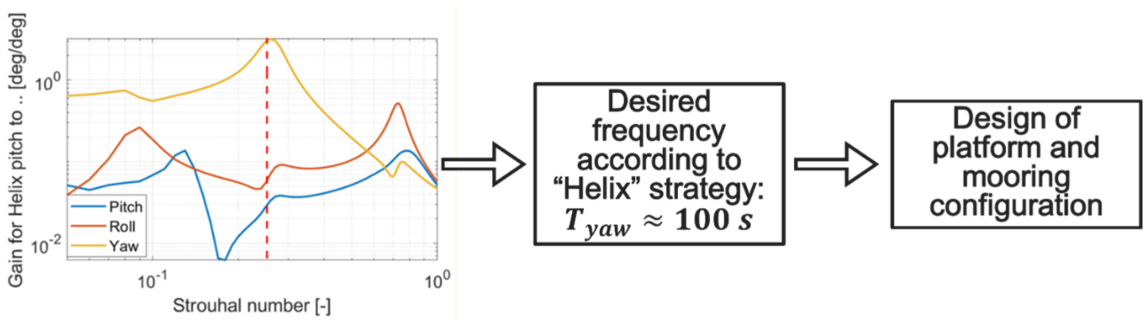

Figure 5.23: Scheme for simplified goal of platform/mooring design.

5.3.1 Selected design space

Based on the sensitivity analysis of the natural frequency to design variables, the parameters selected for the preliminary optimization are shown in Table 5.5.

Table 5.5: Possible design variables

Design variables	Reference Value	Range of variation	
Platform		**Min**	**Max**
Spar distance from yaw axis (x_S)	26 m	23.4 m	33.8 m
Mooring		**Min**	**Max**
Mooring line length factor (MLLF)	1.057	1.040	1.152
Anchor distance from yaw axis (x_A)	600 m	450 m	750 m

In Fig. 5.24, the relevant quantities that will be modified during the preliminary optimization are coloured in blue. The line length factor represents a measure of the mooring line length non-dimensionalized with respect to the distance between the fairlead and the anchor point, that is,

$$\text{MLLF} = \frac{l_{\text{C}}}{\Delta x_{\text{F-A}}} \tag{5.1}$$

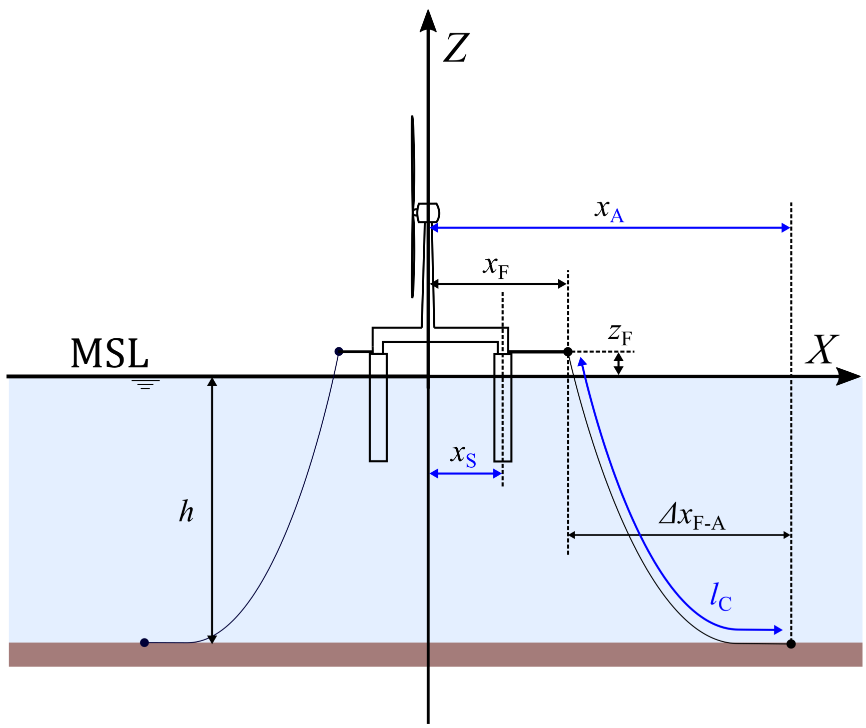

Figure 5.24: Sketch of the DTU 10MW mounted on the Triple Spar. Relevant quantities are defined in Table 5.5. The depth is indicated with h.

5.3.2 Design assumptions

Following an approach common in floating platform for FOWT design, as in [16], some requirements must be verified by the preliminary design, in order to comply with the operation and survival limits of the whole system. The general requirements, which may be considered for the preliminary design, can be summarised as follows,

1. Hydrostatic equilibrium and stability (influencing the most relevant mass and inertia properties).

2. Economic feasibility.

3. Compliant response to hydrodynamic loads (manoeuvring/seakeeping analysis).
4. Compliant mooring system.
5. Good dynamics in fully-coupled design load cases (DLC).
6. Survival to critical load cases.

The Triple Spar reference floating platform geometry, together with the three catenary mooring lines have been designed so that these requirements are satisfied (see also [15]). While a complete re-design of the platform would arguably need a complete set of simulations of Design Load Cases (DLCs), in this preliminary analysis, which requires slight modifications of the reference geometry, only coherency checks on the basic assumptions will be taken into account (verification of points 1., 2. and 4.). At this stage of the design process, only the effects on the yaw dynamic response are investigated in detail; further dynamic effects related to the environmental characteristics, such as turbulence and sea waves, are not taken into account. In particular, the implemented procedure is focused on tuning the yaw natural frequency of the configuration, disregarding the dynamic response of other degrees of freedom.

Buoyancy Equilibrium/Heave Displacement

In the present analysis, the optimization procedure generates a set of candidate configurations with modified geometrical parameters. Such geometry changes are associated with variation of the inertial properties of the floating platform. To simplify the procedure, only the variation in yaw inertia, which are directly related to the target yaw period, are considered, while other mass and inertial parameters are held fixed at the baseline configuration values.

Hydrostatic Stability

Hydrostatic stability constraints have been implemented to check when the thrust of the rotor is at its rated value, so that the heeling angle and the surge displacement are compliant with suggested values found in literature. With regards to the heeling angle, the current value has been selected to avoid an excessive decrease in power production (see [16] and [15]). The surge excursion must also be limited, depending on water depth, to ensure the survival of the electrical cable (see [75]). The equilibrium values at rated thrust conditions for the platform heeling angle and surge are evaluated using the direct terms of the hydrostatic restoring matrix. The assumed expressions and limit values for heeling and surge are reported below:

$$\Delta\theta_{y,\text{rated}} = \frac{T_{\text{rated}} \cdot z_{\text{hub}}}{C_{55}} \leq 5 \text{ deg} \tag{5.2}$$

$$\Delta x_{\text{rated}} = \frac{T_{\text{rated}}}{C_{11}} \leq 25\ m \tag{5.3}$$

where $F_{X,\text{rated}}$ is the rated thrust applied at the hub axis height, z_{hub}, and considered as a constant, C_{11} and C_{55} are the diagonal elements of the hydrostatic stiffness matrix of the whole system. These latter two values are determined by the platform geometry and by the mooring lines properties, neglecting the static effect of the off-diagonal coupling terms. In particular, the surge restoring force is given by the action of mooring lines (the tension at the fairleads), while the pitch restoring moment is given by both the hydrostatic properties of the platform (waterplane area and platform buoyancy centre), the mass distribution of the whole system (centre of gravity) and the restoring moment given by the mooring lines tensions.

Economic feasibility

To ensure that the total cost of the system is not excessively increased by the change of floating platform and mooring lines configuration, the variation of costs must be taken into account into the objective function. The definition of the total cost function is split into two parts; one accounting for the variation of cost of the floating platform, and the other accounting for the variation of cost of mooring lines.

Cost variation of the floating platform

With regards to the costs of the floating platform, the following simplified assumptions are made:

- the cost of the spars does not change due to modifications of the floating platform during the optimization;
- the cost of the steel tripod braces (horizontal legs in the following) changes as a direct function of the braces length (related also to the brace section size and to overall material weight);
- the tripod braces length is assumed equal to the distance of the spars from the yaw axis (x_{S});
- to preserve the same structural integrity of the floating platform, the same stress level in the tripod braces should be maintained.

To ensure the same stress level, the following procedure was established. First, we approximate the maximum tension in a tripod brace as:

$$\sigma = \frac{M}{S} \tag{5.4}$$

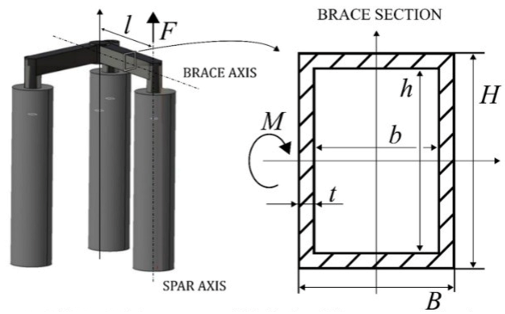

Figure 5.25: Sketch section view of the brace of the Triple Spar.

where M is the maximum bending moment on the brace and S is the elastic section modulus. Relevant quantities of this paragraph are shown in Fig. 5.25. For the moment acting on the most stressed section of the brace a simplified expression (hydrodynamic and hydrostatic forces) is assumed in order to assess the effect of the brace length, l:

$$M = Fl \tag{5.5}$$

with F force applied from a column at the end of a horizontal leg of the tripod and l length of a brace. Considering a hollow rectangular section with height H, width B, thickness t, internal height $h = H - 2t$, internal width $b = B - 2t$, as shown in Fig. 5.25, the following elastic section modulus is assumed:

$$S = \frac{1}{6H}\left(BH^3 - bh^3\right) \tag{5.6}$$

Rearranging in terms of thickness and neglecting terms of the second order in t:

$$\begin{aligned}
S &= \frac{1}{6H}\left(BH^3 - (B-2t)(H-2t)^3\right) \\
&= \frac{1}{6H}\left(BH^3 - (B-2t)\left(H^3 - 6H^2t + 12Ht^2 - 8t^3\right)\right) \\
&= \frac{1}{6H}\left(BH^3 - BH^3 + 6BH^2t - 12BHt^2 + 8Bt^3 + 2H^3t - 12H^2t^2 + 24Ht^3 - 16t^4\right) \\
&= \frac{1}{6H}\left(6BH^2t + 2H^3t + O\left(t^2\right)\right) \approx \frac{BHt}{6}\left(6 + \frac{2H}{B}\right) \\
&= BHt\left(1 + \frac{1}{3}\frac{H}{B}\right)
\end{aligned}$$

With the assumed simplifications, the stress in the brace can be expressed approximately as

$$\sigma = \frac{Fl}{S} \approx \frac{Fl}{BHt\left(1+\frac{1}{3}\frac{H}{B}\right)} = \frac{F\left(\frac{l}{H^2}\right)}{\frac{B}{H}t\left(1+\frac{1}{3}\frac{H}{B}\right)} \tag{5.7}$$

hence

$$\frac{\sigma}{F} = \frac{\left(\frac{l}{H^2}\right)}{\frac{B}{H}t\left(1+\frac{1}{3}\frac{H}{B}\right)} \tag{5.8}$$

It is assumed that a constant force is applied by the hydrodynamic actions on the columns. Moreover, a constant thickness and a constant aspect ratio of the section, $H/B = 1$ (square section) are assumed. In order to preserve the same stress level, the following relation between brace length, l, and section height, H, in the tripod braces, is derived:

$$\frac{l}{H^2} = cost \tag{5.9}$$

For the initial design, as reported in [112], the above indicated ratio is equal to:

$$\frac{l_{REF}}{H^2_{REF}} = 1.22\ m^{-1} \tag{5.10}$$

The thickness of the original design, as reported in the cited document is equal to

$$t = 0.0564\ m \tag{5.11}$$

The area of the section (recalling that $H = B$) can be approximately expressed as

$$A = \left(H^2 - (H-2t)^2\right) = \left(H^2 - H^2 + 4Ht - 4t^2\right) \approx 4Ht \tag{5.12}$$

With the above assumptions, the increase in weight and the total mass can be expressed as follows:

$$W_{braces,\ REF} = 948.36\ \text{t} \tag{5.13}$$

$$\Delta W_{braces} \approx 3 \cdot 4Ht\,(l - l_{REF})\,\rho_s \tag{5.14}$$

$$W_{braces} = W_{braces,REF} + 3 \cdot 4Ht\,(l - l_{REF})\,\rho_s \tag{5.15}$$

In this way, the maximum excursion of the total weight of the system can be calculated. When the tripod braces are at their maximum length, the total weight increase due to the three braces is

$$\Delta W_{braces,MAX} = 3 \cdot 4\sqrt{\frac{l_{MAX}}{1.22}}t\,(l_{MAX} - l_{REF})\,\rho_s = 95.65\ \text{t} \tag{5.16}$$

which only accounts for 0.32% of the total weight of the system. The cost increase due to the length of the tripod brace is approximately expressed as

$$C_{\text{TB}} = c_{TB}W_{braces} = c_{TB}\left(W_{braces,REF} + 3 \cdot 4Ht\,(l - l_{REF})\,\rho_s\right) \tag{5.17}$$

with $\rho_s = 7850\ \text{kg/m}^3$, steel density. The cost per unit mass is assumed equal to $c_{TB} = 5$ €/kg. This value is, clearly, subject to market variations; moreover, beside the raw material cost, the actual cost is also incremented by the manufacturing cost. This increment can be estimated through a complexity factor according to the following formula.

$$c_{TB} = c_{steel}(1 + CF_{man.steel}) \tag{5.18}$$

Where c_{steel} is equal to 0.9 €/kg and $CF_{man.steel} = 4.25$ according to [117]. The value c_{steel} is considered around 0.7 €/kg in [118]. In [119], the maximum cost comprising bulk material and manufacturing (c_{TB}) estimated for steel structures for a semisubmersible floating offshore platform is around 3 €/kg. The value assumed in this work is the most conservative estimate found in the most recent work found in literature. More accurate values would require an accurate market study and a detailed manufacturing analysis, beyond the scope of a preliminary design assessment. Considering the assumed relation between brace height and length, $l/H^2 = 1.22\ \mathrm{m}^{-1}$, the cost of the braces, C_{TB}, can be expressed as

$$C_{\mathrm{TB}} = c_{TB}\left(W_{braces,REF} + 3 \cdot 4\sqrt{\frac{l}{1.22}}\ t\ (l - l_{REF})\,\rho_s\right) \tag{5.19}$$

which only depends on the brace length. The initial cost, $C_{\mathrm{TB},0}$, is assumed equal to the above expression with $l = l_0 = 26$ m.

Cost variation of mooring lines

The cost of the mooring line can be expressed, according to [75], as

$$C_{\mathrm{lines}} = 3 \cdot (0.0591 \times \mathrm{MBL} - 89.69)\ l_{\mathrm{C}} \tag{5.20}$$

with MBL Minimum breaking load and l_{C} chain length. The original unstretched length is equal to 610 m and is associated to the assumed initial cost of a chain line $C_{\mathrm{lines}0}$.

5.3.3 Optimization target function and constraints

As stated above, the main objective of the design process is to find a configuration with a natural yaw period closer to a target value, trying tho improve the motion response for wake mixing. The first part of the objective function will thus represent the percentage difference of the natural frequency with respect to target frequency, which is defined as follows

$$\Delta f = \frac{\left(f_{\mathrm{peak}} - f_{\mathrm{target}}\right)}{f_{\mathrm{target}}} \tag{5.21}$$

The natural frequency is determined finding the PSD peak of the yaw free decay time simulation. A second term is introduced in the coat function to account for

cost variation from the reference configuration value. The two terms of the target function are summed up after multiplication by a weighting constant, which allows to vary the relative importance of the two optimization goal (targeting the desired natural frequency and avoid excessive cost variations). The complete expression of the optimization target function here introduced will be reported in more detail later.
The static limits to surge excursion and heeling angle are imposed as constraints to the optimization search algorithm. Once the hydrostatic stiffness matrix has been calculated in the pre-processing phase, the values of heeling and surge at rated thrust are evaluated and the configurations not complying with the limiting values are rejected, before running the free decay time simulation.

5.3.4 Simulations setup and response analysis

The simulations setup for the first implementation of the optimization framework, similarly to the assumptions made in the preliminary analysis, is the following:

- still air;
- still water;
- deactivated control system;
- fixed rotor;
- constant force along the rotor shaft axis, modelling the rated thrust of the rotor.

The procedure to obtain f_{peak} can be described as follows:

1. A given displacement (5 deg) on the yaw DOF is imposed as the initial condition.
2. A simulation time equal to 1800 s is assumed.
3. A frequency domain analysis of the free decay response is performed, determining the PSD frequency peak(f_{peak}) for the yaw motion.

5.3.5 Design space exploration – Design of Experiments

In a first phase of the optimization study, a limited set of simulations was carried out trying to explore a wide combination of the input variables with the "latin hypercube sampling method", first described by [120]. The characteristics of the "latin hypercube sampling method" can be described as follows,

1. For each design variable (say we have k variables), the design space is divided into N intervals.

2. The design space would be represented completely by N^k combinations of design variables.

3. "Latin hypercube sampling method" selects N combinations in the design space which do not present repetitions of the same values for each design variable, as shown in Fig. 5.26.

Instead of performing N^k simulations to cover the entire design space, sufficient information can be extracted from only N simulations. This exploration had two

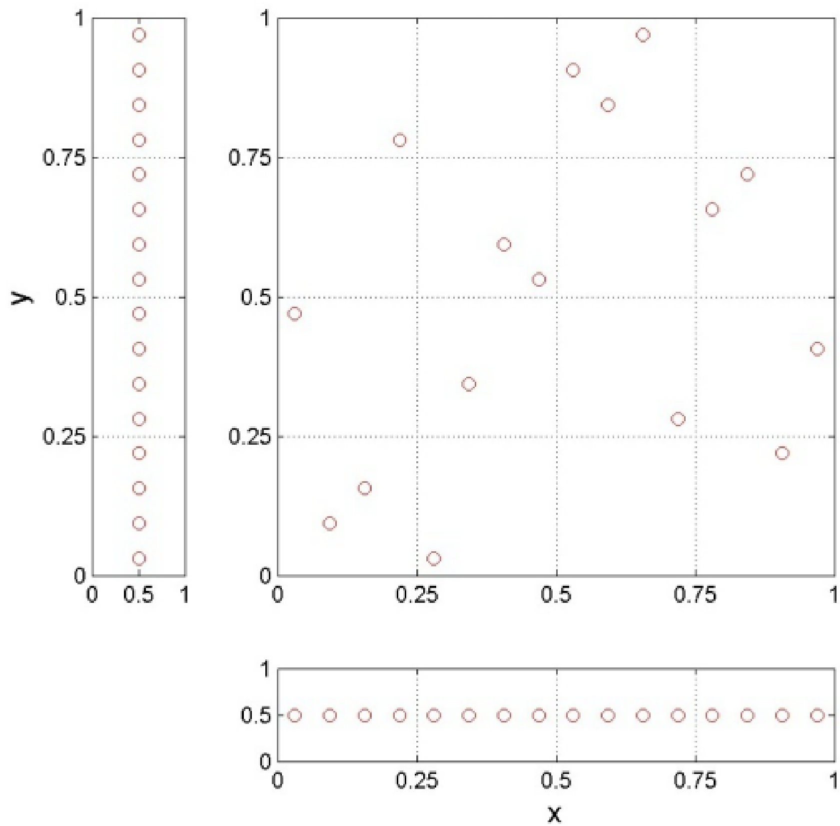

Figure 5.26: Latin Hypercube Sampling in a design space composed by 2 design variables (x and y) with 16 intervals. From [121].

main objectives:

- find trends of the output variables that would indicate the possibility to find an optimum, as a validation of the preliminary analyses on the mooring system and to check the possible effects of added configuration variables;

- find appropriate range of the selected input variables.

The results of the DoE analysis are shown in Fig. 5.27 as a correlation matrix. A legend of the quantities represented in the figure is given below in Table 5.6.

Table 5.6: Legend of DoE correlation matrix shown in Fig. 5.27.

Name in Correlation Matrix	**Variable**	**Units**
Anchor Radius	x_{A}	m
LineLengthFactor	MLLF	-
SparDistance	x_{S}	m
Surge	$\Delta x_{\mathrm{rated}}$	m
Heel Mean	$\Delta\theta_{y,\mathrm{rated}}$	deg
FreqObjFunc	Δf	Hz
DeltaChainCost	$\frac{\lvert C_{\mathrm{lines}}-C_{\mathrm{lines}\,0}\rvert}{C_{\mathrm{lines}\,0}}$	-
DeltaBracesCost	$\frac{\lvert C_{\mathrm{TB}}-C_{\mathrm{TB},0}\rvert}{C_{\mathrm{TB},0}}$	-

The diagonal plots in the correlation matrix represent the distribution of each variable. As expected, the input variables seem equally distributed in the design space, but a lack of simulations with high values of the line length factor (values higher than 1.10) appears. This is due to the check on the constraint on the surge excursion, applied in the run scheduling routine before running the simulations: only configurations with surge lower than 50 m were simulated and configurations with high values of the MLLF present excessively slack moorings. This can also be seen in the plot relating MLLF and surge, which indicates that MLLF should be limited to prevent large values of surge. A small number of individuals with MLLF > 1.10 was simulated anyway, which all present decreasing value of the anchor radius. These considerations seem important because of the (negative) correlation between MLLF and the yaw natural frequency, which can be seen in the MLLF $-\ \Delta f$ plot, which clearly indicates that the target frequency can only be reached with high values of MLLF. This means that in order to reach the desired natural frequency, one must accept a compromise on surge excursion, or conversely that the yaw natural frequency can only be approached but never reached if the constraint on surge is satisfied. With regards to the anchor radius, there is no significant correlation with output variables, apart from the trivial correlation with the cost of moorings. This is because the slack level of the moorings is directly related to the ratio between the length and the distance between the fairlead and the anchor. A slightly significant correlation exists between the spar distance and the target frequency. It arguably seems that the target frequency can only be reached with values of the spar distance higher than 30 m. Given the necessity of taking into account also the increase of costs due to braces, this means that a slight increase on costs will be necessary to reach the desired frequency. As regards the other possible constraint, that is the heel angle, all the simulations returned values that far below the limit (5 deg), indicating that any configuration in the explored design space is compliant in terms of heel angle.

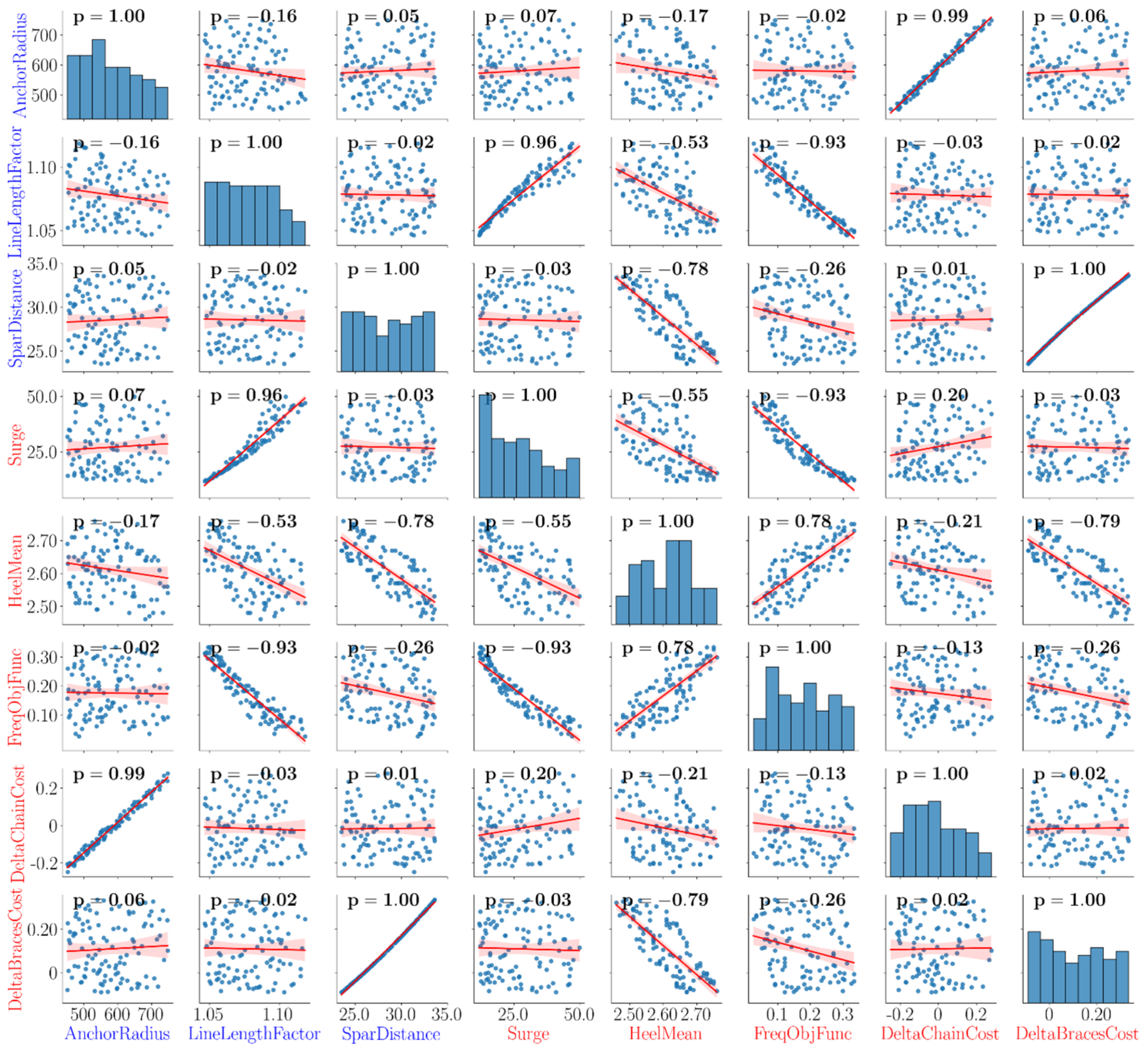

Figure 5.27: Correlation matrix of the input (blue) and output (red) variables of 107 simulations carried-out to explore the range of the design space and the trends of the output variables. Anchor radius, spar distance, surge are in [m], line length factor, frequency objective function and the variation of costs are non-dimensional. Mean heel angle is in degrees. The shaded area around the regression line represents the confidence interval of the regression with respect to the scattered data, using a binned discretization of the independent values, see [122].

5.3.6 Optimization cost function including both natural frequency and tripod-mooring costs

The complete objective function, including the cost of the tripod brace and moorings together with the target natural frequency can be represented by the following expression:

$$F_{\text{obj.}} = w_f \frac{\left(f_{\text{peak}} - f_{\text{target}}\right)}{f_{\text{target}}} + w_C \left[\frac{|C_{\text{lines}} - C_{\text{lines,0}}|}{C_{\text{lines,0}}} + \frac{|C_{\text{TB}} - C_{\text{TB,0}}|}{C_{\text{TB,0}}}\right] \tag{5.22}$$

The weighting factors, w_f, w_C can be introduced in order to account for a different "importance" attributed to each of the two components of the target function (natural frequency, costs). As regards the costs, the minimization of the target function will lead to a solution that is still close to the reference one (trying to minimize the absolute value of the difference in costs). This is done to avoid solutions with excessively different structural safety margins both for the platform structure and for the mooring lines.

5.3.7 Optimization framework

Due to the number of design variables and the non-linearity of the output objective function, a heuristic method was chosen to find the best-performing platform geometry/mooring lines combination. The aforementioned differential evolution scheme implemented in the Scipy Python™ module was chosen (which was implemented based on the theoretical work presented in [93]). The differential evolution algorithm is a stochastic population-based method used for global optimization problems. The algorithm creates a series of initial candidate solutions trying to encompass all the design space (latin hypercube method), then at each iteration it generates new candidate solutions by mixing some selected candidates (cross-over) with each other or stochastically modifes the design variables of some selected individuals (mutation), using a selection criterion based on the value of the target function.

5.3.8 Optimization scheme

Two optimizations were carried out with a total number of 30 iterations for each optimization, with 60 individuals created for each iteration. Accounting for a greater interest in enhancing the yawing response, the weighting factors were set as $w_f = 0.70$ and $w_C = 0.30$ for the first optimization, and as $w_f = 0.90$ and $w_C = 0.10$ for the second one. The assumed design variables, the considered constraints and the overall optimization scheme are represented in Fig. 5.28. As mentioned above, a check on the constraint on surge was applied before running the simulations to speed-up the process, as already seen in the case of the DoE analysis. The constraint relations are applied as defined in Equation 5.2 and 5.3.

When the constraints are not satisfied, a very large value (around 1000) of the objective function is assigned to the individual (representing a "penalty" in the optimization process). These "penalized" individuals were very common at the beginning of the optimization run, but they disappear almost completely after 3-4 iterations.

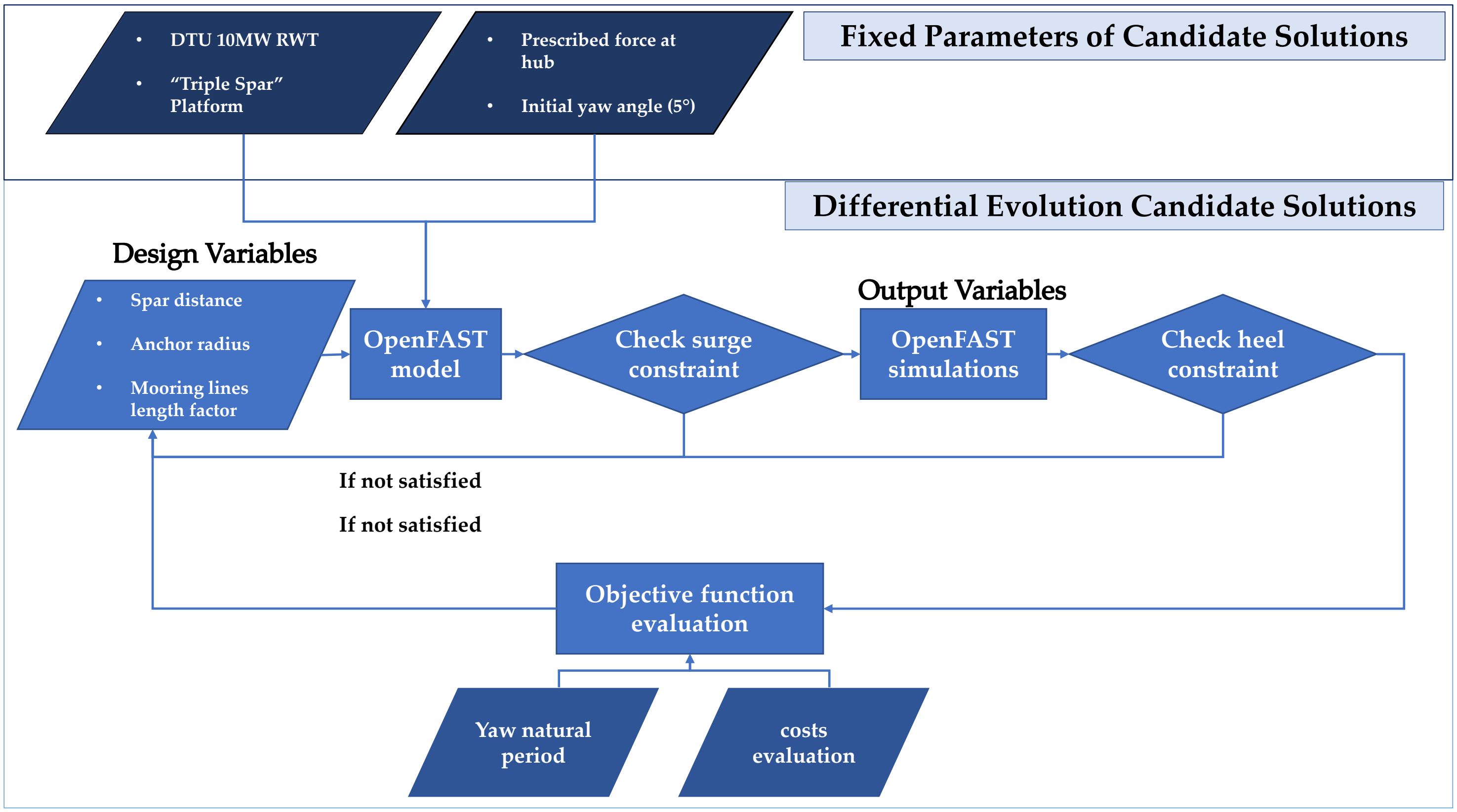

Figure 5.28: Optimization scheme with indication of operations performed for the evaluation of the objective function for each candidate solution inside the differential evolution algorithm.

5.3.9 Optimization results

First optimization run

This subsection describes the first optimization test run, performed with weighting factors of the optimization target function respectively equal to $w_f = 0.70$ and $w_C = 0.30$. At each iteration the best performing candidate was selected automatically by the algorithm. The evolution of the best candidates for each iteration is shown in Figure 5.29. The optimization process was performed on a Intel® Core™ i7-3770 CPU @ 3.40GHz employing 6 cores and taking up to 5 days to complete. The combination of design variables with output variables is shown for each generated candidate solution (every solution is a single dot) in Fig. 5.30. The unfeasible solutions have been excluded from the analysis. The darker dots represent solutions with low (optimized) values of the objective function. In the first row (from above) of the figure the clouds of points are thicker around the starting value of anchor distance, which means that the costs of mooring lines are kept close to those of the initial configuration. In the second row, observing the darker rows of points, it is clear that the objective function is minimized only with MLLF close to 1.08, which leads to the consideration that the slack level of the mooring system has the most effective impact on the yaw natural period, at least for this floating platform-mooring lines configuration. In the second plot of the third row, we can observe the presence of a front limiting to the right the yaw natural frequency with respect to the spar distance. It can be noted that, as already highlighted from the DoE analysis, the search algorithm can not reach a configuration with the desired yaw natural frequency unless the spar distance is increased. Table 5.7 lists the main characteristics of the initial and final configuration. As already seen in the DoE the MLLF is increased by 1.9% in order to decrease the yaw natural frequency (or conversely to increase the period). Meanwhile the anchor radius is decreased by 2.2% and the spar distance is increased by 0.05%. As it can be seen from the last row in Table 5.7, the mooring line length is unvaried, which means that the optimization seems governed by the minimization of the difference in costs of the mooring lines. The cost of braces is increased by 0.5% due to the larger distance of the spars from the yaw axis.

Second optimization run

In this paragraph a second optimization run with $w_f = 0.90$ and $w_C = 0.10$ is described. Given the higher weighting factor assigned to the frequency objective function, a final value of the yaw natural period closer to the target one (100 s) was reached. Surprisingly, the mooring line length factor converges to exactly the same value as the first optimization. Slacker moorings are necessary to increase yaw natural period. The optimization process also tends to keep the cost of the moorings as similar as possible to the baseline one. To do this and to reach the desired mooring line length factor, the optimization process modifies both the anchor distance and the spar distance to keep the mooring line length constant, while increasing the MLLF.

5.4 Motion amplitude optimization

The results obtained through the first optimization runs rely on the assumption that the yaw motion of the platform is amplified when the natural frequency of the floater/mooring system matches the desired excitation frequency. The

Table 5.7: Design variables and output variables of starting and final configurations, first optimization results.

Design variables	**Start Config.**	**Final Config.**
Platform		
Spar distance from yaw axis (x_{S})	26 m	26.12 m
Moorings		
Mooring line length factor (MLLF)	1.057	1.077
Anchor distance from yaw axis (x_{A})	600 m	586.84 m
Output variables		
Objective function ($F_{\text{obj.}}$)	0.212	0.134
Frequency objective function (Δf)	0.212 Hz	0.188 Hz
Yaw natural period (T_{yaw})	78.8 s	81.2 s
Delta chain costs $\left(\frac{\lvert C_{\text{lines}} - C_{\text{lines},0}\rvert}{C_{\text{lines},0}}\right)$	-	-0.3%
Delta braces costs $\left(\frac{\lvert C_{\text{TB}} - C_{\text{TB},0}\rvert}{C_{\text{TB},0}}\right)$	-	+0.5%
Surge excursion with rated thrust (Δx_{rated})	15.3 m	25.0 m
Heel angle with rated thrust ($\Delta\theta_{y,\text{rated}}$)	2.04 deg	2.95 deg
Mooring Line Length (l_{C})	609.87 m	609.61 m

Table 5.8: Design variables and output variables of starting and final configurations, second optimization results.

Design variables	**Start Config.**	**Final Config.**
Platform		
Spar distance from yaw axis (x_{S})	26 m	33.68 m
Moorings		
Mooring line length factor (MLLF)	1.057	1.077
Anchor distance from yaw axis (x_{A})	600 m	592.41 m
Output variables		
Objective function ($F_{\text{obj.}}$)	0.212	0.150
Frequency objective function (Δf)	0.212 Hz	0.129 Hz
Yaw natural period (T_{yaw})	78.8 s	87.1 s
Delta chain costs $\left(\frac{\lvert C_{\text{lines}} - C_{\text{lines},0}\rvert}{C_{\text{lines},0}}\right)$	-	-0.6%
Delta braces costs $\left(\frac{\lvert C_{\text{TB}} - C_{\text{TB},0}\rvert}{C_{\text{TB},0}}\right)$	-	+33.8%
Surge excursion with rated thrust (Δx_{rated})	15.3 m	25.0 m
Heel angle with rated thrust ($\Delta\theta_{y,\text{rated}}$)	2.04 deg	2.49 deg
Mooring Line Length (l_{C})	609.87 m	609.61 m

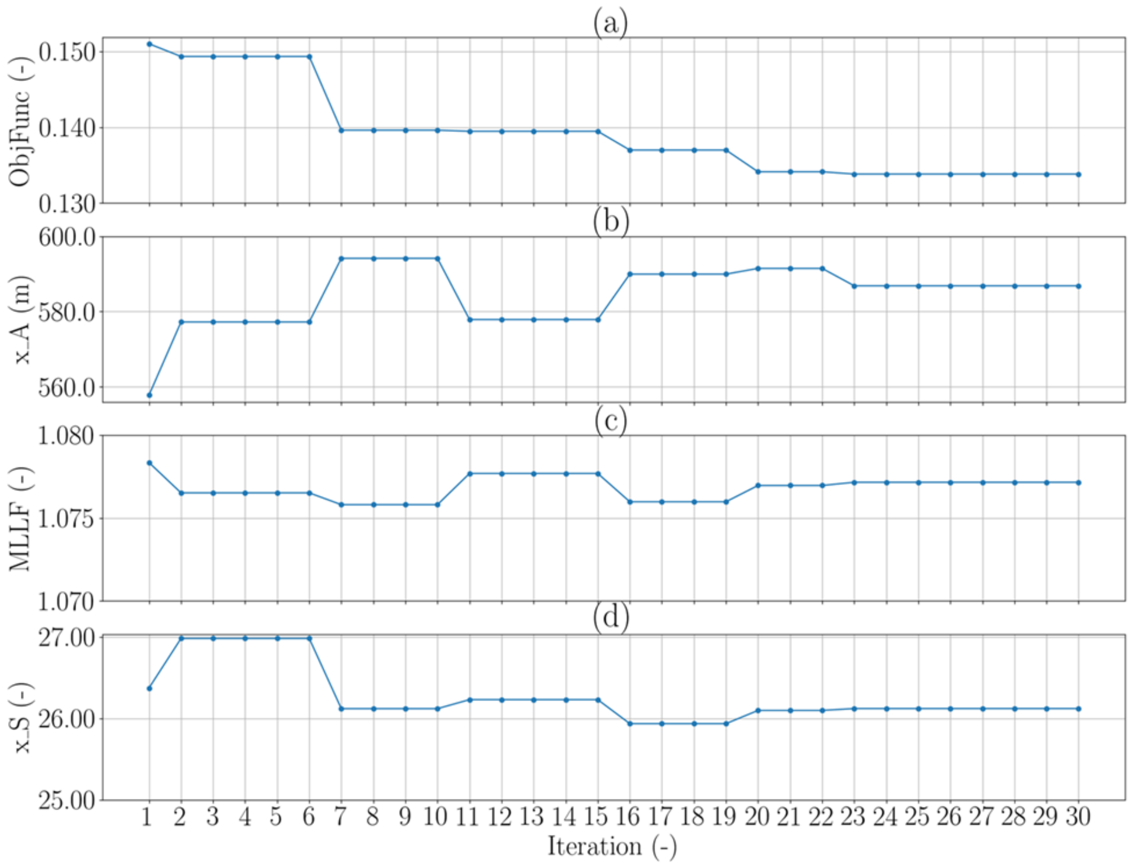

Figure 5.29: Evolution of each iteration best candidates design variables and objective function evaluations. The optimization has been stopped after 30 iterations for computational time reasons, even if it appears that some margin of objective function minimization is still present.

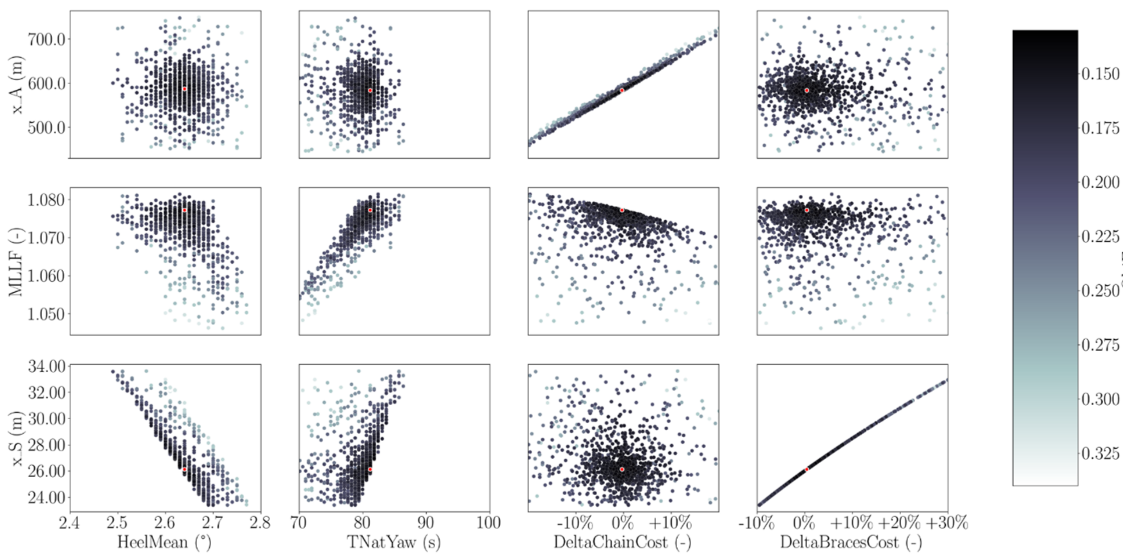

Figure 5.30: Combination of design variables (y-axis) and output variables (x-axis) of each individual generated by the genetic algorithm that satisfied the constraints. Each coloured dot represents an individual. The colour of each dot represents the objective function value of the individuals, the darker the dot, the lower is the objective function value, as indicated in the color-bar on the right. Red dots represent the best performing individuals of the 30 iterations (actually merged into one point because of small variations).

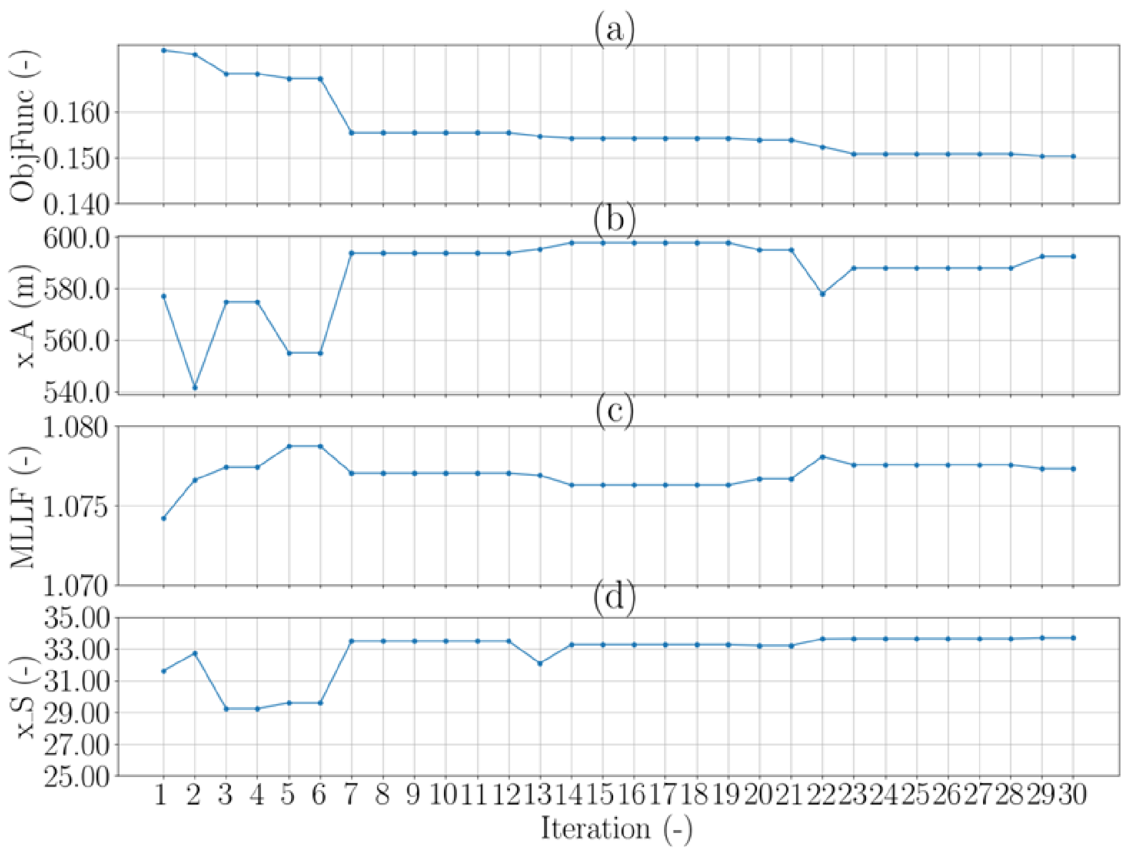

Figure 5.31: Evolution of each iteration best candidates design variables and objective function evaluations. The optimization has been stopped after 30 iterations for computational time reasons, even if it appears that some margin of objective function minimization is still present.

actual amplitude of the motion is now considered, taking into account not only the exciting frequency requirement but also the damping of the system, which may play a fundamental role in the dynamics at the natural frequency. To obtain the forced motion of the system, with a slight increase in the complexity of the simulation model, a time-varying periodic yaw moment was applied at the tower-top with an assigned time history, simulating the effect of the chosen control logic ("helix strategy") on the loads applied to the rotor. The individual pitch-control is able to generate a yaw moment which is transferred from the rotor shaft to the nacelle and finally from the nacelle-tower connection to the tower top. This moment induces a yaw motion in floating offshore wind turbines. The yaw moment time history shown in Fig. 5.32 is added as an independent load at the tower top, together with a fixed thrust. The uncoupled superposition of the effects generated by the two independent loads is assumed to evaluate the amplitude of yaw motion and surge displacement, no coupling between the loads and motions has been modelled so far. All loads described here and shown in Fig. 5.33 are applied to the same wind turbine baseline configuration as in the previous analyses.

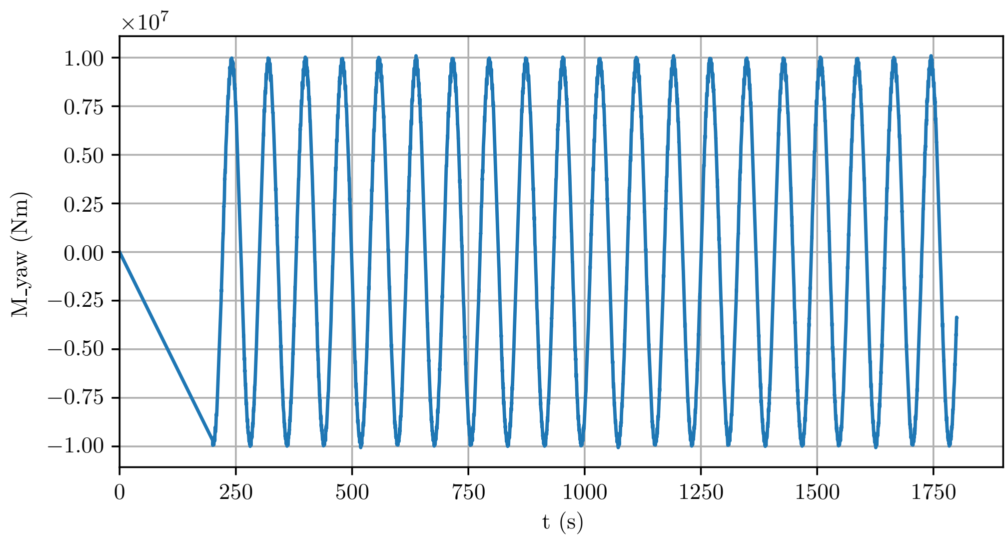

Figure 5.32: Yaw moment time history for the model for yaw amplitude maximization.

5.4.1 Optimization cost function including both yaw amplitude and tripod-mooring costs

A different objective function is used in this approach. The complete objective function, including the cost of the tripod brace and moorings together with the

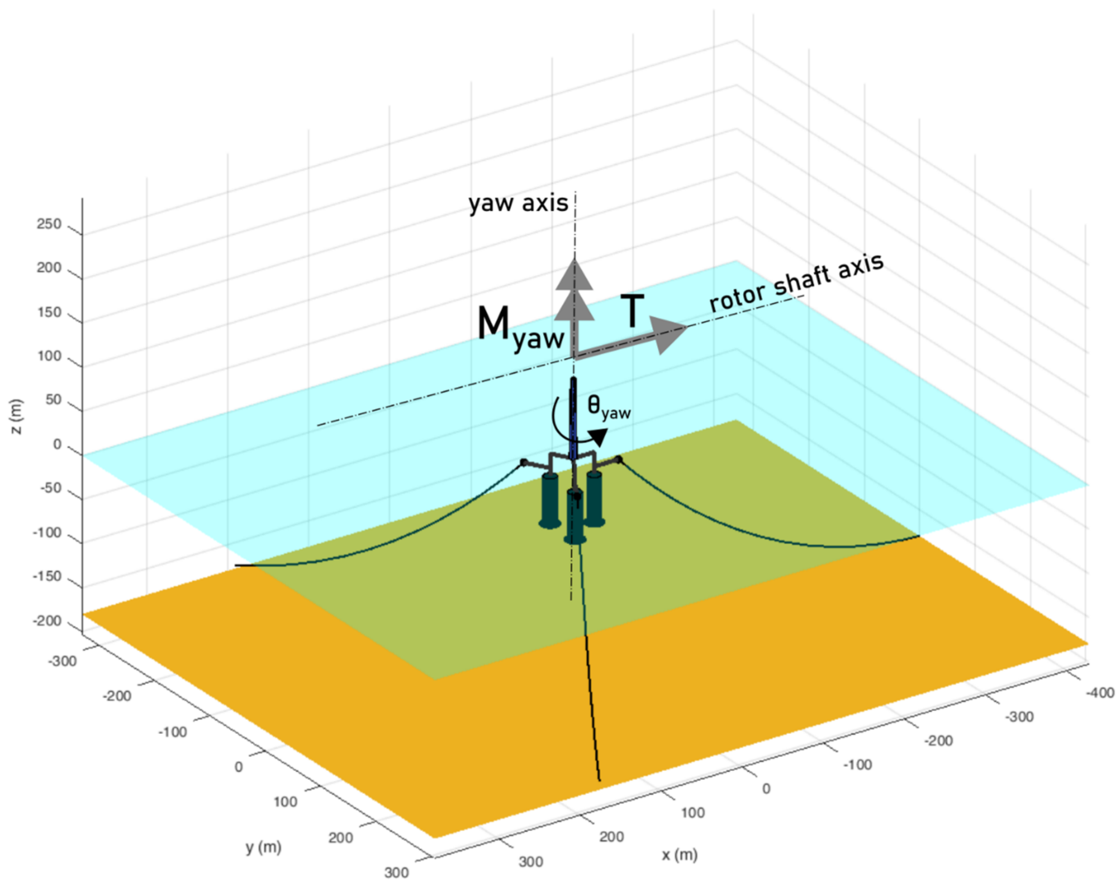

Figure 5.33: Baseline configuration with thrust and yaw moment applied in the model simulated in the motion amplitude optimization. The rotor and nacelle are not shown for best visualization of the loads.

maximization of yaw amplitude, can be represented by the following expression:

$$F_{\text{obj.}} = w_f \frac{1}{\Delta\theta_{z,\text{peak}}} + w_C \left[\frac{|C_{\text{lines}} - C_{\text{lines},0}|}{C_{\text{lines},0}} + \frac{|C_{\text{TB}} - C_{\text{TB},0}|}{C_{\text{TB},0}} \right] \tag{5.23}$$

The first part of the objective function allows the maximization of the yaw motion. The procedure to evaluate the term $\Delta\theta_{z,\text{peak}}$, representing the maximum yaw oscillation amplitude, is described in the next paragraph. As regards the costs, the same considerations done for the optimization scheme previously described are valid.

5.4.2 Simulations setup and response analysis

The simulations setup for the optimization of yaw amplitude motion are the following:

- still air;
- still water;
- deactivated control system;
- fixed rotor;
- constant force applied along the rotor shaft axis, modelling the rated thrust of the rotor;
- periodic yaw moment applied to the tower top from 200 s to the end of simulation, resembling the loads generated by the chosen control strategy.

The procedure to obtain $\Delta\theta_{z,\text{peak}}$ can be described as follows:

1. A simulation time equal to 1800 s is assumed.
2. A frequency domain analysis of the yaw response in the last 800 s is performed, determining the normalized Fourier transform of the signal. The peakvalue is stored for each simulation (the aforementioned $\Delta\theta_{z,\text{peak}}$) representing the maximum amplitude of the yaw motion at the "steady" periodic state due to the yaw moment excitation.

5.4.3 Optimization results

Two optimization runs were carried out with a total number of 50 iterations for each optimization, with 60 individuals created for each iteration. Accounting for a greater interest in enhancing the yawing response, the weighting factors were set as $w_f = 0.90$ and $w_C = 0.10$ for the first optimization, and as $w_f = 1.00$ and $w_C = 0$ for the second one.

First optimization run (with imposed tower-top yaw moment)

In this paragraph the main results of the first optimization run (with $w_f = 0.90$ and $w_C = 0.10$) are described. At each iteration the best performing candidate was selected automatically by the algorithm. The evolution of the best candidates for each iteration is shown in Fig. 5.34. The optimization process was performed on a Intel® Core™ i9-10940X CPU @ 3.30GHz employing 12 cores and taking up to 2 days to complete. The combination of design variables with output variables is shown for each generated candidate solution (every solution is a single dot) in Fig. 5.35. The unfeasible solutions, not complying with the assumed constraints, have been excluded from the analysis. The lighter dots represent solutions with low (optimized) values of the objective function. Table 5.9 lists the main characteristics of the initial and final configurations.

Table 5.9: Design variables and output variables of starting and final configurations, first optimization (with tower-top yaw moment) results.

Design variables	**Start Config.**	**Final Config.**
Platform		
Spar distance from yaw axis (x_S)	26 m	26 m
Moorings		
Mooring line length factor (MLLF)	1.057	1.075
Anchor distance from yaw axis (x_A)	600 m	589.23 m
Output variables		
Objective function ($F_{\mathrm{obj.}}$)	0.113	0.075
Yaw amplitude objective function	0.113	0.075
Yaw amplitude	7.9 deg	12.0 deg
Delta chain costs $\left(\frac{\lvert C_{\mathrm{lines}} - C_{\mathrm{lines},0}\rvert}{C_{\mathrm{lines},0}}\right)$	-	-0.02$\%$
Delta braces costs $\left(\frac{\lvert C_{\mathrm{TB}} - C_{\mathrm{TB},0}\rvert}{C_{\mathrm{TB},0}}\right)$	-	-0.02$\%$
Surge excursion with rated thrust ($\Delta x_{\mathrm{rated}}$)	15.3 m	24.0 m
Heel angle with rated thrust ($\Delta\theta_{y,\mathrm{rated}}$)	2.04 deg	2.75 deg
Mooring Line Length (l_C)	609.87 m	609.75 m

Second optimization run (with imposed tower-top yaw moment)

In this paragraph the main results of the second optimization run (with $w_f = 1.0$ and $w_C = 0$) are described. At each iteration the best performing candidate was selected automatically by the algorithm. The evolution of the best candidates for each iteration is shown in Fig. 5.36. The optimization process was performed on a Intel® Core™ i9-10940X CPU @ 3.30GHz employing 12 cores and taking up to 2 days to complete. The combination of design variables with output variables is shown in Fig. 5.37 for each generated candidate solution (every solution is a single

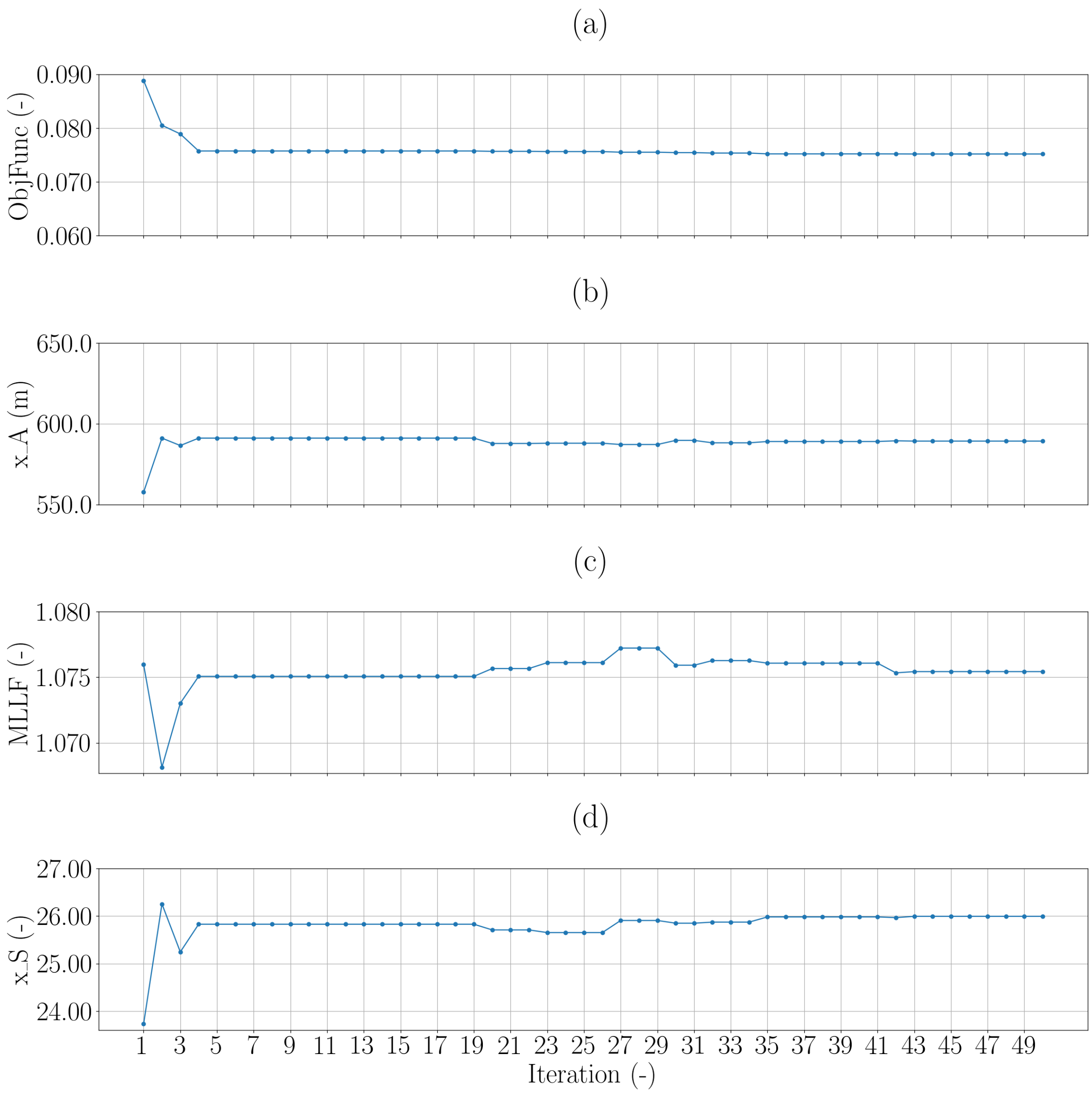

Figure 5.34: Evolution of each iteration best candidates design variables and objective function evaluations. The optimization has been stopped after 50 iterations for computational time reasons.

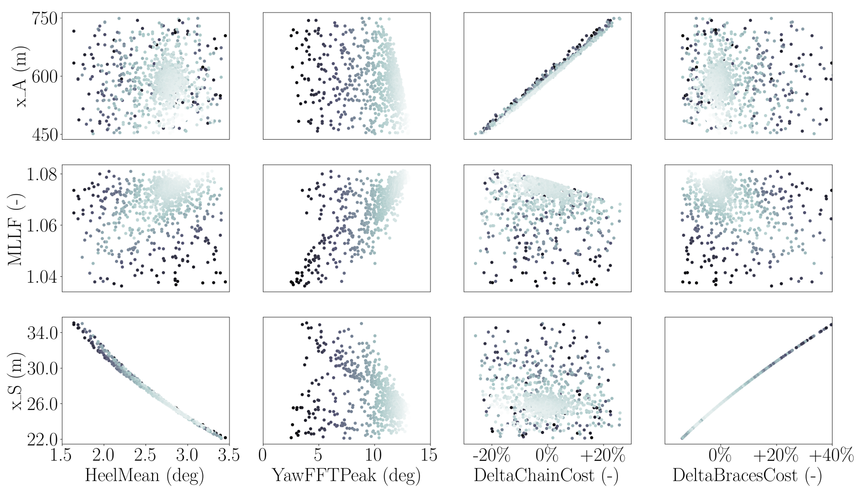

Figure 5.35: Combination of design variables (y-axis) and output variables (x-axis) of each individual generated by the genetic algorithm that satisfied the constraints. Each coloured dot represents an individual. The colour of each dot represents the yaw amplitude associated to the individuals, the lighter the dot, the higher is the yaw amplitude, as indicated in the color-bar on the right.

dot). The unfeasible solutions have been excluded from the analysis. The lighter dots represent solutions with low (optimized) values of the objective function. Table 5.10 lists the main characteristics of the initial and final configuration.

5.4.4 Discussion of the assumptions and of the results of motion amplitude optimization scheme

Summarising what was previously reported, the second approach to the optimization procedure presented in the last paragraphs has two main advantages compared to the preliminary optimization approach:

- on the one hand, it provides a slight improvement in the modelling accuracy of the control action, directly accounting for the actual input yaw moment related to the adopted control strategy, instead of considering the free decay response. Anyway, the model is still significantly simplified (still water, fixed thrust force), due to the large number of runs with limited computational resources;
- this approach allows the evaluation of the motion response amplitude, for a given frequency and amplitude of the exciting input yaw moment, instead of simply looking for a desired peak frequency, thus giving more information to

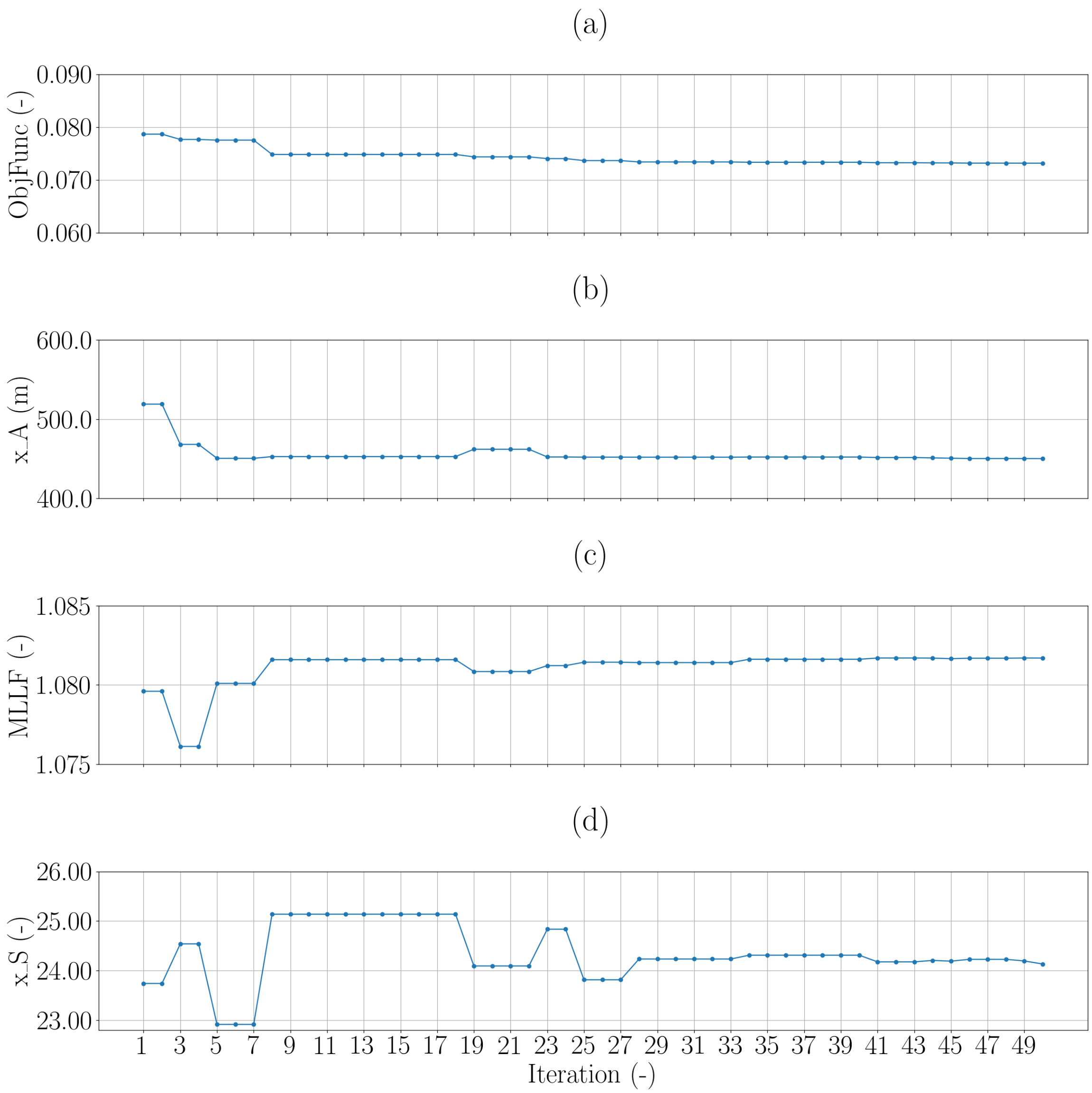

Figure 5.36: Evolution of each iteration best candidates design variables and objective function evaluations. The optimization has been stopped after 50 iterations for computational time reasons.

Table 5.10: Design variables and output variables of starting and final configurations, second optimization (with tower-top yaw moment) results.

Design variables	**Start Config.**	**Final Config.**
Platform		
Spar distance from yaw axis (x_S)	26 m	24.1 m
Moorings		
Mooring line length factor (MLLF)	1.057	1.082
Anchor distance from yaw axis (x_A)	600 m	451.6 m
Output variables		
Objective function ($F_{\mathrm{obj.}}$)	0.125	0.073
Yaw amplitude objective function	0.125	0.073
Yaw amplitude	7.9 deg	13.6 deg
Delta chain costs $\left(\frac{\lvert C_{\mathrm{lines}}-C_{\mathrm{lines},0}\rvert}{C_{\mathrm{lines},0}}\right)$	-	-21.7%
Delta braces costs $\left(\frac{\lvert C_{\mathrm{TB}}-C_{\mathrm{TB},0}\rvert}{C_{\mathrm{TB},0}}\right)$	-	-6.9%
Surge excursion with rated thrust $(\Delta x_{\mathrm{rated}})$	15.3 m	25.0 m
Heel angle with rated thrust $(\Delta\theta_{y,\mathrm{rated}})$	2.04 deg	3.08 deg
Mooring Line Length (l_C)	609.87 m	475.0 m

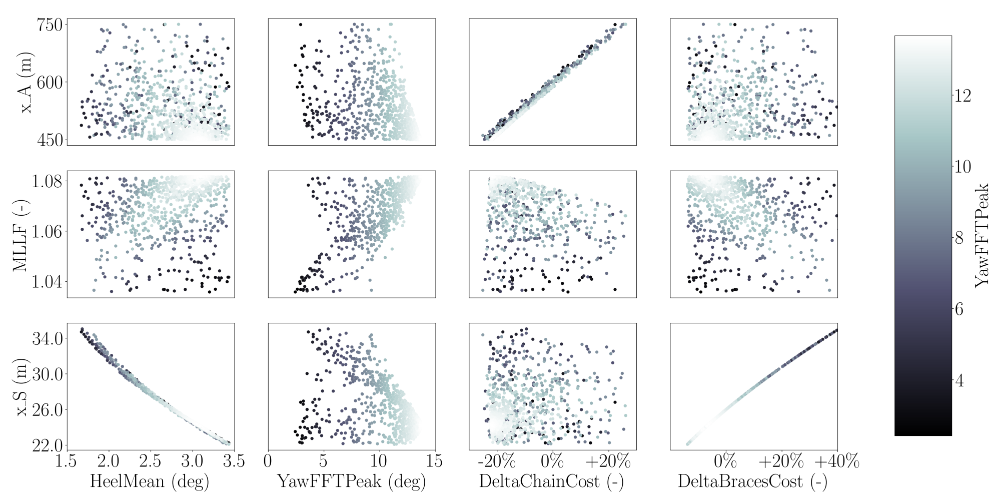

Figure 5.37: Combination of design variables (y-axis) and output variables (x-axis) of each individual generated by the genetic algorithm that satisfied the constraints. Each coloured dot represents an individual. The colour of each dot represents the yaw amplitude associated to the individuals, the lighter the dot, the higher is the yaw amplitude, as indicated in the color-bar on the right.

evaluate the effectiveness of the control strategy to be optimized in the next development of the work.

Observing the results of the two presented optimization runs, the following consideration may be drawn:

- as already observed from the preliminary optimization runs, the parameters related to the mooring line configuration seem to have a major impact on the response related part of the objective function, especially when the cost is accounted for in the optimization.
- As it can be seen in the first optimization run, despite the relatively low weight attributed to the cost target ($w_c = 0.10$), the geometry of the platform (i.e. the spar distance from yaw axis) is practically unchanged between the initial and final (optimized) configurations, while the mooring line length factor (MLLF) and the anchor distance from yaw axis (x_A) show more significant changes.
- In the second run, where no cost constraint is applied ($w_c = 0$), a larger variation of the platform geometry can be seen, with a somehow surprising reduction of the mooring and platform costs. It has to be remembered that the cost target in the objective function has been defined as a cost variation from the baseline configuration. Thus the minimization of this component of the objective function tends to reduce the cost variations from the initial configuration, both in increase and in reduction. This is necessary because the cost variations estimates are based on scaling reasoning around the initial configuration: getting too far from the initial configuration reduces the accuracy of the assumed cost model. When the weight of cost in the objective function is set to zero, as is in this case, the optimization algorithm explores also solutions further from the starting point. In this sense the optimization procedure finds a significantly larger reduction of costs (anyway it has to be noted that, probably, cost estimations are less accurate, when large differences from the starting point are considered).
- Thus, two configurations are presented,
  1. one essentially based only on a mooring line configuration change (first run), which is probably more reliable, as closer to the original platform geometry;
  2. one with a significant reduction in cost, but with larger geometry variation from the initial configuration and thus potentially less reliable, due to the larger difference from the original geometry.

–6–
Design issues in developing an innovative semisubmersible platform

Research has concentrated on solutions for large (MW scale) wind turbines, while small and medium size wind turbines have been largely left outside the radar. Wind farms composed by small and medium size wind turbines may even represent the best compromise between a sufficient green energy supply and a low environmental impact for Mediterranean islands, as shown for example in the optimal patterns for energy supply of small greek islands in [6]. A scalable new conceptual design of a semi-submersible platform for FOWTs is presented in this section. The aim is to search for a configuration which, in a later phase of optimization, would be scalable to small, medium and large wind turbines, in a site which is representative of the Mediterranean coastlines. To reduce the development costs of a prototype model, an existing and commercially available wind turbine is considered. This choice has two main objectives:

1. to reduce design costs by eliminating the need to design the wind turbine and allowing research efforts to be concentrated on the innovative part of the study, that is the development of the floating platform;

2. increase the reliability of the system, using a technological solution already tested in onshore applications.

The criteria for selecting the wind turbine which have been considered in this work are

- the limitation of rated power;

- the limitation of the overall size of the system (to decrease the cost and so to increase the chances of a possible realization of an intermediate size prototype);

- consistency with the metocean characteristics of the site of possible installation.

In particular, a small-size wind turbine, with rated power of 60 kW and rated wind speed 10 m/s, was selected to prove the concept, of a newly developed platform configuration, to be used in a possible demonstrator installation. The choice of this small size turbine is mainly motivated by the availability of data for the chosen wind turbine and the reduction of costs for a preliminary test prototype in a real sea environment (see main properties in Table 6.1, where the rotor thrusts already include safety factors from [70]). These characteristics are, in fact, compatible with features typically used in mini-wind turbine installation sites with moderate speeds (with annual averages in the order of 5-6 m/s) as expected for the area of possible installation.

Table 6.1: Properties of selected wind turbine.

Dimension	Symbol	Value	Units
Rated power	P_{rated}	60	kW
Rated thrust (onshore calculations)	T_{rated}	19	kN
Maximum thrust (onshore calculations)	$T_{\max}$	44	kN
Parked rotor thrust (onshore calculations)	$T_{\max}$	39.6	kN
Rated wind-speed	$V_{\text{w,rated}}$	10	m/s
RNA mass	m_{RNA}	5.99	t
Tower mass	m_{tower}	6.55	t
Tower length	h_{tower}	22	m
Hub height from tower top	Δh_{hub}	1	m

The height of the tower is reduced compared to the heights typically used for onshore installations to reduce the moment transmitted to the connection between the tower and the floating platform: as a result, both the structural stresses and the tilting actions applied to the platform are reduced, with benefits for costs and safety. This height allows the minimum distance of the blade tip from the access areas to the base of the tower to be respected (as indicated in [70]), but is compatible with the above-mentioned requirements for floating offshore installations.

6.1 Site of installation and metocean conditions analysis

The chosen installation site is characterised by a limited depth (around 40 m) at a short distance from the coast of Tuscany, Italy, in order to reduce the installation and maintenance costs of a possible prototype demonstrator system. The following figure shows a distribution of average annual wind speeds in an area of possible interest (data from the Atlante Eolico Italiano [123]). A typical value for the average wind speed in the proximity of the installation site is $V_{\text{avg.}} = 5.08$ m/s. In order to define the design requirements for the platform, a preliminary analysis

Figure 6.1: Colour map of the average wind speed in the proximity of a candidate installation site for the demonstrator prototype.

of the metocean conditions has been performed. Data has been gathered from the ECMWF public database ERA5. The available data comprise significant wave height $H_{\mathrm{w,S}}$ and peak period $T_{\mathrm{w,P}}$. The sea states considered in the present analysis have a 1-hour duration and the data span a time interval of 12 years. The purpose of the analysis is to evaluate the main statistical characteristics of the local wave climate. Following DNV standard for loads and site conditions [77], the zero-crossing period $T_{\mathrm{w,Z}}$ was estimated from $T_{\mathrm{w,P}}$ in order to apply an extrapolation procedure suggested in the same standard. The following formula was used:

$$T_{\mathrm{w,Z}} = T_{\mathrm{w,P}}\sqrt{\frac{5+\gamma}{11+\gamma}} \tag{6.1}$$

where γ is defined as:

$$\gamma = \begin{cases} 5.0 & \text{if} \quad T_{\mathrm{w,P}}/\sqrt{H_{\mathrm{w,S}}} < 3.6 \\ e^{\left(5.75-1.15T_{\mathrm{w,P}}/\sqrt{H_{\mathrm{w,S}}}\right)} & \text{if} \quad 3.6 < T_{\mathrm{w,P}}/\sqrt{H_{\mathrm{w,S}}} < 5.0 \\ 1.0 & \text{if} \quad 5.0 < T_{\mathrm{w,P}}/\sqrt{H_{\mathrm{w,S}}} \end{cases} \tag{6.2}$$

The time histories of the main quantities of interest are shown in the following Fig. 6.2 and Fig. 6.3, while the joint occurrences are represented in the colored plot shown in Fig. 6.4.

The most frequent sea state is characterized by a significant wave height comprised between 0.5 and 1.5 m and a zero-crossing period comprised in the interval

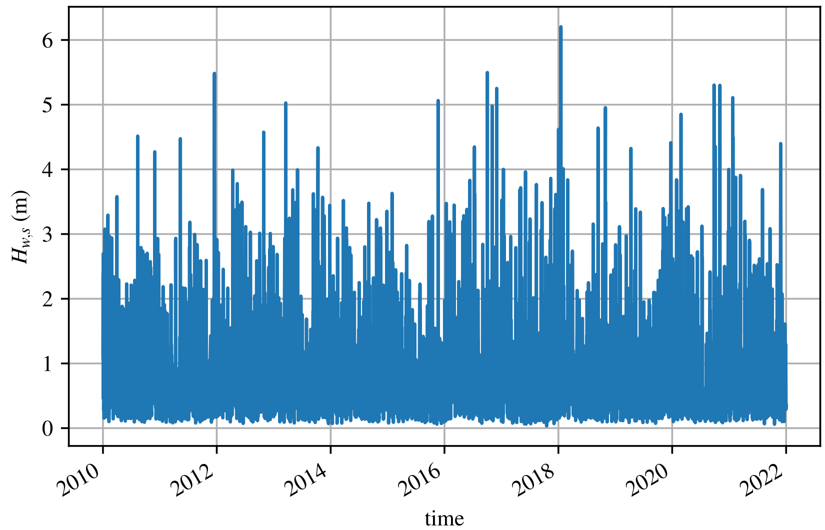

Figure 6.2: Time history of significant wave height from 2010 to 2022 of sea states with a 1-hour duration at the assumed site of installation.

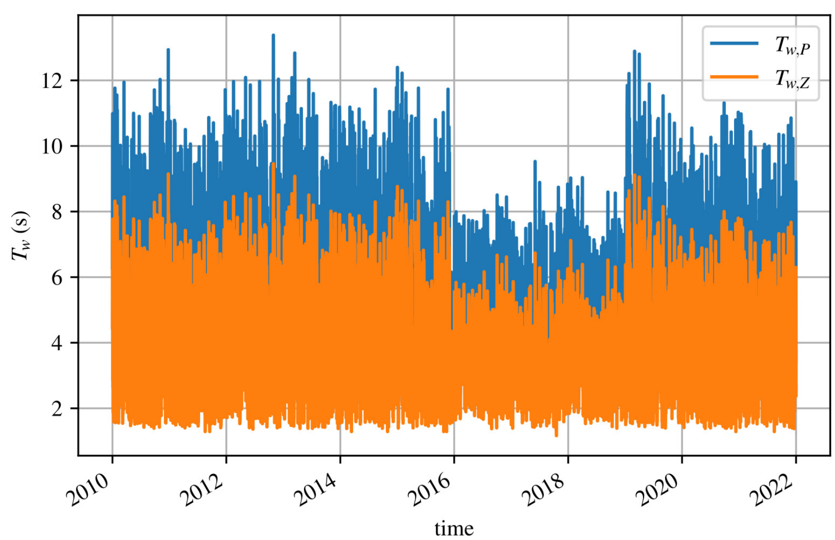

Figure 6.3: Time histories of zero-crossing and peak periods from 2010 to 2022 of sea states with a 1-hour duration at the assumed site of installation.

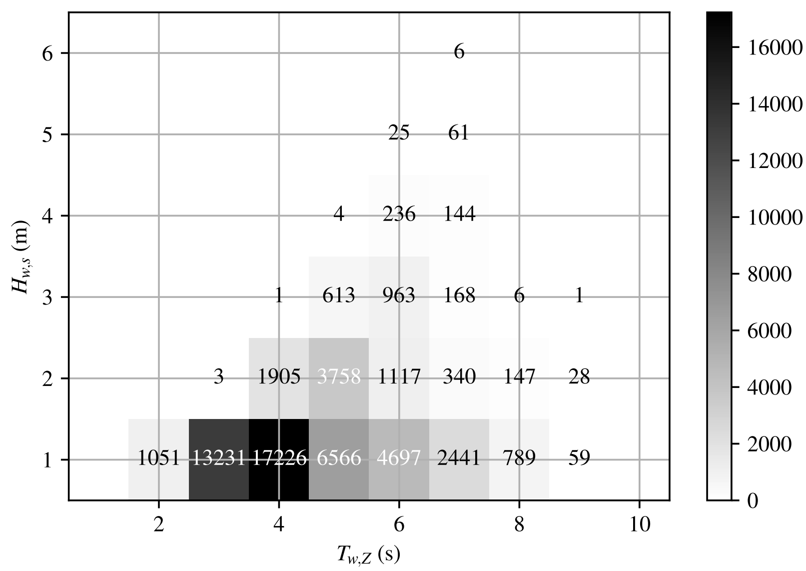

Figure 6.4: Joint occurrence matrix of significant wave height and zero-crossing period in 1 h sea-states from 2010 and 2022. The numbers represent the number of occurrences. Bins have unitary width and height (coloured rectangles have dimensions [1 s;1 m]).

3.5 - 4.5 s. The overall wave climate of the examined site can be represented by the joint statistical distribution of the significant heights, $H_{\mathrm{w,s}}$, and the peak periods, $T_{\mathrm{w,P}}$, or, equivalently, zero-crossing periods, $T_{\mathrm{w,Z}}$. The environmental contour technique has been used to estimate a curve in the $H_{\mathrm{w,s}} - T_{\mathrm{w,Z}}$ plane with a given return period. The "ViroCon" Python™ library has been used [124] to find the statistical distributions and environmental contours. To estimate a contour with given return period, following the approach reported in the standard [77], the IFORM method has been used together with a statistical model relating $H_{\mathrm{w,s}}$ and $T_{\mathrm{w,Z}}$. The statistical model used for the current fitting is a "global hierarchical model" (in which the zero up-crossing period statistical distribution depends upon the significant wave height) recommended by DNVGL and described in section 3.6.3. of [125]. The contours for 1-year and 50-year return periods are shown in the following Fig. 6.5. The 1-year sea-state is not used in this work, but is usually considered in some standards requirements. It can be noted that some of the sea states, which represent observations spanning 12 years, are outside of the 50-year boundary contour, showing a clear inadequacy of the fitting model to the considered site metocean conditions. The shape of the estimated contour and its position with respect to the scattered data is influenced by the method used for its evaluation. Several reasons may contribute to the discrepancy between observed sea states and the environmental contours predicted through the current methodology, visible in Fig.

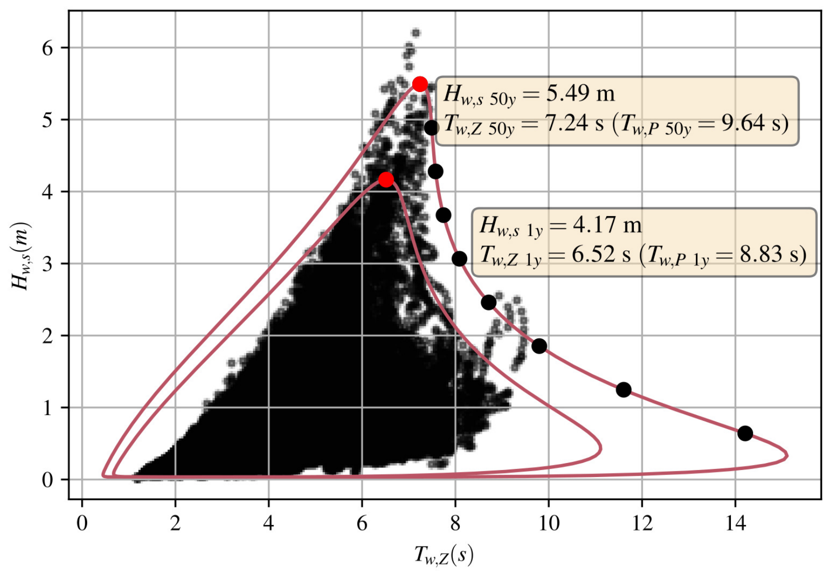

Figure 6.5: Scatter plot of joint occurrences of significant wave height and zero-crossing period in sea-states with a duration of 1 hour from 2010 to 2022 in the selected site, and related environmental contour with 50 years and 1 year return periods. Text boxes indicate the sea-states with the highest significant wave heights on the contours (also shown as red dots).

6.5. As already shown in more recent studies on environmental contour estimation, e.g. [126], the fitting model used in the current work does not include a physical background of the dependence functions which is used to link the zero-up crossing period and significant wave height statistical distributions. This may results in non-conservative values for the maximum values of significant wave height on environmental contours with high return periods (as in Fig. 6.5.) The estimation of an improved environmental contour will be carried-out in a later phase of the project, possibly using sea states which spans more years of observation and an improved definition of the statistical model for the joint distribution, currently not available in literature for the Mediterranean sites, to the knowledge of the writer. Some standard, as [77], suggest a sea state duration of 3 hours and consider a correction to be applied if the available sea state wave height data are obtained for different sea state durations. This correction, which is not shown here for the sake of brevity, has been applied to the values found in the database from [76]. Finally, the 50-year significant wave height for a 3-hour (corrected) sea state was calculated. In the following Table 6.2, the significant wave height and the peak period (needed to generate a wave spectrum) have been selected for two representative sea-states with a duration of 3 hours for the preliminary analyses performed in this work, one representing a sea state with high frequency of occurrency (sea-state **A**) and the other on the contour of 50-year return period with maximum significant wave height (sea-state **B**).

Table 6.2: Corrected 3 hours sea-states selected for preliminary analysis.

Denomination	Type	$H_{\mathrm{w,s}}$	$T_{\mathrm{w,P}}$
A	Normal	0.50 m	4.50 s
B	Extreme	5.13 m	9.64 s

6.2 Description of the system

In this section the most relevant considerations on the preliminary design are shown, following the philosophy of the procedure of Fig. 3.1. A semi-submersible type platform was chosen based on the following considerations:

- semi-submersible floating platforms are the easiest to transport and install (as opposed to both spar type and TLPs);
- semi-submersible can be installed in relatively shallow waters (as opposed to spar), which may be an interesting solution for offshore installation near coastlines, which is an extremely important feature for FOWTs demonstrators (see Hexafloat demonstrator [5]).

The so-called *HydraSparV1* semi-submersible platform, shown in Fig. 6.6, is composed of four inclined spars, which join together in a central body, ballasted at the bottom. The four inclined spars are also supported by horizontal braces that connect to the central body and contribute to withstand the loads on spars. The wind turbine is installed at the top of the central body, while at the bottom an heave-plate is placed under the body and supported by gussets, to improve the behaviour in heave motion. Four catenary chain lines (of assumed grade R3 studless chain link) connect the floating platform to the seabed, where four gravity-based anchors are laid down. In this preliminary study, all parts of the floating platform are considered to be manufactured in structural steel with surface treatment for marine environment and then welded together. It is deemed possible to adopt reinforced concrete for some parts of the platform, which would allow a lower cost of the material. Ideally, the floating platform is built at a construction site in the proximity of the installation site, and transported to the site by tugboat, with (as it was done for mostly of the already installed demonstrators, as indicated in [127]) or without the wind turbine installed on it (in the second case the turbine can be installed at the installation site, but an offshore crane vessel is required). The geometry of the platform is determined by the following parameters:

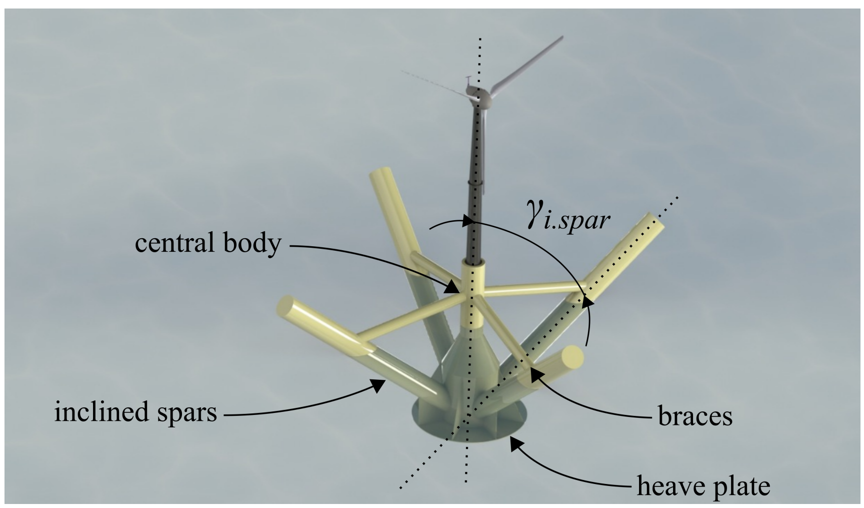

Figure 6.6: View of the HydraSparV1 floating platform. Mooring lines are omitted.

- diameter of the inclined spars;
- length of the inclined spars;
- angle of inclination of the inclined spars;
- diameter of the lower section of the central spar;
- diameter of the upper section of the central spar.

Additional elements with a structural function (e.g. reinforcing gussets) or with a hydrodynamic function (e.g. vibration damping plates, heave plates) are introduced in the course of the design development, if required by considerations arising during the analyses. The number of inclined spars is also subject to evaluation. Among the solutions currently proposed in similar projects for offshore floating turbines, one of the most popular design choices is to use three spars (usually vertical). Based on the design procedures described in Chapter 4, a preliminary study of a wind turbine on a floating platform was developed, with varying degrees of complexity and approximation. The models developed comprise various analysis tools, which are used in subsequent phases of the study activity:

- preliminary spreadsheet calculations for the evaluation of weights and volumes;
- preliminary model for mooring lines;
- preliminary model for evaluating static stability;
- hydrodynamic model of the system, based on potential flow theory for the evaluation of hydrodynamic coefficients (frequency domain analysis);
- dynamic model of the time response of the floating platform under wave action and turbine thrust;
- analysis of elastic stresses in the structure.

These analyses are preparatory to the development of an overall model capable of representing both the aeroelastic response of the wind turbine and the hydrodynamic behaviour of the turbine. Based on preliminary analyses of the platform's static stability, a configuration with four inclined spars was chosen to increase the expected level of stability, as recommended by standards for projects with innovative solutions. The possibility to vary several parameters of the geometry increases the scalability of the proposed concept, assuming to fit the choice of these parameters in a further optimization phase for larger scales and different sites of installation.

6.2.1 Floating platform dimensions and stability

Based on the design procedures and the driving requirements described in the previous chapters, the following scheme for the components of the floating platform has been used to estimate the masses, inertia and hydrostatic properties of the system. Using equations presented in Chapter 4 and the scheme of Fig. 6.7, the following procedure has been used:

1. assuming to use construction steel ($\rho_{mat.} = 7850$ kg/m^3) for the structures, write the mass of the floating platform $m_{\text{plat.}}$ as function of the thickness, the draft, angle of construction $\gamma_{\text{inc.spar}}$ and dimensions of the spars;

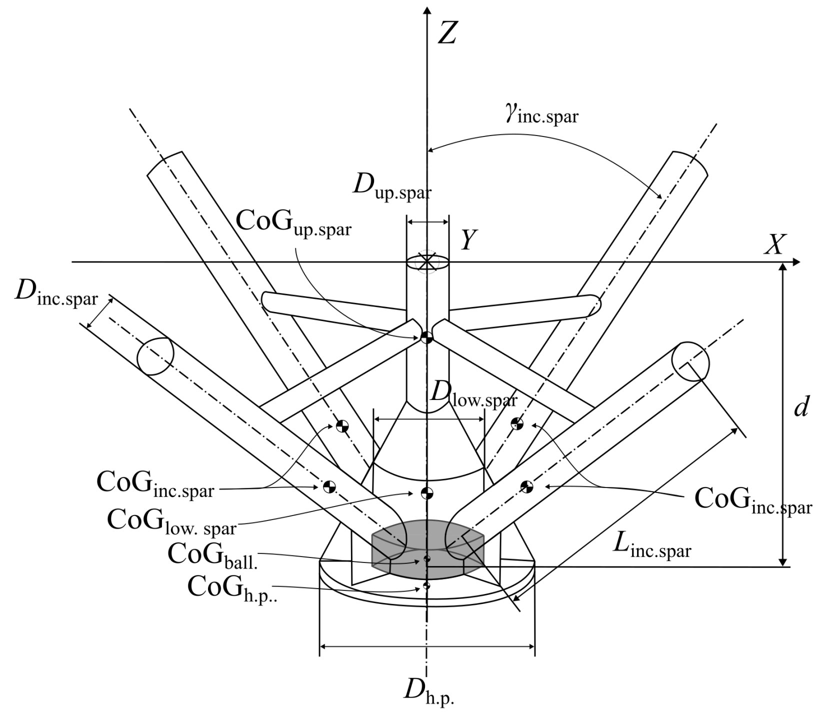

Figure 6.7: Scheme of the floating platform substructures used for the first phases of the design.

2. write the displaced volume $\forall_d$ as a function of the dimensions of the spars;
3. choose the ballast mass $m_{ball.}$ to verify the buoyancy equilibrium;
4. calculate the center of mass and of the floating platform;
5. calculate the simplified hydrostatic properties of the platform;
6. check the static heeling angle due to an overturning moment equal to the rated thrust of the assumed wind turbine times the arm between the thrust and the center of buoyancy;
7. if the constraint on the static stability is not satisfied go back to point 1.

After the definition of an initial configuration, the stability curve needed to verify the constraint defined previously in Fig. 3.3 has been obtained using Ansys AQWA. The top view of the AQWA model is illustrated in Fig. 6.8, with an indications of the two directions used for the hydrostatic equilibrium analysis. As shown in Fig. 6.9, the floating platform presents a stable behaviour (the areas below the righting moment are significantly larger than the minimum stability requirements, according to [70]). The static heeling angle is below the threshold of 5deg when the rated thrust is generated by the turbine, and below 10deg when the maximum thrust is applied.

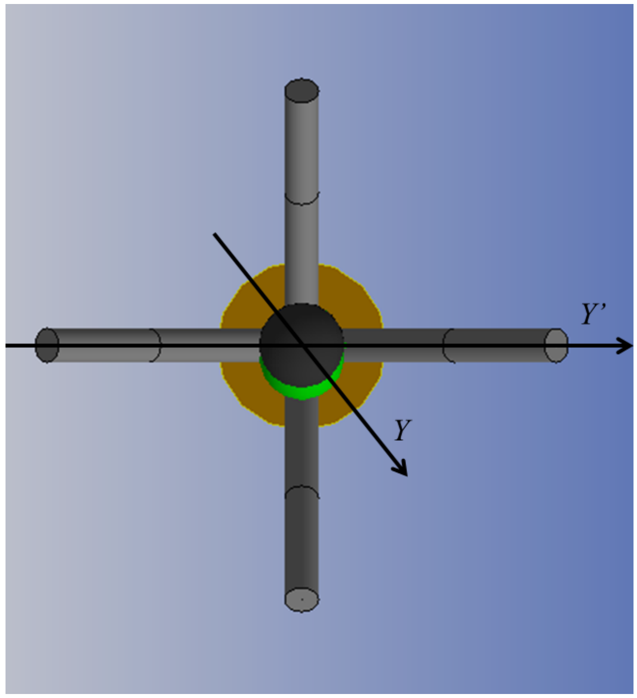

Figure 6.8: Top view of AQWA model for the floating platform hydrostatic stability calculations.

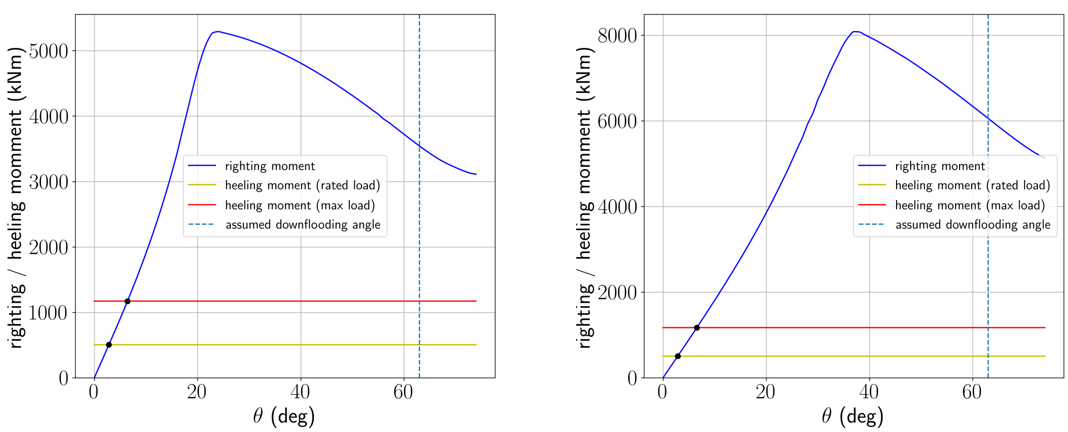

(a) Y direction.

(b) Y' direction.

Figure 6.9: Results of the AQWA hydrostatic stability analysis.

6.3 Mooring lines design

Following the procedure described in section 4.3, to obtain a preliminary multi-lines mooring system configuration, some quantities have been prescribed as inputs to the process. In particular:

- the site of installation is 40 m deep;
- the position of fairleads has been chosen to comply with the dimensions of the lateral spars;
- an admissible displacement of 5 m has been selected to comply with guidelines found in literature (see [54], conservatively the surge offset has been chosen equal to 15% of the depth);
- a maximum horizontal force of 100 kN has been imposed at the fairlead; this value is conservatively accounting for both the thrust of the wind turbine and wave surge drift forces. This value is only indicative at this stage of the design and must be revised in a later phase of the design in coupled simulations.

An initial chain diameter of 30 mm has been chosen to search for complying mooring lines. The characteristics of the complying mooring lines configurations are represented as functions of the chain diameter $D_{\text{ch.}}$ in Fig. 6.10. It can be noted that, as shown in the last graph of Fig. 6.10, the safety margin is largely beyond the requirement, hence the designer can consider configurations with small chain diameter, as long as the anchor radius and cable length do not become too large (large footprint of the mooring system). A trial candidate mooring system has been selected for further analyses, with the characteristics shown in Table 6.3.

Table 6.3: Characteristics of preliminary mooring system

	N_{lines}	$D_{\text{ch.}}$	Anchor Radius	l_{C}	$w_{\text{air,C}}$
Initial configuration	4	60 mm	99.7 m	105.7 m	78.8 kg/m

6.4 Preliminary estimation of natural periods

The natural periods were analysed using Ansys AQWA boundary element method. As regards the natural periods listed in Table 6.4, the values seem to fall within the range of possible sea waves periods. A possible mitigation action was undertaken enlarging the heave plate and changing the weights and inertia of the system. Anyway due to the small size of the floating platform, it seems very difficult to avoid these possible resonating behaviour in operating condition; such issue has to be properly accounted for in future phases of the design.

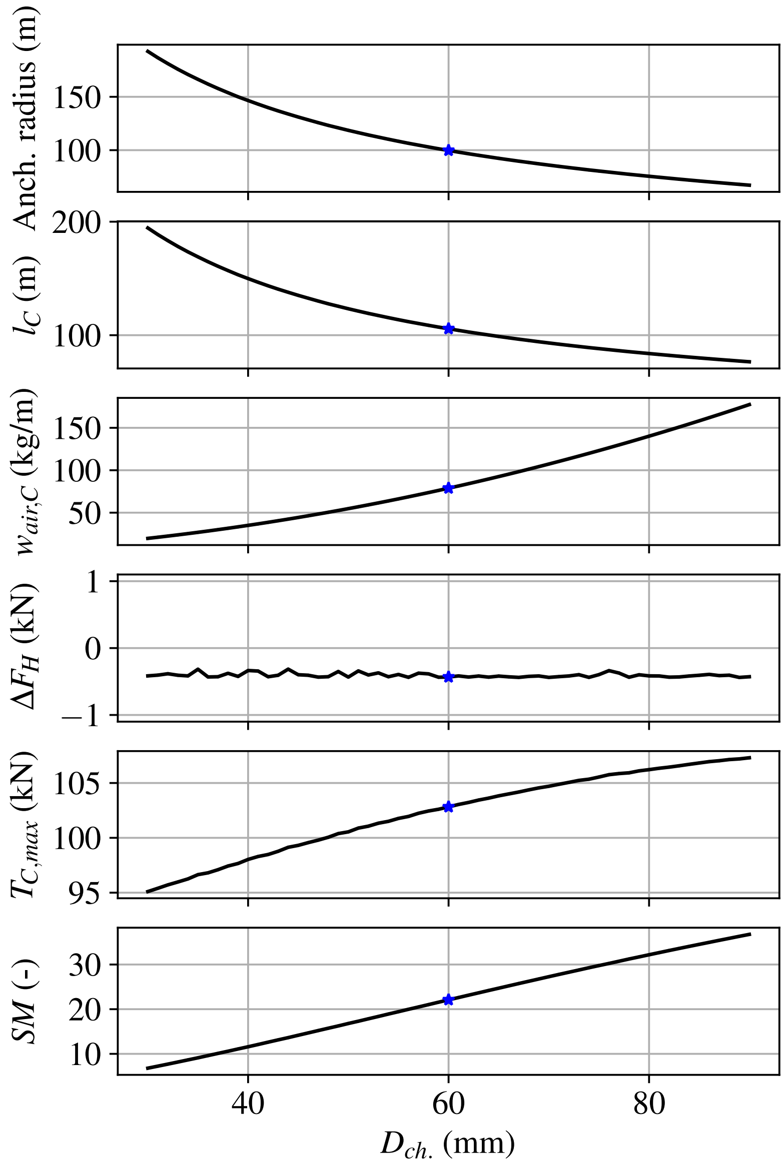

Figure 6.10: Graph of the characteristics of the configurations complying with the requirements of the mooring lines design procedure, as function of the chain diameter. A blue point indicates the chosen configuration for initial design.

Table 6.4: Natural periods of substructure (with mooring lines)

	Surge	**Sway**	**Heave**	**Pitch**	**Roll**	**Yaw**
$T_{\mathbf{nat.}}$	43.0 s	43.0 s	10.6 s	7.2 s	7.2 s	27.4 s

6.5 Preliminary simulations

As a "final" step of the pre-design of the floating platform, two time domain analyses were performed to check the dynamic and structural response of the system, in normal and abnormal operating conditions (represented by sea-states **A** and **B**). The aerodynamic loads were modelled in the simulations through a constant point force acting on the hub axis, shown as a yellow arrow in Fig. 6.11b. These preliminary analyses were intended as a check of the structural integrity and behaviour of the preliminary design in normal and extreme conditions. Further more detailed analyses are needed in order to assess the effects of rotor servo-aeroelastic coupling and fatigue phenomena which are planned in the rest of the project development. The time domain analyses were carried-out using AQWA, a commercial code comprised in the Ansys framework. AQWA allows the calculation of the hydrodynamic performance of rigid substructures in the frequency domain and the simulation in the time domain of pressure distribution and mooring lines response. The hydrodynamic solver used in this study is based on potential flow model, and no additional contribution due to viscous damping has been added in this phase. This assumption is deemed conservative in the estimation of the overall dynamic response. The model is shown in Fig. 6.11. The first result from these analyses was the need to reconfigure the mooring lines, which, for the simulation of extreme sea state **B**, were responsible of high mean uplift forces at anchors, which is a condition to be avoided for gravity anchors. A parametric analysis performed with increasing anchor scope and cable length showed that the mean uplift forces at anchors could be decreased to an acceptable value with the characteristics of the mooring system listed in Table 6.6. The maximum values showed an high peak for the final configuration which must be verified through more accurate analyses. The mean, maximum and significant values of the anchor uplift $F_{\mathrm{V,A_1}}$ for the initial and final configuration in the sea state **B** are shown in Table 6.5. Furthermore, AQWA's

Table 6.5: Anchor uplift force for most elongated line during 3 h simulation of sea-state **B** with thrust force generated by parked rotor (39 kN).

Configuration of mooring lines	$F_{\mathbf{V,A}_{1,\mathrm{mean}}}$	$F_{\mathbf{V,A}_{1,1/3}}$	$F_{\mathbf{V,A}_{1,\mathrm{max}}}$
Initial configuration	1.9 kN	16 kN	144 kN
Final configuration	0.3 kN	3.3 kN	117 kN

output can be used in a one-way coupling with Ansys structural analysis solver. A simple Finite-Element-Method (FEM) model of the structures have been developed

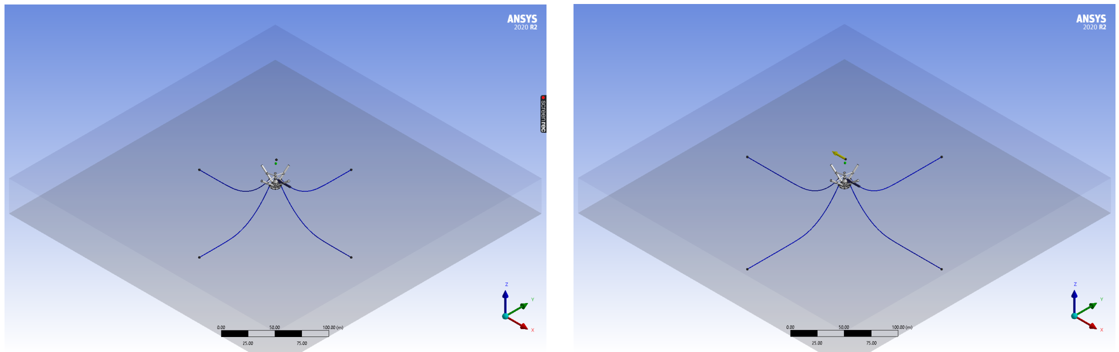

(a) Initial model (short mooring lines). (b) Final model (increased mooring lines).

Figure 6.11: AQWA models for time-domain analyses.

using shell elements, coupled with the hydrodynamic and mooring loads coming from the time domain analyses, allowing to estimate the stress distribution at each time step of the simulations. The largest tested significant wave height associated to a relatively close period to the predicted resonance showed loads compliant with the strength of the materials.

6.6 Final configuration results

The main dimensions of the floating platform and the mooring lines configuration obtained after hydrostatic stability, natural frequencies and mooring lines verification, are given in Table 6.6. This configuration is the results of many iterations in the process of design, which is still ongoing. Despite being a provisional (sub-optimal) configuration for a rather small wind turbine (suitable for a real-environment demonstrator), the ratio between total weight and power (which is an indicator of the feasibility of the technology used in [128]) is close to more developed floating platform concept for big wind turbines (Maximiano et. al [128] estimate a value of approximately 0.40 W/kg for the systems supporting 15 MW wind turbines in [129]). It must be remarked that the power to mass ratio is influenced by the scale of the system and serves as an appropriate comparison indicator only for systems of the same scale.

6.6.1 Dynamic response in AQWA

The dynamic response of the system was analysed under the action of irregular waves simulated time histories (3 hours) generated by the selected sea-states **A** and **B** (through JONSWAP spectrum), and subjected to a point force equal to the rated thrust for the normal operating condition, and the thrust generated by the parked rotor for the extreme condition. The normal sea-state with rated thrust generate a relatively high mean value of the pitch angle (around 7 deg) Fig. 6.12,

Table 6.6: Main dimensions of the HydraSparV1 and mooring lines configuration

Dimension	Short name	Value	Units
Platform mass w/o ballast	$m_{\mathrm{plat.}}$	196	t
Ballast mass	$m_{\mathrm{ball.}}$	50	t
Draft	d	9	m
Total displaced volume	$\forall_{\mathrm{d}}$	271.6	m^3
Angle of inclined spars	$\gamma_{\mathrm{inc.spar}}$	50	deg
Platform freeboard	$FB_{\mathrm{plat.}}$	6	m
Inclined column diameter	$D_{\mathrm{inc.spar}}$	2	m
Central body upper diameter	$D_{\mathrm{up.spar}}$	2	m
Central body lower diameter	$D_{\mathrm{low.spar}}$	5	m
Heave plate diameter	$D_{\mathrm{h.p.}}$	5	m
Braces diameter	D_{braces}	1	m
Anchor distance (radius) from yaw axis	$d_{\mathrm{A,0}}$	127.6	m
Anchor depth from MSL	$h_{\mathrm{A,0}}$	-40	m
Fairlead distance (radius) from yaw axis	d_{F}	7.3	m
Fairlead depth from MSL	h_{F}	-4.2	m
Unstretched length of mooring lines	l_{C}	133.6	m
Weight in air of mooring lines	$w_{\mathrm{air,C}}$	78.8	kg/m
Power to mass ratio	PM	0.23	W/kg

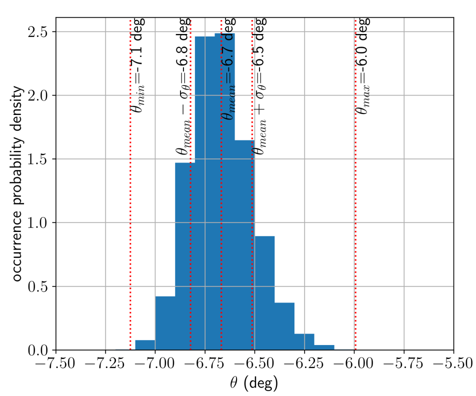

Figure 6.12: Pitch angle statistical distribution. Sea-state **A** and rated thrust. The probability density is normalized over a bin width of size 0.1 deg.

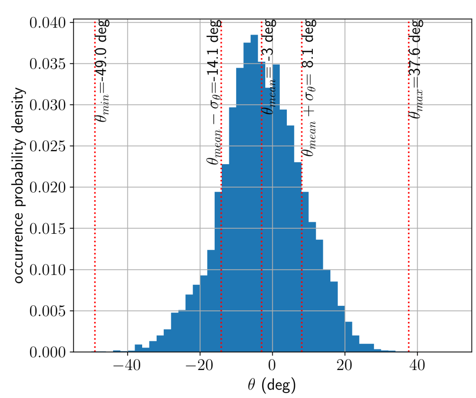

Figure 6.13: Pitch angle statistical distribution. Sea-state **B** and parked rotor thrust. The probability density is normalized over a bin width of size 2 deg.

while the oscillation around this value seem to be very contained. This could be explained by the presence of the rated thrust, which has a different weight on the dynamics with respect to severe and normal sea states. The large extreme pitch values seen in Fig. 6.13 are mainly due to large waves with very low probability of occurrence. The surge response, reported in fig.6.14, shows a small excursion under the action of the extreme sea state. A preliminary structural integrity check has

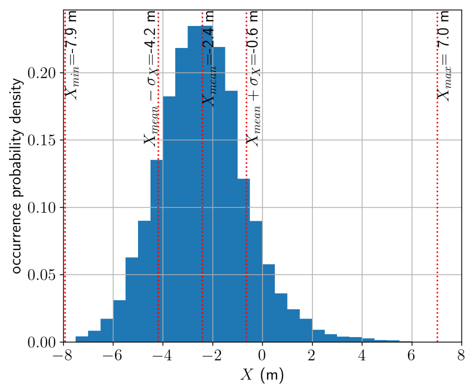

Figure 6.14: Surge displacement statistical distribution. Sea-state **B** and parked rotor thrust both in X direction. The probability density is normalized over a bin width of size 0.5 m.

been performed in all considered conditions, by integrating in a one-way coupling the hydrodynamic response with a FEM structural module (also available in Ansys Workbench). All the performed analyses showed a maximum value of the Von Mises equivalent stress under the yield strength of typical structural steel. These analyses are still on-going and will be documented further in future works. The main design issues considered in this design assessment procedure have been:

- the hydrostatic stability of the floating platform;
- the loads on the mooring system;
- the dynamic response and structural integrity under extreme sea states.

The configuration has been checked against the prescribed design constraints. Futher work is planned to account for other significant design problems, such as the fatigue behaviour and the optimization of structural weight.

6.7 Numerical-experimental comparison

After the preliminary design phase, a multiphysics simulation model has been setup for the complete turbine, floating platform and mooring system assembly.

Coupled numerical analyses of the full scale system were performed using the simulation tool OpenFAST. Full scale numerical results were then compared to the outcome of an experimental campaign carried-out to verify the main characteristics of the floating platform under investigation. The scaling ratio (λ), chosen to fit the model size to the towing tank of University of Naples "Federico II", was chosen as:

$$\lambda_{\text{model}} = 1 : 20 \tag{6.3}$$

6.7.1 Experimental setup

Based on the scaling relationships given in section 3.5, the dimensions of the model shown in the following figures were defined. For the execution of the tests, additional supporting structures for the catenaries were made to simulate the scaled depth of the seabed, as shown in Fig. 6.15. The model is made to reproduce, according to Froude's scaling laws, the geometric, mass and inertia characteristics of the full scale platform. The area at the top of the wind turbine tower (nacelle) has been modified to house a simplified thrust generation system, which is simulated using a speed-controlled ducted fan. The model nacelle also houses a load cell for measuring the applied thrust. Fluid properties such as kinematic viscosity and density for full scale and model scale are assumed equivalent. The model tested in the naval tank,shown in Fig. 6.16 consists of the following components:

- scale model of the reference turbine, consisting in turn of the following components:
  - model of the floating platform;
  - model of the tower (tubular structure);
  - model of the nacelle comprising a fan for thrust simulation, a support structure and an electronic fan control system comprising a speed control module (ESC) and a power supply with a maximum current of 50 A;
- four mooring lines consisting of chains with a nominal diameter of 3 mm (unit weight approx. 200 g/m); two connecting eyebolts at each end; one connecting snap hook to four load cells;
- four anchors placed on the supports. The anchor point is raised w.r.t. the bottom of the wave tank by 2 m, to obtain an effective depth of the anchor point of 2 m, simulating (on a scale of 1:20) the desired depth of approximately 40 m;
- control and measurement systems:
  - control system consisting of an electronic board that allows a fan rotation speed to be prescribed, simulating a thrust of the desired magnitude at the tower top.

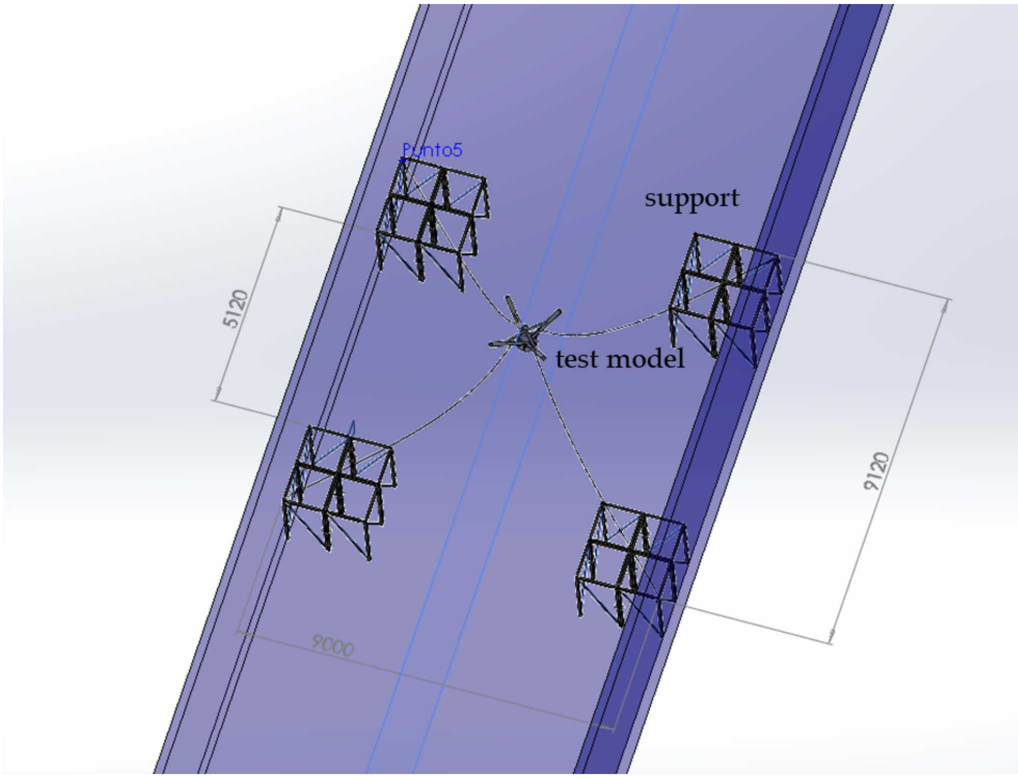

(a) 3D view.

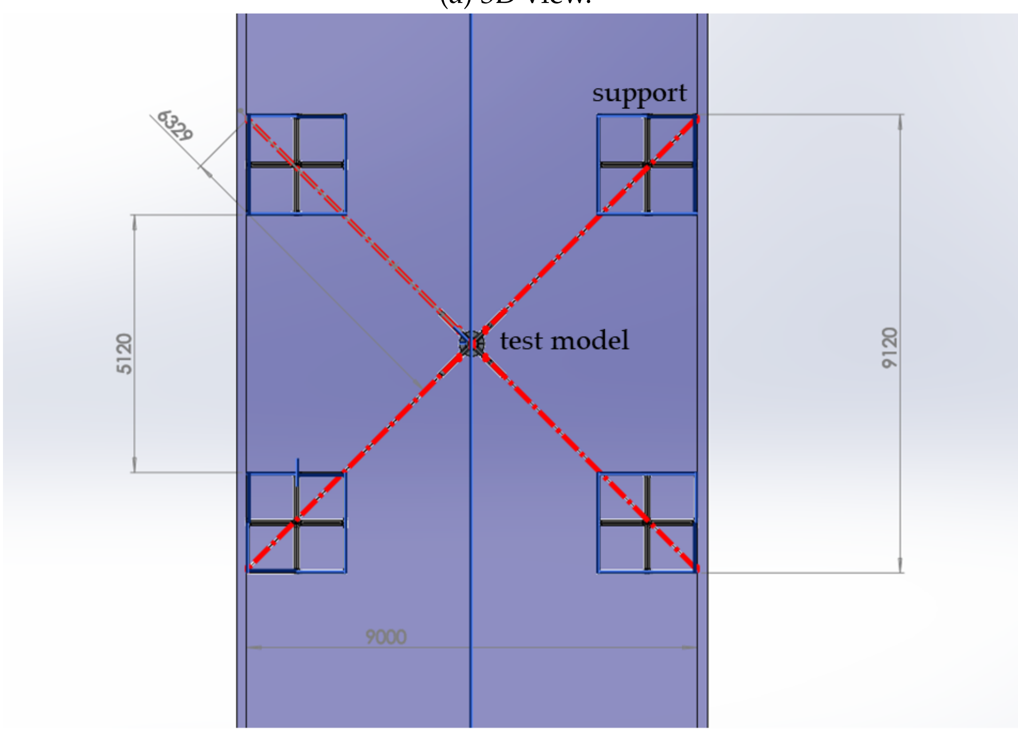

(b) Top view.

Figure 6.15: Illustrations of the configuration of the test model in the towing tank.

- four axial load cells, placed at the connection points of the mooring lines to the platform structure;
- a load cell placed on the nacelle, to measure the thrust exerted by the fan;
- an optical system for detecting the position and attitude of the platform (Qualisys™), consisting of a set of dedicated cameras, connected to a graphic processor, capable of detecting the motion of the platform by tracking the position of a set of pointers (targets) attached to the platform;
- an inertial platform with wireless transmission of the detected turbine attitude data (used in redundancy and to verify the data detected by the main optical measurement system);
- four capacitive probes for wave height measurement.

The test campaign was performed in the wave/towing tank of the University of Naples "Federico II", which is a basin with a length of 120 m, a width of 9 m and a depth of 4 m. The towing tank facility comprises a dynamometric carriage which is generally used for towing ship hulls along the tank and hosts the measuring equipments. During the current tests the dynamometric carriage was still and placed close to the test model. The towing tank is equipped with a wave maker which is able to reproduce regular and irregular waves of given characteristics. The most suitable mooring line configuration w.r.t. the site dependent wave directions should be chosen so as to engage more than one line in order to reduce fatigue loads both on the lines and on fairleads. The configuration of the mooring lines and the floating platform of Fig. 6.16 shows a rotation of 45 deg w.r.t. the previous analyses (e.g. w.r.t. Fig.6.11). In the following analyses both the experiments and the simulations are carried-out in this configuration. The X direction shown in Fig. 6.17 corresponds to the most probable incoming waves direction. The Qualisys™ instrumentation allows the calculation of the position and attitude of the floating turbine using image analysis techniques. The reference system adopted in the following analyses is defined in Fig. 6.17.

6.7.2 Free decay tests

The estimation of natural periods was carried-out with a frequency domain analysis of the free decay time histories of pitch and heave. Simulations of free oscillations with a given initial displacement in heave (amplitude of 1 m in the full scale model, corresponding to 50 mm in the scale model) were performed with the following assumptions:

- still air and still water;
- deactivated control system;

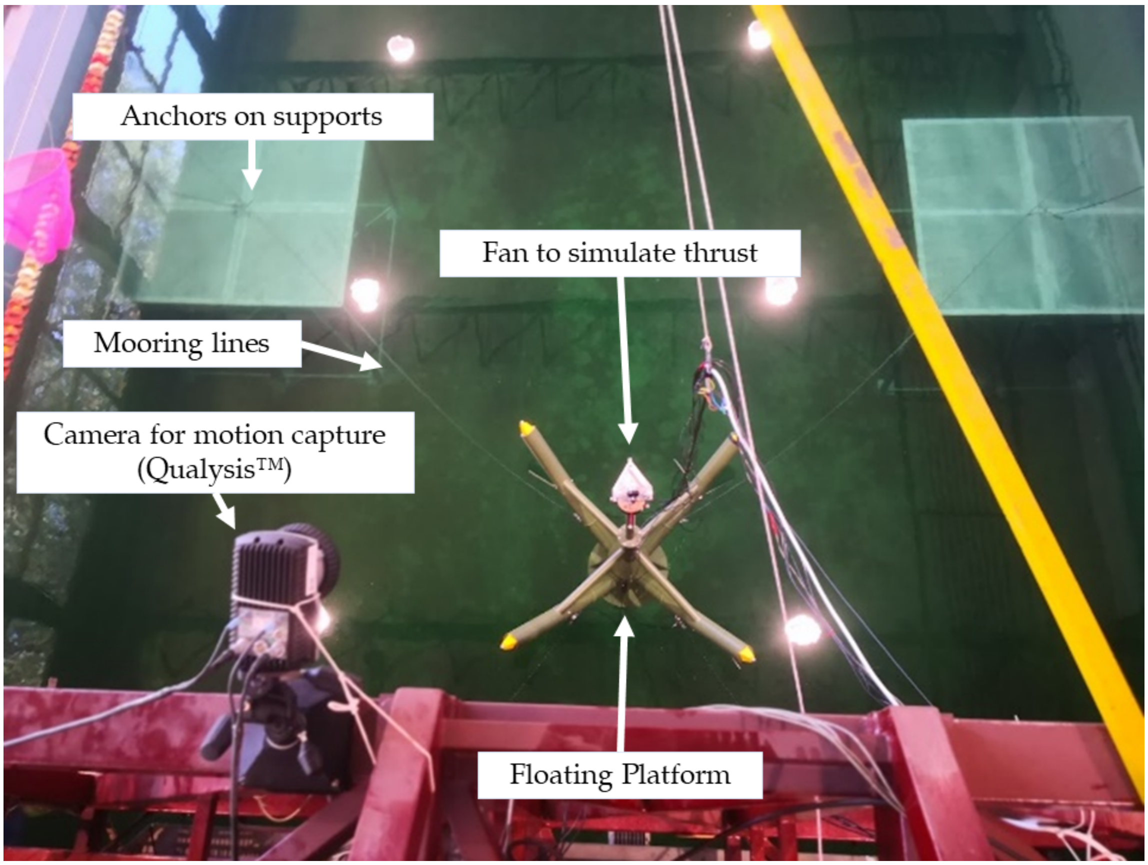

Figure 6.16: Top view picture of the experimental setup. Taken from approximately 3 m above the model test.

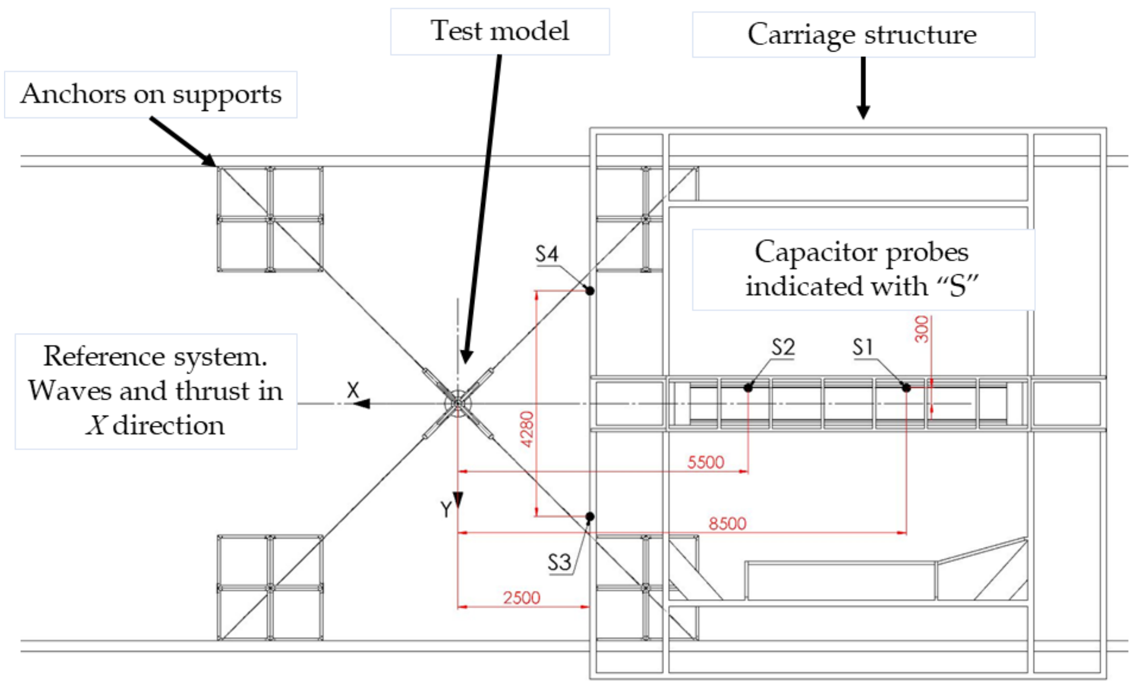

Figure 6.17: Illustration of the experimental setup with indication of the reference system.

- fixed rotor;
- transverse resistance coefficient of the cylinders: $C^{\mathrm{n}}_{D,\mathrm{cyl}} = 0.7$;
- coefficient of resistance of the heave plate (disc at the base of the central column): $C^{\mathrm{ax}}_{D,\mathrm{h.p.}} = 1.0$.

The analysis procedure can be described as follows:

- damped oscillations after a given displacement are observed;
- a simulation time of around 600 s is assumed (600 s of the simulation are analyzed in the frequency domain);
- a frequency domain analysis of the free decay response is performed, determining the FFT (Fast Fourier Transform) frequency peak for each degree of freedom. The peak value represents the natural frequency.

The simulations were carried out by assuming first-attempt values for the resistance coefficients to be used in the model. These values were roughly estimated by comparison with models found in the literature. The data available in the literature do indeed present considerable variability, and more reliable values for the particular model under consideration can be assessed following future developments of the study with dedicated parametric identification surveys. The values used are relatively low in favour of the conservativeness of the design analyses. It can be assumed that the value of the damping mainly affects the amplitudes of the oscillations and has a smaller effect on the frequency. The numerical simulations of free-decay are shown in Fig. 6.18 and Fig. 6.19. Several repetitions were performed in the experimental campaign, displacing the turbine and measuring the free oscillations following the release of the turbine from the imposed initial conditions. The damped natural frequency is estimated by means of an analysis based on the determination of the Fourier transform peak of the measured oscillation signal. The time histories and the relative Fast Fourier Transforms (FFT) of the repetitions are shown in Fig. 6.20 and Fig. 6.21. The peak frequencies were then scaled to full scale, and compared to the numerical values. The comparison of the experimental values and the numerical ones is listed in the Table 6.7.

It is observed that the numerical prediction of the oscillation periods shows an error of approximately 4% in both cases, compared to the measured periods, with an overestimation of the numerical result compared to the measured value. The possible causes of this discrepancy observed are:

- underestimated damping value compared to the actual value: the estimation of damping presents several difficulties because it is connected to non-linear phenomena related to viscosity, which presents high modelling uncertainty. Furthermore, the difference in scale of the model with respect to the prototype makes it difficult to scale the results to the full-scale value: the magnitude

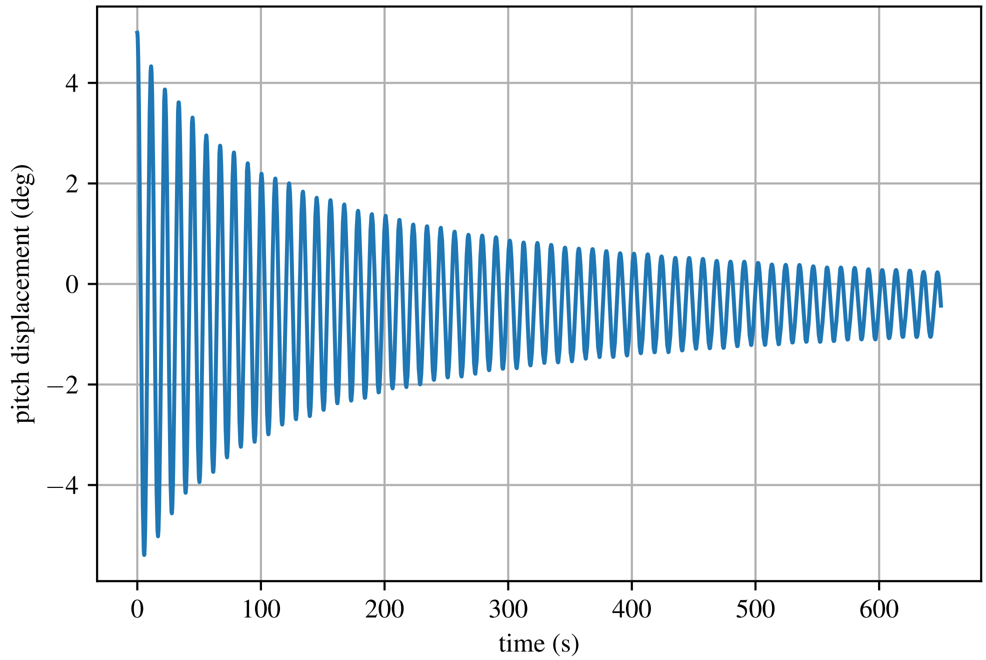

(a) Pitch time history.

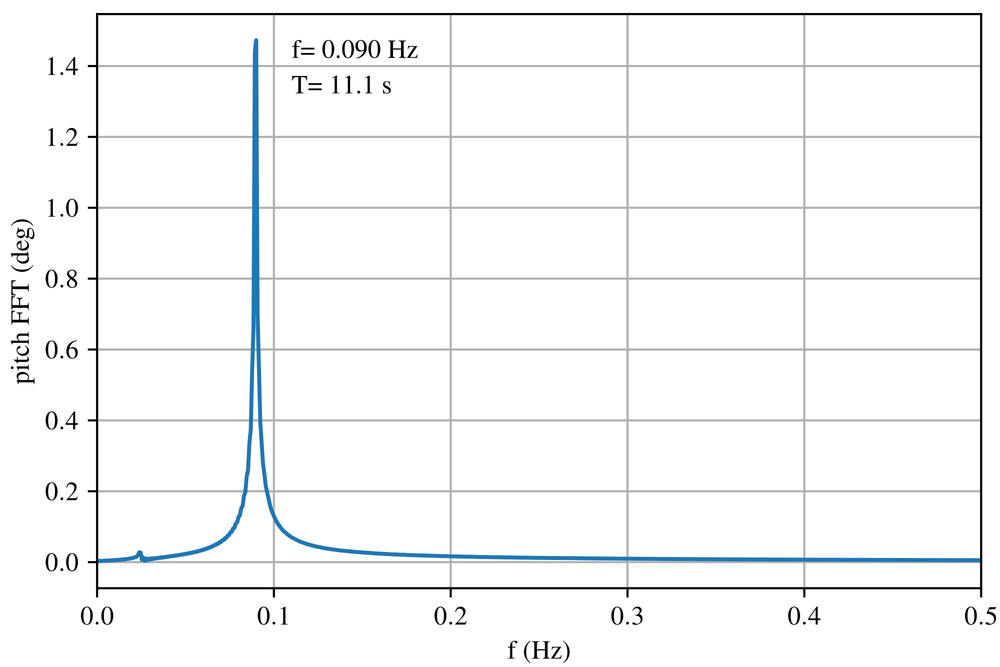

(b) Pitch FFT.

Figure 6.18: Pitch decay numerical simulation. Time history on the top, and FFT on the bottom, with indication of the peak frequency and period.

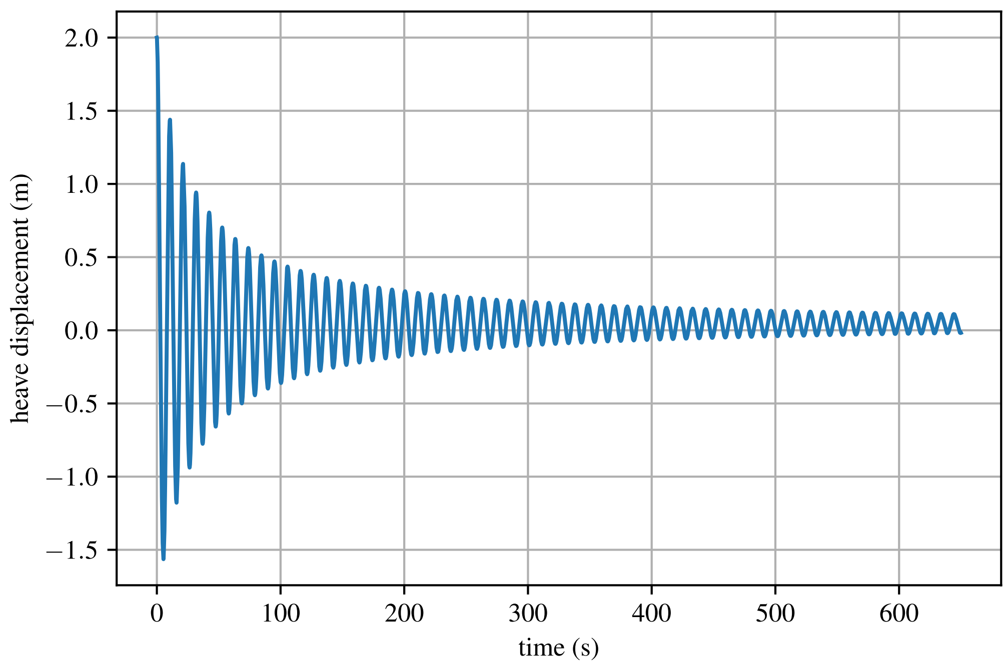

(a) Heave time history.

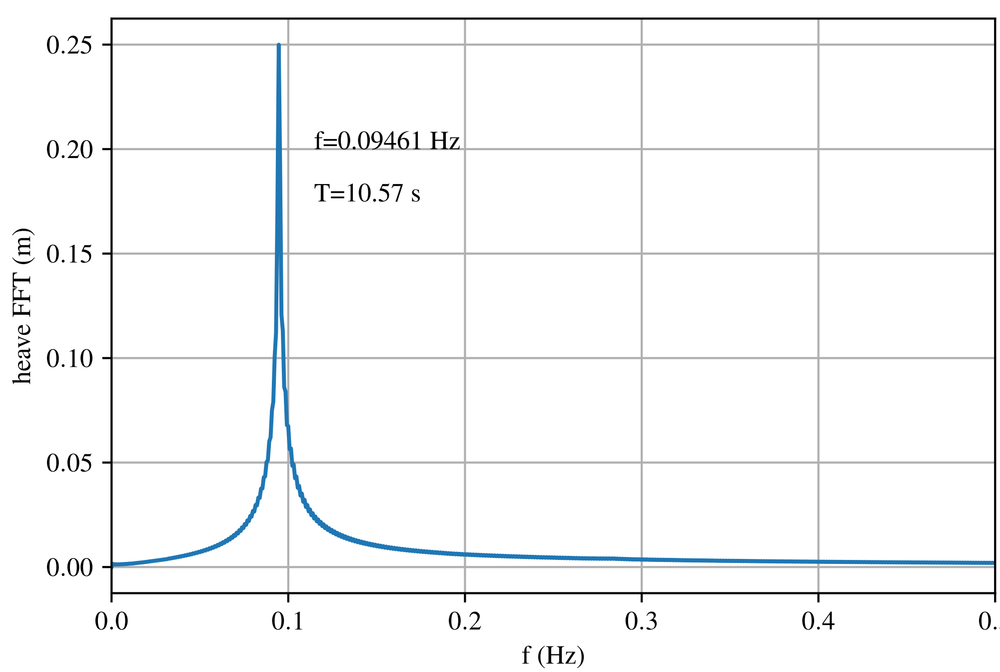

(b) Heave FFT.

Figure 6.19: Heave decay numerical simulation. Time history on the left side, and FFT on the right side, with indication of the peak frequency and period.

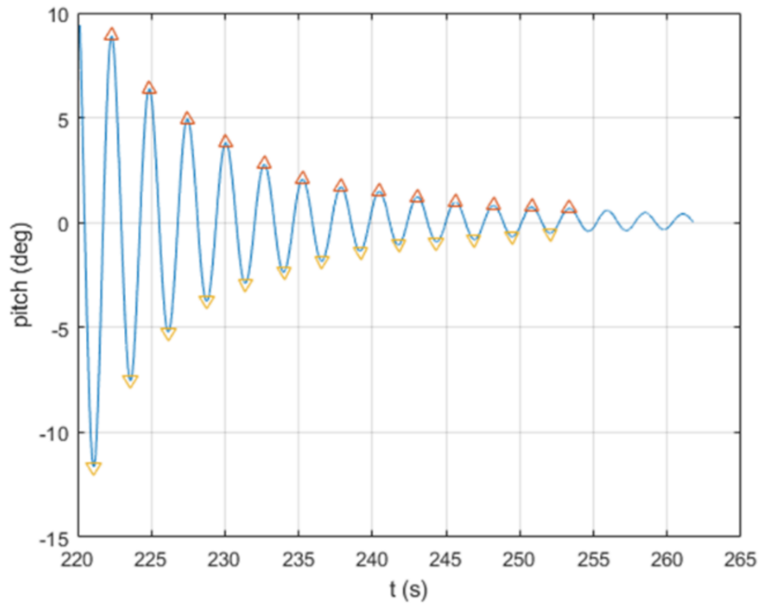

(a) Time history 1.

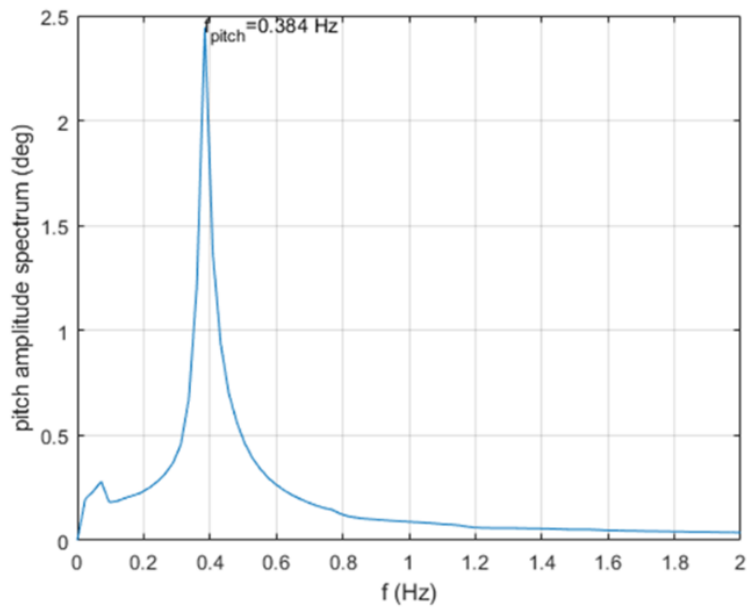

(b) FFT 1.

Figure 6.20: Pitch decay experiment. Time history above, with indication of the considered oscillations (between the red and yellow triangles), and FFT on the bottom, with indication of the peak frequency.

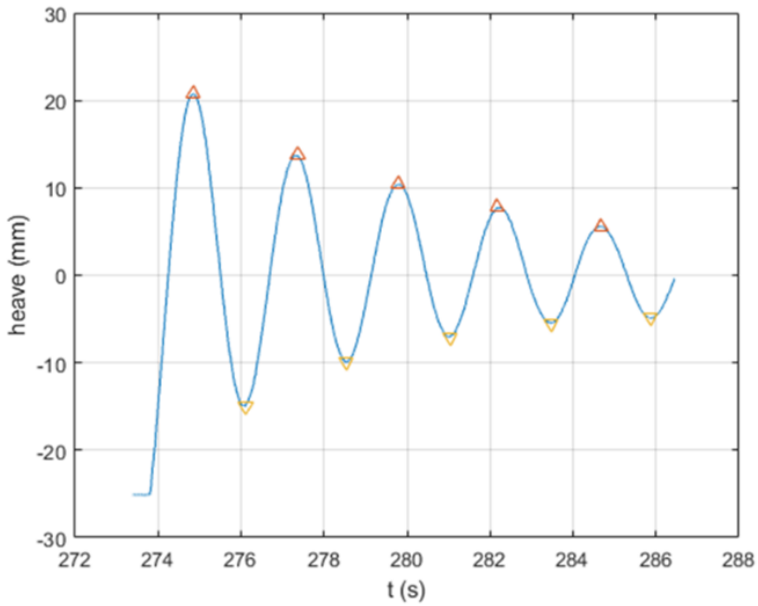

(a) Heave time history 1.

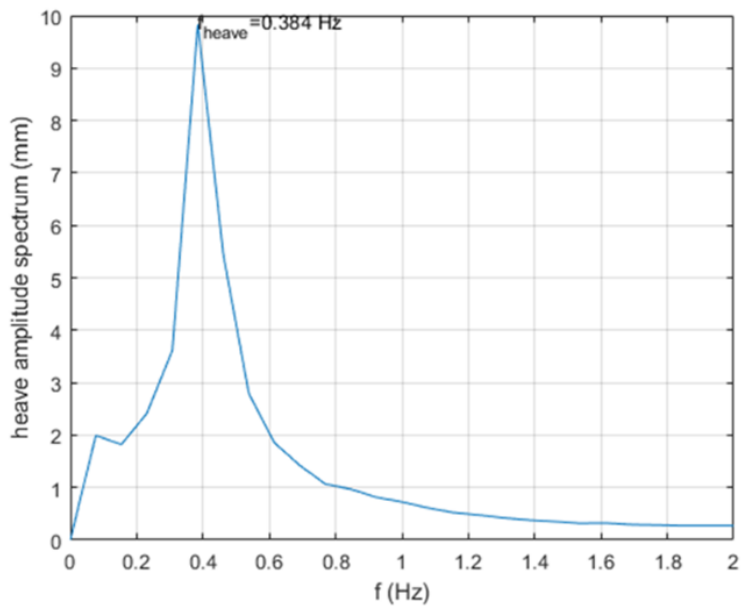

(b) Heave FFT 1.

Figure 6.21: Heave decay experiment. Time history above, with indication of the considered oscillations (between the red and yellow triangles), and FFT on the bottom, with indication of the peak frequency.

Table 6.7: Natural periods of substructure (with mooring lines). Numerical values from OpenFAST simulations.

Pitch	**Full-scale $T_{\mathbf{pitch,nat.}}$**	**Model-scale $T_{\mathbf{pitch,nat.}}$**
Numerical	11.10 s	(downscaled) 2.46 s
Experimental	(upscaled) 11.53 s	2.58 s
Difference	**- 3.9%**	
Heave	**Full-scale $T_{\mathbf{heave,nat.}}$**	**Model-scale $T_{\mathbf{heave,nat.}}$**
Numerical	10.57 s	(downscaled) 2.36 s
Experimental	(upscaled) 11.00 s	2.46 s
Difference	**- 4.1%**	

of the damping actions in the small-scale model may be overestimated with respect to the real prototype given the difference in Reynolds number;

- differences between the model and reality: the additional weight of the load cells, which are not simulated in the full-scale numerical model, may have an additional effect on the period estimation, having introduced a slight change in the moment of inertia, which is also difficult to calculate for the motion of the load cells.

6.7.3 Regular waves

Regular waves experiments and numerical simulations were performed to analyse the dynamic response of the system subjected to the wave action. The experiments were performed with monochromatic regular waves with different amplitudes and frequencies, with the aim of reconstructing the frequency responses, and investigating non-linear variation effects with the wave amplitude. The characteristics of the waves are shown in Table 6.8 and 6.9. The heights indicated are nominal values

Table 6.8: Frequencies of regular waves tested in experiments.

$f_{\mathbf{w}}$ **(Hz)**	0.28	0.34	0.40	0.41	0.43	0.445	0.46	0.50	0.51	0.53	0.64	0.75

Table 6.9: Heights of regular waves tested in experiments.

$H_{\mathbf{w}}$ **(m)**	0.10	0.15	0.20

of the wave generation system. For each wave condition tested, the actual height is evaluated from the average of the heights measured by the capacitive probes installed on the dynamometer carriage in the vicinity of the floating platform. The choice of heights and frequencies was made on the basis of a preliminary

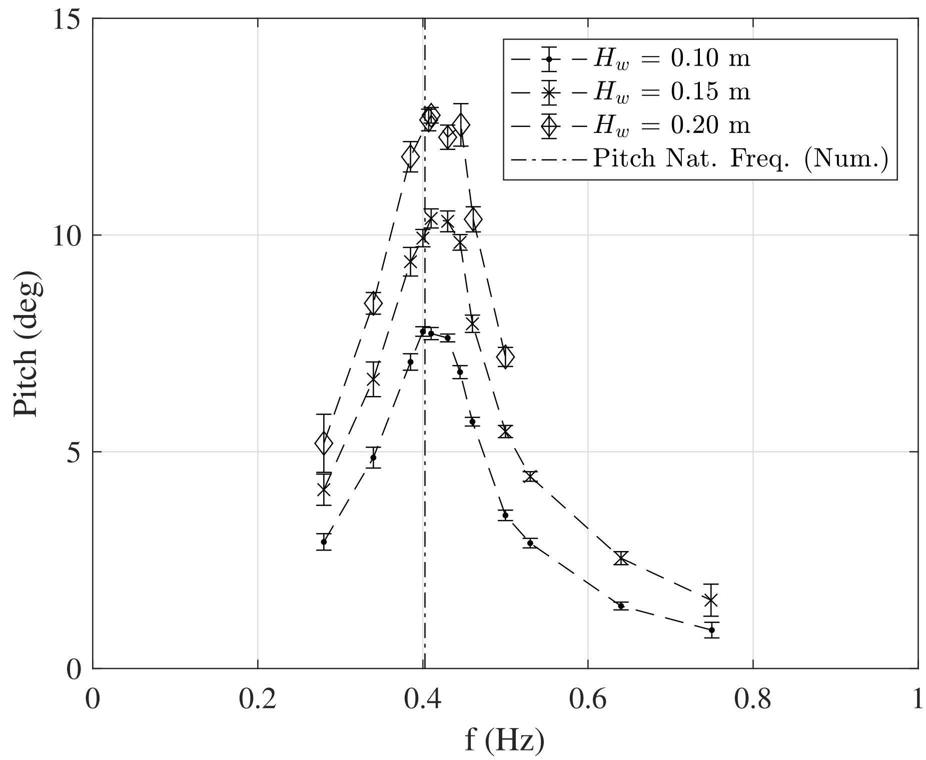

Figure 6.22: Pitch amplitude mean values and standard deviation (errorbars) for regular waves experiments. Indication of the downscaled numerical natural frequency for comparison.

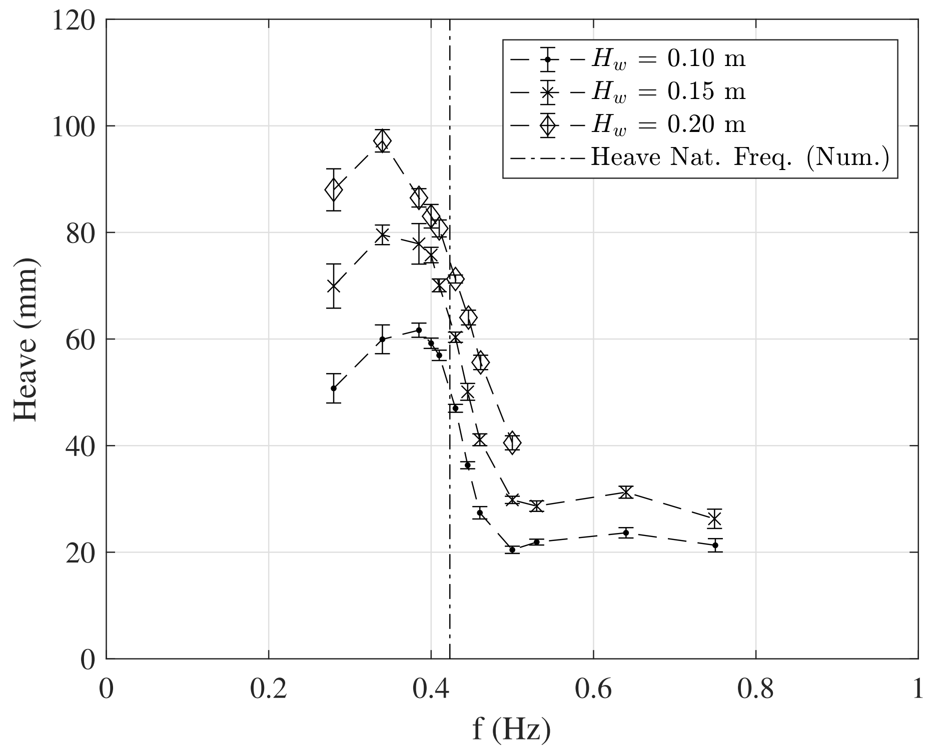

Figure 6.23: Heave amplitude mean values and standard deviation (errorbars) for regular waves experiments. Indication of the downscaled numerical natural frequency for comparison.

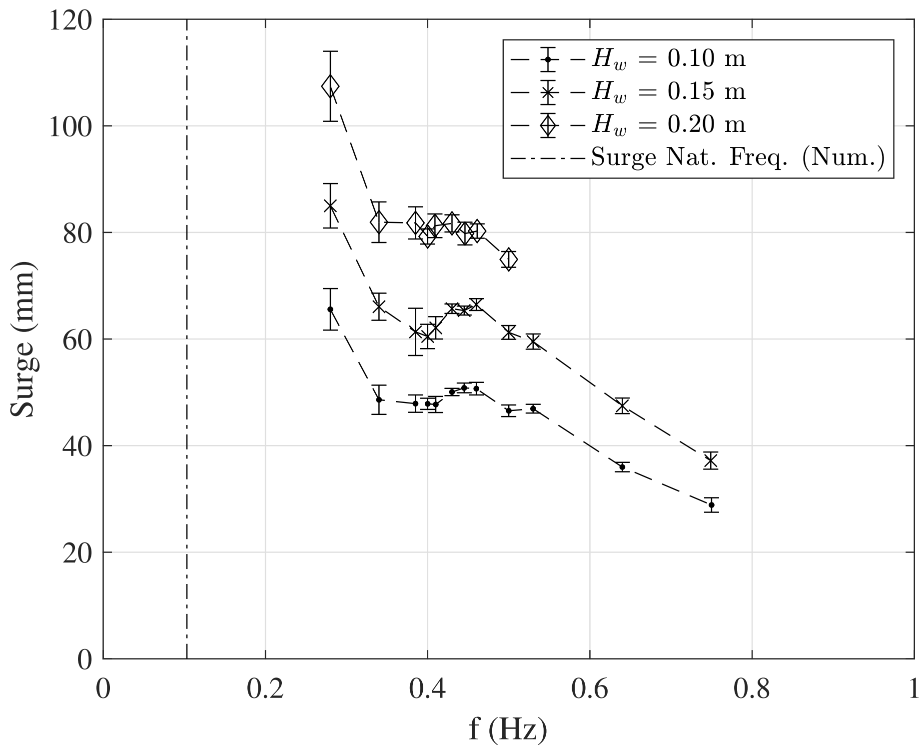

Figure 6.24: Surge amplitude mean values and standard deviation (errorbars) for regular waves experiments. Indication of the downscaled numerical natural frequency for comparison.

exploration of the platform response aimed at identifying peak frequencies. In the Figures 6.22, 6.23 and 6.24, the experimental values of the amplitudes of pitch, heave and surge are shown for different values of the regular wave amplitudes, to show the overall trends. The discrepancy between the peaks and the numerical natural frequency is also visible, especially in Fig. 6.23. Furthermore, it can be seen that for smaller wave amplitudes, the amplitude peaks are generally higher. This trend can be justified by the fact that viscous, velocity-dependent effects are less significant for lower amplitudes and oscillation velocities. To further investigate the dynamic response of the system to regular waves, the experimental campaign values have been compared to numerical ones. In Fig. 6.25, a comparison between the experiments and the numerical simulations downscaled values is shown. By comparing the maximum value of pitch amplitude (close to the

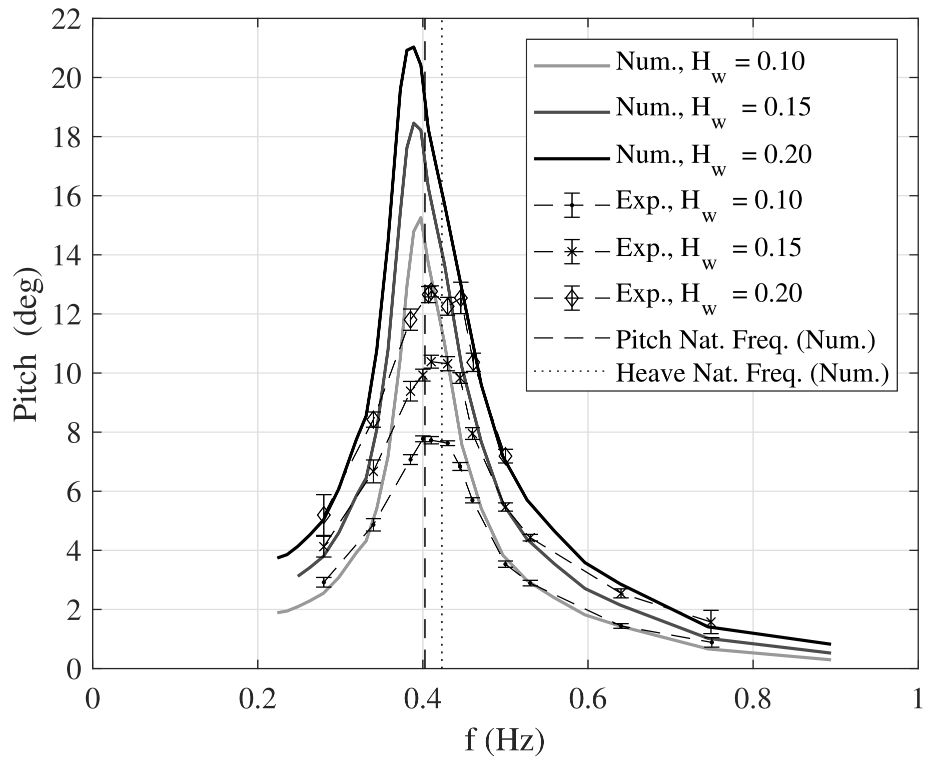

Figure 6.25: Comparison between experimental and numerical pitch amplitude mean values and standard deviation (errorbars) for regular waves simulations. Indication of the downscaled numerical natural frequency for comparison.

natural frequency) and the corresponding experimental value, it is clear that, for all wave amplitudes the numerical simulations are overpredicting the response of the system. This is fundamentally due to the different scale of viscous phenomena, which may strongly affect the peak values. In the remainder of this section, linear displacements are normalised with respect to the wave amplitude A_w and angular displacements are normalised with respect to the $k_\mathrm{w}A_\mathrm{w}$ product of the wave number k_w times the wave amplitude. This representation is often used to define response amplitude operators (RAO), which represent the magnitude of the response, in an assigned DOF, to the action of the forcing generated by an incident wave of unit amplitude and assigned frequency. They are defined as follows:

$$RAO_{\text{heave}} = \frac{A_{\text{heave}}}{A_{\text{w}}} \tag{6.4}$$

$$RAO_{\text{pitch}} = \frac{A_{\text{pitch}}}{k_{\text{w}} A_{\text{w}}} \tag{6.5}$$

$$RAO_{\text{surge}} = \frac{A_{\text{surge}}}{A_{\text{w}}} \tag{6.6}$$

where A_{heave}, A_{pitch}, A_{surge} are the amplitudes of oscillation in heave, pitch and surge. RAOs have been obtained from numerical simulations and experimental values. The three mainly investigated modes (surge, heave, pitch) RAOs comparison are shown in Fig. 6.26, 6.27 and 6.28. In the figures below, additional numerical values have been obtained from OpenFAST simulations with an increased Morison's equation drag coefficient term (indicated with $C_{D,\text{h.p.}}$) for the heave plate (axial coefficient). Significant differences are observed between the numerical

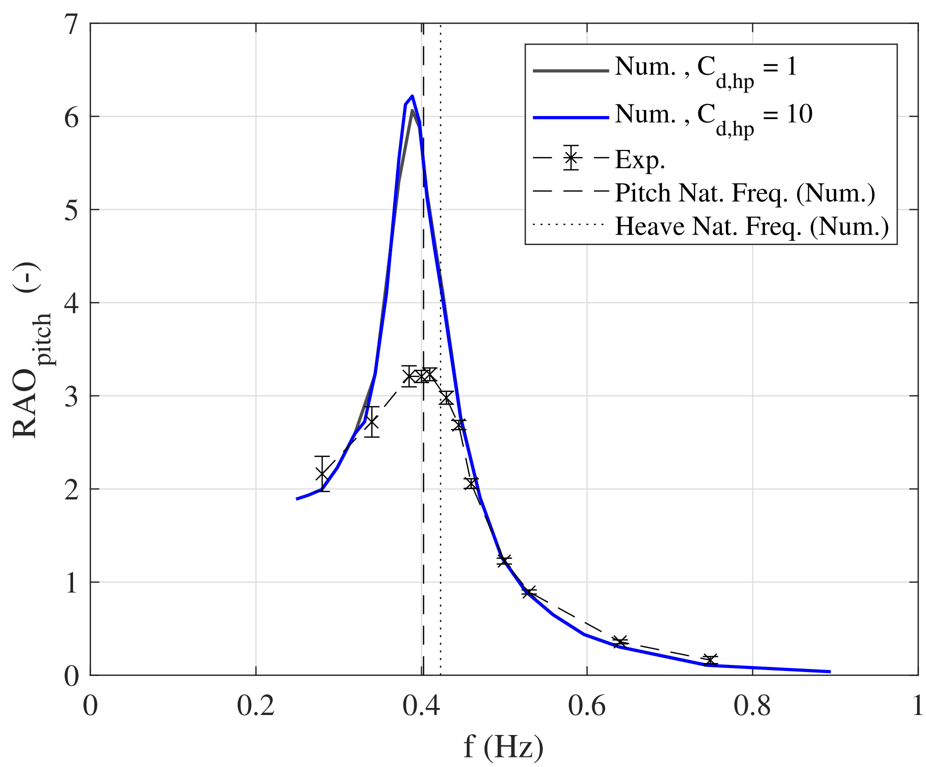

Figure 6.26: Comparison between experimental and numerical RAOs for pitch amplitude. Indication of the downscaled numerical natural frequency for comparison.

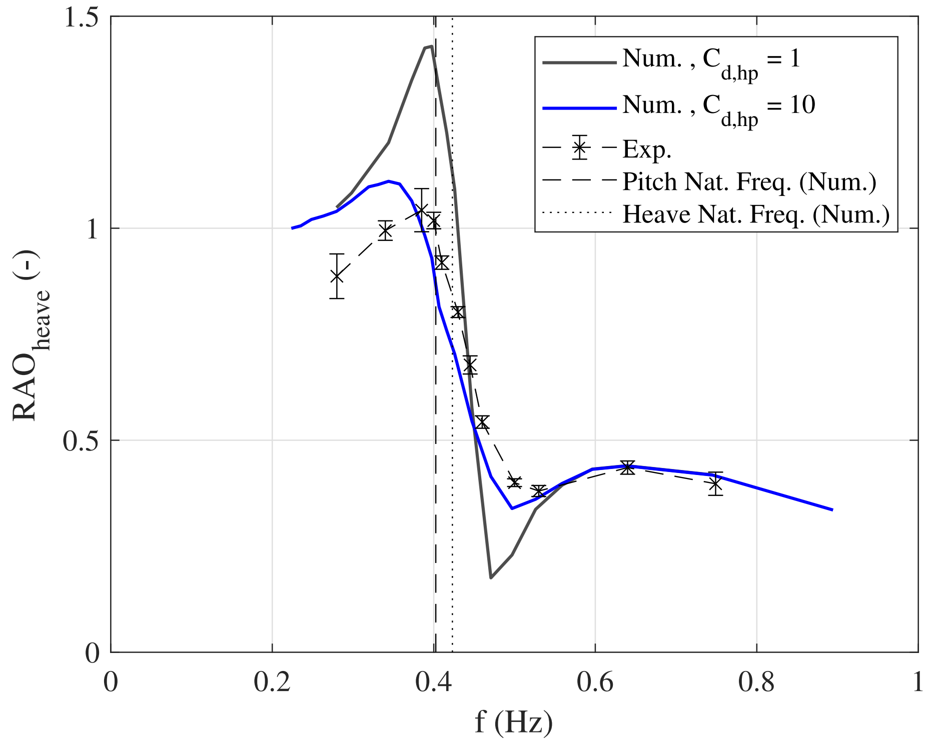

Figure 6.27: Comparison between experimental and numerical RAOs for heave amplitude. Indication of the downscaled numerical natural frequency for comparison.

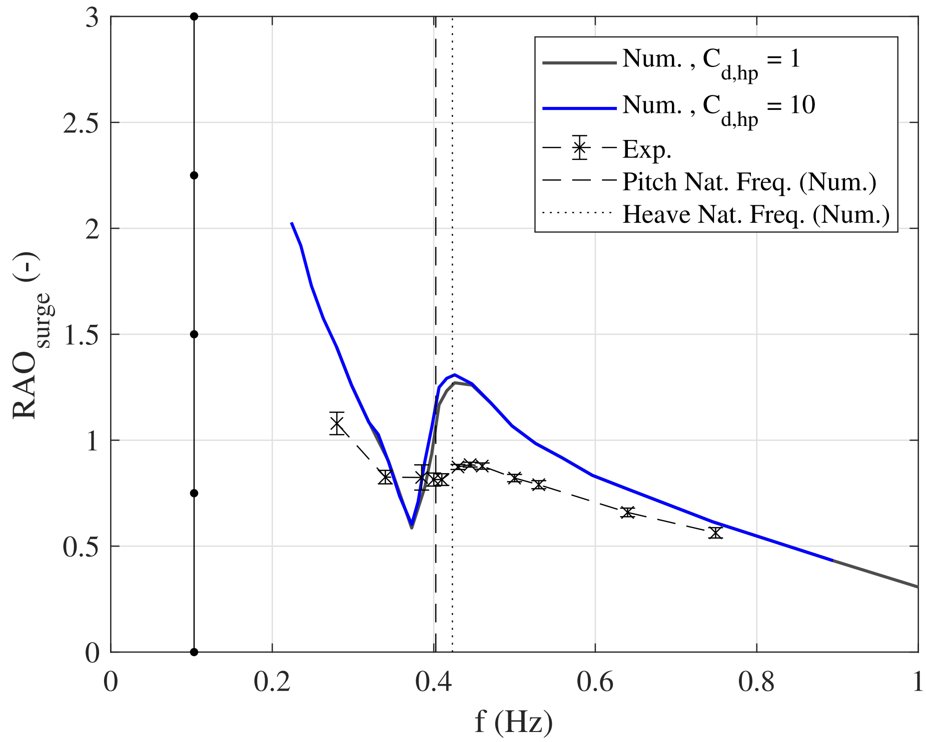

Figure 6.28: Comparison between experimental and numerical RAOs for surge amplitude. Indication of the downscaled numerical natural frequency for comparison.

estimates and the observations, with the greatest differences observed at the peak response. The greatest differences are observed precisely at the peaks, which are relatively well predicted in frequency, but with overestimated amplitudes. Part of the discrepancy can be attributed to the presence of the load cells and the variations in buoyancy and inertia levels in the scaled-down model compared to the full-scale model. A further significant contribution to the observed differences in response amplitude may be related to the effects of viscosity, which are only partially represented in the numerical model of the real system. The models based on potential theories, in fact, although presenting considerable computational advantages with respect to more complex alternative models, such as CFD, do not directly include the effects of viscosity, which must be included in the model through appropriately defined elements to introduce the damping actions (Morison's elements), characterised by assigned drag coefficients. The selection of drag coefficient values requires a further dedicated parametric identification study.

6.7.4 Irregular waves

A series of tests were conducted in irregular seas with assigned spectra. In particular, the following sea states were examined, as listed in Table 6.10. The experimental

Table 6.10: Irregular sea states tested in towing tank. The sea states examined were scaled according to Froude's laws and the experiments were conducted with and without the thrust applied by the fan at the tower top.

Analysed sea states														
SS	**Full-scale**							**Model-scale**						
No.	$H_{\mathbf{w,s}}$	$T_{\mathbf{w,P}}$	$\gamma_{JON.}$	**Windspeed**	T	**time**		$H_{\mathbf{w,s}}$	$T_{\mathbf{w,P}}$	$\gamma_{JON.}$	$f_{\mathbf{w,P}}$	T		**time**
(-)	(m)	(s)	(-)	(m/s)	(kN)	(s)		(m)	(s)	(-)	(Hz)	(N)	(gf)	s
1	1.47	5.83	1.25	9.00	12.8	3600		0.074	1.30	1.25	0.767	1.603	163.4	805
2	2.50	6.95	2.01	12.40	8.2	3600		0.125	1.55	2.01	0.644	1.027	104.7	805
3	3.50	7.78	2.63	14.99	6.1	3600		0.175	1.74	2.63	0.575	0.767	78.2	805
4	4.50	8.66	2.87	17.44	5.5	3600		0.225	1.94	2.87	0.516	0.689	70.2	805
5	5.19	8.32	4.71	18.69	5.3	3600		0.260	1.86	4.71	0.538	0.659	67.2	805
Extreme sea state with maximum thrust														
SS	**Full-scale**							**Model-scale**						
No.	$H_{\mathbf{w,s}}$	$T_{\mathbf{w,P}}$	$\gamma_{JON.}$	**Windspeed**	T	**time**		$H_{\mathbf{w,s}}$	$T_{\mathbf{w,P}}$	$\gamma_{JON.}$	$f_{\mathbf{w,P}}$	T		**time**
(-)	(m)	(s)	(-)	m/s	(kN)	(s)		(m)	(s)	(-)	(Hz)	(N)	(gf)	(s)
6	5.49	9.64	2.77	N/A	48.2	3600		0.275	2.16	2.77	0.464	6.023	614.0	805

spectra were derived by Welch's method, using a subdivision of the observation period into 20 intervals. FFT calculation was performed using of zero-padding to increase the resolution of the spectrum in the interval of interest. Table 6.11 shows a comparison of the main statistical parameters of the measured and experimental spectrum. The value $H_{\mathrm{w},1/3}$ shown in the table represents the average of the highest third of the waves observed in the sea state.

Table 6.11: Statistical parameters of measured and ideal wave spectra. Test **without** thrust.

SS	**Ideal JONSWAP spectrum**			**Measured spectrum**				**Difference**	
No.	$H_{\mathrm{w,s}}$	$T_{\mathrm{w,P}}$	$\gamma_{JON.}$	$H_{\mathrm{w,s}}$	$T_{\mathrm{w,P}}$	$H_{\mathrm{w},1/3}$	N_w	$\Delta H_{\mathrm{w,s}}$	$\Delta T_{\mathrm{w,P}}$
(-)	(mm)	(s)	(-)	(mm)	(s)	(mm)	(-)		
1	74	1.30	1.25	83	1.10	75.635	871	12.2%	-15.1%
2	125	1.55	2.01	120	1.55	112.84	550	-4.3%	-0.2%
3	175	1.74	2.63	162	1.79	142.32	634	-7.2%	3.1%
4	225	1.94	2.87	215	1.90	177.24	602	-4.4%	-2.0%
5	260	1.86	4.71	236	1.83	214.09	555	-9.4%	-1.8%
6	275	2.16	2.77	261	2.04	219.33	618	-5.0%	-5.3%

Table 6.12: Statistical parameters of measured and ideal wave spectra. Test **with** thrust.

SS	**Ideal JONSWAP spectrum**			**Measured spectrum**				**Difference**	
No.	$H_{\mathrm{w,s}}$	$T_{\mathrm{w,P}}$	$\gamma_{JON.}$	$H_{\mathrm{w,s}}$	$T_{\mathrm{w,P}}$	$H_{\mathrm{w},1/3}$	N_w	$\Delta H_{\mathrm{w,s}}$	$\Delta T_{\mathrm{w,P}}$
(-)	(mm)	(s)	(-)	(mm)	(s)	(mm)	(-)		
1	74	1.30	1.25	97	1.16	85.71	801	31.4%	-10.7%
2	125	1.55	2.01	137	1.56	121.87	874	9.4%	0.4%
3	175	1.74	2.63	174	1.79	148.81	688	-0.3%	2.8%
4	225	1.94	2.87	209	1.96	181.46	586	-7.3%	0.9%
5	260	1.86	4.71	257	1.90	227.17	583	-1.0%	2.4%
6	275	2.16	2.77	275	2.19	236.77	570	0.1%	1.2%

It can be seen that the maximum differences between the measured and theoretical spectra are found in the case of the spectrum with the lowest significant height, with differences on the order of about 15%. Excluding this test, the maximum differences are on the order of about 10% or less. To characterize the response to the action of the assigned spectrum, some statistical parameters related to the platform response are given. In particular, the mean value and standard deviation for pitch oscillation and surge displacement are shown in Fig. 6.29 and Fig.6.30. The maximum tensions acting on the most elongated mooring lines are shown in Fig. 6.31. As regards the tensions, the reported characteristic values are calculated from the averaged values of the two front lines, to remove effects of any installation asymmetries. In Fig. 6.33 the maximum tension in the most elongated cable is given for the experiments performed with two mooring lines aligned with the thrust and waves, as shown in Fig. 6.32, which was used for the preliminary design (and is deemed more demanding for the mooring system design). The tensions

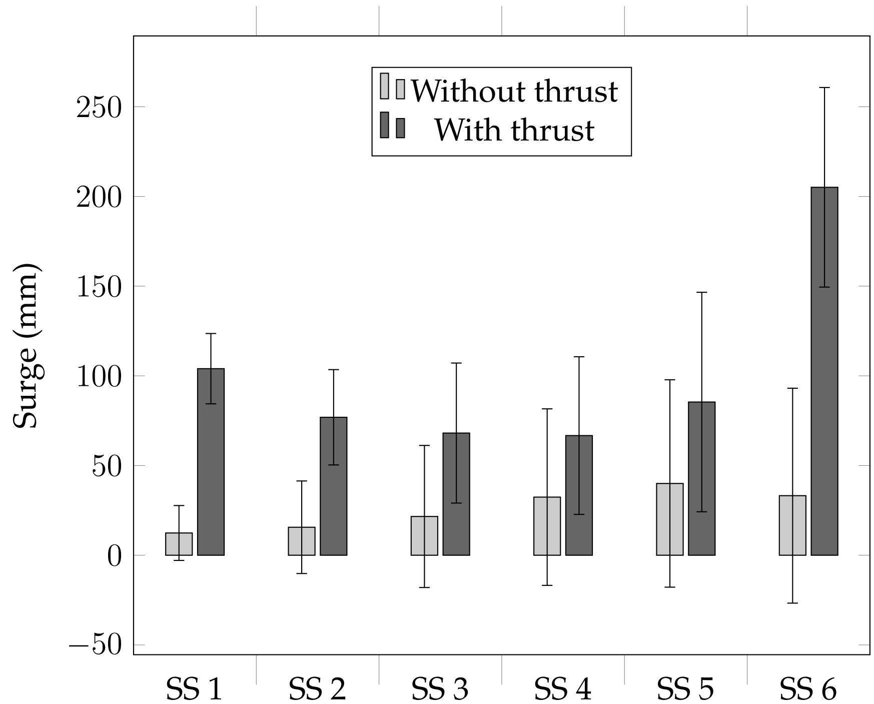

Figure 6.29: Bar plots of mean surge displacement in irregular sea states. Error bars represent surge standard deviation.

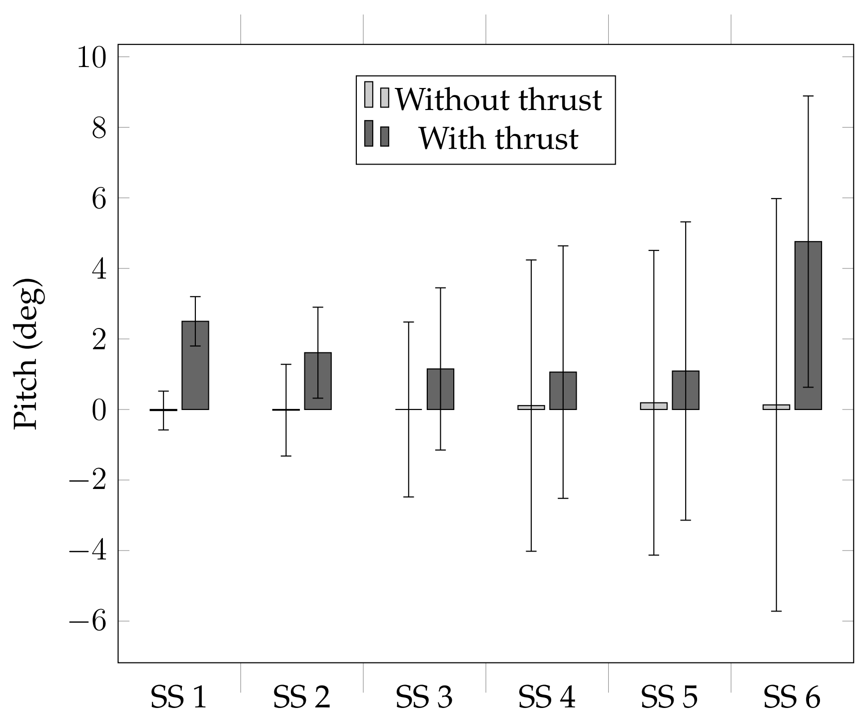

Figure 6.30: Bar plots of mean pitch angle in irregular sea states. Error bars represent pitch standard deviation.

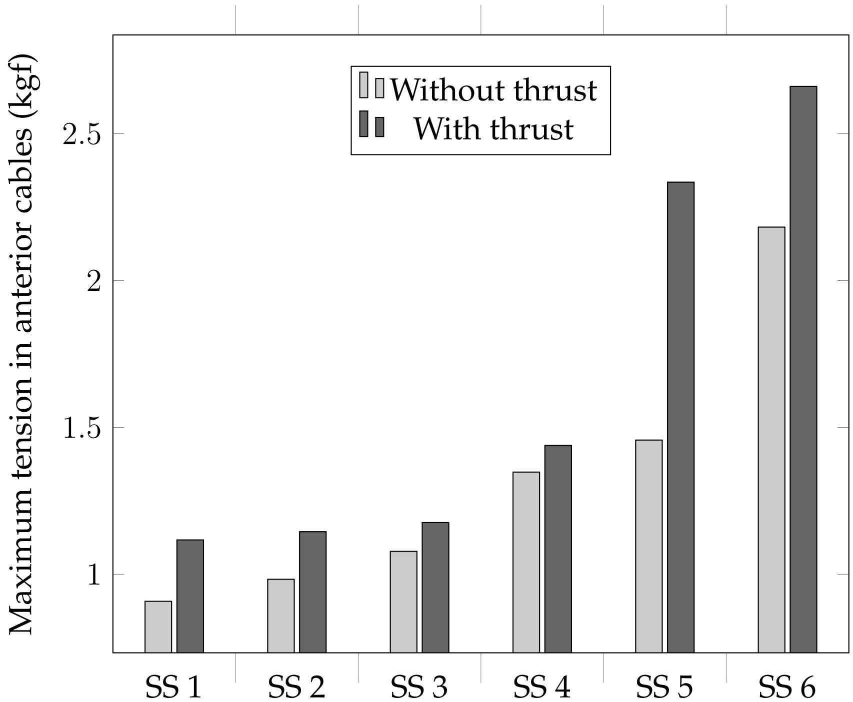

Figure 6.31: Bar plots of maximum tension in anterior cables in irregular sea states.

of the most elongated lines in the two configurations are compared in Fig. 6.34 The maximum tension in the extreme conditions (SS 5-SS 6) is observed in the case of the 0° configuration, which can be explained by only one mooring line being massively loaded in this condition. It should be noted, however, that surprisingly enough, for sea states with lower significant height, the loads are greater in the 45° configuration. This phenomenon may not be entirely attributed to the effect of the thrust, which is very low in SS 5 (see Table 6.10). A possible alternative explaination for the high tension in the cables seen in SS 5 is given by high pitch and surge oscillations (caused by high significant height and peak period closer to the natural frequencies of the system) which may cause inertial loads which increase the maximum values of the tensions in the mooring lines. In order to compare irregular waves experiments with numerical simulations, the following values are upscaled and compared to full-scale model.

The maximum tension on the observed anterior cable, found in the condition with mooring line aligned to the waves and thrust, is equal to

$$T_{\text{C,max,model}} = 3.2 \text{ kgf} \tag{6.7}$$

which corresponds to the following full-scale value according to Froude's scaling laws with scale ratio 1:20:

$$T_{\text{C,max,full-scale}} = 25600 \text{ kgf} = 251\text{kN} \tag{6.8}$$

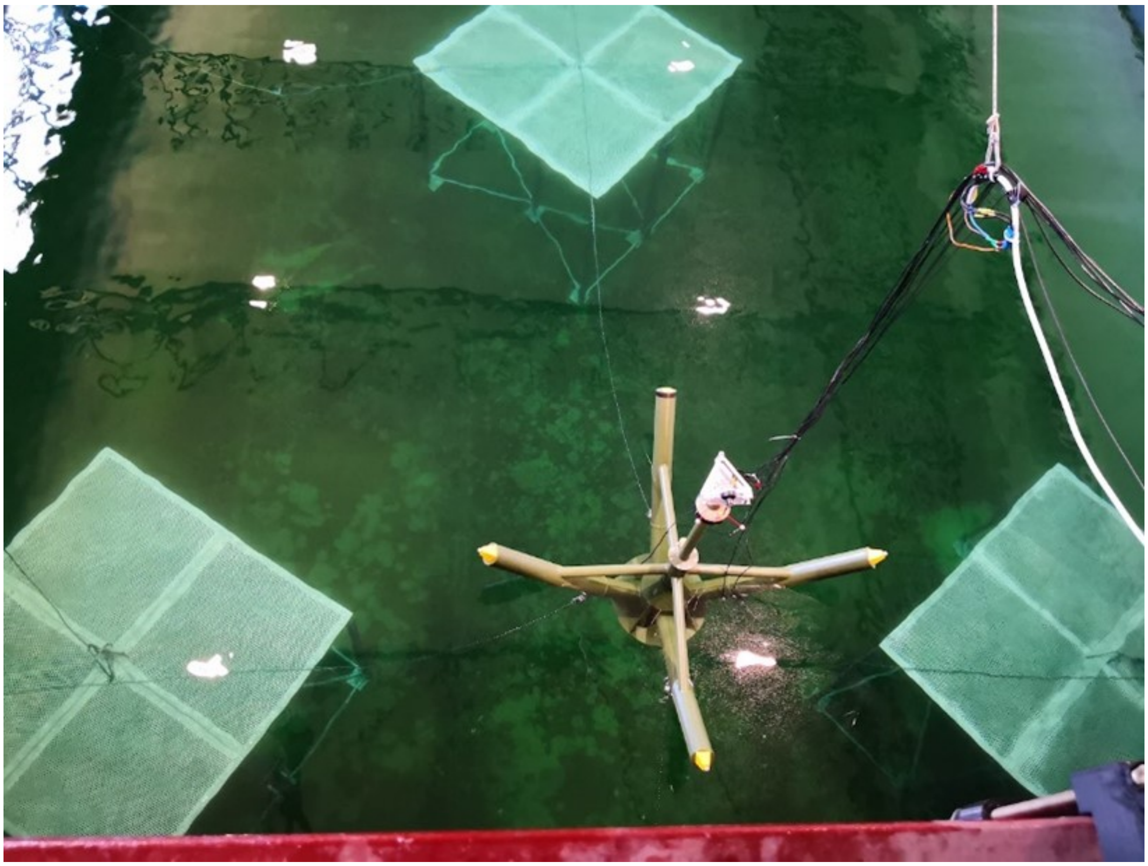

Figure 6.32: Top view picture of the experimental setup with two mooring lines aligned to the wave and thrust direction.

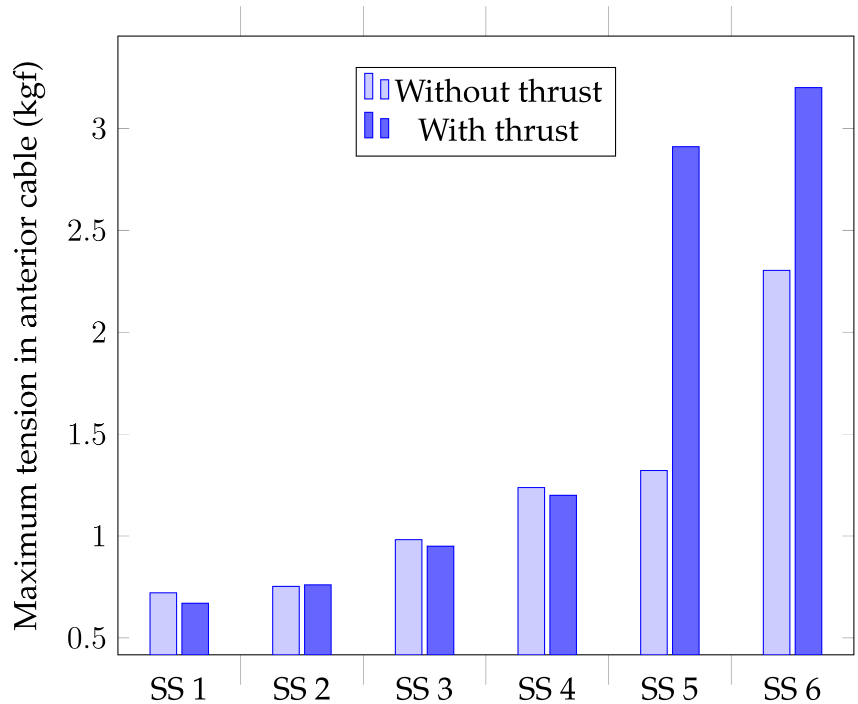

Figure 6.33: Maximum tension in anterior cables bar plot.

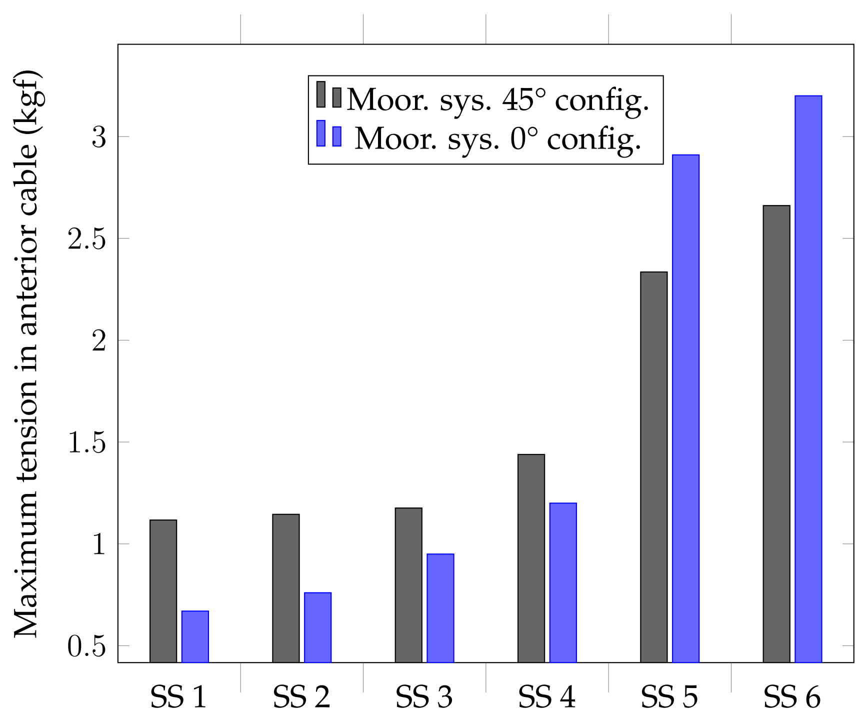

Figure 6.34: Comparison of maximum tension in anterior cables for the two configurations.

This value of the maximum tension exerted on the fairlead is considerably higher than the chosen horizontal tension value employed for the preliminary design of the mooring lines (but still lower than the MBL of the line). This discrepancy suggests that the iterative procedure of design of the mooring lines must be refined with values extracted by numerical simulations, possibly tuned with experiments. Further studies may allow an improvement in the agreement of the developed model results with the experimental data through a review of the general characteristics (actual stiffness and inertia and their modelling) and through a study aimed to the evaluation of the coefficients adopted in the model (damping coefficients, added mass, and hydrodynamic force), for example, through parametric identification methods. Further studies are also possible to improve the resonance behavior by trying to move the observed frequencies away from the typical range of waves at the site. It should be noted that the size of the prototype under consideration was assumed to be considerably smaller than the typical size of the offshore turbines currently being researched, for reasons of reducing production costs and simplifying construction in the realization of an initial experimental prototype with the aim of validating the platform concept being developed. Smaller size and masses are related to potentially problematic lower natural periods for observed sea states at possible installation sites in the Mediterranean. Revising the design for larger size scales may, at least in principle, reduce such possible resonances with the natural frequencies.

Conclusions

Simplified routines to design geometrical and structural properties of the floating platforms and mooring lines employed in FOWTs have been illustrated, complying with the most used standards in the field (DNV-ST-0119 and IEC 61400-3-2). The usage of these routines to optimize an existing floating platform-mooring lines configuration and the design of a new configuration from scratch has been shown. An optimization framework, written in Python™, implementing the modification of chosen properties of floating platforms and mooring lines and employing a simulation-based approach was developed. By integrating a pre-processor to modify selected dimensions of the floating platform and mooring lines properties and an open-source floating offshore wind turbine simulation tool (OpenFAST), the frequency and amplitude of oscillation were optimized in compliance with the operation of an innovative wake control scheme. Moreover, a simplistic model of the structural modification of a specified platform and mooring lines was developed and its effects on costs were taken into account to avoid cost-ineffective solutions. Due to the number of design variables and the non-linearity of the output objective function, a heuristic method was chosen to find the best-performing platform geometry and mooring lines combination. A differential evolution method already implemented in an open source Python™ module was chosen for the optimization process. The spars' distance of a semi-submersible platform and the distance of anchors and length of mooring lines were selected as design variables. Based on assumptions found in literature, constraints on static stability and surge excursion were imposed during the optimization. These constraints resulted in a restriction of the design space. The current optimization framework can be described by the following points:

- the optimization framework includes constraints and objective functions related to the design, performance and costs of the system.
- the optimization framework is customizable (with little coding effort) in three ways:
  - the design variables (and even the overall shape of the floating platform) can be adapted to the specific case;
  - the constraints and objectives of the optimization can be modified to suit the designer's need;

  - the level of complexity of the simulations can be varied (and thus the computational time) depending on the specific phenomena to be included in the case;

- the newly developed optimization framework may be used to optimize innovative concepts of floating platforms and mooring lines, e.g. for the installation of systems in the Mediterranean basin;

A Design of Experiments (DoE) methodology was applied to show trends and correlations of the design variables with the output variables of interest. It showed that the ratio between the length of a mooring line and the fairlead-to-anchor distance, which represents the slackness of the mooring lines, have the greatest impact on the yaw natural period. Finally, several optimization processes were carried-out using a "differential evolution" heuristic algorithm, to find the optimal combination of design variables, which amplifies the yaw motion of the system, in compliance with the innovative wake control strategy. A first approach to optimize the configuration was based on the yaw free decay response analysis, determining the yaw natural frequency, and trying to match it with the excitation frequency of the control strategy. As already observed from the preliminary DoE, the parameters related to the mooring line configuration seemed to have a major impact on the response, and a configuration with an increased slackness of the mooring lines was found to decrease the yaw natural frequency, accordingly to the control strategy requirements. A second approach to the optimization procedure, directly accounting for the actual input yaw moment related to the adopted control strategy, instead of considering the free decay response, was developed. The following points sum up the optimization runs carried out in this work:

- a test-case of the optimization framework has been carried-out for the specific need of an innovative wind farm wake control (namely "wake mixing"); this test case aimed to the modification of yaw natural frequency and damping of the system, in order to maximize the yaw motion amplitudes for the DTU 10MW Turbine mounted on the Triple Spar.

- two optimized configurations were found for this specific objective:

  1. one with an amplification of the yaw amplitude of about 50% with the prescribed forcing moment w.r.t. the baseline configuration, and an increase in the surge and heeling angle (due to the rated thrust of the turbine) within the limits imposed by design requirements.
  2. another optimized configuration showed an increase of 70% of the forced yaw amplitude w.r.t. the baseline configuration in still water, with the surge and heeling angle within the admissible limits, but both the mooring lines and structure presented significant changes (-25% mooring line length and -10% braces length), hence a more detailed analysis would be necessary to check structural integrity.

In the second part of the work, the design routines have been used to develop a novel, scalable, concept of floating platform, which has been verified with preliminary numerical simulations and experiments in the towing tank; In particular:

- the natural periods of the system were successfully verified with free decay tests in the experimental campaign (error less than 5%);
- the discrepancies between numerical simulations and experimental results are significant for both regular waves and irregular sea states;
- the dynamic response of the system seems to be overpredicted by numerical simulations; in particular, it was noted that RAO peaks of heave, pitch and surge of numerical simulations are higher than experimental RAO peaks; with a modification of the drag coefficient used in Morison's equation of the heave plate the numerical heave RAO seems to converge to the experimental curve.

Bibliography

[1] *Floating offshore wind: The next five years*. Tech. rep. DNV, 2022. URL: https://www.dnv.com/focus-areas/floating-offshore-wind/floating-offshore-wind-the-next-five-years.html.

[2] K. Staschus, I. Kielichowska, C. Ramaekers L .and Wouters, B. Vree, A. Villar Lejarreta, L. Sijtsma, F. Krönert, S. Lindroth, and G. Rundqvist Yeomans. *Study on the offshore grid potential in the Mediterranean region : final report*. Publications Office of European Commission, 2020. DOI: doi/10.2833/742284.

[3] M. Jensen. "LCOE: update on recent trends offshore". In: *6th Wind Energy Systems Engineering Workshop*. Aug. 30, 2022.

[4] CATAPULT Offshore Renewable Energy. *Floating Offshore Wind: Cost Reduction Pathways to Subsidy Free*. Tech. rep. Floating Offshore Wind Centre of Excellence, Jan. 27, 2022. URL: https://ore.catapult.org.uk/wp-content/uploads/2021/01/FOW-Cost-Reduction-Pathways-to-Subsidy-Free-report-.pdf.

[5] CNR. *COMUNICATO STAMPA - Varata la piattaforma per turbina eolica galleggiante "Hexafloat"*. July 22, 2021. URL: https://www.cnr.it/it/comunicato-stampa/10484/varata-la-piattaforma-per-turbina-eolica-galleggiante-hexafloat.

[6] I. Kougias, S. Szabó, A. Nikitas, and N. Theodossiou. "Sustainable energy modelling of non-interconnected Mediterranean islands". In: *Renewable Energy* 133 (Apr. 2019), pp. 930–940. DOI: 10.1016/j.renene.2018.10.090.

[7] EWEA. *Operational Offshore Wind Farms 2009*. Nov. 21, 2010. URL: http://ewea.org/fileadmin/ewea_documents/documents/statistics/OperationalOffshoreFarms2009.pdf.

[8] B. Snyder and M. J. Kaiser. "Ecological and economic cost-benefit analysis of offshore wind energy". In: *Renewable Energy* 34.6 (June 2009), pp. 1567–1578. DOI: 10.1016/j.renene.2008.11.015.

[9] D. Roddier and J. Weinstein. "Floating Wind Turbines". In: *Mechanical Engineering* 132.04 (Apr. 2010), pp. 28–32. DOI: 10.1115/1.2010-apr-2.

[10] A. R. Henderson, B. Bulder, R. Huijsmans, J. P., J. Pierik, E. Snijders, M. van Hees, G. H. Wijnants, and M. J. Wolf. “Feasibility Study of Floating Windfarms in Shallow Offshore Sites”. In: *Wind Engineering* 27.5 (Sept. 2003), pp. 405–418. DOI: 10.1260/030952403322771002.

[11] S. Butterfield, W. Musia, J. Jonkman, and P. Sclavounos. “Engineering Challenges for Floating Offshore Wind Turbines”. In: *Copenhagen Offshore Wind Conference*. Oct. 26, 2005.

[12] S. K. Chakrabarti. *Handbook of offshore engineering*. Elsevier, 2005. ISBN: 9780080523811.

[13] J. M. Jonkman. “Dynamics of offshore floating wind turbines-model development and verification”. In: *Wind Energy* 12.5 (July 2009), pp. 459–492. DOI: 10.1002/we.347.

[14] National Renewable Energy Laboratory. *OpenFAST Documentation*. Accessed 14.04.2022. 2022. URL: https://openfast.readthedocs.io/en/main/.

[15] F. Lemmer, K. Müller, A. Pegalajar-Jurado, M. Borg, and H. Bredmose. *LIFES50+ D4.1 - Simple numerical models for upscaled design*. Tech. rep. 2016.

[16] F. Sandner, Y. Wie, D. Matha, E. Grela, J. Azcona, S. Munduate, S. Voutsinas, and A. Natarajan. *INNWIND D4.3.3 - Innovative Concepts for Floating Structures*. Tech. rep. 2014.

[17] I. Fylling and P. A. Berthelsen. “WINDOPT: An Optimization Tool for Floating Support Structures for Deep Water Wind Turbines”. In: *Volume 5: Ocean Space Utilization: Ocean Renewable Energy*. ASMEDC, Jan. 2011. DOI: 10.1115/omae2011-49985.

[18] A. Pegalajar-Jurado, H. Bredmose, M. Borg, J. G. Straume, T. Landbø, H. S. Andersen, W. Yu, K. Müller, and F. Lemmer. “State-of-the-art model for the LIFES50+ OO-Star Wind Floater Semi 10MW floating wind turbine”. In: *Journal of Physics: Conference Series* 1104 (Oct. 2018), p. 012024. DOI: 10.1088/1742-6596/1104/1/012024.

[19] A. Pratt. *Floating Wind Turbines*. Nov. 30, 2012. URL: http://large.stanford.edu/courses/2012/ph240/pratt1/.

[20] DTU. *Global Wind Atlas*. URL: https://globalwindatlas.info/en.

[21] Principle Power. *Kincardine Offshore Wind Farm*. URL: https://www.principlepower.com/projects/kincardine-offshore-wind-farm.

[22] Principle Power. *WindFloat Atlantic*. URL: https://www.principlepower.com/projects/windfloat-atlantic.

[23] Equinor. *Hywind Tampen*. URL: https://www.equinor.com/energy/hywind-tampen.

[24] BW-IDEOL. *France's First Offshore Wind Turbine and BW IDEOL's First Unit - FLOATGEN*. URL: https://www.bw-ideol.com/en/floatgen-demonstrator.

[25] T. Landbø. *OO-STAR WIND FLOATER the Future of Offshore Wind?* Jan. 19, 2018. URL: https://www.sintef.no/globalassets/project/eera-deepwind-2018/presentations/closing_landbo.pdf.

[26] J. M. Jonkman and D. Matha. "Dynamics of offshore floating wind turbines-analysis of three concepts". In: *Wind Energy* 14.4 (Jan. 2011), pp. 557–569. DOI: 10.1002/we.442.

[27] M. Leimeister, A. Kolios, and M. Collu. "Critical review of floating support structures for offshore wind farm deployment". In: *Journal of Physics: Conference Series* 1104 (Oct. 2018), p. 012007. DOI: 10.1088/1742-6596/1104/1/012007.

[28] R. Taninoki, K. Abe, T. Sukegawa, D. Azuma, and M. Nishikawa. "Dynamic cable system for floating offshore wind power generation". In: *SEI Technical review* 84.53-58 (2017), p. 146.

[29] L. Martinelli, A. Lamberti, P. Ruol, P. Ricci, P. P. Kirrane, and L. J. Fenton. "Power umbilical for ocean renewable energy systems - Feasibility and dynamic response analysis." In: 2010.

[30] K. Ma, Y. Wu, S. F. Stolen, L. Bello, M. ver der Horst, and Y. Luo. "Mooring Designs for Floating Offshore Wind Turbines Leveraging Experience From the Oil and Gas Industry". In: *Volume 1: Offshore Technology*. American Society of Mechanical Engineers, June 2021. DOI: 10.1115/omae2021-60739.

[31] F. G. Nielsen, T. D. Hanson, and B. Skaare. "Integrated Dynamic Analysis of Floating Offshore Wind Turbines". In: *Volume 1: Offshore Technology Offshore Wind Energy Ocean Research Technology LNG Specialty Symposium*. ASMEDC, Jan. 2006. DOI: 10.1115/omae2006-92291.

[32] H. Mitsuyasu. "A Historical Note on the Study of Ocean Surface Waves". In: *Journal of Oceanography* 58.1 (2002), pp. 109–120. DOI: 10.1023/a:1015880802272.

[33] M. Hansen. *Aerodynamics of Wind Turbines*. Routledge, May 2015. DOI: 10.4324/9781315769981.

[34] W. Z. Shen, R. Mikkelsen, J. N. Sørensen, and C. Bak. "Tip loss corrections for wind turbine computations". In: *Wind Energy* 8.4 (2005), pp. 457–475. DOI: 10.1002/we.153.

[35] H A. Madsen, R. Mikkelsen, S. Øye, C. Bak, and J. Johansen. "A Detailed investigation of the Blade Element Momentum (BEM) model based on analytical and numerical results and proposal for modifications of the BEM model". In: *Journal of Physics: Conference Series* 75 (July 2007), p. 012016. DOI: 10.1088/1742-6596/75/1/012016.

[36] Y. Li, K.-J. Paik, T. Xing, and P. M. Carrica. "Dynamic overset CFD simulations of wind turbine aerodynamics". In: *Renewable Energy* 37.1 (Jan. 2012), pp. 285–298. DOI: 10.1016/j.renene.2011.06.029.

[37] E. P. N. Duque, M. D. Burklund, and W. Johnson. "Navier-Stokes and Comprehensive Analysis Performance Predictions of the NREL Phase VI Experiment". In: *Journal of Solar Energy Engineering* 125.4 (Nov. 2003), pp. 457–467. DOI: 10.1115/1.1624088.

[38] Y. Liu, Q. Xiao, A. Incecik, C. Peyrard, and D. Wan. "Establishing a fully coupled CFD analysis tool for floating offshore wind turbines". In: *Renewable Energy* 112 (Nov. 2017), pp. 280–301. DOI: 10.1016/j.renene.2017.04.052.

[39] S. Hauptmann, M. Bülk, L. Schön, S. Erbslöh, K. Boorsma, F. Grasso, M. Kühn, and P. W. Cheng. "Comparison of the lifting-line free vortex wake method and the blade-element-momentum theory regarding the simulated loads of multi-MW wind turbines". In: *Journal of Physics: Conference Series* 555 (Dec. 2014), p. 012050. DOI: 10.1088/1742-6596/555/1/012050.

[40] M. T. Landahl and V. J. E. Stark. "Numerical lifting-surface theory - Problems and progress." In: *AIAA Journal* 6.11 (Nov. 1968), pp. 2049–2060. DOI: 10.2514/3.4936.

[41] J. Katz and A. Plotkin. *Low-Speed Aerodynamics*. Cambridge University Press, Feb. 2001. DOI: 10.1017/cbo9780511810329.

[42] D. Marten, C. O. Paschereit, X. Huang, M. Meinke, W. Schröder, J. Müller, and K. Oberleithner. "Predicting Wind Turbine Wake Breakdown Using a Free Vortex Wake Code". In: *AIAA Journal* 58.11 (Nov. 2020), pp. 4672–4685. DOI: 10.2514/1.j058308.

[43] D. Marten, J. Peukert, G. Pechlivanoglou, C. Nayeri, and C. Paschereit. "QBLADE: An open Source Tool for Design and Simulation of Horizontal and Vertical Axis Wind Turbines". In: *International Journal of Emerging Technology and Advanced Engineering* 3 (2013), pp. 264–269.

[44] J. N. Newman. *Marine Hydrodynamics*. The MIT Press, 2018, p. 448. ISBN: 9780262534826.

[45] J. Palm, C. Eskilsson, G. M. Paredes, and L. Bergdahl. "Coupled mooring analysis for floating wave energy converters using CFD: Formulation and validation". In: *International Journal of Marine Energy* 16 (Dec. 2016), pp. 83–99. DOI: 10.1016/j.ijome.2016.05.003.

[46] T. T. Tran and D.-H. Kim. “The coupled dynamic response computation for a semi-submersible platform of floating offshore wind turbine”. In: *Journal of Wind Engineering and Industrial Aerodynamics* 147 (Dec. 2015), pp. 104–119. DOI: `10.1016/j.jweia.2015.09.016`.

[47] S. Burmester, G. Vaz, S. Gueydon, and O. el Moctar. “Investigation of a semi-submersible floating wind turbine in surge decay using CFD”. In: *Ship Technology Research* 67.1 (Dec. 2018), pp. 2–14. DOI: `10.1080/09377255.2018.1555987`.

[48] M. R. Dhanak and N. I. Xiros, eds. *Springer Handbook of Ocean Engineering*. Springer International Publishing, 2016. DOI: `10.1007/978-3-319-16649-0`.

[49] A. Babarit and G. Delhommeau. “Theoretical and numerical aspects of the open source BEM solver NEMOH”. In: *11th European Wave and Tidal Energy Conference (EWTEC2015)*. Proceedings of the 11th European Wave and Tidal Energy Conference. Nantes, France, Sept. 2015. URL: `https://hal.archives-ouvertes.fr/hal-01198800`.

[50] W.E. Cummins. “The impulse response function and ship motions”. In: *Shiffstechnik* (1961), pp. 101–109.

[51] O. Faltinsen. *Sea Loads on Ships and Offshore Structures (Cambridge Ocean Technology Series)*. Cambridge University Press, 1993, p. 336. ISBN: 9780521458702.

[52] F. Lemmer. “Low-order modeling, controller design and optimization of floating offshore wind turbines”. en. PhD thesis. 2018. DOI: `10.18419/OPUS-10526`.

[53] P. Catalano, M. Wang, G. Iaccarino, and P. Moin. “Numerical simulation of the flow around a circular cylinder at high Reynolds numbers”. In: *International Journal of Heat and Fluid Flow* 24.4 (Aug. 2003), pp. 463–469. DOI: `10.1016/s0142-727x(03)00061-4`.

[54] G. Benassai, A. Campanile, V. Piscopo, and A. Scamardella. “Ultimate and accidental limit state design for mooring systems of floating offshore wind turbines”. In: *Ocean Engineering* 92 (Dec. 2014), pp. 64–74. DOI: `10.1016/j.oceaneng.2014.09.036`.

[55] A.H. Pevrot and A.M. Goulois. “Analysis of cable structures”. In: *Computers & Structures* 10.5 (Oct. 1979), pp. 805–813. DOI: `10.1016/0045-7949(79)90044-0`.

[56] M. Masciola, J. Jonkman, and A. Robertson. “Implementation of a Multisegmented, Quasi-Static Cable Model”. In: International Ocean and Polar Engineering Conference. ISOPE-I-13-127. June 2013.

[57] Diaz H. and Guedes Soares C. "Review of the current status, technology and future trends of offshore wind farms". In: *Ocean Engineering* 209 (Aug. 2020), p. 107381. DOI: 10.1016/j.oceaneng.2020.107381.

[58] M. Dicorato, G. Forte, M. Pisani, and M. Trovato. "Guidelines for assessment of investment cost for offshore wind generation". In: *Renewable Energy* 36.8 (Aug. 2011), pp. 2043–2051. DOI: 10.1016/j.renene.2011.01.003.

[59] Serrano González J., González Rodriguez Á.G., Castro Mora J., Burgos Payán M., and Riquelme Santos J. "Overall design optimization of wind farms". In: *Renewable Energy* 36.7 (July 2011), pp. 1973–1982. DOI: 10.1016/j.renene.2010.10.034.

[60] N. O. Jensen. *A note on wind generator interaction*. Vol. 2411. Citeseer, 1983.

[61] Y.-K. Wu, C.-Y. Lee, C.-R. Chen, K.-W. Hsu, and H.-T. Tseng. "Optimization of the Wind Turbine Layout and Transmission System Planning for a Large-Scale Offshore WindFarm by AI Technology". In: *IEEE Transactions on Industry Applications* 50.3 (May 2014), pp. 2071–2080. DOI: 10.1109/tia.2013.2283219.

[62] J. Meyers, C. Bottasso, K. Dykes, P. Fleming, P. Gebraad, G. Giebel, T. Göçmen, and J.-W. van Wingerden. "Wind farm flow control: prospects and challenges". In: *Wind Energy Science* 7.6 (Nov. 2022), pp. 2271–2306. DOI: 10.5194/wes-7-2271-2022.

[63] E. Bossanyi. "Combining induction control and wake steering for wind farm energy and fatigue loads optimisation". In: *Journal of Physics: Conference Series* 1037 (June 2018), p. 032011. DOI: 10.1088/1742-6596/1037/3/032011.

[64] J. A. Frederik, R. Weber, S. Cacciola, F. Campagnolo, A. Croce, C. Bottasso, and J.-W. van Wingerden. "Periodic dynamic induction control of wind farms: proving the potential in simulations and wind tunnel experiments". In: *Wind Energy Science* 5.1 (Feb. 2020), pp. 245–257. DOI: 10.5194/wes-5-245-2020.

[65] J. A. Frederik, B. M. Doekemeijer, S. P. Mulders, and J.-W. Wingerden. "The helix approach: Using dynamic individual pitch control to enhance wake mixing in wind farms". In: *Wind Energy* 23.8 (2020), pp. 1739–1751. DOI: https://doi.org/10.1002/we.2513.

[66] J. Aldersey-Williams and T. Rubert. "Levelised cost of energy – A theoretical justification and critical assessment". In: *Energy Policy* 124 (Jan. 2019), pp. 169–179. DOI: 10.1016/j.enpol.2018.10.004.

[67] C. Maienza, A.M. Avossa, F. Ricciardelli, D. Coiro, G. Troise, and C.T. Georgakis. "A life cycle cost model for floating offshore wind farms". In: *Applied Energy* 266 (May 2020), p. 114716. DOI: 10.1016/j.apenergy.2020.114716.

[68] D. Matha, F. Sandner, C. Molins, A. Campos, and P. W. Cheng. "Efficient preliminary floating offshore wind turbine design and testing methodologies and application to a concrete spar design". In: *Philosophical Transactions of the Royal Society A: Mathematical, Physical and Engineering Sciences* 373.2035 (Feb. 2015), p. 20140350. DOI: 10.1098/rsta.2014.0350.

[69] F. Lemmer, W. Yu, K. Müller, and P. W. Cheng. "Semi-submersible wind turbine hull shape design for a favorable system response behavior". In: *Marine Structures* 71 (May 2020), p. 102725. DOI: 10.1016/j.marstruc.2020.102725.

[70] *DNV-ST-0119 - Floating wind turbine structures*. Standard. DNV, June 2021.

[71] *IEC TS 61400-3-2 - Wind energy generation systems – Part 3-2: Design requirements for floating offshore wind turbines*. Technical Specification. IEC, 2019.

[72] M. E. McCormick. *Ocean engineering mechanics. with applications*. Cambridge University Press, 2009. ISBN: 9780521859523.

[73] A. Robertson, J. Jonkman, M. H. Song, A. Goupee, A. Coulling, and C. Luan. *Definition of the Semisubmersible Floating System for Phase II of OC4*. Tech. rep. NREL, Sept. 2014.

[74] G. Ferri, E. Marino, and C. Borri. "Optimal Dimensions of a Semisubmersible Floating Platform for a 10 MW Wind Turbine". In: *Energies* 13.12 (June 2020), p. 3092. DOI: 10.3390/en13123092.

[75] M. Ikhennicheu et al. *COREWIND D2.1 - Review of the state of the art of mooring and anchoring designs, technical challenges and identification of relevant DLCs*. Tech. rep. Feb. 2020.

[76] European Centre for Medium-Range Weather Forecasts. *ERA5*. URL: https://www.ecmwf.int/en/forecasts/datasets/reanalysis-datasets/era5.

[77] *DNVGL-ST-0437 - Loads and site conditions for wind turbines*. Standard. DNV GL AS, Nov. 2016.

[78] M. I. Kvittem and T. Moan. "Time domain analysis procedures for fatigue assessment of a semi-submersible wind turbine". In: *Marine Structures* 40 (Jan. 2015), pp. 38–59. DOI: 10.1016/j.marstruc.2014.10.009.

[79] C. Bak, F. Zahle, R. Bitsche, T. Kim, A. Yde, L. C. Henriksen, M. H. Hansen, J. P. Albergaria Amaral Blasques, M.Mac Gaunaa, and A. Natarajan. *The DTU 10-MW Reference Wind Turbine*. "https://orbit.dtu.dk/en/publications/the-dtu-10-mw-reference-wind-turbine". 2013.

[80] J. Azcona et al. *INNWIND D4.3.7 - Design Solutions for 10MW Floating Offshore Wind Turbines*. Tech. rep. 2017.

[81] H.A. Abbass, R. Sarker, and C. Newton. "PDE: a Pareto-frontier differential evolution approach for multi-objective optimization problems". In: *Proceedings of the 2001 Congress on Evolutionary Computation (IEEE Cat. No.01TH8546)*. 2 vols. IEEE, 2001. DOI: 10.1109/cec.2001.934295.

[82] M. Leimeister. "Reliability-based optimization of floating wind turbine support structures". PhD thesis. 2020. DOI: 10.48730/8B9C-A537.

[83] M. Hall, B. Buckham, and C. Crawford. "Evolving offshore wind: A genetic algorithm-based support structure optimization framework for floating wind turbines". In: *2013 MTS/IEEE OCEANS - Bergen*. IEEE, June 2013.

[84] M. Karimi, M. Hall, B. Buckham, and C. Crawford. "A multi-objective design optimization approach for floating offshore wind turbine support structures". In: *J. Ocean Eng. Mar. Energy* 3 (2017), pp. 69–87.

[85] A. Pegalajar-Jurado, M. Borg, and H Bredmose. "An efficient frequency-domain model for quick load analysis of floating offshore wind turbines". In: *Wind Energy Science* 3 (2018), pp. 693–712.

[86] G. Ferri, E. Marino, N. Bruschi, and C. Borri. "Platform and mooring system optimization of a 10 MW semisubmersible offshore wind turbine". In: *Renewable Energy* 182 (2022), pp. 1152–1170.

[87] M. Philippe, A. Babarit, and P. Ferrant. "Aero-Hydro-Elastic Simulation of Semi-Submersible Floating Wind Turbine". In: *Journal of Offshore Mechanics and Arctic Engineering* 2 (2014).

[88] F. Huijs, R. de Bruijn, and F. Savenije. "Concept design verification of a semi-submersible floating wind turbine using coupled simulations". In: *Energy Procedia* 53 (2014), pp. 2–12.

[89] M. Leimeister. "Python-Modelica Framework for Automated Simulation and Optimization". In: *Proceedings of the 13th International Modelica Conference* (Regensburg, Germany). 2019.

[90] F. Lemmer, W. Yu, K. Müller, R. Faerron Guzmán, and M. Kretschner. *LIFES50+ D4.3 - Optimization framework and methodology for optimized floater design*. Tech. rep. 2016.

[91] A.E. Eiben and J.E. Smith. *Introduction to Evolutionary Computing*. Springer Berlin Heidelberg, 2015. DOI: 10.1007/978-3-662-44874-8.

[92] P. Virtanen et al. “SciPy 1.0: fundamental algorithms for scientific computing in Python”. In: *Nature Methods* 17.3 (Feb. 2020), pp. 261–272. DOI: 10.1038/s41592-019-0686-2.

[93] R. Storn and K. Price. “Differential Evolution - A Simple and Efficient Heuristic for Global Optimization over Continuous Spaces”. In: *Journal of Global Optimization* 11 (1997), pp. 341–359. DOI: 10.1023/A:1008202821328.

[94] C. L. Bottasso, F. Campagnolo, and V. Petrović. “Wind tunnel testing of scaled wind turbine models: Beyond aerodynamics”. In: *Journal of Wind Engineering and Industrial Aerodynamics* 127 (Apr. 2014), pp. 11–28. DOI: 10.1016/j.jweia.2014.01.009.

[95] T. A. Burdett and K. W. Van Treuren. “Scaling Small-Scale Wind Turbines for Wind Tunnel Testing”. In: *Volume 6: Oil and Gas Applications; Concentrating Solar Power Plants; Steam Turbines; Wind Energy*. American Society of Mechanical Engineers, June 2012. DOI: 10.1115/gt2012-68359.

[96] Adrien Courbois. “Étude expérimentale du comportement dynamique d’une éolienne offshore flottante soumise à l’action conjuguée de la houle et du vent”. PhD thesis. Ecole Centrale de Nantes (ECN), July 5, 2013.

[97] F. Duan, Z. Hu, and J. Wang. “Model Tests of a Spar-Type Floating Wind Turbine Under Wind/Wave Loads”. In: *Volume 9: Ocean Renewable Energy*. American Society of Mechanical Engineers, May 2015. DOI: 10.1115/omae2015-41391.

[98] A. J. Goupee, M. J. Fowler, R. W. Kimball, J. Helder, and E.-J. de Ridder. “Additional Wind/Wave Basin Testing of the DeepCwind Semi-Submersible With a Performance-Matched Wind Turbine”. In: *Volume 9B: Ocean Renewable Energy*. American Society of Mechanical Engineers, June 2014. DOI: 10.1115/omae2014-24172.

[99] F. Lemmer, Wei Yu, Po Wen Cheng, A. Pegalajar-Jurado, M. Borg, R. Mikkelsen, and H. Bredmose. “The TripleSpar Campaign: Validation of a Reduced-Order Simulation Model for Floating Wind Turbines”. In: *Volume 10: Ocean Renewable Energy*. American Society of Mechanical Engineers, June 2018. DOI: 10.1115/OMAE2018-78119.

[100] J. Kim and H. Shin. “Validation of a 750kW semi-submersible floating offshore wind turbine numerical model with model test data, part II: Model-II”. In: *International Journal of Naval Architecture and Ocean Engineering* 12 (2020), pp. 213–225. DOI: 10.1016/j.ijnaoe.2019.07.004.

[101] J. Azcona, F. Bouchotrouch, M. González, J. Garciandia, X. Munduate, F. Kelberlau, and T. A. Nygaard. "Aerodynamic Thrust Modelling in Wave Tank Tests of Offshore Floating Wind Turbines Using a Ducted Fan". In: *Journal of Physics: Conference Series* 524 (June 2014), p. 012089. DOI: 10.1088/1742-6596/524/1/012089.

[102] V. Arnal. "Modélisation expérimentale d'une éolienne flottante par une approche 'software-in-the-loop'". PhD thesis. Ecole Centrale de Nantes (ECN), Dec. 11, 2020.

[103] M. Hall and A. J. Goupee. "Validation of a hybrid modeling approach to floating wind turbine basin testing". In: *Wind Energy* 21.6 (Feb. 2018), pp. 391–408. DOI: 10.1002/we.2168.

[104] P. de Jong. *Offshore Hydromechanics Module 1*. Ed. by TU Delft. URL: https://ocw.tudelft.nl/wp-content/uploads/2.OffshoreHydromech1_FloatingStability.pdf.

[105] *DNVGL-OS-E302 - Offshore mooring chain*. Tech. rep. DNV GL AS, July 2018.

[106] D. van den Berg, D. de Tavernier, and J.-W. van Wingerden. "Using The Helix Mixing Approach On Floating Offshore Wind Turbines". In: *Journal of Physics: Conference Series* 2265.4 (May 2022), p. 042011. DOI: 10.1088/1742-6596/2265/4/042011.

[107] D. Marten. *Qblade Website*. http://www.q-blade.org. 2022.

[108] C. Geuzaine and J.-F. Remacle. "Gmsh: A 3-D finite element mesh generator with built-in pre- and post-processing facilities". In: *International journal for Numerical Methods in Engineering* 79 (2009), pp. 1309–1331.

[109] R. Rongere. *Meshmagick User's Guide*. 2021. URL: %7Bhttps://lheea.github.io/meshmagick/%7D (visited on 02/16/2022).

[110] M. Ancellin and F. Dias. "Capytaine: a Python-based linear potential flow solver". In: *journal of Open Source Software* 4.36 (2019), p. 1341.

[111] A. Babarit and G. Delhommeau. "Theoretical and numerical aspects of the open source BEM solver NEMOH". In: *Proceedings of the 11th European Wave and Tidal Energy Conference (EWTEC2015)* (Nantes, France). 2015.

[112] F. Lemmer, S. Raach, D. Schlipf, and R. F. Guzmán. *Definition of the SWE-TripleSpar Floating Platform for the DTU 10MW Reference Wind Turbine*. Tech. rep. Univerisity of Stuttgart - Institute of Aircraft Design, 2016.

[113] *DNV-RP-0286 - Coupled analysis of floating wind turbines*. Recommended Practice. DNV, May 2019.

[114] M. Borg, A. Pegalajar-Jurado, H. Sarlak, F. J. Madsen, H. Bredmose, F. Lemmer, F. Borisade, M. Kretschmer, and Y. Wei. *LIFES50+ D4.7 - Models for advanced load effects and loads at component level*. Tech. rep. 2018.

[115] J. Jonkman and W. Musial. *Offshore Code Comparison Collaboration (OC3) for IEATask 23 Offshore WindTechnology and Deployment*. Tech. rep. NREL, Dec. 2010.

[116] ANSYS Inc. *AQWA Reference Manual*. Tech. rep. 2019.

[117] S. Santhakumar, C. Heuberger-Austin, H. Meerman, and A. Faaij. "Technological learning potential of offshore wind technology and underlying cost drivers". In: *Preprint* (Jan. 2022). DOI: `10.21203/rs.3.rs-1298062/v1`.

[118] M. Leimeister, M. Collu, and A. Kolios. "A fully integrated optimization framework for designing a complex geometry offshore wind turbine spar-type floating support structure". In: *Wind Energy Science* 7 (2022), pp. 259–281.

[119] A. Myhr, C. Bjerkseter, A. Ågotnes, and T. A. Nygaard. "Levelised cost of energy for offshore floating wind turbines in a life cycle perspective". In: *Renewable Energy* 66 (June 2014), pp. 714–728. DOI: `10.1016/j.renene.2014.01.017`.

[120] M. McKay, R. Beckman, and W Conover. "A Comparison of Three Methods for Selecting Values of Input Variables in the Analysis of Output From a Computer Code". In: *Technometrics* 21.2 (1979), pp. 239–245.

[121] K. Dalbey and G. Karystinos. "Fast Generation of Space-filling Latin Hypercube Sample Designs". In: *13th AIAA/ISSMO Multidisciplinary Analysis Optimization Conference* (Fort Worth, Texas). 2010.

[122] M. Waskom. *Visualizing regression models*. 2022. URL: `https://seaborn.pydata.org/tutorial/regression.html#visualizing-regression-models`.

[123] RSE - Ricerca Sistema Energetico. *ATLA EOLICO Nuovo - Atlante Eolico*. 2023. URL: `https://atlanteeolico.rse-web.it/start.phtml`.

[124] A. F. Haselsteiner, J. Lehmkuhl, T. Pape, K.-L. Windmeier, and K.-D. Thoben. "ViroCon: A software to compute multivariate extremes using the environmental contour method". In: *SoftwareX* 9 (Jan. 2019), pp. 95–101. DOI: `10.1016/j.softx.2019.01.003`.

[125] *DNVGL-RP-C205 - Environmental conditions and environmental loads*. Recommended Practice. DNVGL, 2017.

[126] A. F. Haselsteiner, A. Sander, J.-H. Ohlendorf, and K.-D. Thoben. "Global Hierarchical Models for Wind and Wave Contours: Physical Interpretations of the Dependence Functions". In: *Volume 2A: Structures, Safety, and Reliability*. American Society of Mechanical Engineers, Aug. 2020. DOI: `10.1115/omae2020-18668`.

[127] R. C. Ramachandran, C. Desmond, F. Judge, J.-J. Serraris, and J. Murphy. "Floating offshore wind turbines: Installation, operation, maintenance and decommissioning challenges and opportunities". In: *Wind Energy Science - Discussions* (Oct. 2021). DOI: 10.5194/wes-2021-120.

[128] A. Maximiano, G. Vaz, R. Torres, L. Voltá, and T. Lourenço. *D5.4 Benchmark of PivotBuoy Compared to Other Offshore Wind Floating Systems*. en. Tech. rep. PivotBuoy. DOI: 10.13140/RG.2.2.31161.65120.

[129] Y. Mahfouz, M. Salari, F. Vigara, S. Hernandez, C. Molins, P. Trubat, H. Bredmose, and A. Pegalajar-Jurado. *COREWIND D1.3 - Public design and FAST models of the two 15MW floater-turbine concepts*. 2020. DOI: 10.5281/ZENODO.4385727.